

AD-A093 517

DNA 5073F

ESTIMATES OF THERMAL RADIATION ENVIRONMENTS FOR PLANNING A THERMAL SIMULATION ON A HE TEST

Burton S. Chambers, III
John A. Hasdal
Science Applications, Inc.
P.O. Box 1303
McLean, Virginia 22102

30 March 1979

Final Report for Period 17 April 1978–31 December 1978

CONTRACT No. DNA 001-78-C-0204

APPROVED FOR PUBLIC RELEASE;
DISTRIBUTION UNLIMITED.

THIS WORK SPONSORED BY THE DEFENSE NUCLEAR AGENCY
UNDER RDT&E RMSS CODE B344078462 H42AAXSX31002 H2590D.

Prepared for
Director
DEFENSE NUCLEAR AGENCY
Washington, D. C. 20305

Destroy this report when it is no longer needed. Do not return to sender.

PLEASE NOTIFY THE DEFENSE NUCLEAR AGENCY,
ATTN: STTI, WASHINGTON, D.C. 20305, IF
YOUR ADDRESS IS INCORRECT, IF YOU WISH TO
BE DELETED FROM THE DISTRIBUTION LIST, OR
IF THE ADDRESSEE IS NO LONGER EMPLOYED BY
YOUR ORGANIZATION.



UNCLASSIFIED

SECURITY CLASSIFICATION OF THIS PAGE (When Data Entered)

UNCLASSIFIED

SECURITY CLASSIFICATION OF THIS PAGE(When Data Entered)

UNCLASSIFIED

SECURITY CLASSIFICATION OF THIS PAGE(When Data Entered)

PREFACE

The research reported herein was directed towards producing information needed for experimental planning of a high explosive (HE) field test simulating synergistic effects on targets due to air blast and thermal radiation. Estimates were made of the thermal radiation environment from a 1 kiloton surface burst, and some planning and analyses were performed that will assist future placement of thermal radiation simulation devices in a HE test.

The principal investigator for this effort was Mr. Burton S. Chambers, III, principally assisted by Dr. John A. Hasdal who developed and coded the models used to predict the nuclear thermal radiation environments. Mr. John Dishon provided the description and data on the SAI thermal radiation simulator, as well as fruitful discussions on results of past experiments he performed.

Special thanks are given to Dr. Walter F. Dudziak of Information Science, Inc., for providing thermal radiation data from some nuclear shots. The authors also thank Mr. Tom Kennedy, who monitored the technical performance of this effort for the Defense Nuclear Agency, for his helpful guidance and suggestions.

Conversion factors for U.S. customary
to metric (SI) units of measurement.

To Convert From	To	Multiply By
atmosphere (normal)	kilo pascal (kPa)	1.013 25 X E +2
bar	kilo pascal (kPa)	1.000 000 X E +2
calorie (thermochemical)	joule (J)	4.184 000
cal (thermochemical)/cm ²	mega joule/m ² (MJ/m ²)	4.184 000 X E -2
erg	joule (J)	1.000 000 X E -7
erg/second	watt (W)	1.000 000 X E -7
foot	meter (m)	3.048 000 X E -1
inch	meter (m)	2.540 000 X E -2
kilotons	terajoules	4.183
pound-force/inch ² (psi)	kilo pascal (kPa)	6.894 757

TABLE OF CONTENTS

<u>Section</u>		<u>Page</u>
	PREFACE.....	1
	LIST OF ILLUSTRATIONS.....	5
	LIST OF TABLES.....	16
1	INTRODUCTION.....	17
2	THERMAL RADIATION ENVIRONMENTS FROM A NUCLEAR 1 KT SURFACE BURST.....	18
	2.1 AFWL PREDICTIONS AND MODELS OF THE THERMAL RADIATION FROM A NUCLEAR BURST.....	18
	2.2 CALCULATION OF THE THERMAL RADIATION ENVIRONMENTS ON THE GROUND.....	33
	2.3 RESULTS FROM SAI THERML CODE.....	49
	2.4 UNCERTAINTIES IN THE ESTIMATES OF NUCLEAR THERMAL RADIATION.....	60
3	RADIATIVE OUTPUT FROM THERMAL RADIATION SIMULATION DEVICES.....	67
	3.1 THE SAI THERMAL RADIATION SIMULATOR.....	67
	3.2 COMPUTING THE RADIATIVE OUTPUT OF TRS DEVICES.....	81
	3.3 NEED FOR ADDITIONAL CHARACTERIZATION.....	87
4	TRS PLACEMENT IN AN AIRBLAST ENVIRONMENT.....	91
	4.1 OBTAINING THE FLUENCE AND FLUX.....	93
	4.2 SHOCK INTERACTIONS WITH FIREBALL.....	97
	4.3 EFFECT OF OTHER EXPERIMENTS.....	107
	4.4 NEED FOR ADDITIONAL WORK.....	110
5	CONCLUSIONS AND RECOMMENDATIONS.....	113
	REFERENCES.....	117

TABLE OF CONTENTS
(continued)

<u>Section</u>	<u>Page No.</u>
APPENDICES	
A - ESTIMATE OF THERMAL RADIATION FROM A 1 KILOTON NUCLEAR SURFACE BURST DETECTOR ELEVATION 0 DEGREES.....	119
B - ESTIMATE OF THERMAL RADIATION FROM A 1 KILOTON NUCLEAR SURFACE BURST DETECTOR ELEVATION 30 DEGREES.....	139
C - ESTIMATE OF THERMAL RADIATION FROM A 1 KILOTON NUCLEAR SURFACE BURST DETECTOR ELEVATION 60 DEGREES.....	159
D - ESTIMATE OF THERMAL RADIATION FROM A 1 KILOTON NUCLEAR SURFACE BURST DETECTOR ELEVATION 90 DEGREES.....	179

LIST OF ILLUSTRATIONS

<u>Figure No.</u>		<u>Page No.</u>
1	Sharp's fit to SPUTTER data compared with SPUTTER results (at sea level) for time to second maximum.....	21
2	Sharp's fit to SPUTTER data compared with SPUTTER results (at sea level) for power out at second maximum.....	22
3	FB21 radius of pressure peaks.....	24
4	FB21 power out (cal/sec).....	25
5	FB21 energy radiated.....	26
6	Thermal power as a function of yield.....	27
7	Thermal power for FB-21 (1 kt at sea level)....	30
8	Thermal power for FB-7A (198 kt at sea level)..	31
9	Comparison of function result with blackbody spectra for 0 km burst altitude.....	32
10	Thermal spectrum for FB-21 (1 kt at sea level). .	34
11	Thermal spectrum for FB-7A (198 kt at 9 km).....	35
12	General relationship of a detector at P to a truncated sphere at C.....	37
13	Fireball shape factor for hemisphere.....	45
14	Variation of δ with β	46
15	Detector orientation.....	52
16	Effect of detector orientation on flux.....	53

LIST OF ILLUSTRATIONS
(continued)

<u>Figure No.</u>		<u>Page No.</u>
17	Effect of detector orientation on fluence.....	54
18	1 KT surface burst : detector facing GZ.....	55
19	1 KT surface burst : detector facing GZ.....	56
20	1 KT surface burst : detector facing up.....	57
21	1 KT surface burst : detector facing up.....	58
22	Thermal efficiencies (radius at 2nd max).....	63
23	Thermal efficiencies (radius at early time)....	64
24	An early E-system TRS module.....	69
25	Photograph of an early E-system TRS module.....	70
26	The effect of the O ₂ /HE weight ratio on TRS fluence of E-system TRS modules.....	72
27	Scaled power curves for two E-system TRS designs.....	75
28	A 4 module vertical C-system TRS array.....	77
29	A 12 module vertical E-system TRS array.....	78
30	Normalized power outputs of multiple module TRS arrays.....	80
31	Geometry for computing contribution from k th source.....	83
32	Orientation of detector and thermal simulator module.....	85
33	Variation of geometric view factor with number of source points for thermal simulator module.....	86
34	Ensemble of thermal radiation simulator modules.....	88

LIST OF ILLUSTRATIONS
(continued)

<u>Figure No.</u>		<u>Page No.</u>
35	Effect of range on geometrical view factor.....	89
36	Contours of estimated maximum geometric view factors from an 8-module ensemble (normalized to output from one module).....	90
37	Fireball radius-time model for 1 KT surface burst (and 1 KT free-field).....	92
38	An example of module placement.....	95
39	Airblast interaction with TRS device fireball..	98
40	Idealization in one-dimension of shock propagating through fireball.....	99
41	Comparison of velocity at observer approximately 2 meters beyond fireball.....	102
42	Comparison of velocity at observer approximately 7 meters beyond fireball.....	103
43	Comparison of overpressure at observer approximately 7 meters beyond fireball.....	104
44	Comparison of overpressure at observer approximately 5 meters in <u>front</u> of fireball.....	105
45	Comparison of velocity at observer approximately 5 meters in <u>front</u> of fireball.....	106
46	An example calculation.....	108
47	An example experimental layout.....	109
48	Possible effect of confinement on fireball growth.....	111
49	Fluence from 1 kt surface burst crossing detector with orientation 0 degrees at 30.48 meters ground range.....	120

LIST OF ILLUSTRATIONS
(continued)

<u>Figure No.</u>		<u>Page No.</u>
50	Flux from 1 kt surface burst crossing detector with orientation 0 degrees at 30.48 meters ground range.....	121
51	Average flux from 1 kt surface burst crossing detector with orientation 0 degrees at 30.48 meters ground range.....	122
52	Fluence from 1 kt surface burst crossing detector with orientation 0 degrees at 60.96 meters ground range.....	123
53	Flux from 1 kt surface burst crossing detector with orientation 0 degrees at 60.96 meters ground range.....	124
54	Average flux from 1 kt surface burst crossing detector with orientation 0 degrees at 60.96 meters ground range.....	125
55	Fluence from 1 kt surface burst crossing detector with orientation 0 degrees at 91.44 meters ground range.....	126
56	Flux from 1 kt surface burst crossing detector with orientation 0 degrees at 91.44 meters ground range.....	127
57	Average flux from 1 kt surface burst crossing detector with orientation 0 degrees at 91.44 meters ground range.....	128
58	Fluence from 1 kt surface burst crossing detector with orientation 0 degrees at 152.4 meters ground range.....	129
59	Flux from 1 kt surface burst crossing detector with orientation 0 degrees at 152.4 meters ground range.....	130
60	Average flux from 1 kt surface burst crossing detector with orientation 0 degrees at 152.4 meters ground range.....	131

LIST OF ILLUSTRATIONS
(continued)

<u>Figure No.</u>		<u>Page No.</u>
61	Fluence from 1 kt surface burst crossing detector with orientation 0 degrees at 304.8 meters ground range.....	132
62	Flux from 1 kt surface burst crossing detector with orientation 0 degrees at 304.8 meters ground range.....	133
63	Average flux from 1 kt surface burst crossing detector with orientation 0 degrees at 304.8 meters ground range.....	134
64	Fluence from 1 kt surface burst crossing detector with orientation 0 degrees at 609.6 meters ground range.....	135
65	Flux from 1 kt surface burst crossing detector with orientation 0 degrees at 609.6 meters ground range.....	136
66	Average flux from 1 kt surface burst crossing detector with orientation 0 degrees at 609.6 meters ground range.....	137
67	Fluence from 1 kt surface burst crossing detector with orientation 30 degrees at 30.48 meters ground range.....	140
68	Flux from 1 kt surface burst crossing detector with orientation 30 degrees at 30.48 meters ground range.....	141
69	Average flux from 1 kt surface burst crossing detector with orientation 30 degrees at 30.48 meters ground range.....	142
70	Fluence from 1 kt surface burst crossing detector with orientation 30 degrees at 60.96 meters ground range.....	143
71	Flux from 1 kt surface burst crossing detector with orientation 30 degrees at 60.96 meters ground range.....	144

LIST OF ILLUSTRATIONS
(continued)

<u>Figure No.</u>		<u>Page No.</u>
72	Average flux from 1 kt surface burst crossing detector with orientation 30 degrees at 60.96 meters ground range.....	145
73	Fluence from 1 kt surface burst crossing detector with orientation 30 degrees at 91.44 meters ground range.....	146
74	Flux from 1 kt surface burst crossing detector with orientation 30 degrees at 91.44 meters ground range.....	147
75	Average flux from 1 kt surface burst crossing detector with orientation 30 degrees at 91.44 meters ground range.....	148
76	Fluence from 1 kt surface burst crossing detector with orientation 30 degrees at 152.4 meters ground range.....	149
77	Flux from 1 kt surface burst crossing detector with orientation 30 degrees at 152.4 meters ground range.....	150
78	Average flux from 1 kt surface burst crossing detector with orientation 30 degrees at 152.4 meters ground range.....	151
79	Fluence from 1 kt surface burst crossing detector with orientation 30 degrees at 304.8 meters ground range.....	152
80	Flux from 1 kt surface burst crossing detector with orientation 30 degrees at 304.8 meters ground range.....	153
81	Average flux from 1 kt surface burst crossing detector with orientation 30 degrees at 304.8 meters ground range.....	154
82	Fluence from 1 kt surface burst crossing detector with orientation 30 degrees at 609.6 meters ground range.....	155

LIST OF ILLUSTRATIONS
(continued)

<u>Figure No.</u>		<u>Page No.</u>
83	Flux from 1 kt surface burst crossing detector with orientation 30 degrees at 609.6 meters ground range.....	156
84	Average flux from 1 kt surface burst crossing detector with orientation 30 degrees at 609.6 meters ground range.....	157
85	Fluence from 1 kt surface burst crossing detector with orientation 60 degrees at 30.48 meters ground range.....	160
86	Flux from 1 kt surface burst crossing detector with orientation 60 degrees at 30.48 meters ground range.....	161
87	Average flux from 1 kt surface burst crossing detector with orientation 60 degrees at 30.48 meters ground range.....	162
88	Fluence from 1 kt surface burst crossing detector with orientation 60 degrees at 60.96 meters ground range.....	163
89	Flux from 1 kt surface burst crossing detector with orientation 60 degrees at 60.96 meters ground range.....	164
90	Average flux from 1 kt surface burst crossing detector with orientation 60 degrees at 60.96 meters ground range.....	165
91	Fluence from 1 kt surface burst crossing detector with orientation 60 degrees at 91.44 meters ground range.....	166
92	Flux from 1 kt surface burst crossing detector with orientation 60 degrees at 91.44 meters ground range.....	167
93	Average flux from 1 kt surface burst crossing detector with orientation 60 degrees at 91.44 meters ground range.....	168

LIST OF ILLUSTRATIONS
(continued)

<u>Figure No.</u>		<u>Page No.</u>
94	Fluence from 1 kt surface burst crossing detector with orientation 60 degrees at 152.4 meters ground range.....	169
95	Flux from 1 kt surface burst crossing detector with orientation 60 degrees at 152.4 meters ground range.....	170
96	Average flux from 1 kt surface burst crossing detector with orientation 60 degrees at 152.4 meters ground range.....	171
97	Fluence from 1 kt surface burst crossing detector with orientation 60 degrees at 304.8 meters ground range.....	172
98	Flux from 1 kt surface burst crossing detector with orientation 60 degrees at 304.8 meters ground range.....	173
99	Average flux from 1 kt surface burst crossing detector with orientation 60 degrees at 304.8 meters ground range.....	174
100	Fluence from 1 kt surface burst crossing detector with orientation 60 degrees at 609.6 meters ground range.....	175
101	Flux from 1 kt surface burst crossing detector with orientation 60 degrees at 609.6 meters ground range.....	176
102	Average flux from 1 kt surface burst crossing detector with orientation 60 degrees at 609.6 meters ground range.....	177
103	Fluence from 1 kt surface burst crossing detector with elevation 90 degrees at 30.48 meters ground range.....	180
104	Flux from 1 kt surface burst crossing detector with orientation 90 degrees at 30.48 meters ground range.....	181

LIST OF ILLUSTRATIONS
(continued)

<u>Figure No.</u>		<u>Page No.</u>
105	Average flux from 1 kt surface burst crossing detector with orientation 90 degrees at 30.48 meters ground range.....	182
106	Fluence from 1 kt surface burst crossing detector with orientation 90 degrees at 60.96 meters ground range.....	183
107	Flux from 1 kt surface burst crossing detector with orientation 90 degrees at 60.96 meters ground range.....	184
108	Average flux from 1 kt surface burst crossing detector with orientation 90 degrees at 60.96 meters ground range.....	185
109	Fluence from 1 kt surface burst crossing detector with orientation 90 degrees at 91.44 meters ground range.....	186
110	Flux from 1 kt surface burst crossing detector with orientation 90 degrees at 91.44 meters ground range.....	187
111	Average flux from 1 kt surface burst crossing detector with orientation 90 degrees at 91.44 meters ground range.....	188
112	Fluence from 1 kt surface burst crossing detector with orientation 90 degrees at 152.4 meters ground range.....	189
113	Flux from 1 kt surface burst crossing detector with orientation 90 degrees at 152.4 meters ground range.....	190
114	Average flux from 1 kt surface burst crossing detector with orientation 90 degrees at 152.4 meters ground range.....	191
115	Fluence from 1 kt surface burst crossing detector with orientation 90 degrees at 304.8 meters ground range.....	192

LIST OF ILLUSTRATIONS
(continued)

<u>Figure No.</u>		<u>Page No.</u>
116	Flux from 1 kt surface burst crossing detector with orientation 90 degrees at 304.8 meters ground range.....	193
117	Average flux from 1 kt surface burst crossing detector with orientation 90 degrees at 304.8 meters ground range.....	194
118	Fluence from 1 kt surface burst crossing detector with orientation 90 degrees at 609.6 meters ground range.....	195
119	Flux from 1 kt surface burst crossing detector with orientation 90 degrees at 609.6 meters ground range.....	196
120	Average flux from 1 kt surface burst crossing detector with orientation 90 degrees at 609.6 meters ground range.....	197

LIST OF TABLES

<u>Table No.</u>		<u>Page No.</u>
1	SPUTTER runs used in generating AFWL thermal output model.....	20
2	SPUTTER data from FB21 usertape (1 kt free-field at sea level).....	48
3	Overpressures and arrival times.....	59
4	Approximate values of fluence and flux at shock arrival.....	61
5	Aluminum oxidation reactions.....	68
6	Computational parameters.....	100

SECTION 1

INTRODUCTION

An important difference between a nuclear explosion (NE) and a chemical high explosive (HE) is the relatively large amount of energy released during the nuclear explosion in the form of thermal radiation. Synergistic effects due to air blast and thermal radiation are known to exist. These effects have been difficult to obtain in the field primarily due to the lack of large scale thermal simulation devices that produce significant radiative output.

SAI has been developing a large scale thermal radiation simulator for DNA, and it seems feasible to now consider fielding such arrays on a planned HE event, MISTY CASTLE. This program was conducted to develop data and guidelines that will assist future experimental planning.

SAI accomplished two tasks in preparation for planning an HE field simulation of a low yield nuclear event detonating on the ground. The objective of the first task was to provide a description of the thermal radiation environments that are to be simulated in the HE event. The objective of the second task was to provide a first look at how an ensemble of DNA thermal simulation devices might be positioned to achieve an acceptable simulation at various ground ranges from the HE detonation site without seriously distorting the airblast flow fields. The results from these two tasks are expected to help guide subsequent test planning and lay the foundation for estimating reasonable expectations for success in achieving combined thermal and airblast environments.

SECTION 2

THERMAL RADIATION ENVIRONMENT FROM A NUCLEAR 1 KT SURFACE BURST

A general description of the radiative output characteristics from a nuclear weapon can be found in references 1 and 2. However, more detailed theoretical predictions of thermal radiation from free-air nuclear explosions have been modeled and were used for this effort. The models for the fireball thermal radiative output are described in Section 2.1. How these were utilized is described in Section 2.2. Results of calculations using these models are presented in Section 2.3 (and the appendices). Finally, in Section 2.4 a discussion is presented of possible uncertainties that may exist from effects not modeled. An example of such an effect is the interaction of the radiation with the ground and how this might influence the radiative output of the fireball. This effect is important to this effort since the simulation is of a surface burst.

2.1 THE AFWL PREDICTIONS AND MODELS OF THE THERMAL RADIATION FROM A NUCLEAR BURST

The Air Force Weapons Laboratory conducted a seven year theoretical effort (1963-1970) to predict early time fireball growth* (i.e., times from x-ray deposition into the cold air surrounding the nuclear device to a time at least ten times that of second maximum) using a code called SPUTTER (see references 3 and 4). As a result of the AFWL effort, detailed radiative and hydrodynamic environments could be predicted for singular nuclear weapons bursting at various altitudes from 0 to 60 km in the atmosphere. Weapon yields ranged from 20 tons to 100 megatons. The predictions were free-field (i.e., no account was

*Under sponsorship by DASA, ARPA and the Air Force.

taken of presence of the ground) computer calculations, which now serve as an extensive fireball data base. They agree well with experimental data taken in the late 50's and early 60's in the U.S. above-ground nuclear testing (references 5 and 6).

Some of the important features of the SPUTTER results were then modeled at the AFWL in the early 70's in order to obtain simple algorithms (references 7 and 8). For example at sea level the power out at second maximum from a free-field nuclear fireball was found to be well represented by

$$P = 3.53 \times 10^{12} W^{0.59} \text{ cal/sec} \quad (1)$$

where W = total yield in kt. Similarly the time to second maximum at sea level is well represented by

$$t_{2\max} = 0.038 W^{0.44} \text{ seconds.} \quad (2)$$

For 1 kt the AFWL algorithm agrees quite well with the SPUTTER calculation at 0 km. Table 1 lists the SPUTTER calculations serving as a data base for the AFWL modeling study of radiative output. Each entry represents a detailed one-dimensional radiative hydrodynamics computation taking over 50 hours on a CDC 6600 using SPUTTER. The calculations employ many electromagnetic frequency groups (typically 20) to represent thermal radiation since grey body approximations were found to be inadequate (reference 5); hence a large computation time results when coupled with zoning requirements for modeling the hydrodynamics.

The agreement of the AFWL algorithm for power and time at second maximum with SPUTTER is quantitatively good as indicated by Figures 1 and 2. Where the SPUTTER data are considered reliable, the AFWL models are good representations. Results of the FB21 SPUTTER calculation used in the AFWL study, are included and show results for a 1 kt free-field (no yield doubling, see Section 2.3) burst detonating at sea level (0 km altitude).*

*These results have to be scaled to be used for a 1 kt surface burst.

Table 1. SPUTTER runs used in generating
AFWL thermal output model.

Extracted from Reference 7

Ident (FB No.)	Simulated Yield (kt)	Detonation Alt		
		Air Density (gm/cm ³)	Ratio of Air Density to Density at Sea Level	Altitude (km)
20	0.1 (0.094)*	1.225E-03	1	0**
21	1 (1)	1.225E-03	1	0
2	10 (10)	8.253E-05	0.06737	20.3
14	30 (30)	1.225E-03	1	0
11	30 (30)	1.161E-04	0.09477	18.3
23	30 (30)	1.355E-05	0.01106	32
19	30 (30)	1.351E-06	0.001103	48.3
7A	198 (198)	1.225E-03	1	0
13	198 (199)	4.587E-04	0.37445	9.1
3F	198 (200)	1.308E-04	0.106776	18.3
5	198 (200)	1.356E-05	0.01107	32
S2	198 (199)	7.2579E-06	0.0059248	36
S5	198 (200)	4.6267E-06	0.0037769	39
15	198 (198)	3.996E-06	0.003262	40
S4	198 (198)	3.4564E-06	0.002821	41
S3	198 (197)	2.995E-06	0.002445	42
S1	198 (197)	2.2589E-06	0.001844	43
1B	198 (198)	1.351E-06	0.001103	48
12	1000 (993)	1.161E-04	0.09477	18.3
10	3800 (3843)	1.225E-03	1	0
18	3800 (3776)	1.161E-04	0.09477	18.3
9	3800 (3773)	2.780E-06	0.0022694	43
26	3800 (3773)	1.269E-06	0.001036	48.3
25	155000 (155000)	1.161E-04	0.09477	18.3

*Numbers in parentheses are yields based on the total energy as determined during the actual SPUTTER CALCULATION.

**This altitude corresponds to sea level. However, there is no account of ground in the SPUTTER calculations, they are free-field.

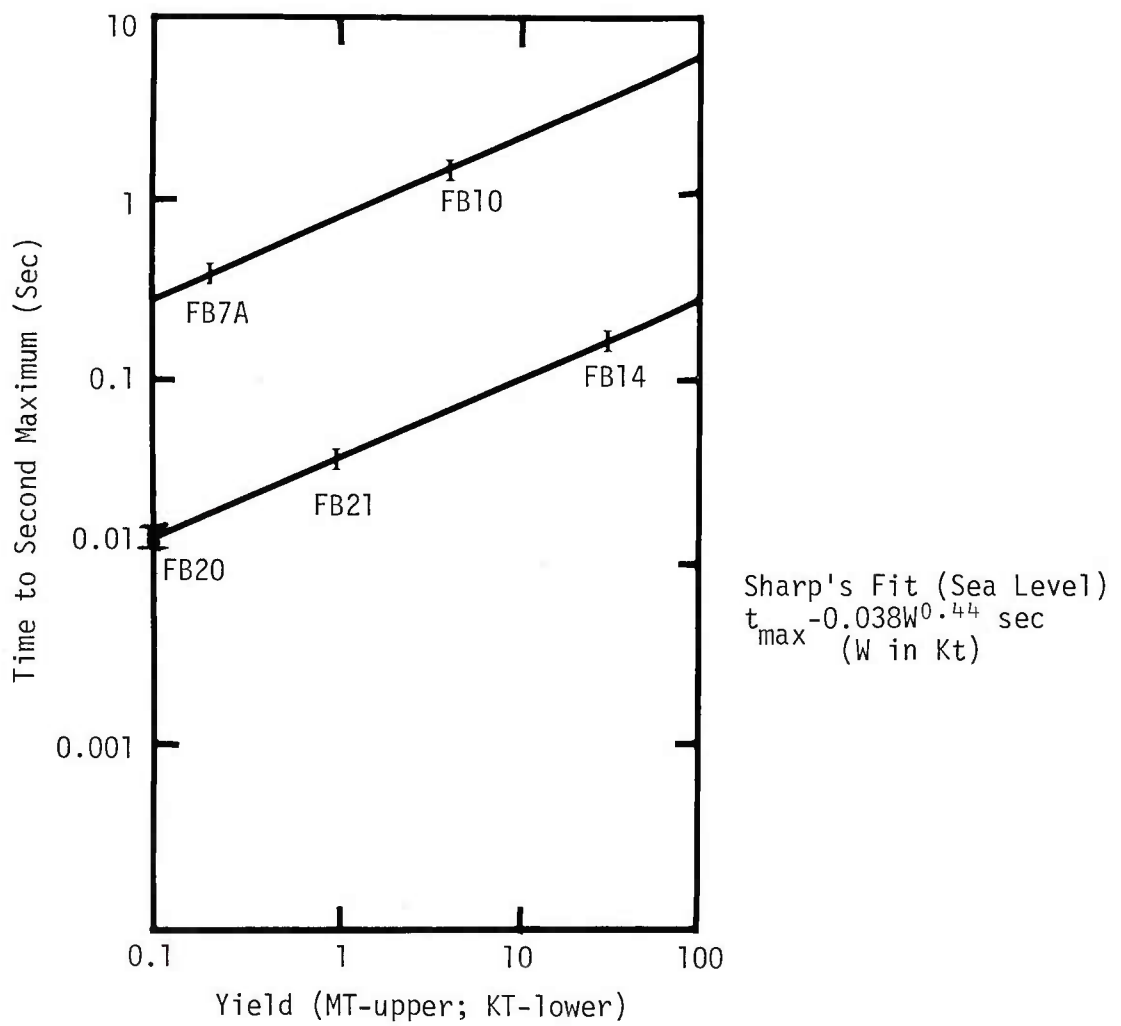
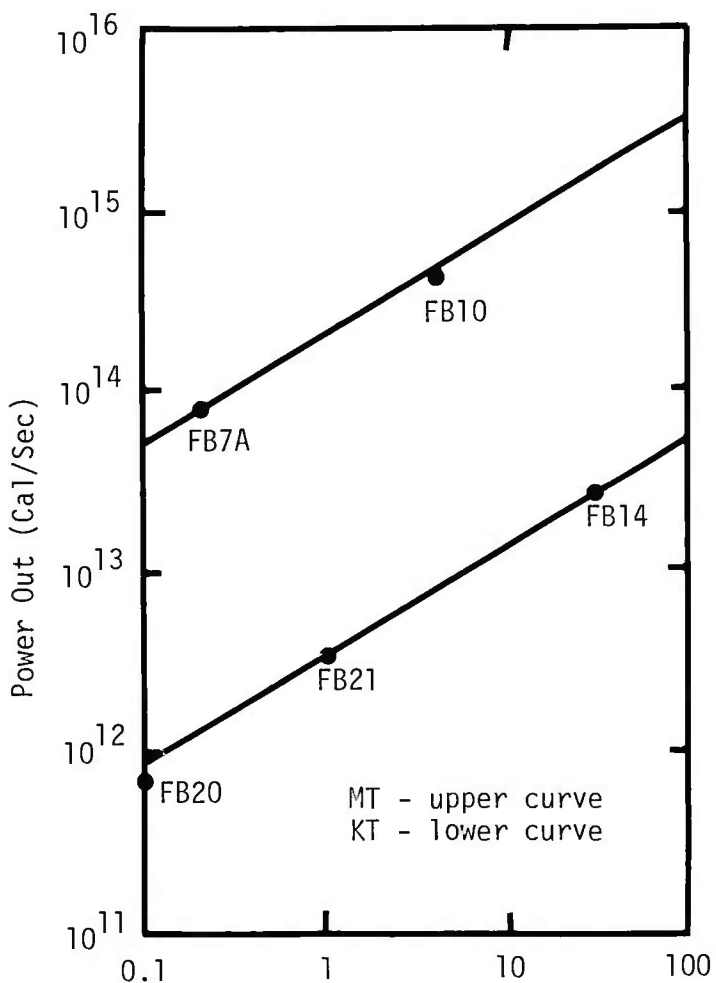


Figure 1. Sharp's fit to SPUTTER data compared with SPUTTER results (at sea level) for time to second maximum.



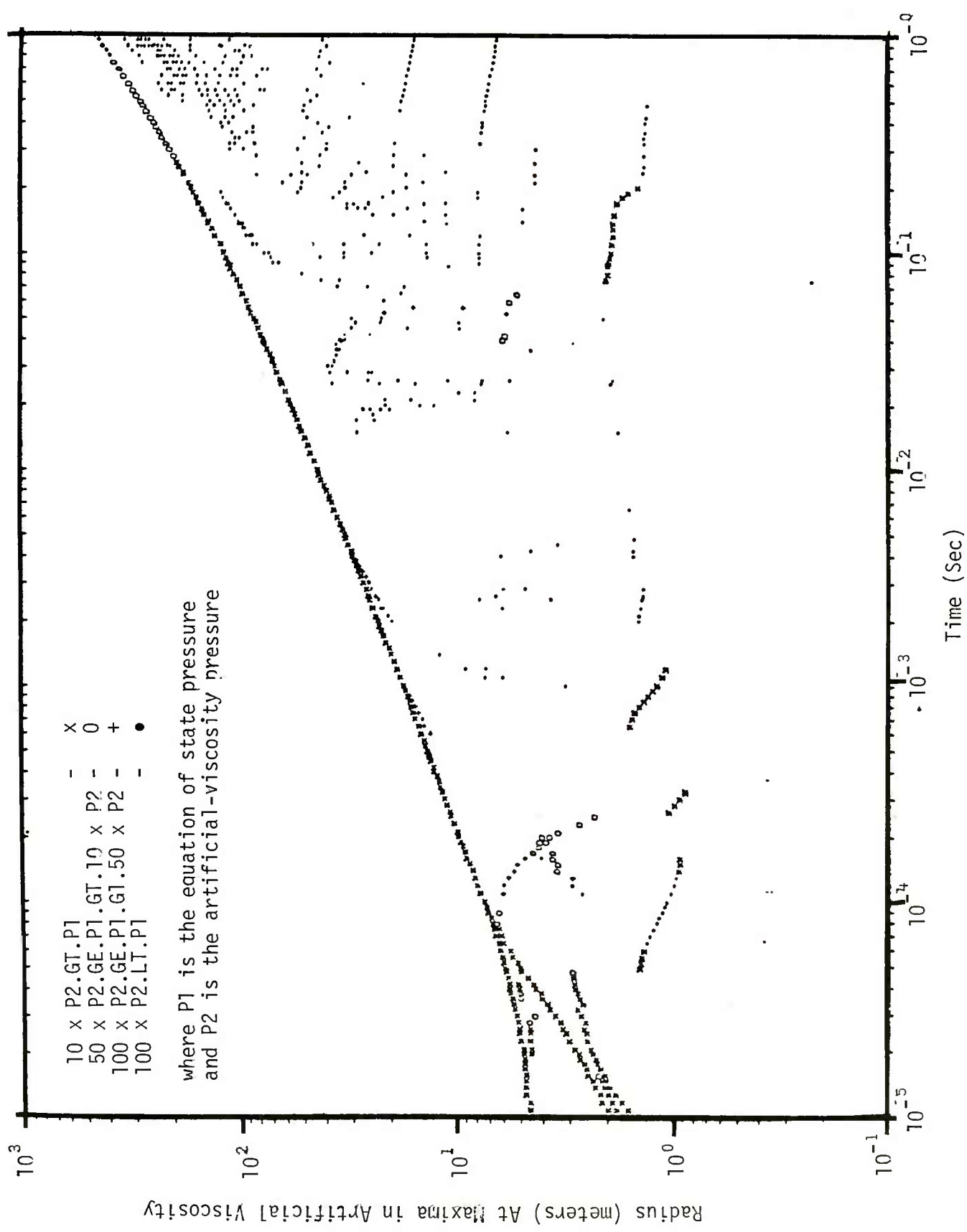
Sharp's Fit: (Sea Level Power Out $3.53E12W^{0.59}$
cal / sec) (W in Kt)

Figure 2. Sharp's fit to SPUTTER data compared with SPUTTER results (at sea level) for power out at second maximum.

Figure 3 presents the radius of various pressure fronts versus time for this same calculation, and is shown as a frame of reference to briefly familiarize the reader with the calculation. The very early fireball is about 4 m in radius. As the fireball develops and grows radiatively, the air in front of the hot radiating fireball starts to shock, and as this air shock develops it becomes optically opaque so that for some time the fireball and air shock appear to grow together. At about 0.07 msec the faster moving debris shock catches up with the main air shock and this interaction reinforces the main shock reflecting another shock back towards the burst point.* At some time after debris shock arrival (not obvious from the figure) the air shock breaks away from the fireball. Both continue to grow, the fireball slower than the air shock. Finally, fireball growth is slowed appreciably as it comes into pressure equilibrium and the main air shock continues on. At some intervening time (tens of msec) the shock no longer is optically opaque and the true interior fireball can be seen. Until such time, the apparent fireball was the air shock. Figure 4 presents the corresponding time sequence of power out from the FB21 fireball and it clearly shows the second maximum. First minimum occurs near 3 milliseconds. Figure 5 is the total energy radiated away from the fireball; approximately 35% of the yield has been thermally radiated by 1 second. Data shown for times earlier than 1 millisecond are unreliable, as will be discussed later.

The AFWL model also provides the time and yield dependence of the radiative output. Figure 6 shows the power radiated from 10^{-7} seconds to 100 seconds for seven different yields. The power radiated out is seen to be yield dependent although the ratio of total radiation to total yield

*This shock "reflects" from the center and moves outward again. The process repeats, with shocks becoming weaker, and leads to many weak pressure fronts seen in Figure 3. The coarse zoning tends to smear these fronts leaving numerical noise. The criteria for representing a pressure front are based on the relative values of the artificial viscosity pressure, P_2 , and the equation-of-state pressure, P_1 .



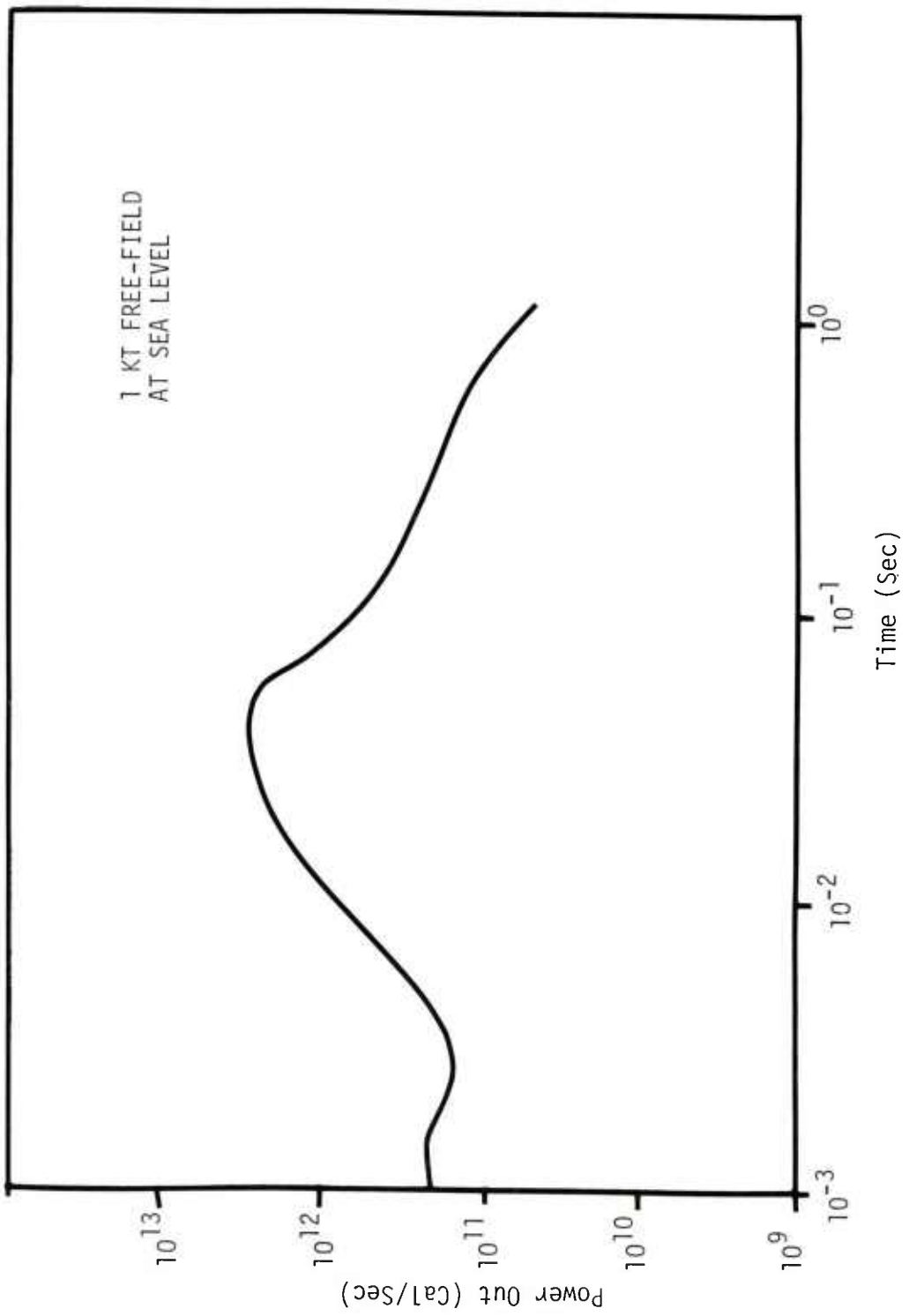


Figure 4. FB21 power out (cal/sec).
(1 Kt at sea level)

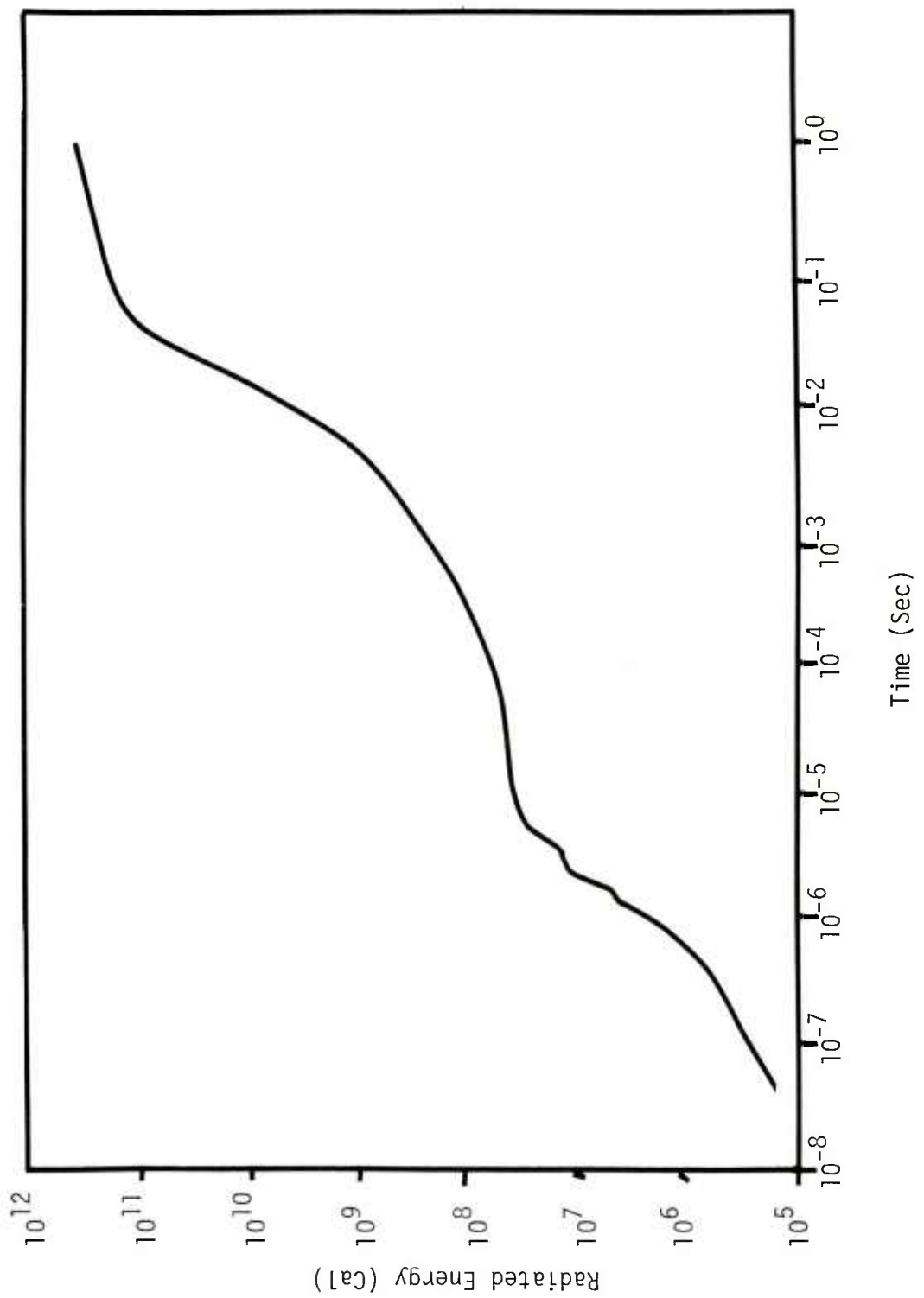


Figure 5. FB21 energy radiated.

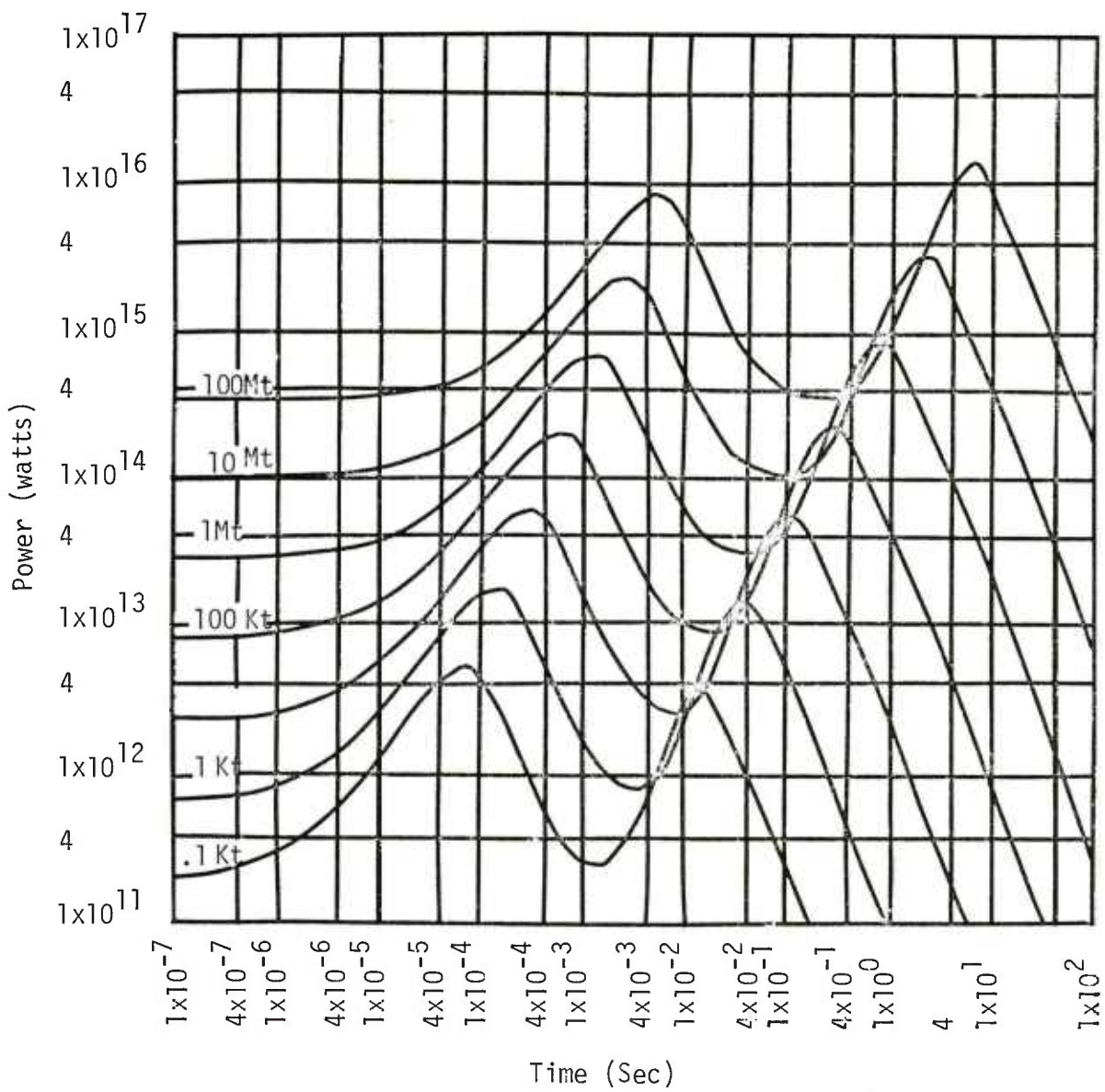


Figure 6. Thermal power from free-field burst at sea level as a function of yield. (Extracted from reference 7).

is relatively the same at both small and large yields. However, even though the total radiation to yield ratio is fairly constant, it is inappropriate to conclude that total fluence will scale with yield in the same fashion as the hydrodynamics scale. As can be easily demonstrated, higher yields will produce higher total fluence*at the same hydrodynamically scaled range; this total fluence will scale as $W^{1/3}$. Consider a nuclear device of yield, W , detonating above the ground at scaled height, h , and ground range, r . Distance in all directions can be scaled, where

$$\text{Scaled distance} \equiv \frac{\text{true distance}}{W^{1/3}} .$$

This scaling is useful since airblast at any position becomes relatively insensitive to yield. But the fluence arriving at comparatively scaled positions is proportional to the product of the thermal efficiency, ϵ , and yield, W , divided by R^2 .** Since ϵ is only weakly dependent on yield,*** total fluence remains approximately proportional to $W^{1/3}$ at a fixed hydrodynamically scaled range.

Instantaneous flux is not so simply scaled, since the time phasing of the radiated power is complex. If the time to second maximum is proportional to $W^{0.44}$ then the time shift in hydrodynamically scaled time****will be $W^{0.11}$. The flux at second maximum scales as $W^{-0.08}$ when comparing hydrodynamically scaled ranges. A comparison can be made between the data in Figure 4 and the 1 kiloton curve in Figure 6 (1 cal/sec \cong 4.2 watts) and is shown as Figure 7. The

*Fluence is sometimes called radiant exposure and is the energy per unit area incident on some target surface. Conventionally its units are cal/cm².

**Since the height of burst and ground range have all been proportionally scaled as $W^{1/3}$, the angle of arrival for the radiation is scale independent.

***The AFWL fit for sea level efficiency is $0.3505W^{0.0253}$ where W is the yield in kilotons (reference 7).

****Scaled time = $\frac{\text{true time}}{W^{1/3}}$.

SPUTTER data represented by the circles, are not shown for first maximum because they are not considered reliable. Inspection of the very early time SPUTTER power data by the authors (not shown in this report) shows that the radiated power oscillates rapidly about the expected values. This is due to the zoning used in the SPUTTER calculations which is inadequate to accurately represent radiation fronts at those times. Since the mean free path of the dominant radiation at early times is of the order of tenths of centimeters, zones of tens of meters in size will either be too transparent or opaque and will rapidly change from transparent to opaque to transparent again as the radiation front moves through any cell. This will alternately allow too much radiation to leak out, and then too little. For the first maximum, nuclear data were used to suggest the relationships established (see reference 7).

The agreement between the AFWL model and the detailed SPUTTER power data for FB21 are reasonable, although, there are significant variations beyond the time of second maximum as was seen in Figure 7. The AFWL model produces better agreement with the SPUTTER data for large yields as seen in Figure 8 showing a 200 kiloton calculation. However, this effort addresses low yields, so the effect of these inaccuracies is considered.

The spectral content of the radiation is also yield dependent. This is shown in Figure 9, which also shows the spectral content of three blackbodies (6000, 3000, and 2450 degrees Kelvin). This figure represents another AFWL model of the SPUTTER data. The SPUTTER calculations included the calculation of the radiative transport through the fireball for a number of intervals in the electromagnetic spectrum (typically 20), hence spectral data are available averaged over these intervals. Details of the intervals used can be found in references 4, 5, 6 and 8. For comparison the same two representative calculations shown above were chosen to illustrate the agreement between the AFWL model of the time dependence of the spectrum. FB21 (1 kt at sea level)

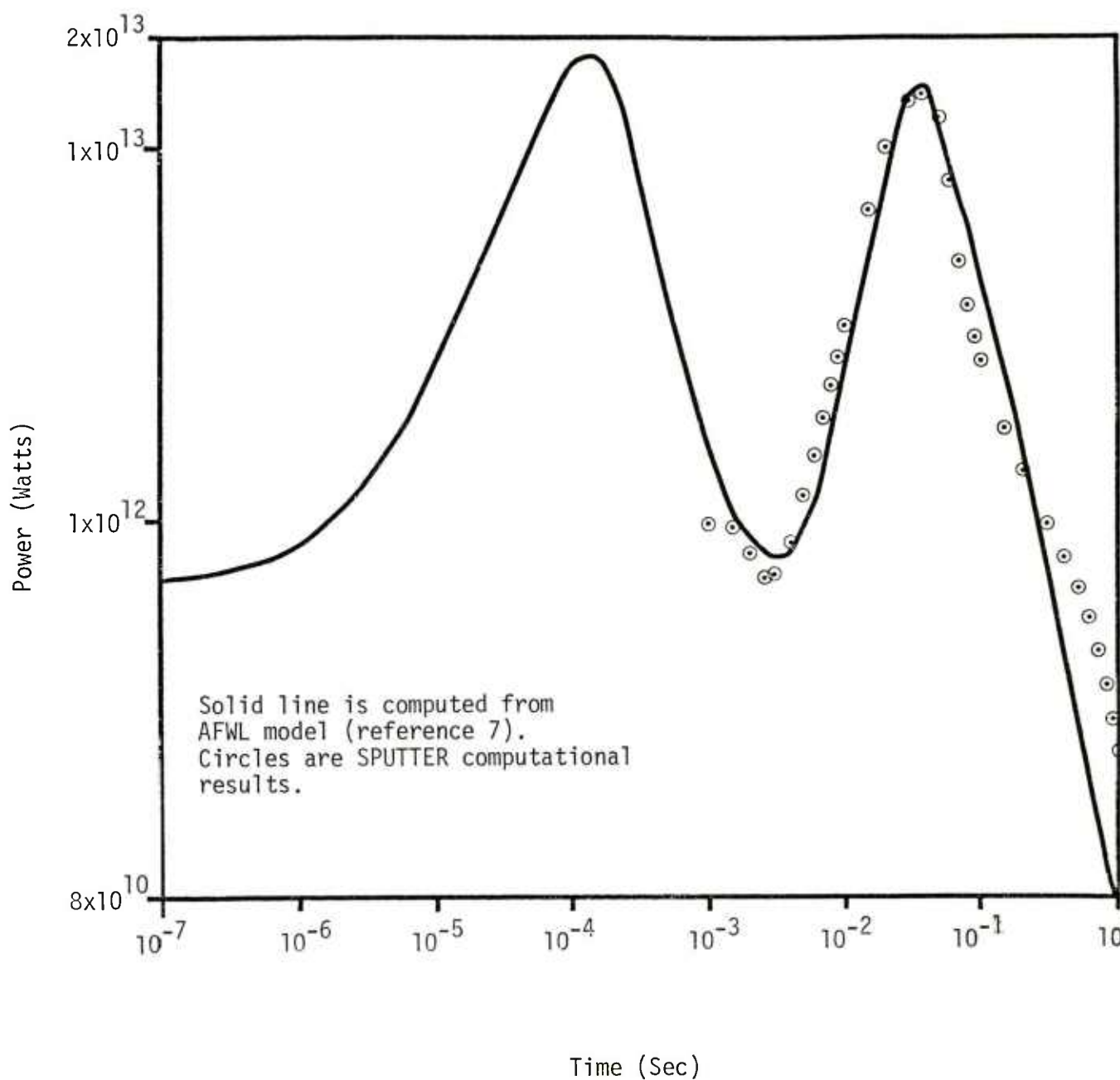


Figure 7. Thermal power for FB-21 (1 kt at sea level).

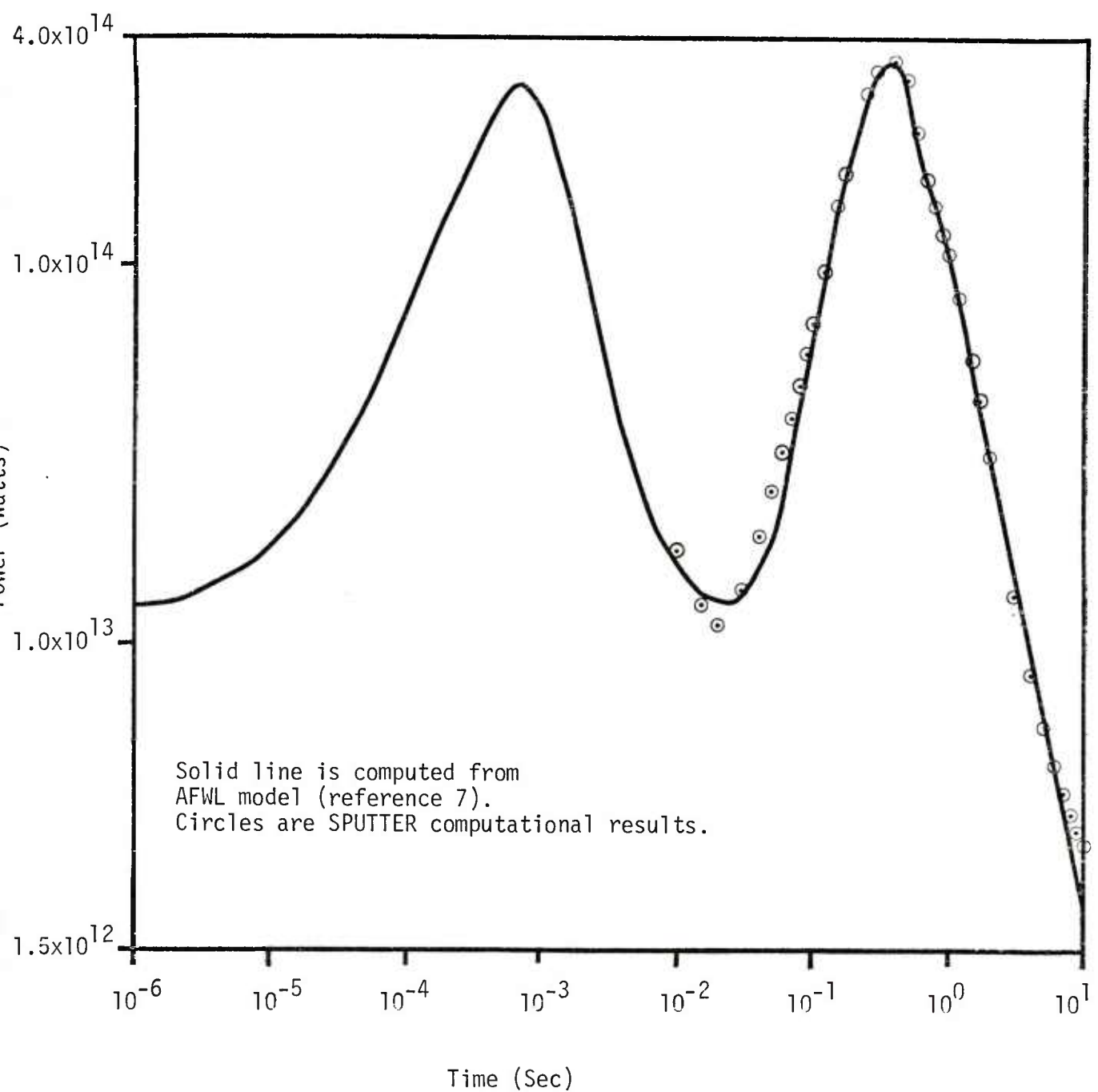


Figure 8. Thermal power for FB-7A (198 kt at sea level)
(Extracted from reference 7).

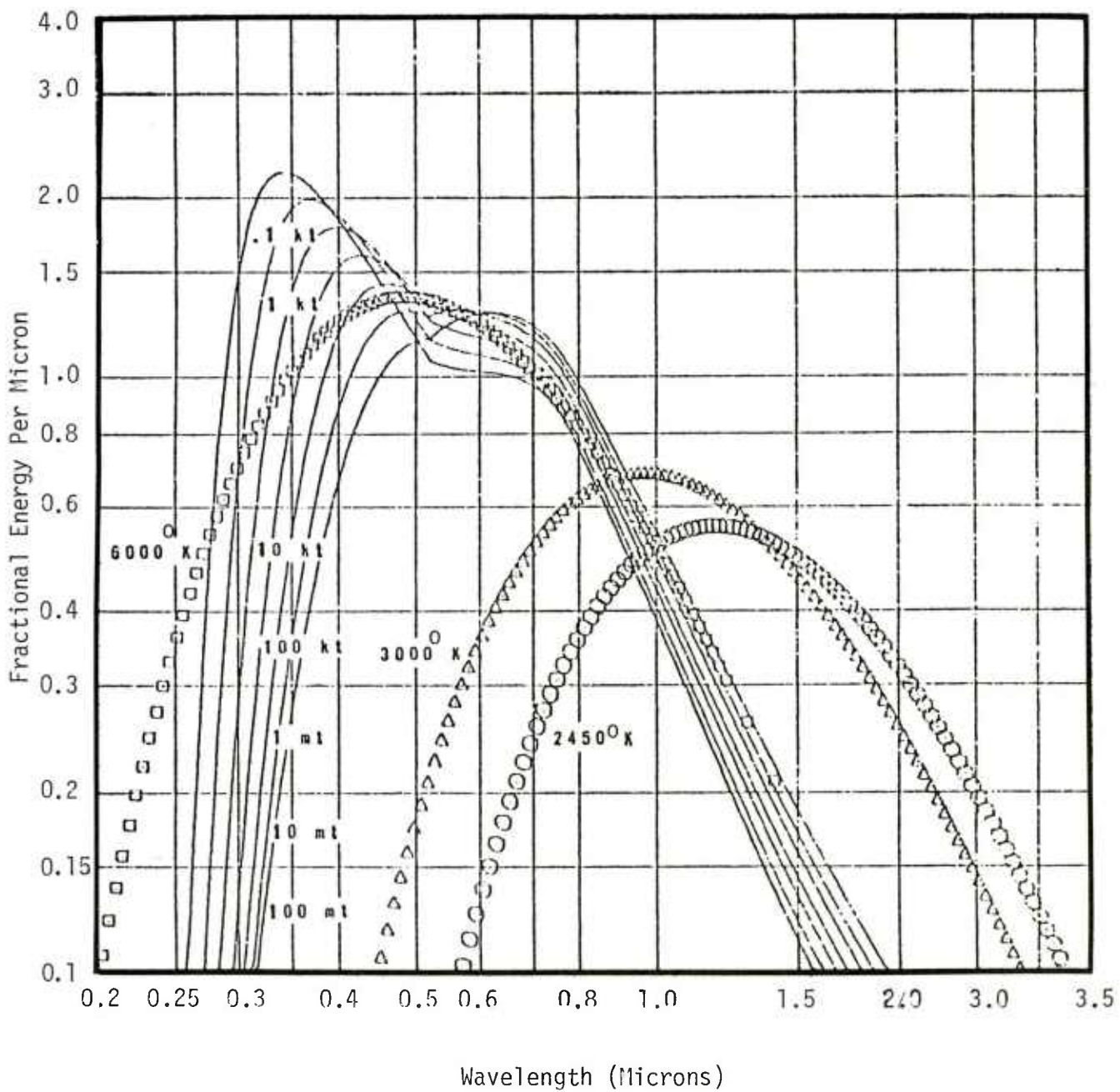


Figure 9. Comparison of function result with blackbody spectra for 0 km burst altitude.
 (Extracted from reference 8, Figure 64.)

is shown as Figure 10 and FB7A (200 kt at sea level) is shown as Figure 11. The circles are again the specific SPUTTER data used by the AFWL in the generation of their models. Here again the agreement for the 200 kiloton yield is definitely better than that for 1 kiloton. The SPUTTER calculation suggests a hotter fireball for 1 kiloton than obtained from the AFWL model.

Additional information on these calculations and models can be found in References 3 through 8.

2.2 CALCULATION OF THE THERMAL RADIATION ENVIRONMENTS ON THE GROUND

Once the details of the radiative output of the nuclear weapon fireball are available, the problem of calculating the radiation reaching a detector located outside of the fireball becomes one of appropriately integrating over the sources of radiation, assuming propagation path absorption and scattering are insignificant (references 9 and 10). For the ranges involved here (i.e., 250 m or closer) for 1 kiloton, total power absorption is insignificant on a clear day when visibility is high. When visibility is low it can become significant. For example, when the visibility is 1 mile the transmittance is about 0.8 for a range of 250 m.

For the effort reported here the fireball was approximated as an isotropic surface emitter. Since the interest at DNA is simulating a 1 kiloton surface burst, certain geometric simplifications were possible when integrating over the surface of the fireball to obtain detector radiation. These simplifications are discussed within Section 2.2.3. The following derivation, which is more general than that needed for the surface burst case, is for a detector whose normal is in the plane perpendicular to the earth and containing the points of detection and burst.

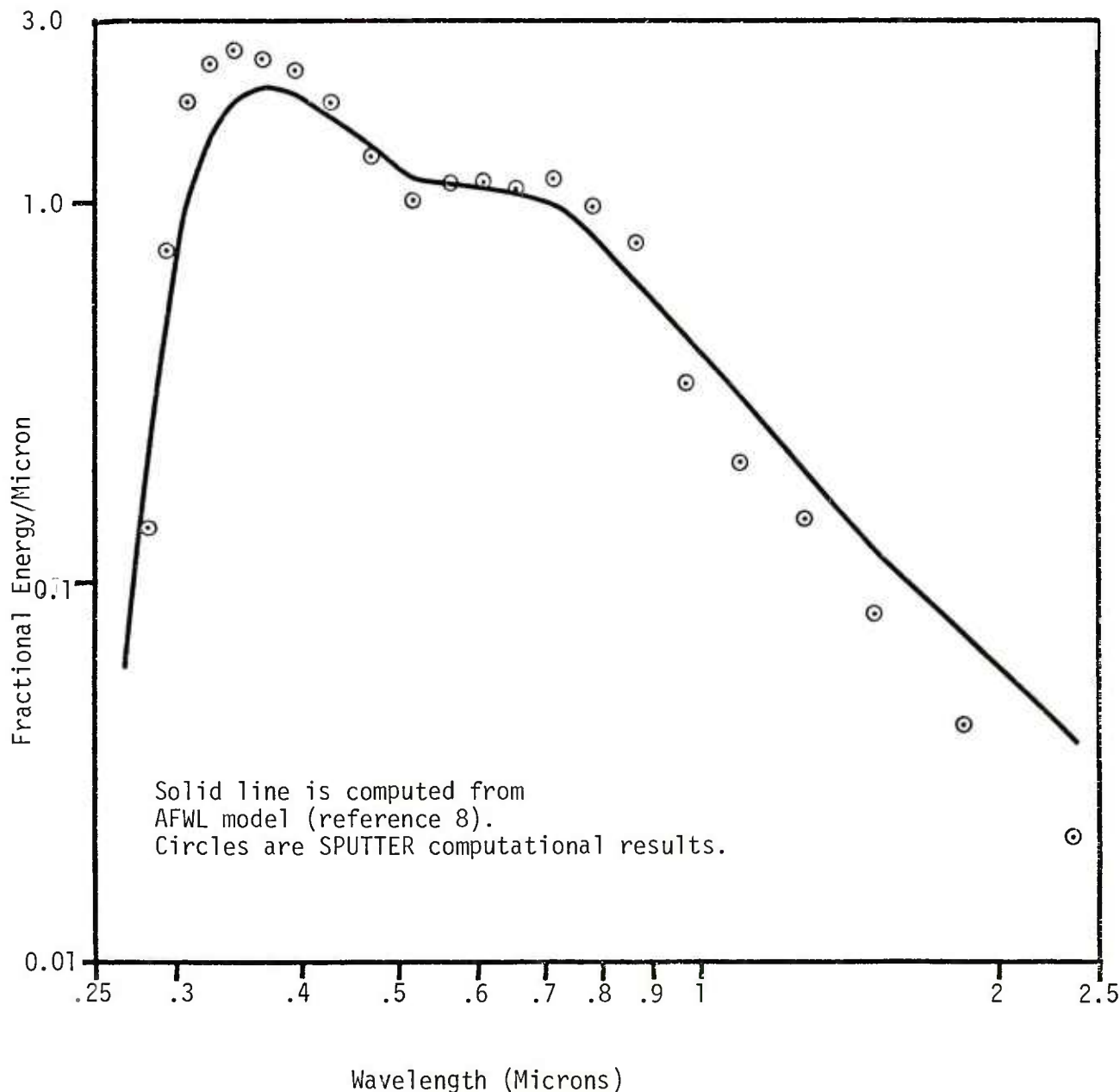


Figure 10. Thermal spectrum for FB-21 (1 kt at sea level).
(Extracted from reference 8)

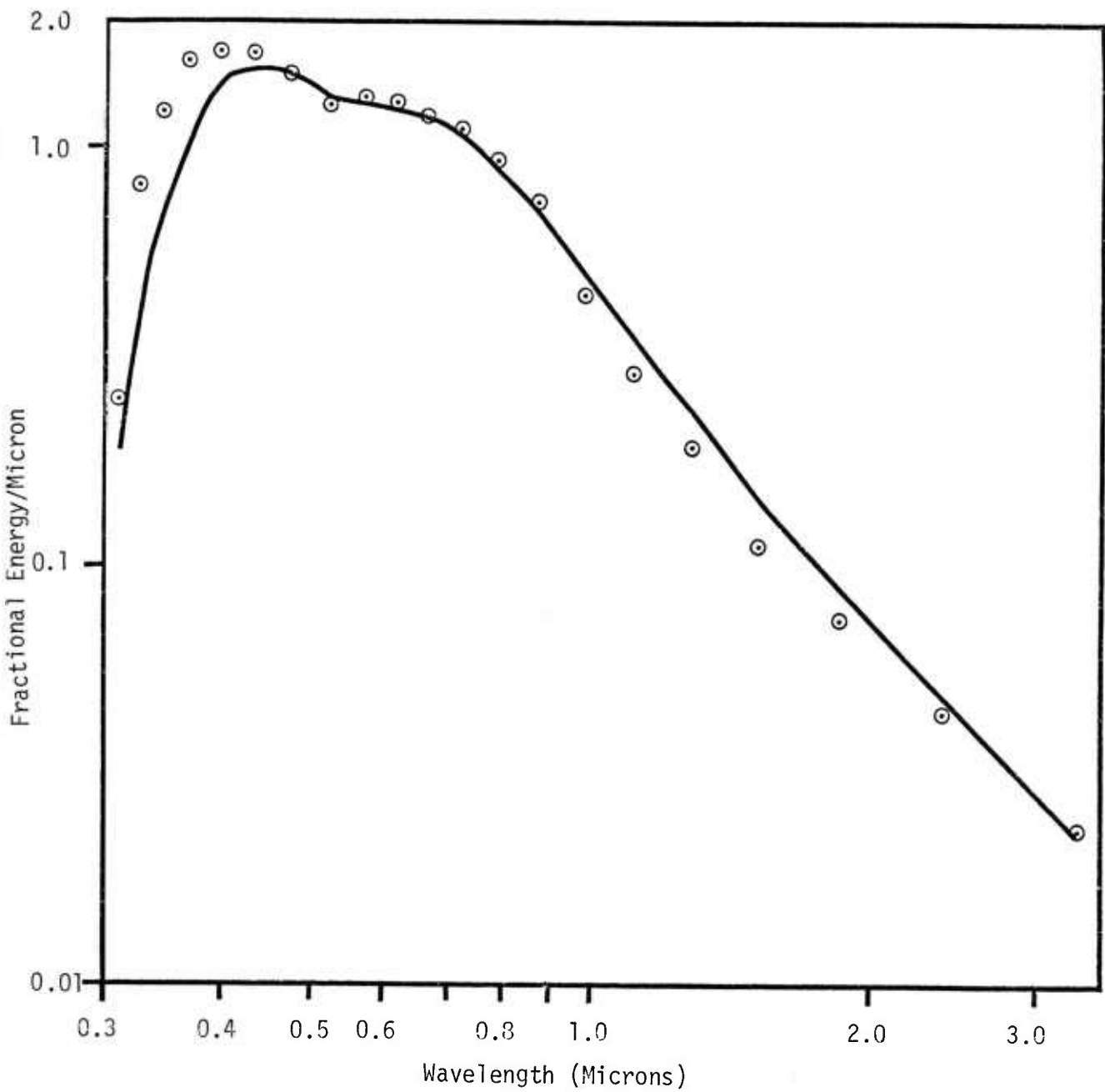


Figure 11. Thermal spectrum for FB-7A (198 kt at 9 km).
(Extracted from reference 8).

2.2.1 Formulation for the Truncated Radiating Sphere

A field point P (Figure 12) is positioned on a ground plane a distance r from the center of a sphere a distance h above the ground plane. The surface of the sphere is assumed to be a diffuse isotropic radiator; if the line segment, R , connects the field point and an element, dA , of the surface of the sphere, then the radiation from dA in the direction of the field point is proportional to $\cos\mu$, where μ is the angle between R and the outward normal to dA . The radiation from dA which is intercepted by a detector placed at P is proportional to $\cos\beta$, where β is the angle between R and the normal to the detector. It is required that $\alpha \leq (\pi/2)$; for $\alpha > (\pi/2)$ the detector truncates the sphere to less than a hemisphere.

Using the notation of Figure 12, the total flux incident on the detector can be expressed as:

$$F(\alpha, r, h, B) = S \int_A \cos\beta \frac{\cos\mu}{\pi} \frac{dA}{R^2} \quad (3)$$

where

F is the flux at the detector in $\text{cal-cm}^{-2}\text{-sec}^{-1}$

S is the spherical surface radiation rate $\text{cal-cm}^{-2}\text{-sec}^{-1}$, and for this analysis is independent of the position on the surface of the sphere

α is the angle between r and the detector normal

B is the radius of the sphere in cm

and A is the area of the spherical surface which is above the ground plane and visible from P.

To evaluate this integral the various line segments, angles, and integration limits must be expressed in terms of the constant quantities α, r, h, B and the integration variables θ, ϕ . These expressions include

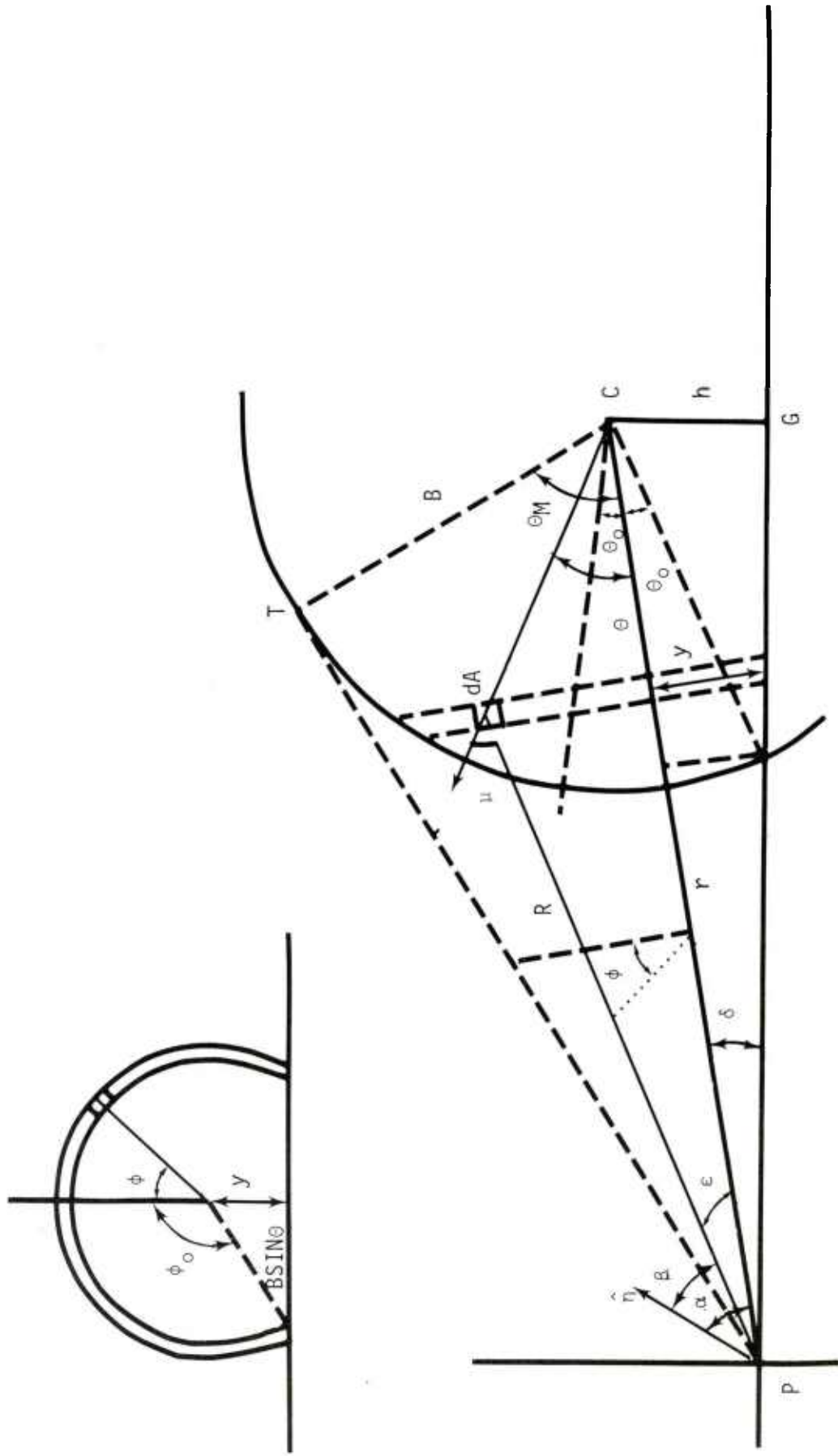


Figure 12. General relationship of a detector at P to a truncated sphere at C .

$$R = (r^2 + B^2 - 2rB\cos\theta)^{\frac{1}{2}} \quad (4)$$

$$\beta = \beta(\alpha, \varepsilon, \phi) \quad (5)$$

$$\varepsilon = \varepsilon(\theta) \quad (6)$$

$$\mu = \mu(\varepsilon, \theta), \mu = \theta + \varepsilon \quad (7)$$

for the integration limits

$$0 \leq \theta \leq \theta_M \quad (8)$$

$$\theta_M = \cos^{-1}(B/r) \quad (9)$$

$$0 \leq \phi \leq \phi_0 \quad (10)$$

$$\phi_0 = \pi \text{ if } \theta \leq \theta_0 \quad (11)$$

The remaining relations are developed in the following discussion.

The spherical triangle relation can be used to express β in terms of other variables as

$$\cos\beta = \cos\alpha\cos\varepsilon + \sin\alpha\sin\varepsilon\cos\phi. \quad (12)$$

Forming a pair of right triangles from the triangle which contains the angles ε, θ , it is seen that

$$R\sin\varepsilon = B\sin\theta. \quad (13)$$

The small diagram in the upper left of the figure is used to obtain one relation for the line segment, y ; that is:

$$y = B\sin\theta\cos(\pi - \phi_0) \quad (14)$$

where $B\sin\theta$ is the radius of the partial ring of elemental areas at $\theta_0 \leq \theta \leq \theta_M$, between $(-\phi_0, \phi_0)$. From the larger diagram, the relation for y is:

$$y = \tan\delta(r - B\cos\theta) \quad (15)$$

where

$$\delta = \sin^{-1}(h/r). \quad (16)$$

Equating these expressions for y yields:

$$\phi_0 = \cos^{-1} \left\{ -\tan\delta(r - B\cos\theta)/(B\sin\theta) \right\}, \quad (17)$$

which expression is the integration limit on the ϕ integral for $\theta_0 \leq \theta \leq \theta_M$. Using the triangle formed by (P,C,G), it is seen that

$$\delta + \theta_0 + \cos^{-1}(h/B) = \pi/2 \quad (18)$$

or

$$\theta_0 = \cos^{-1}(h/r) - \cos^{-1}(h/B). \quad (19)$$

The expression for the flux at the detector becomes

$$F = \frac{S}{\pi} \int_0^{\theta_M} \int_{-\phi_0}^{\phi_0} \cos\beta \cos\mu \frac{B^2}{R^2} \sin\theta d\phi d\theta \quad (20)$$

where

$$\phi_0 = \begin{cases} \pi & 0 \leq \theta \leq \theta_0 \\ \cos^{-1} \left\{ -\tan[\sin^{-1}(h/r)] (r - B\cos\theta)/(B\sin\theta) \right\} & \theta_0 \leq \theta \leq \theta_M \end{cases} \quad (21)$$

$$\theta_0 = \cos^{-1}(h/r) - \cos^{-1}(h/B) \quad (22)$$

$$\theta_M = \cos^{-1}(B/r) \quad (23)$$

$$\mu = \theta + \varepsilon \quad (24)$$

$$\varepsilon = \sin^{-1}(B \sin \theta / R) \quad (25)$$

$$\beta = \cos^{-1}(\cos \alpha \cos \varepsilon + \sin \alpha \sin \varepsilon \cos \phi) \quad (26)$$

$$R = (r^2 + B^2 - 2rB \cos \theta)^{\frac{1}{2}} \quad (27)$$

2.2.2 The Limit of the Tangent Sphere ($h = B$)

Before proceeding to the case of a surface burst, it is worthwhile to note the limiting case of the tangent sphere where $h = B$; the point source solution should result. Setting $h = B$ the integral simplifies to

$$F = \frac{S}{\pi} \int_0^{\theta_M} \int_{-\pi}^{\pi} \cos \mu \cos \beta \frac{B^2}{R^2} \sin \theta d\phi d\theta. \quad (28)$$

Substituting $\gamma = B/r$ and $\theta_M = \cos^{-1} \gamma$ and performing the integration over ϕ , the intermediate result is

$$F = \frac{S}{\pi} \int_0^{\cos^{-1} \gamma} \cos \mu \cos \alpha \cos \varepsilon \frac{2\pi \gamma^2}{(1+\gamma^2 - 2\gamma \cos \theta)} \sin \theta d\theta. \quad (29)$$

Substitution for μ, ε , and $\cos \theta = x$ yields the algebraic integral form

$$F = 2S\gamma^2 \cos \alpha \int_{\gamma}^1 \frac{[-\gamma + (1 + \gamma^2)x - \gamma x^2] dx}{(1 + \gamma^2 - 2\gamma x)^2}, \quad (30)$$

which results the relation

$$F = S\gamma^2 \cos\alpha = SB^2 \frac{\cos\alpha}{r^2}, \quad (31)$$

which is the point source solution, as expected.

2.2.3 The Limit of the Hemisphere ($h = 0$).

The limiting case of direct interest to this effort is that of a hemisphere wherein $h = 0$; in which case the general integral becomes

$$F = \frac{S}{\pi} \int_0^{\theta_M} \int_{-\pi/2}^{\pi/2} \cos\mu \cos\beta \frac{B^2}{R^2} \sin\theta d\phi d\theta \quad (32)$$

Performing the ϕ -integration and separating the terms with the factors $\cos\alpha$ and $\sin\alpha$, the integral becomes

$$\begin{aligned} F &= S \cos\alpha \int_0^{\theta_M} \cos\mu \cos\epsilon \frac{B^2}{R^2} \sin\theta d\theta \\ &+ S \frac{2}{\pi} \sin\alpha \int_0^{\theta_M} \cos\mu \sin\epsilon \frac{B^2}{R^2} \sin\theta d\theta, \end{aligned} \quad (33)$$

which may be expressed as

$$F = S \cos\alpha I_1 + S \frac{2}{\pi} \sin\alpha I_2, \quad (34)$$

where I_1 and I_2 are treated separately in the following

With the substitutions $\gamma = B/r$ and $x = \cos\theta$, the integral I_1 becomes

$$I_1 = \gamma^2 \int_{\gamma}^1 \frac{[-\gamma + (1 + \gamma^2)x - \gamma x^2]}{(1 + \gamma^2 - 2\gamma x)^2} dx, \quad (35)$$

or

$$I_1 = \gamma^2/2 = \frac{1}{2} \left(\frac{B}{r} \right)^2, \quad (36)$$

and the expression for F becomes* (37)

$$F = \frac{(SB^2)}{2} \frac{\cos\alpha}{r^2} + \frac{2S}{\pi} I_2 \sin\alpha \quad (37)$$

The substitutions $\gamma = B/r$ and $x = \cos\theta$ in integral I_2 result in the form

$$I_2 = \gamma^3 \int_{\gamma}^1 \frac{(x - \gamma)(1 - x^2)^{1/2}}{(1 + \gamma^2 - 2\gamma x)^2} dx. \quad (38)$$

The substitution $y' = 1 + \gamma^2 - 2\gamma x$ is helpful in evaluating I_2 , which becomes, after some manipulation,

$$I_2 = \frac{1}{2} (\sin^{-1}\gamma - \gamma (1 - \gamma^2)^{1/2}). \quad (39)$$

Expansion of both terms demonstrates that I_2 is of the order γ^3 which is anticipated from the original form of the integral.

*At this point it is to be noted that for $\alpha = 0$, the flux at the detector is one half that of the tangent sphere solution, which is to be expected from the symmetry for $\alpha = 0$.

Thus the flux at a detector at field point P for a radiating hemisphere is given by

$$F = \frac{SB^2}{2} \frac{\cos\alpha}{r^2} + \frac{S}{\pi} \sin\alpha \left\{ \sin^{-1} \frac{B}{r} - \frac{B}{r} \left[1 - \frac{B^2}{r^2} \right]^{\frac{1}{2}} \right\}, \quad (40)$$

which for $B \ll r$ is approximately

$$F \approx \frac{SB^2}{r^2} \left(\frac{\cos\alpha}{2} + \frac{2\sin\alpha}{3\pi} \frac{B}{r} \right). \quad (41)$$

2.2.4 Comparison of a Special Case for the Hemisphere with Prior Work.

A special case of the above was solved earlier by a number of investigators for the general case of a truncated sphere and a detector whose normal is perpendicular to the ground plane. For this case the flux, F' , at the detector when $h = 0$ is given (reference 11 or 12) in our notation as:

$$F' = S \left\{ \frac{1}{2} - \frac{1}{\pi} \sin^{-1} \left[\frac{\sqrt{(r/B)^2 - 1}}{(r/B)} \right] - \left[\frac{\sqrt{(r/B)^2 - 1}}{\pi(r/B)^2} \right] \right\}, \quad (42)$$

Converting this form to one similar to our analytical solution, recognizing $\alpha = \pi/2$, yields the comparison:

$$F = \frac{S}{\pi} \left\{ \sin^{-1} \frac{B}{r} - \frac{B}{r} \left[1 - \left(\frac{B}{r} \right)^2 \right]^{\frac{1}{2}} \right\} \quad (43)$$

$$F' = S \left\{ \frac{1}{2} - \frac{1}{\pi} \sin^{-1} \left[\sqrt{1 - \left(\frac{B}{r} \right)^2} \right] - \frac{1}{\pi} \frac{B}{r} \sqrt{1 - \left(\frac{B}{r} \right)^2} \right\}. \quad (44)$$

The last terms are seen to be identical, and by manipulating the first two terms in the relation for F' it is seen that the relations for F ($\alpha = \pi/2$) and F' are identities, as they should be.

2.2.5 Effect of Fireball Radius on the Geometrical Shape Factor.

For the case just analyzed, i.e., the hemispherical fireball radiating to a detector on the ground whose normal is perpendicular to the ground, Figure 9 shows the strong dependence of the radiation* on the ratio of the fireball radius to the detector's range from the burst point. The limit $\beta = 0$ corresponds to a point source on the ground, which will not give any radiation perpendicular to the ground surface. The radiation arriving at the same detector oriented towards the fireball does not depend on the fireball radius at all. In this case the flux will be constant no matter what the fireball radius is, as long as the power radiated from the whole fireball doesn't change. However, the geometrical shape factor as defined will be equal to $\frac{\beta^2}{2}$. It is suggestive, therefore, to also present the dependence of another quantity, call it δ , where $\delta \equiv \frac{K}{\beta^2}$. Since S was defined as the surface radiation flux from the hemispherical fireball surface, the power radiated out, p , is simply $2\pi S B^2$. Therefore δ is proportional to the flux arriving at the detector over the power being emitted, whence δ is a meaningful quantity. Figure 14 shows the dependence of δ on β . This plot shows that when the fireball is nearly on top of the detector, the orientation of the detector between these two limits has no effect on the received flux. At the other extreme, the smaller the fireball radius the greater the effect of detector orientation.

2.2.6 The Fireball Radius Model

Since the radiation received at a detector on the ground can be a strong function of the ratio of the fireball radius to detector ground range from ground zero, a reasonable model of the fireball radius was desirable. Initially, for validating the computer program

*Shown as a geometrical factor, that is equal to the flux (or fluence) crossing the detector divided by the flux (or fluence) emitted from the fireball's surface.

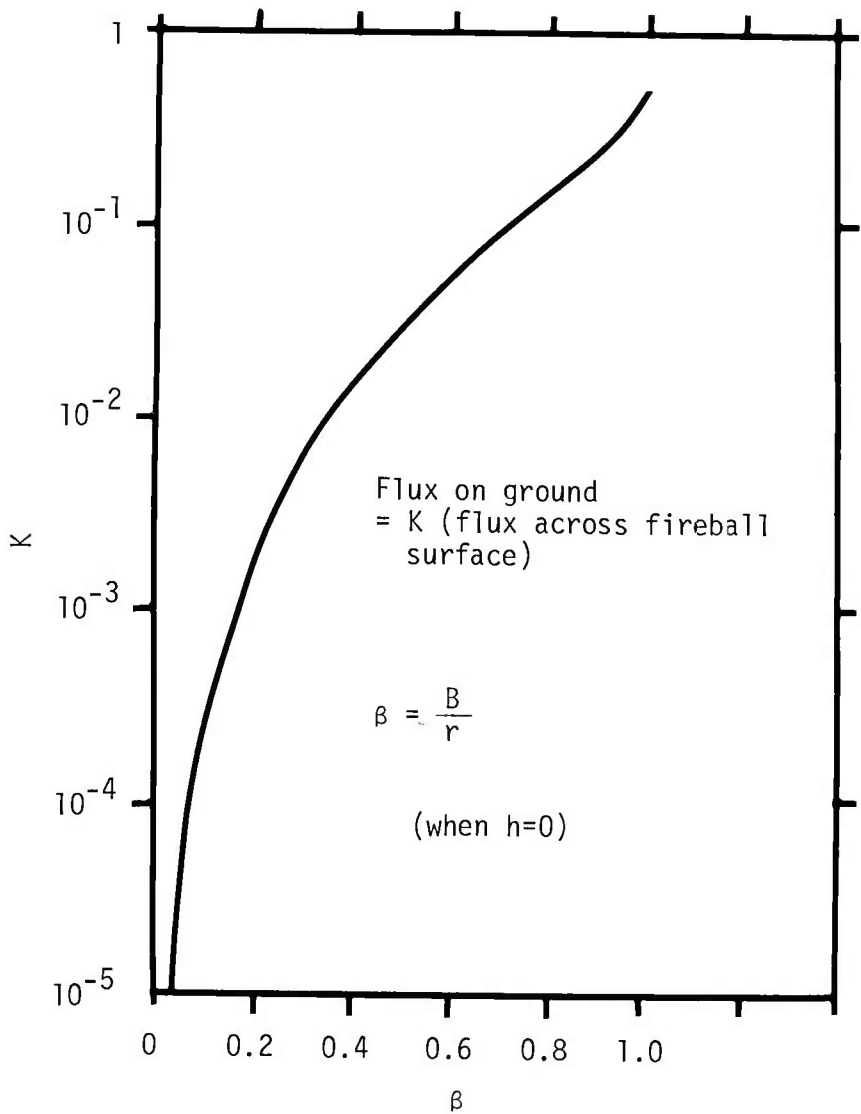


Figure 13. Fireball shape factor for hemisphere.

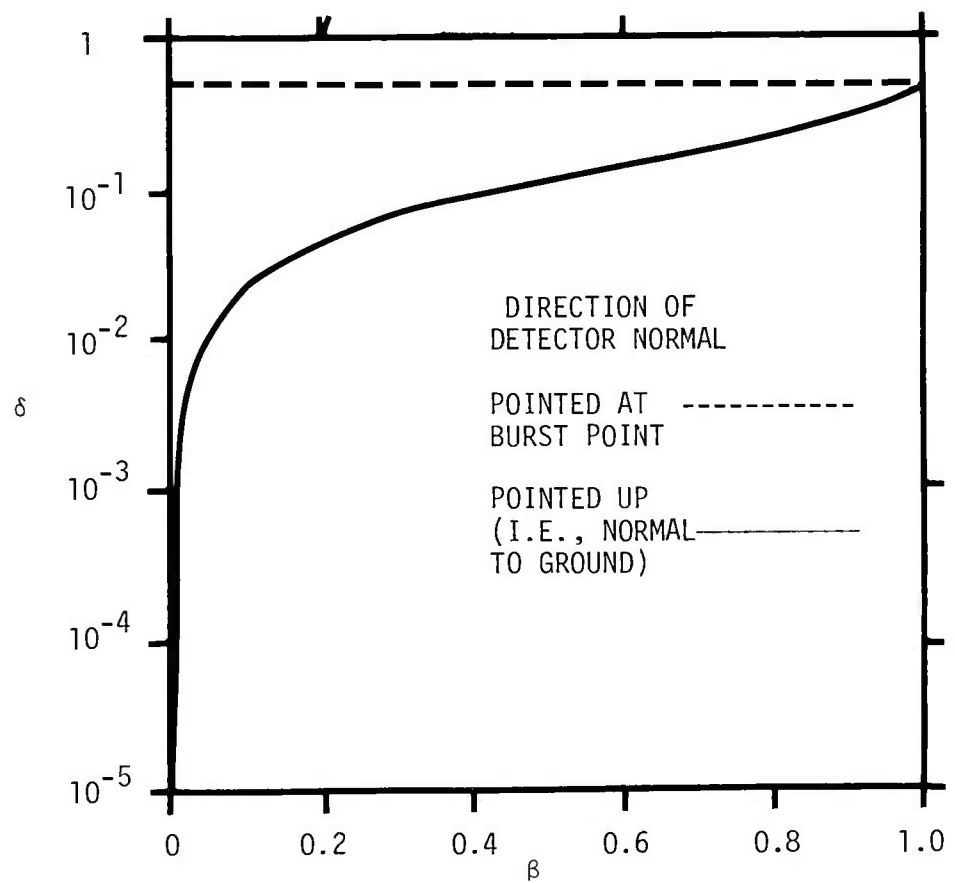


Figure 14. Variation of δ with β .

code, the LAMB fireball model was used, although the AFWL never intended it to represent the fireball radius accurately. To obtain more accurate thermal radiation estimates, another fireball radius model was required. Such a model was obtained using SPUTTER data available on the FB21 usertape.* These data were in the form of snapshots at certain times. Since the early time fireball was difficult to identify from these data, the LAMB fireball model was used for the early time. The LAMB fireball is only slightly smaller than the estimated radius up until 12 milliseconds when they are equal. For times beyond 12 milliseconds the LAMB fireball is certainly too large; and the model developed for this effort is much better. The new representation of the fireball radius should be valid up until about 600 milliseconds for a 1 kiloton free-field environment. It, therefore, provides data until 750 milliseconds when scaled to the 1 kiloton surface burst.

The fireball model used in this effort is presented here, and is defined for scaled time, τ , where

$$\tau = t/W^{1/3} \quad , \quad W = \text{yield in kilotons}, \quad t = \text{time after burst in seconds}.$$

When $\tau \leq 0.012825$

$$R = 2.568 \times 10^2 \tau^{0.395} - 1.6235 \times 10^4 \tau^{3.4962},$$

when $0.012825 < \tau \leq 0.1$

$$R = 1.1565 \times 10^2 \tau^{0.2119},$$

when $0.1 < \tau \leq 0.2$

$$R = 9.703 \times 10^1 \tau^{0.1357}, \text{ and}$$

*Although only three Sputter calculations performed at the AFWL have been documented (references 4 through 6), magnetic tapes were distributed throughout the community that contain the detailed results for each calculation. These were called usertapes.

Table 2. SPUTTER data from FB21 usertape
(1 kt free-field at sea level)

TIME (MILLISECONDS)	ESTIMATE OF FIREBALL RADIUS BOUNDS FROM SPUTTER DATA (FB21)		FIREBALL RADIUS MODEL (m)
	LOWER (m)	UPPER (m)	
1	19.2	19.6	16.8
5	35.0	35.1	31.7
10	42.2	42.4	41.6
15	46.8	47.1	47.5
20	50.3	50.6	50.5
30	55.0	55.4	55.0
40	58.8	59.4	58.5
50	61.5	62.2	61.3
60	64.0	64.8	63.7
70	65.3	66.2	65.8
80	67.4	68.3	67.7
90	68.8	69.6	69.4
100	71.2	72.0	71.0
150	73.1	75.4	75.0
200	76.0	79.2	78.0
300	76.0	79.5	78.0
400	77.9	77.9	78.0
500	78.4	78.4	78.0
600	76.3	76.3	78.0
700	74.5	74.5	(not modeled)

when $0.2 < \tau \leq 0.6$

$$R = 78$$

where R is the scaled radius of the fireball in meters/ $Kt^{1/3}$. The radius of the fireball, r , is then

$$r = RW^{1/3}$$

For scaled times beyond 0.6 seconds/ $Kt^{1/3}$ this fireball radius model is not defined.

For future reference, Table 2 presents estimates interpolated from the SPUTTER usertape data. Where the fireball edge criteria clearly defines the edge the bounds will be equal. The values for the fireball radii were taken at cell boundaries, and in some cases the differences between the lower and upper bound on the radius is a cell width. Also shown for comparison are the results of using the model derived from these data. A plot of the fireball radius versus time resulting from use of this model can be found in Section 4.

2.3 RESULTS FROM SAI THERML CODE

The results presented in this section as well as those in the appendices represent estimates of nuclear radiation environments from a 1 kiloton surface burst. The surface burst is represented as a 1 kiloton hemisphere, and therefore, the radiation output has been computed by scaling out to a 2 kiloton free-field (but at sea level) air burst. No account has been made of any contribution due to scattering from the ground or other objects. The ground is represented as a perfect absorber of radiation falling upon it, except for the radiation forming the fireball.

If the ground is in fact a perfect reflector then yield doubling of the radiative output from the fireball is exact. However, when the assumption regarding scattering from the ground is invalid it can lead to significant errors for some cases. If on the other hand, the earth is in fact a perfect absorber then the yield doubling is inappropriate. The appropriate choice for airblast is to double the yield. The approach taken here for radiation is to treat the ground as a perfect reflector inside the fireball, but then assume it absorbs all radiation incident upon it outside of the fireball. The effect of these assumptions on the calculation of flux and fluence on some detectors can be substantial. The results for a detector whose normal is elevated 90° , i.e., the detector is lying on the ground facing up, will obviously not be affected by the assumption about how the earth scatters. However, the results for such a detector can be a strong function of the fireball radius for small radii (see Figure 13), and the accuracy of the fireball radius depends upon the appropriateness of yield doubling. On the other hand, the detector whose normal is at elevation 0° (facing ground zero) will not depend directly on the fireball radius but will be influenced by the yield doubling models in terms of the timing and magnitude of the power out as well as scattering from the ground. The effect of the approach taken will be discussed further in Section 2.4.

The SAI THERML code was used to predict the environments incident on a detector at ground level. The ranges considered were 30.48, 60.96, 91.44, 152.4, 304.8, and 609.6 meters from ground zero. The results shown in the appendices present the radiation reaching the detector until either the fireball sweeps over the detector or 750 milliseconds has past. Recall that this latter time represents the limit (when scaled) on the model for the fireball radius. For all results shown the fluence is given in cal/cm^2 , and both the flux and average flux are given in $\text{cal/cm}^2/\text{sec}$.

Before discussing the results found in the appendices, it is worthwhile to show the geometry as well as the effect of the orientation of the detector on some of the results for an interesting ground range. Figure 15 shows the detector orientation in terms of an elevation angle, ϵ , measured in degrees. The normal to the detector's surface is seen to be in the plane normal to the earth that passes through ground zero and the field point. Figure 16 traced from the appendices shows the effect of detector orientation on flux from a 1 Kt surface burst crossing a detector 152.4 meters from ground zero. Figure 17 shows the effect on fluence. Four orientations of the detector normal were considered: 0, 30, 60 and 90 $^{\circ}$ orientation. Results for 30 $^{\circ}$ are not shown since they are almost coincident with the 0 $^{\circ}$ results. As expected, for detectors facing up, i.e., 90 $^{\circ}$ orientation, the flux and fluence environments are significantly reduced. Additional curves similar to these can be obtained by tracing over the appropriate ones in the appendices. Appendix A contains the results for 0 $^{\circ}$, B for 30 $^{\circ}$, C for 60 $^{\circ}$ and D contains the 90 $^{\circ}$ results.

Some of the results are summarized in Figures 18 through 21 which together show the flux and fluence at each ground range for two detector orientations (0 $^{\circ}$ and 90 $^{\circ}$). The data for 30.48, 60.96 and 91.44 meters ranges include times up until engulfment by the fireball. Beyond these times, detailed radiation transport solutions are required. Although these data are available from the SPUTTER usertapes, they were not needed for this effort. Since the fireball model does not predict growth beyond 98.15 meters, the data for 152.4, 304.8 and 609.6 meters are complete out to 750 milliseconds.

It can be useful for purposes of simulation to have estimates of the thermal environment at the time of shock arrival. Table 3 presents the overpressure at time of arrival based on a model by Brode for a yield of 2 kiloton free-field (or a 1 Kt surface burst). The equations utilized were

$\vec{\eta}$ and ground zero in same plane

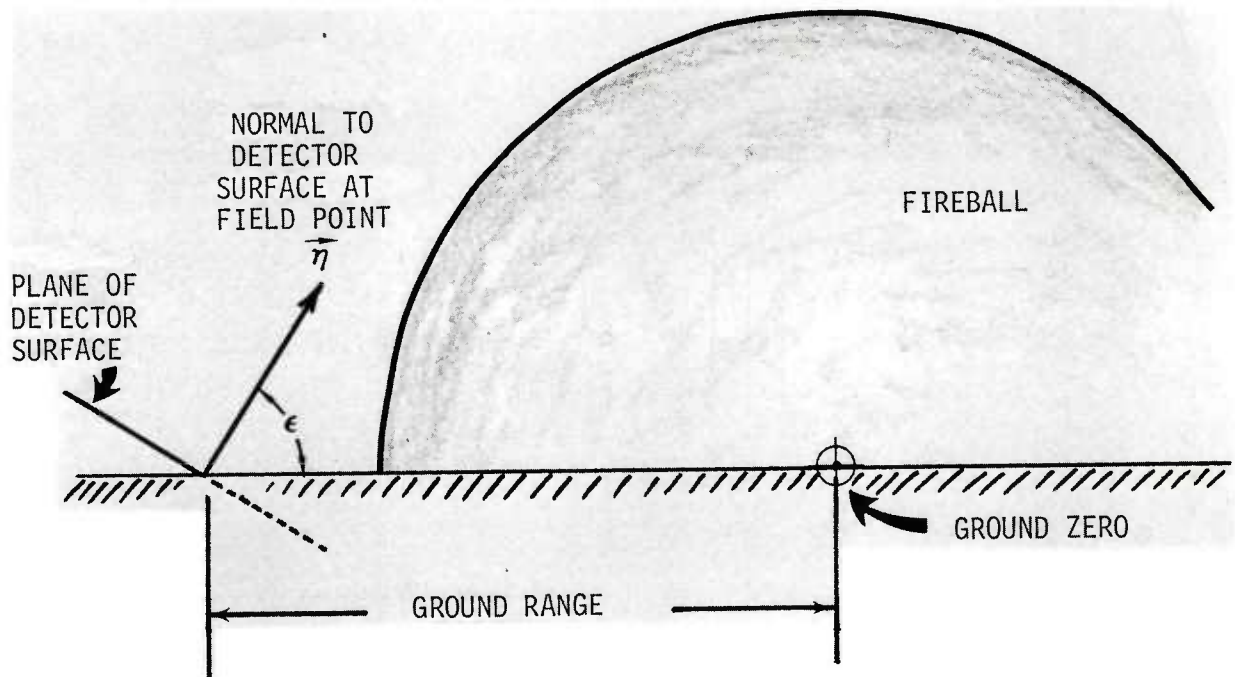


Figure 15. Detector orientation.

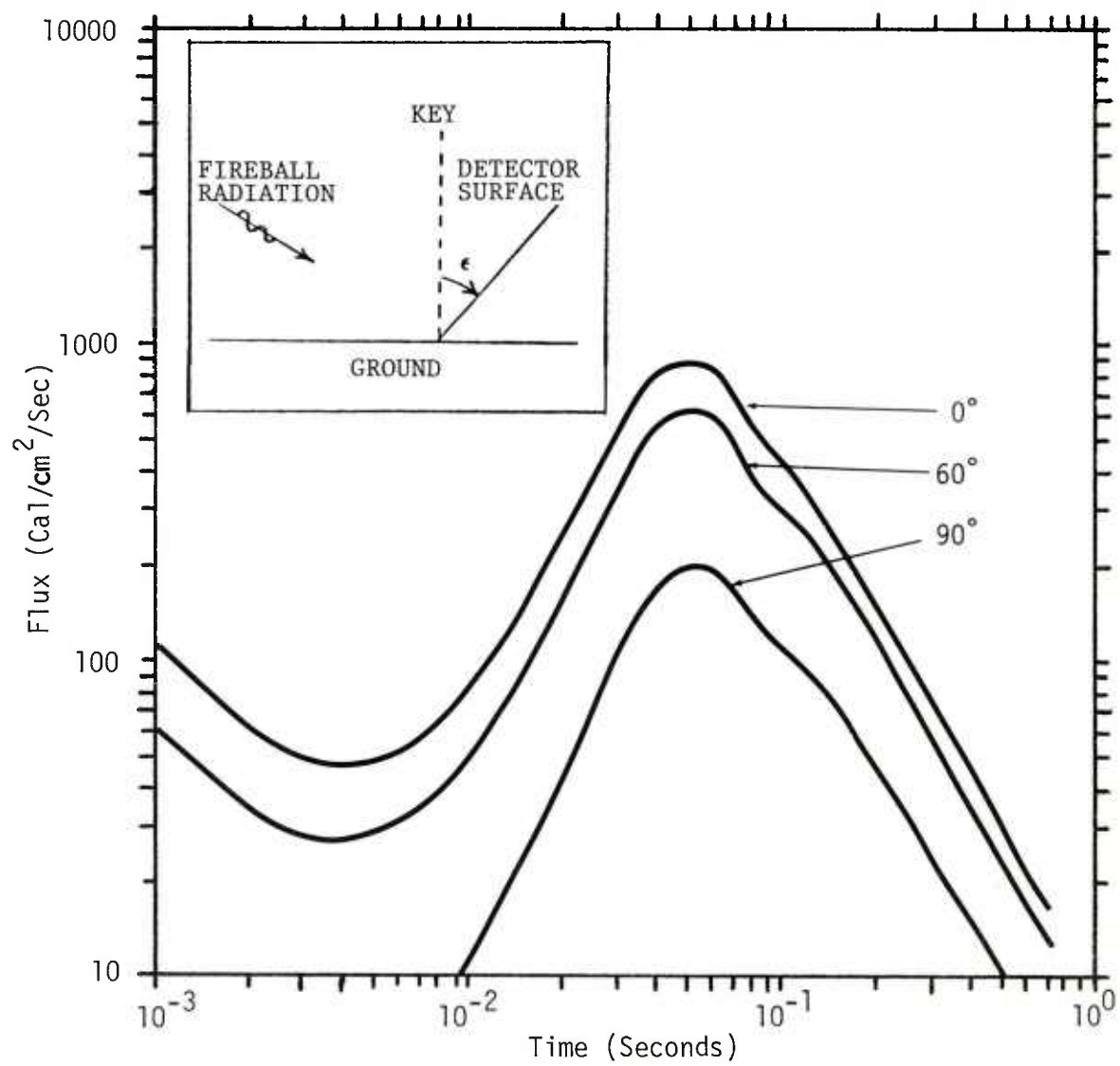


Figure 16. Effect of detector orientation on flux.

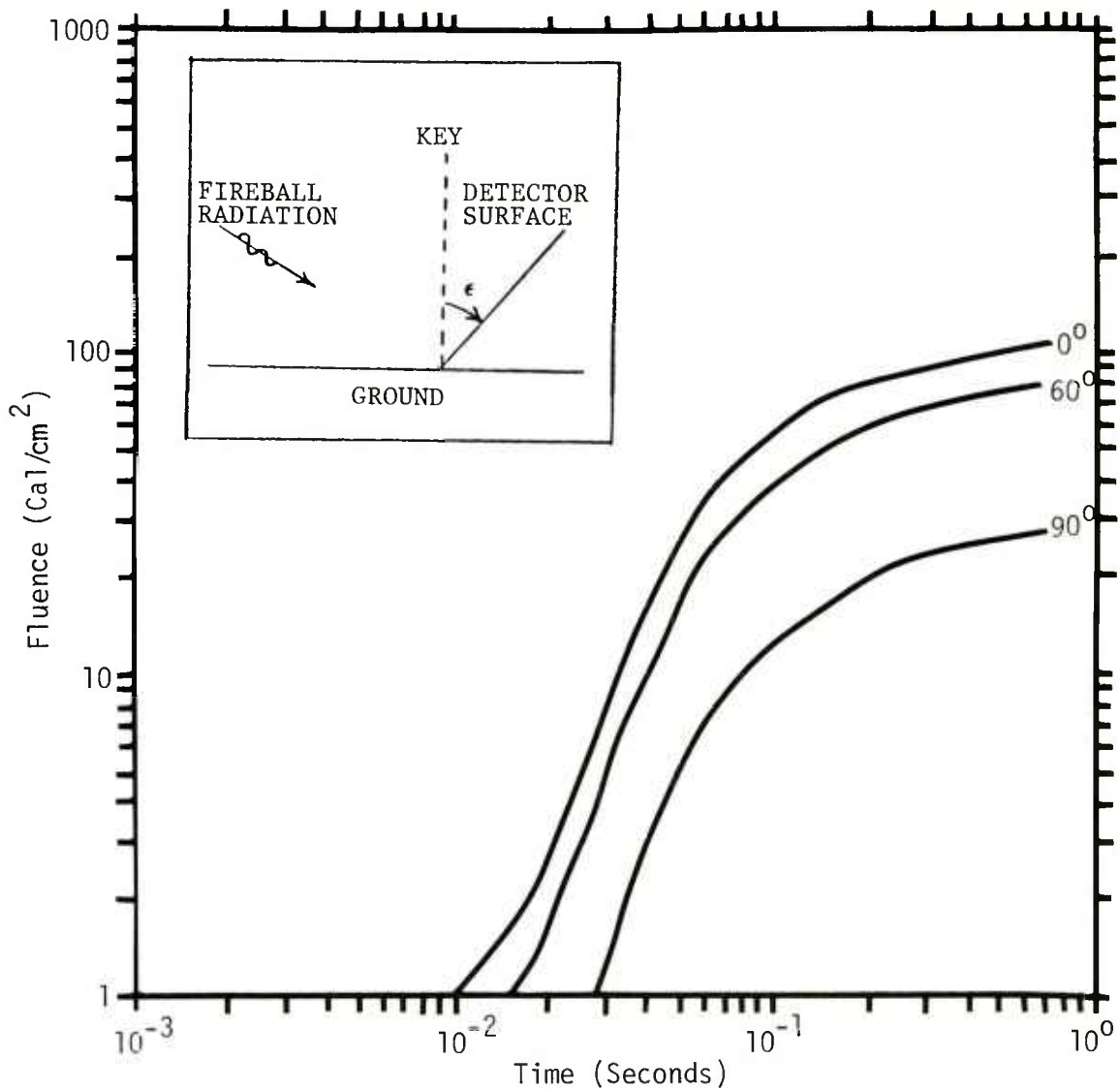


Figure 17. Effect of detector orientation on fluence.

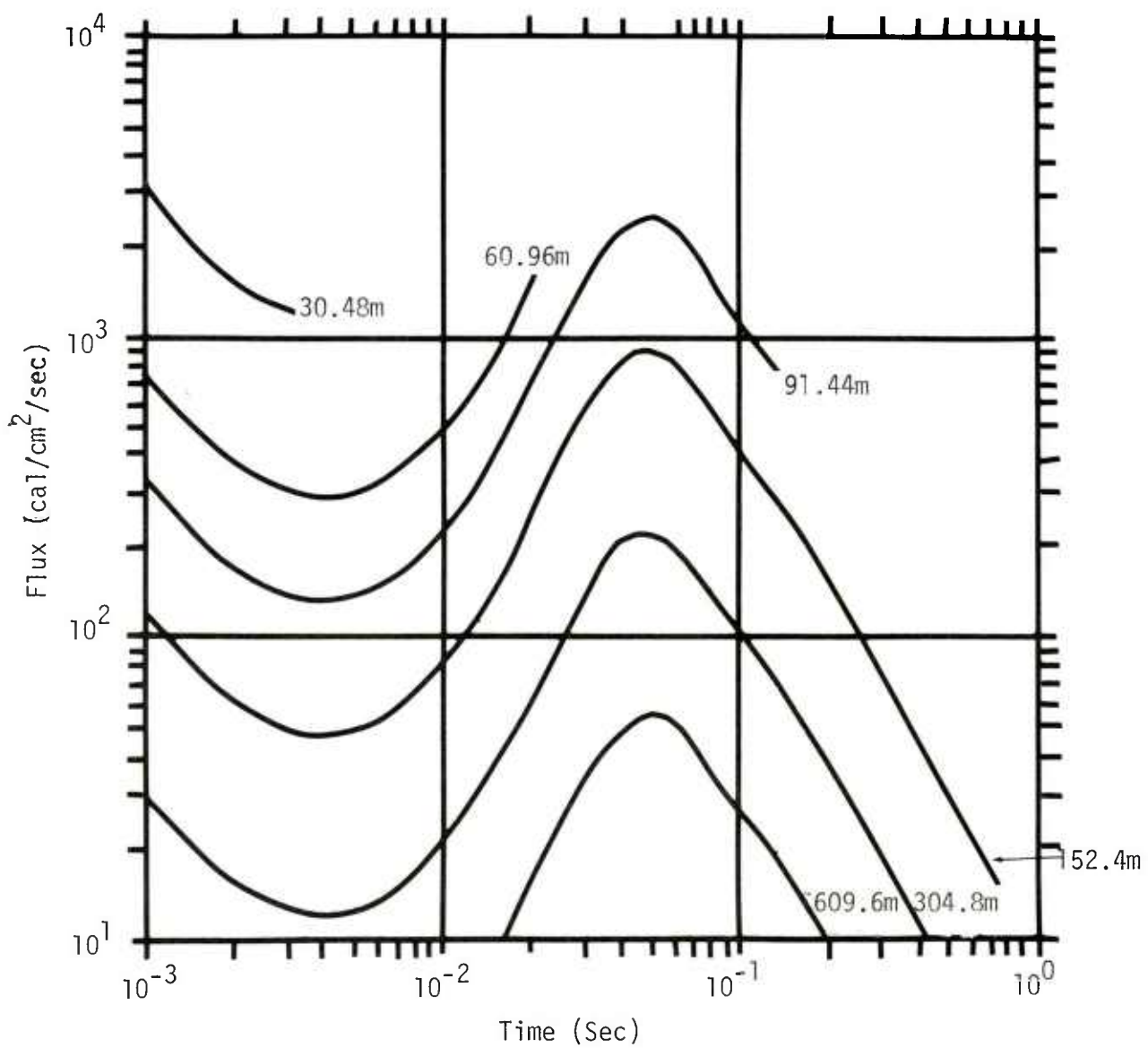


Figure 18. 1 KT surface burst : detector facing GZ.

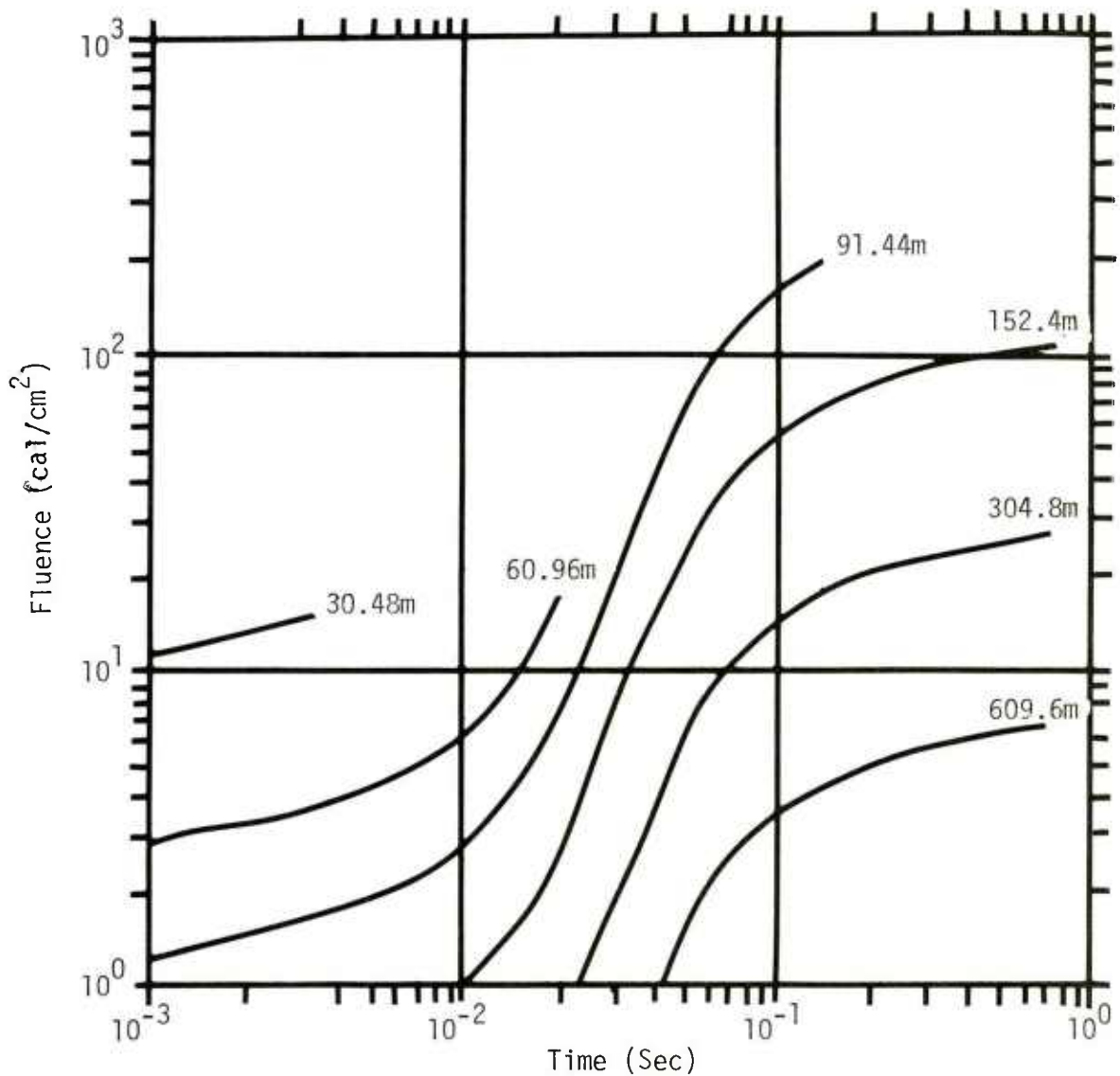


Figure 19. 1 KT surface burst : detector facing GZ.

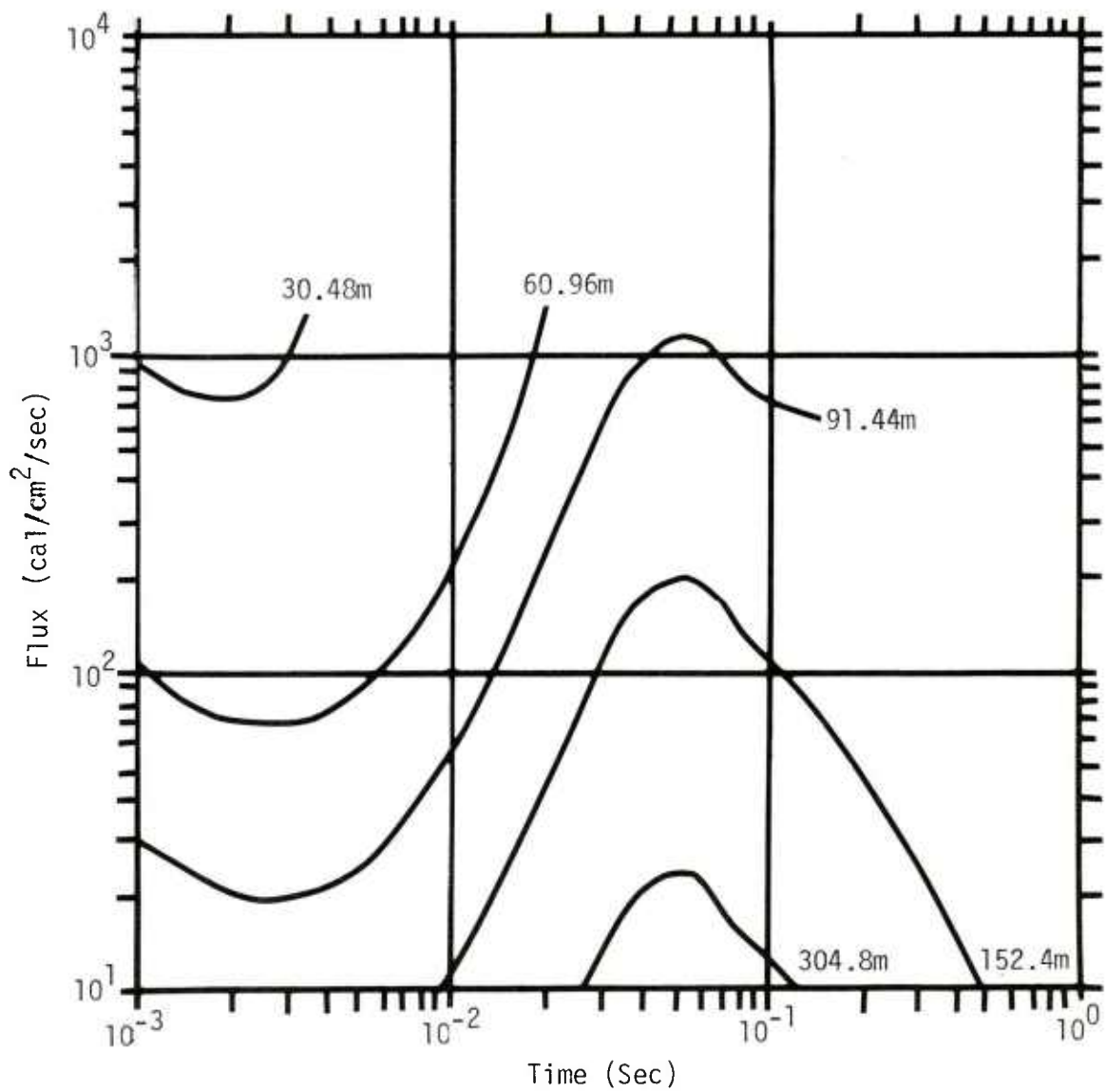


Figure 20. 1 KT surface burst : detector facing up.

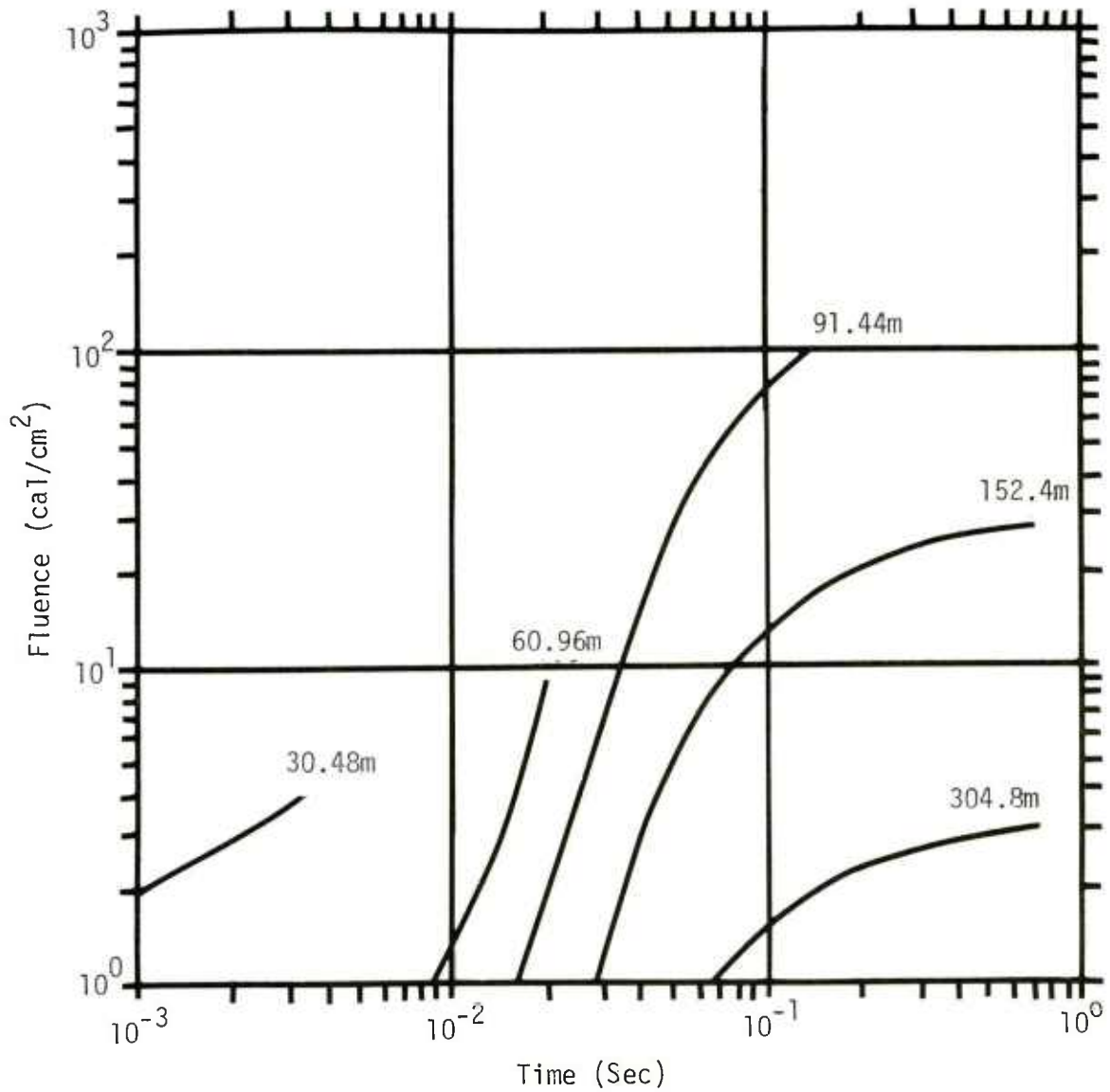


Figure 21. 1 KT surface burst : detector facing up.

Table 3. Overpressures and arrival times.

<u>GROUND RANGE (meters)</u>	<u>FREE-FIELD OVERPRESSURE (psi)</u>	<u>SHOCK ARRIVAL TIME (ms)</u>	<u>FIREBALL ARRIVAL TIME (ms)</u>
30.48	3638	2.5	3.2
60.96	479	14.3	21.
91.44	168	37.0	148.
152.4	49	112.	*
304.8	11	409.	*
609.6	3.7	1190.	*

*Fireball doesn't grow past 98 m.

$$t_a(r,w) = \frac{0.5429w - 21.185rw^{2/3} + 361.8r^2w^{1/3} + 2383r^3}{w^{2/3} + 2.048rw^{1/3} + 2.687r^2} \text{ (msec)} \quad (45)$$

$$\Delta P(t_a, w) = \frac{14843w^{1/3}}{0.0135w^{1/3} + t_a} \left\{ \frac{w^{2/3} + 0.6715w^{1/3}t_a + 0.004813t_a^2}{w^{2/3} + 1.8836w^{1/3}t_a + 0.0261t_a^2} \right\} \text{ (psi)} \quad (46)$$

These equations were obtained from reference 13, page 25, for the special case $t = t_a$. The fireball arrival times were computed with our model. These arrival times were then used with the data in the appendices to obtain the approximate values of the fluence and flux at the time of shock arrival. These are shown as Table 4. The data do not exist for the 609.6 meters case because the shock arrives at a time later than the limit on the fireball radius model.

The results presented in the appendices provide a compendium that can be used to interpolate to needed conditions.

2.4 UNCERTAINTIES IN THE ESTIMATES OF NUCLEAR THERMAL RADIATION

The results that have been presented so far are estimates of thermal radiation to be used for test planning. There are uncertainties associated with some of them. Specifically, there exist uncertainties associated with the details of the weapon-ground and thermal radiation-ground interactions. These uncertainties have not been quantified as yet, primarily due to the difficulty of such a task. The uncertainties introduced by the modeling of SPUTTER results could be quantified; however, it is beyond the scope of this effort to do so. References 3 through 5 provide some comparisons.

The uncertainties that are discussed here should be borne in mind when attempting to plan what environment is being simulated.

Table 4. Approximate values of fluence and flux at shock arrival.

	<u>GROUND RANGE (meters)</u>	1 KILOTON SURFACE BURST	
		<u>FLUENCE (CAL/CM²)</u>	<u>FLUX (CAL/CM²/SEC)</u>
ORIENTATION 0°	30.48	14	1350
	60.96	10	840
	91.44	35	2100
	152.4	62	360
	304.8	24	11
ORIENTATION 30°	30.48	14	1560
	60.96	9	910
	91.44	37	2230
	152.4	60	360
	304.8	23	10
ORIENTATION 60°	30.48	10	1360
	60.96	7	820
	91.44	28	1780
	152.4	43	270
	304.8	15	7
ORIENTATION 90°	30.48	3	790
	60.96	3	500
	91.44	12	840
	152.4	14	100
	304.8	3	2

2.4.1 Effect of Weapon/Ground Interactions

The thermal output can be sensitive to details of weapon/ground interaction. For example, the thermal radiation can be shielded by ejecta. Further there may exist cooling effects on the fireball due to ground mixing. The latter changes the radiative history and spectrum. Reference 14 notes a dependence of the radiative history on height of burst for several NTS shots. For example, it notes that there appears to be strong correlation with the closeness of the fireball with what amounts to be the thermal partition.*

SAI modified the presentation of the NTS data on thermal partition in reference 14 by plotting it versus the volume of a sphere that intersects the ground and represents the height of burst and fireball radius at second maximum for the shots indicated, normalized by the volume of the hemisphere. This yields an interesting and possibly significant significant trend (Figure 22). This figure suggests that within the experimental error an abrupt change in the character of the thermal efficiency occurs when the weapon is very close to the ground. Further, the effect seems to suggest a renormalization with a radius much smaller than the fireball at second maximum.

SAI immediately thought of the x-ray fireball. The SPUTTER radius at second maximum is approximately 70 m for FB21, 1 kt at sea level, whereas the early time fireball is only 4.5 m. Assuming this factor is appropriate for SMALL BOY, SUGAR and LACROSSE just for the sake of argument, SAI obtained a figure similar to Figure 23. The implication is that the effect is pronounced when the initial x-ray deposition (the original fireball) is striking the ground, i.e., when ground material can be literally blown off into the early time fireball (and hence seriously affect its development). SAI then went back to the SPUTTER data, estimated the x-ray fireball radius, scaled these for the nuclear shots shown, and then used these to normalize the data. The result is presented in Figure 23.

*The apparent thermal radiated yield divided by the total yield.

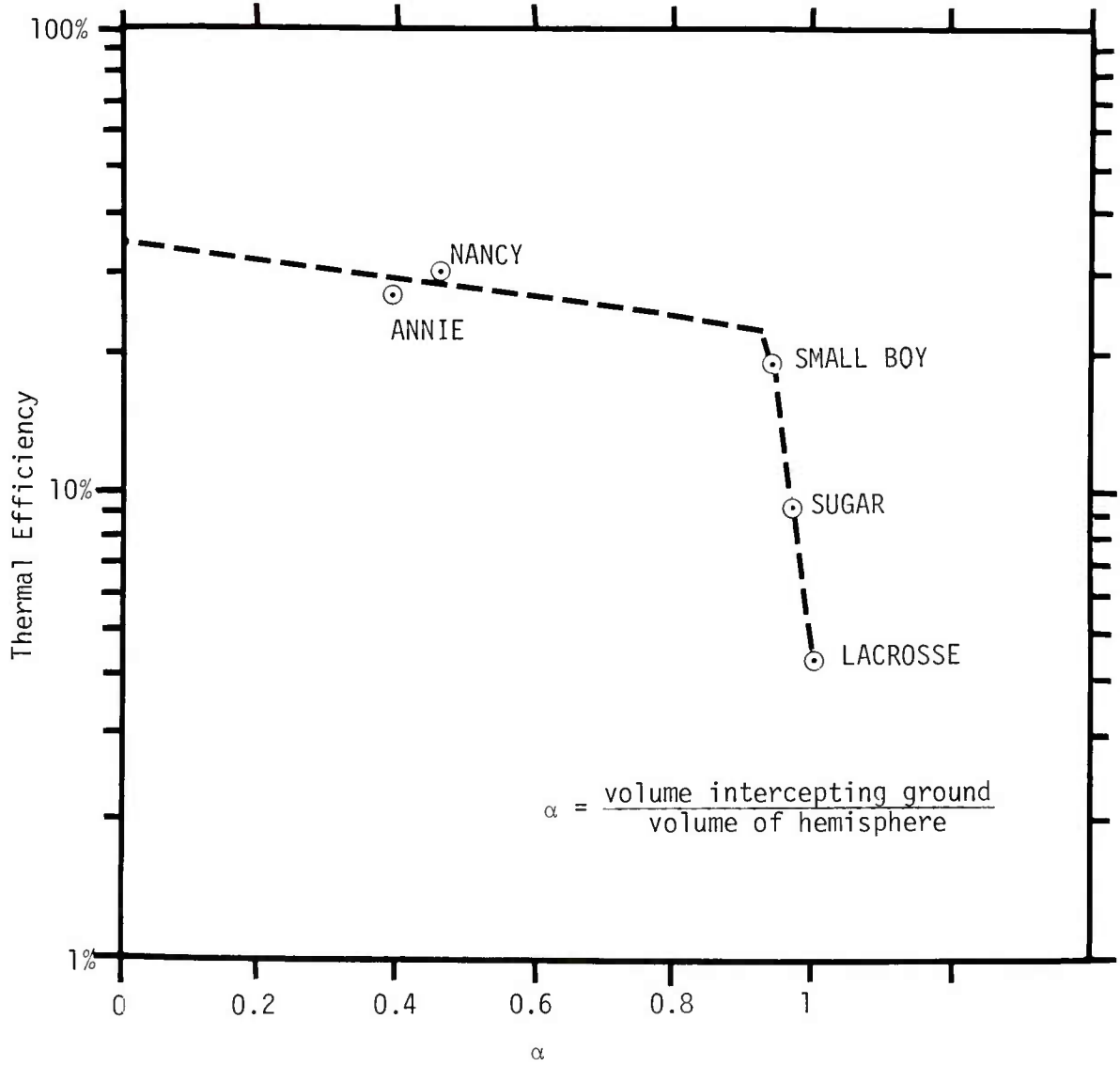


Figure 22. Thermal efficiencies (radius at 2nd max).

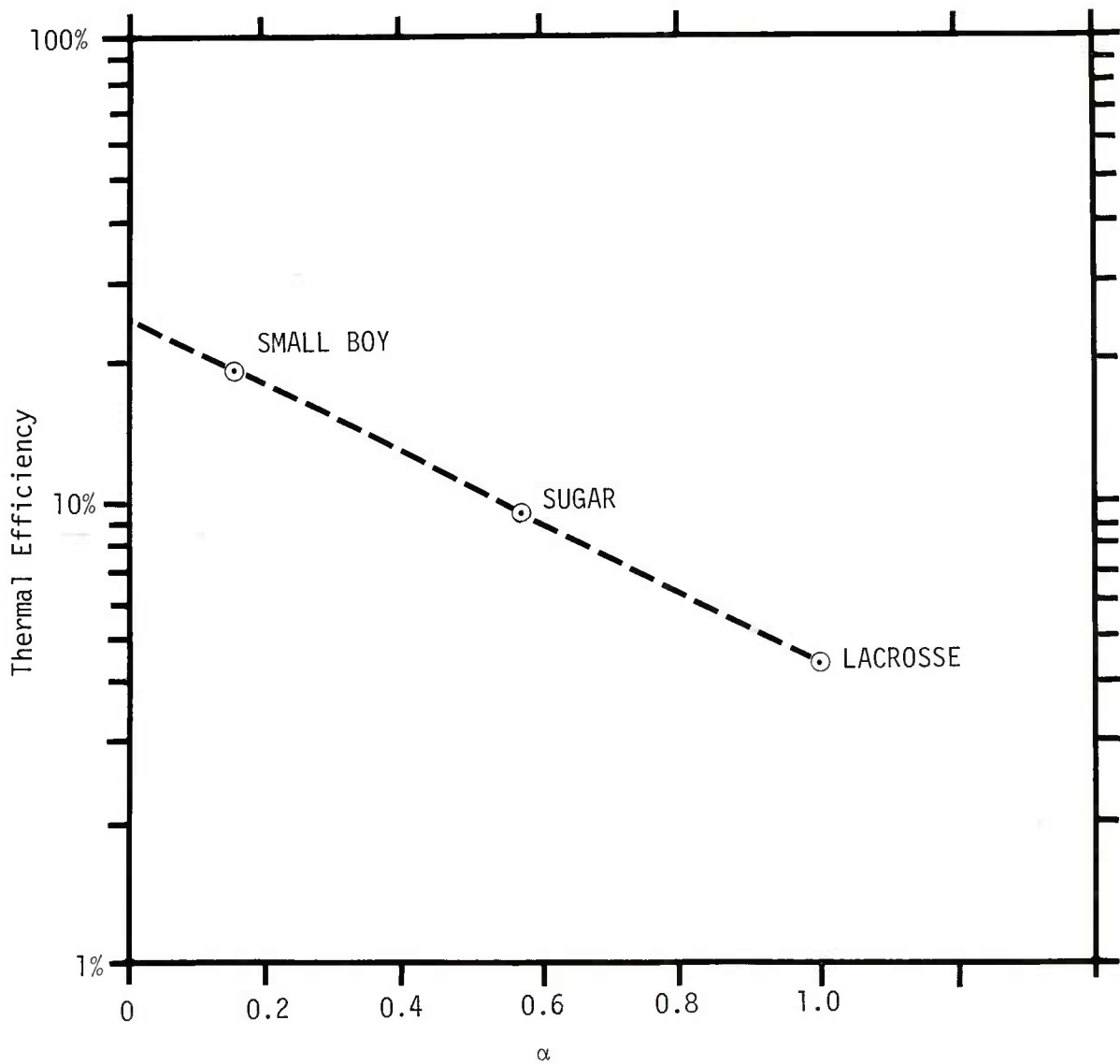


Figure 23. Thermal efficiencies (radius at early time).

Two postulates can be inferred from the above. First if the height of burst is much greater than the x-ray burnout region the large degradation of thermal from the ground's influence (other than ejecta shielding) will be relatively small. Secondly, it may be possible to model in a simple way from existing nuclear data, the degradation of thermal radiation efficiency from very near surface bursts. The data in reference 14 were taken from cameras stationed on the ground, and therefore, the correlation may only hold for the apparent thermal efficiency in that direction. Since this is the direction of interest for this effort, it is suggested that the total thermal efficiency computed could be too high by a factor of 7 for an actual surface burst. Although the correlation may quantify the effect of the weapon-ground interaction on the thermal efficiency, the correlation may only be fortuitous. Further investigation is required and believed highly desirable.

A further comment is appropriate about the effect of weapon-ground interactions on spectrum. Reference 15 reports that near surface bursts (as well as below surface bursts) modify the spectrum of the radiated power as well as the details of the radiative history.

Finally, the effect of the weapon-ground interactions on fireball development has not been quantified. When the x-rays penetrate the ground they cause vaporization; the vaporized material will blow off explosively into the developing fireball. This new material will affect fireball growth and its radiative history.

In summary, the degradation of the radiative history from weapon-ground interactions has not been quantified. It is preferable that the curves shown in the appendices be used to define the simulation allowing study of synergistic thermal and airblast effects for the 1 kiloton surface burst, even though they might overpredict the total energy radiated out. It is probable that such a simulation along with data from a pure airblast environment will bound the phenomena.

2.4.2 Effect of Thermal Radiation/Ground Interactions

The fireball touching the ground will transfer energy to the ground by a combination of radiation, conduction, and convection. Whether these interactions significantly affect the radiative history of the fireball is still an unresolved technical issue. It is not anticipated that this issue will be resolved for some time.

2.4.3 Effects of Other Uncertainties

Crater ejecta can obscure the fireball somewhat and reduce the amount of thermal radiation reaching any position on the ground. The effect can be significant for low yields. What effect this has on the radiative output has not been quantified, although it is expected that shielding by ejecta will not be as important as the effect induced by injection of ground material into the fireball.

SECTION 3

RADIATIVE OUTPUT FROM THERMAL RADIATION SIMULATION DEVICES

The SAI Thermal Radiation Simulation (TRS) devices are described briefly in this section; more details may be found in reference 16. In addition, this section presents how the radiative output of these devices was modeled and identifies the need for additional characterization.

3.1 THE SAI THERMAL RADIATION SIMULATOR

During 1976, a preliminary design for large area high flux thermal radiation generator was conceived. DNA funded a small program during FY 77 to test this concept. The results of the initial tests indicated that a high flux (greater than 200 cal/cm²-sec) over a large area could be achieved. Subsequently DNA funded a full scale development program to develop a TRS device which would produce various thermal radiation pulses of high flux and fluence over areas exceeding 100 square meters. It was to be self-consuming upon ignition and structurally simple.

The TRS device that was ultimately used, radiates considerable amounts of energy during a rapid exothermic oxidation of aluminum. Since the specific energy release of metallic salt is relatively high, most of the chemical energy is released in the form of visible and near infrared light.

Though many pyrotechnic mixtures which produce intense light are available, several criteria were established that limited the choice of mixture and led SAI to adopt aluminum as our fuel. These criteria are:

- a. The mixtures must have a large energy release per unit weight of pyrotechnic mixture.
- b. The pyrotechnic mixture must be safe to handle and ship, and both reactants and products must be non-toxic.

- c. The mixture must have a low cost per unit weight.
- d. The material must be readily available in a convenient form.

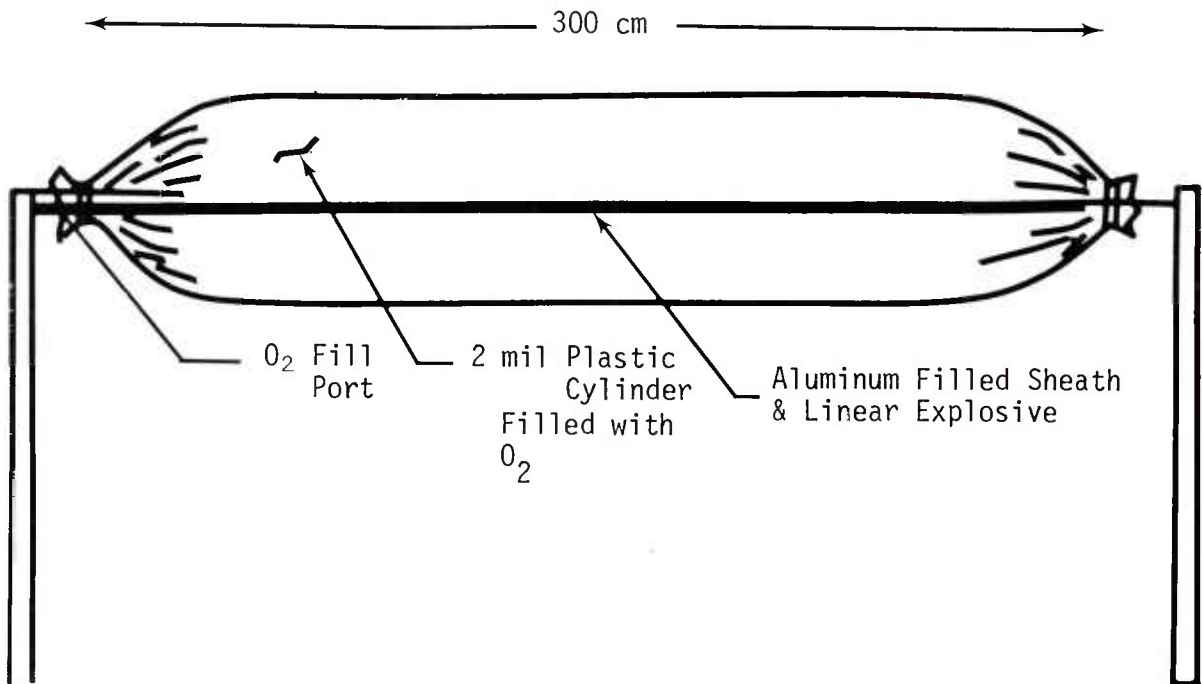
Aluminum powder is a readily available, low cost, commercially produced product that is shipped as a non-hazardous substance, and upon oxidation releases high energy per unit weight.

In order to produce high intensity bursts of thermal energy, large quantities (>1.0Kg) of aluminum must be ignited and burned in a relatively short time (<1 sec). To accomplish this type of burn, the metal must be finely divided and thoroughly intermixed with oxygen. The energy release associated with burning aluminum is listed in Table 5.

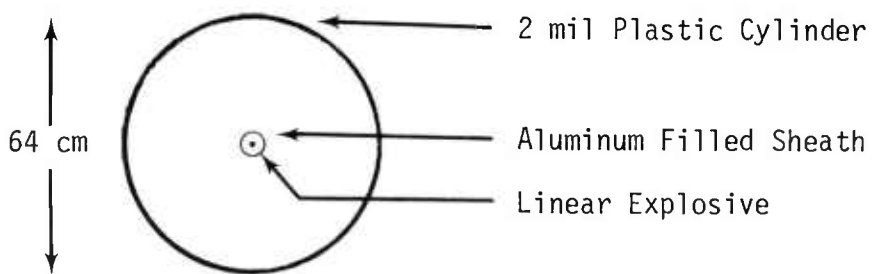
Table 5. Aluminum oxidation reactions.

Reaction	Energy Release per Mole of Product (cal/mole)	Energy Release per gram of Metal (cal/gm _M)
$2\text{Al} + \frac{3}{2} \text{O}_2 \rightarrow \text{Al}_2\text{O}_3$	3.89×10^5	7.21×10^3

Initial work conducted during 1976 proved that aluminum powder could be rapidly mixed with oxygen and burned to created high flux and fluence optical pulses over large areas. Several techniques for mixing and igniting the Al and O₂ mixtures were examined during the tests. The most promising technique was one which mixed and ignited the reactants by use of a small quantity of high explosive (HE). Figure 24 illustrates the explosively mixed system (E-system) used on early TRS tests. Figure 25 shows a photograph of the early E-system TRS module.



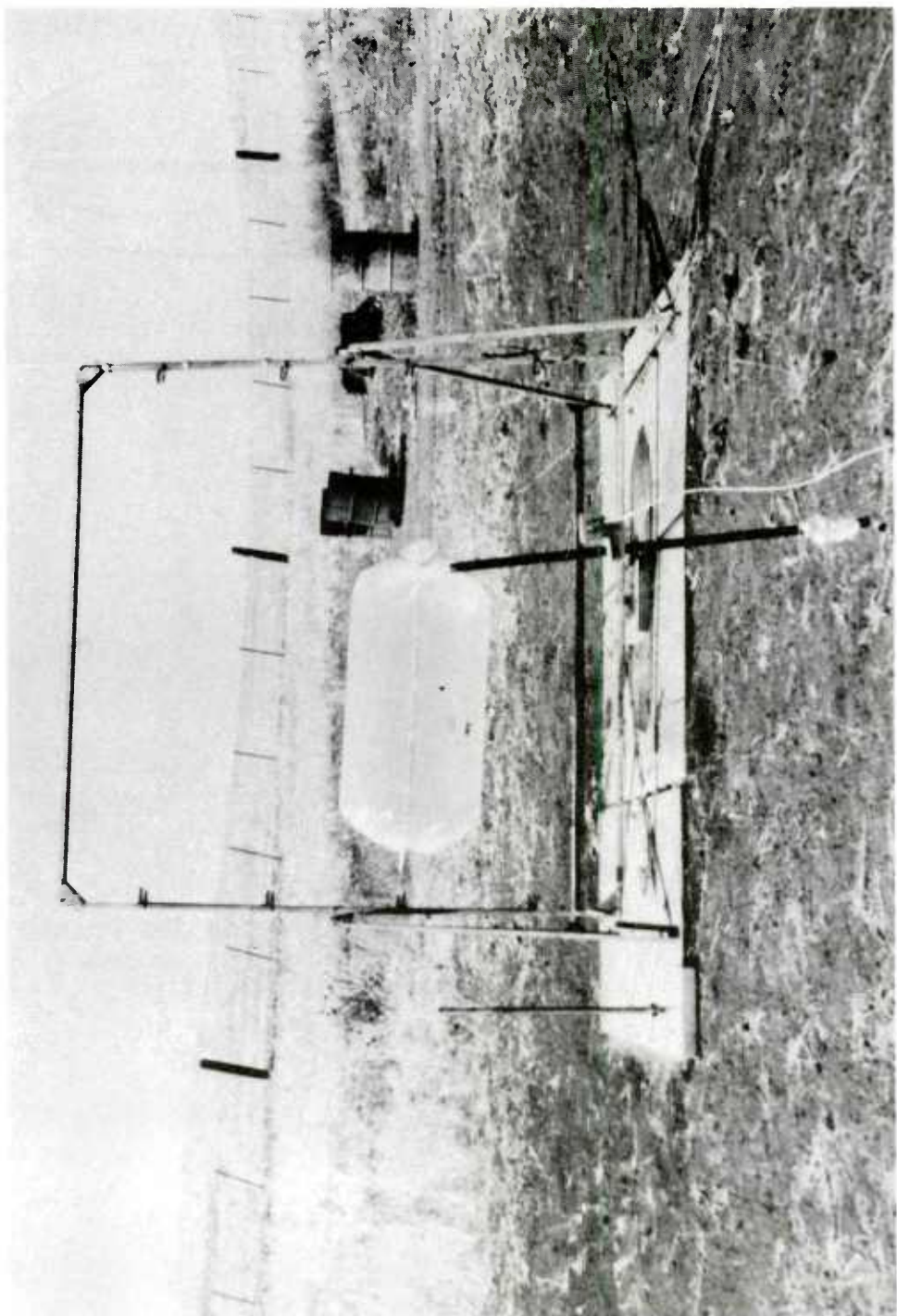
SIDE VIEW OF TRS MODULE



END VIEW OF TRS MODULE

Figure 24. An early E-system TRS module

Figure 25. Photograph of an early E-system TRS module.



These initial tests highlighted areas of research and problems which were to be pursued to develop a useful TRS. Particular problems and research areas uncovered in the early TRS work were:

- a. Early TRS systems produced excessive airblast during TRS ignition.
- b. Waveforms of early TRS systems were difficult to control.
- c. Scaling laws for flux and fluence generated by various yield TRS systems had to be developed.
- d. Techniques for varying pulse signatures had to be developed.
- e. Techniques for the control and calculation of TRS debris had to be developed.

3.1.1 Laboratory Experiments

The most serious problem area was the airblast output generated by TRS ignition and the lack of control over TRS radiation pulse shapes. A small-scale laboratory research program was conducted to study these problem areas and to find mechanisms for their control. These experiments indicated that the macroscopic combustion rate of Al was responsible for generating blast, and that control of the Al combustion rate could lead to control of the TRS pulse shape. Variables that can affect the combustion rate are:

- a. The mixing rate of Al and O₂ in a TRS,
- b. The Al particle size, and
- c. The concentration of O₂ available to the Al-O₂ reaction.

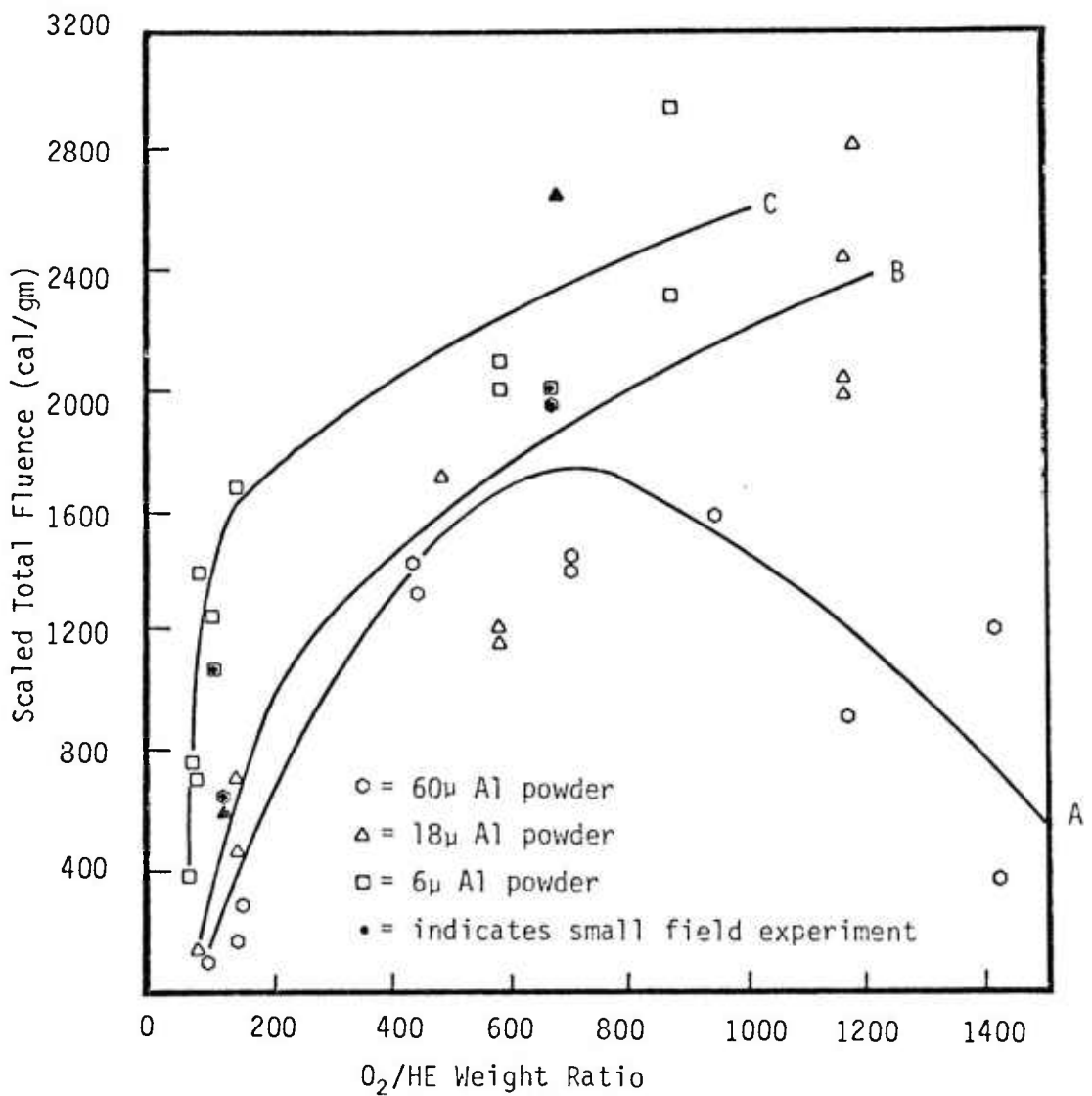


Figure 26. The effect of the O_2 /HE weight ratio on TRS fluence of E-system TRS modules.

A research program was conducted to examine the effect of these as well as other variables on the thermal radiation, airblast, and debris from the simulator. The variables considered were:

- a. Mixing Technique. High explosive dispersal (E-system) and high pressure gas dispersal (C-system) of Al into an oxygen atmosphere were examined.
- b. Mixing Rate. The mixing rates (i.e., the high explosive to Al weight ratio or Al weight to driver gas pressure ratio) of Al and O₂ were varied.
- c. O₂/Al Ratio. The weight ratios of Al to O₂ in the TRS were varied to examine reactant concentration effects on TRS output.
- d. Al Particle Size. The size of Al particles and particle size distribution in a mixture of Al powders were varied.
- e. Physical Size. The physical size of systems were varied to determine Al yield scaling effects on TRS output.

The approach was to change one variable while holding the others constant. Flux, fluence, and airblast were measured on each experiment. These data were recorded, analyzed, and used to design larger TRS systems. Figure 26 represents the type of data taken. The laboratory experiments are described in greater detail in Reference 15.

3.1.2 Small Field Experiments

Since TRS systems of various sizes were required for different thermal radiation experiments, the concept of modularized TRS units came into being. To create larger TRS systems, TRS modules are added together. Practical dimensions for a module were determined by study of the strength of different inflated plastic cylinders. TRS modules with length to diameter ratios of 5 and inflated to an overpressure of 0.1 psi were found to have sufficient structural strength to resist deformation by 35 mps winds. Further, a survey of common plastic

materials indicated that "lay-flat" plastic tubing in 1 m widths (one meter lay-flat tubing inflates to a cylinder with a diameter of 0.64 meters) was readily available, and therefore was chosen for the TRS module.

Small field experiments were performed to create a controlled full-scale TRS module and to examine the effects of Al yield scaling in TRS systems. In addition, the dimensions of these tests allowed examination of TRS debris problems which could not be studied on smaller tests. Field experiments were conducted at the explosive test facility leased by SAI near Pleasanton, California. A series of 12 tests were conducted during this portion of the research program. TRS flux, fluence, and airblast output were measured on each test. Debris and TRS fireball characteristics of each experiment were recorded with high speed photography. The weight ratios of Al to high explosive and O₂ to Al were held constant between lab and field experiments. Aluminum powder yields on these field scale experiments were increased by a factor of 20 over the lab tests.

3.1.3 Lab and Small Field TRS Radiative Output

a) Flux

Figure 27 presents the time dependent power output of lab and field TRS systems. Power outputs of the two experiments have been scaled to equivalent Al powder yields. Variables affecting Al-O₂ combustion rates have been held constant between the two experiments.

b) Fluence

Fluence outputs of the small field TRS systems followed trends that were in agreement with the lab experiments. Field-scale E-system

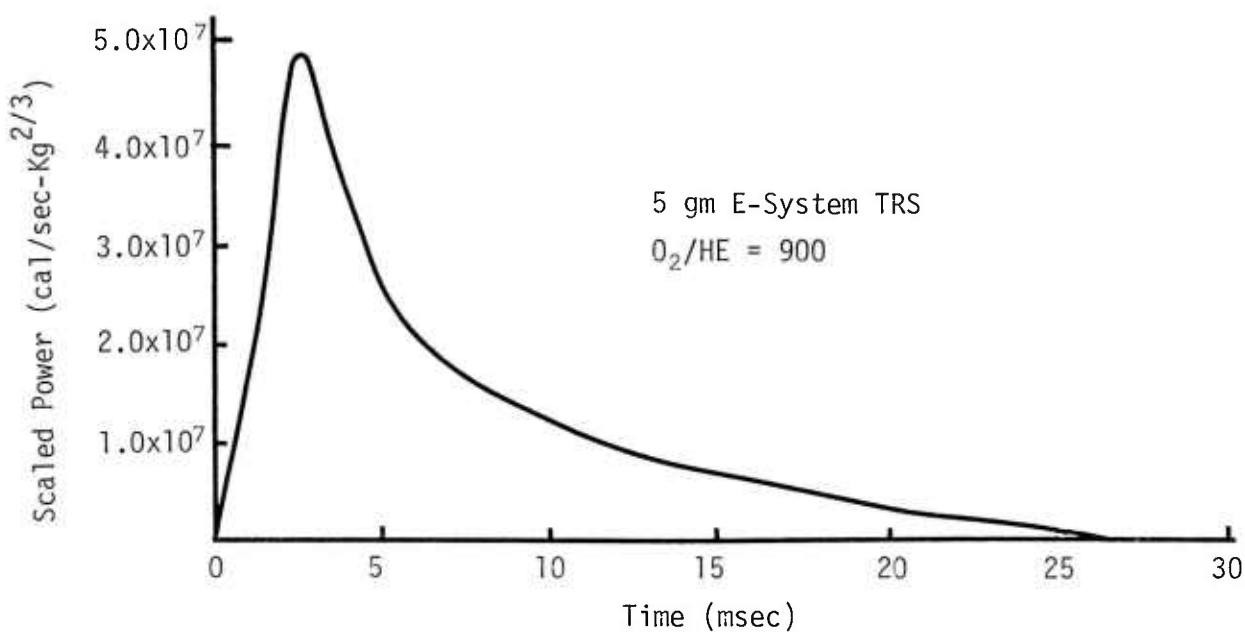


Figure 27a. Lab-scale E-system TRS.

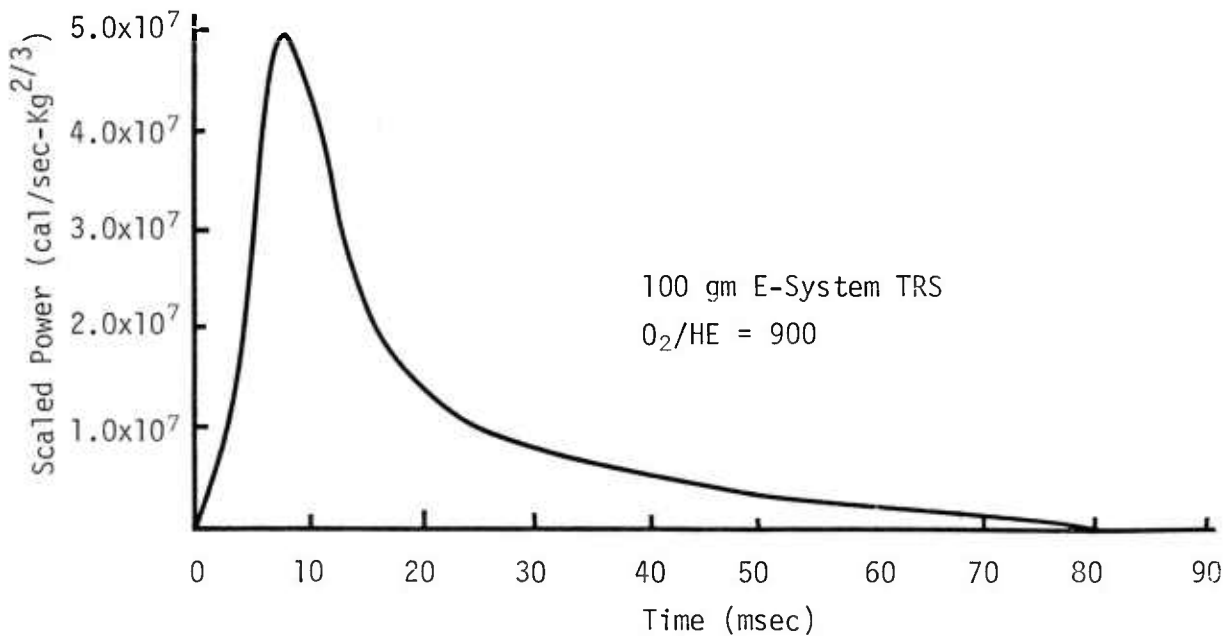


Figure 27b. Small field-scale E-system TRS.

Figure 27. Scaled power curves for two E-System TRS designs.

TRS designs, for given O₂/HE weight ratios, produced scaled total fluence outputs (cal/gm) which were identical to those produced by similar lab experiments. Field-scale C-systems TRS designs which had mixing rates and reactant concentrations similar to those of given lab systems also produced scaled total fluence outputs that were equivalent to lab experiments.

3.1.4 Large Field Experiments

The purpose of the large field experiments was to examine C- and E-system multiple module effects on TRS output. Fourteen large tests were completed during this phase of the research program. Five events conducted during 1976 were also used as data sources. With the completion of the large field experiments, sufficient data had been compiled to allow completion of the TRS development program.

Four different experimental set-ups were used to examine large TRS radiation output. The set-ups were:

- a. Vertical Single Module C-system TRS Designs. A vertical stand which held a single Al Fluidizer unit and a single, large oxygen bag was constructed (not shown).
- b. Vertical Multi-Module C-system TRS Design. A vertical stand which held 4 Al fluidizer units and four oxygen bags was constructed (Figure 28).
- c. Vertical Multi-Module E-system TRS Design. A vertical stand which held 12 E-system TRS modules was constructed (Figure 29).
- d. Horizontal Multi-Module E-system TRS Design. A horizontal frame which held 8 E-system TRS modules and could be raised to a height of 6 meters was constructed (not shown).

Set-ups "a" through "c" were instrumented with FPT-100 photodiodes; CELESCO LC 71, PCB, and TYCO HFG airblast gauges; Medtherm GT-1600 high speed calorimeters, SAI fluence calorimeters; and SAI aspirating thermocouples. Set-up "d" was instrumented with the CELESCO LC 71 airblast gauge and a Medtherm GT-1600 highspeed calorimeter.

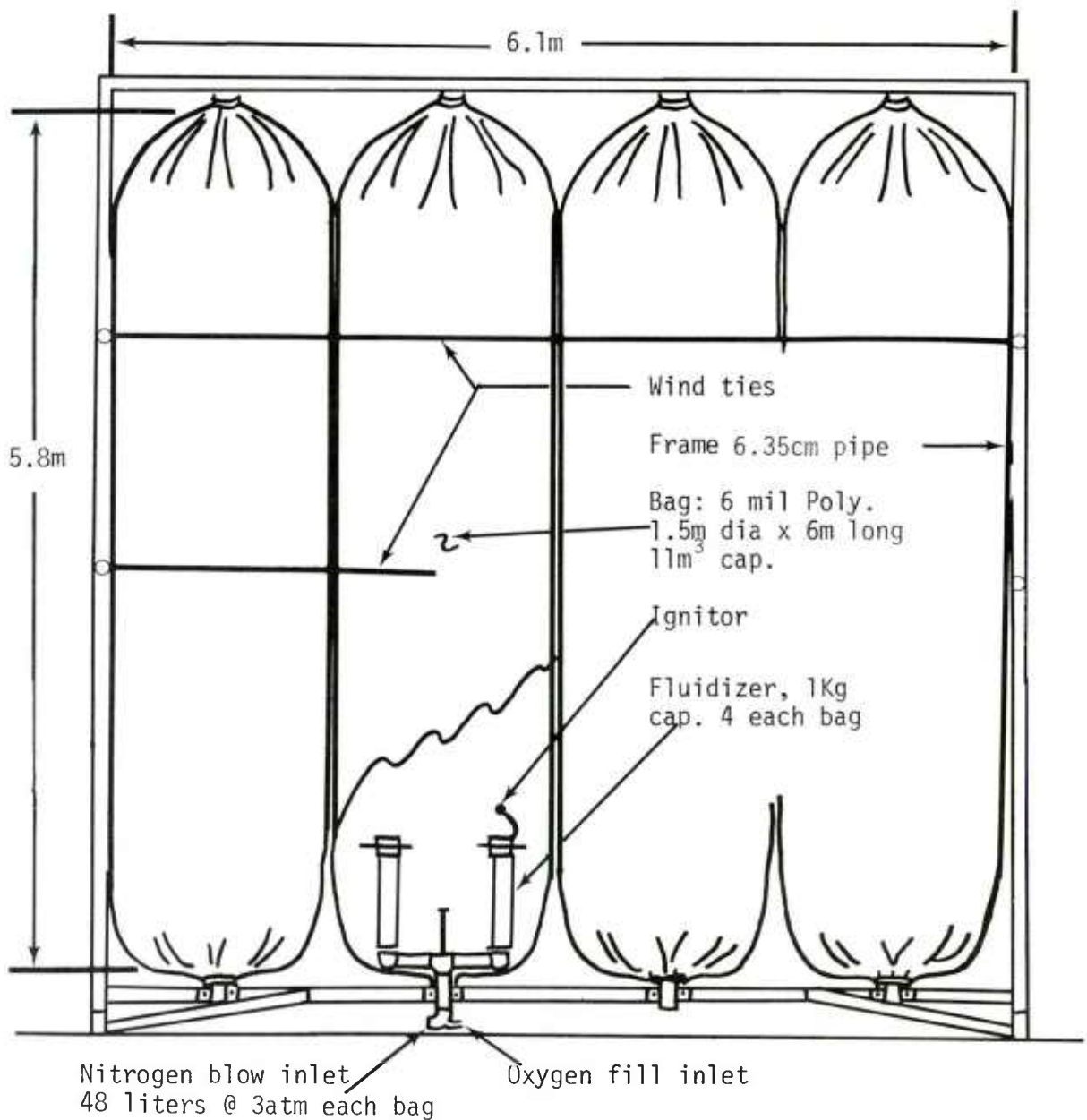


Figure 28. A 4 module vertical C-system TRS array.

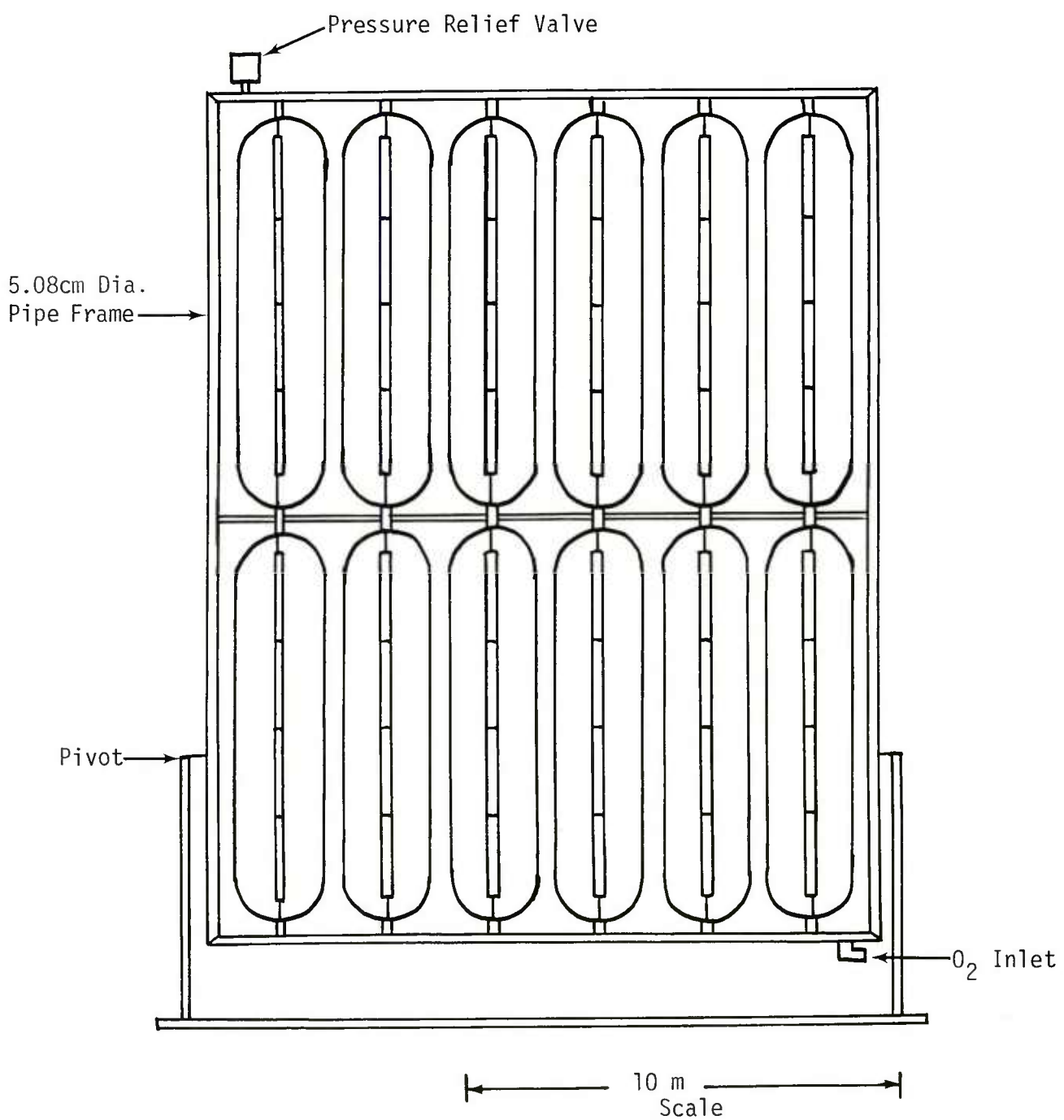


Figure 29. A 12 module vertical E-system TRS array.

Experiments with the Al fluidizer and a cost analysis of hardware associated with it indicated that the fluidizer should inject 4 to 5 kg of Al powder into a single TRS module. Field experiments proved that the fluidizer could easily spray and mix Al over a vertical distance of 6 meters. To maintain structural integrity in the module, a plastic cylinder with an L/D ratio of 4 was chosen to contain the oxygen of the TRS. When inflated to an overpressure of 0.1 psi, the C-system TRS module became a cylinder with a length of 6 meters and a diameter of 1.52 m. This cylinder provided an Al/O₂ weight ratio in the TRS module of 3.5. Peak power outputs for the single C-system TRS module vary from 1×10^7 cal/sec to 3.5×10^7 cal/sec. The total energy output of a module is approximately 9×10^6 calories.

3.1.5 Large Field TRS Radiative Output

a) Flux

The peak power generated by each TRS studied in this portion of the research program was measured in a plane, perpendicular to the plane of the TRS. In general, the peak power generated by TRS systems with multiple modules of similar combustion properties (i.e., Al/O₂ and Al/HE weight ratios, mixing techniques, and Al yields), was a linear function of the number of modules composing the TRS. Figure 30 presents the normalized peak power outputs of several multi-module TRS systems.

The peak power output of the C-system module was studied on several experiments. In general, the C-system module can rise to peak power over controlled time periods which can be varied from 25 msec to 500 msec. The peak power output is dependent upon the TRS ignition system, fluidizer mixing rate, and Al particle size.

b) Fluence

In general, two problems were investigated in the TRS fluence study. First the fluence output of C-system TRS module was measured, and second the effect of multiple modules on TRS fluence output was investigated.

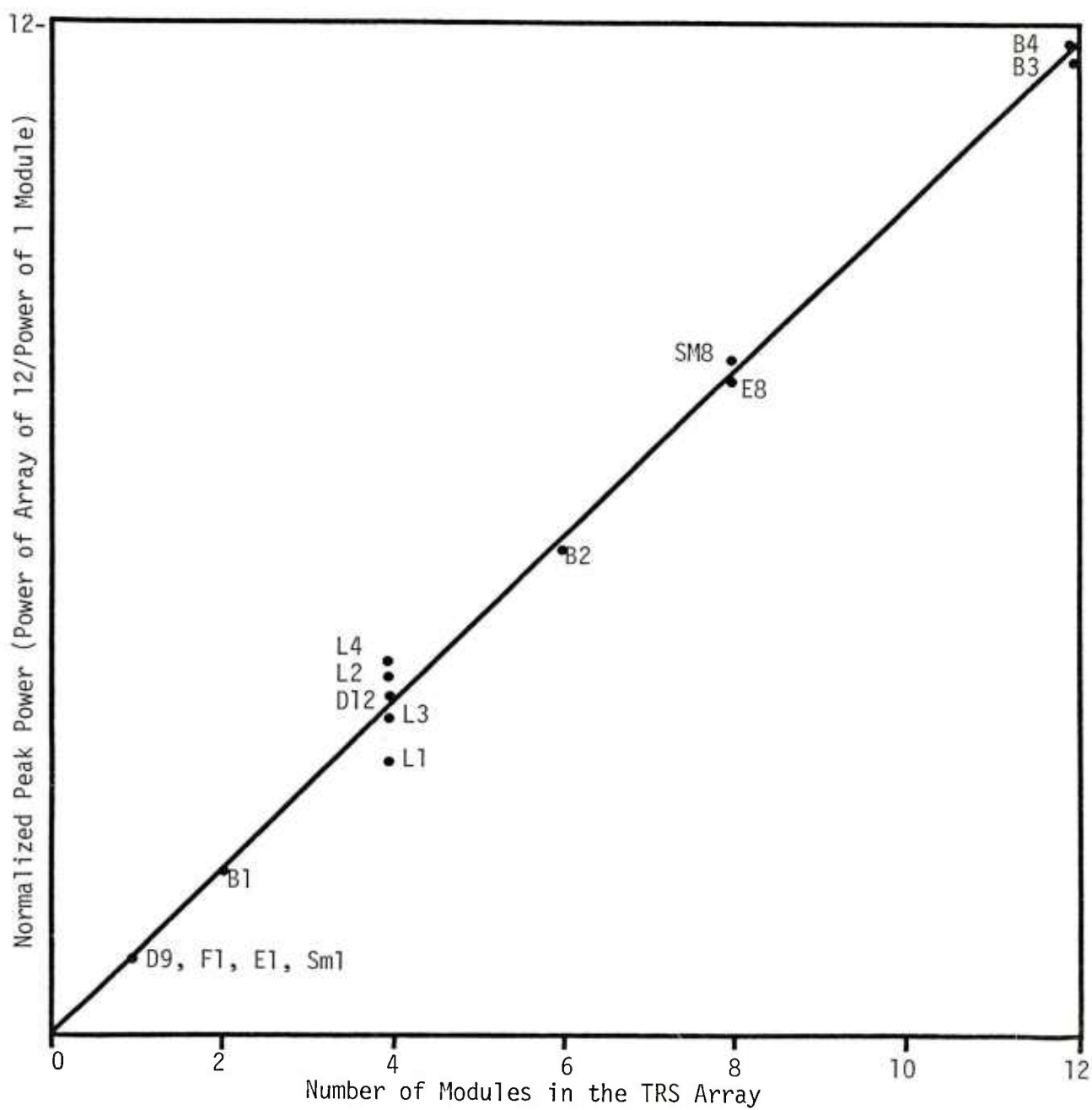


Figure 30. Normalized power outputs of multiple module TRS arrays.

During the investigations it was found that TRS systems which burned 18 μ Al powder were more efficient than TRS systems which burned 6 μ Al powder. For given combustion conditions (i.e., Al/O₂ and HE/O₂ ratios, ignition conditions, and Al yield) the scaled fluence output of multi-module TRS systems was similar to the single module output. This indicated that the energy output from multi-moduled TRS systems increases linearly with the number of modules used in the TRS. However, more needs to be learned about the transport of radiation through any intervening TRS.

With the completion of the initial TRS testing program, a large high flux and fluence TRS had been developed. Fluxes of 200 cal/cm²-sec and fluences of 100 cal/cm² had been achieved. Since the completion of the research program the TRS has been used to successfully irradiate soils, aircraft, shelter, missiles, and tank components. Some problems concerning thermal pulse rise time, convective vs radiative heating, and pulse reproducibility have been encountered since the initial research project. These problems need to be further addressed.

3.2 COMPUTING THE RADIATIVE OUTPUT OF TRS DEVICES

When the TRS device is ignited the aluminum near the source of ignition combusts. The chemical reaction spreads in a complex manner depending on where the aluminum happens to be, how much oxygen is available and how much energy is available to initiate the combustion. This process quickly forms a radiating growing fireball, which eventually cools. Ideally, the combustion occurs homogeneously and uniformly throughout the fireball simplifying the process of estimating the radiative output. Practically, this doesn't occur, and therefore, the approach taken in computing the radiative output is approximate.

During this effort a computer program that treats each module as an ensemble of point sources was developed. Each module is treated as a linear array of point sources along the module centerline. The program has been written to facilitate its modification to treat a module as a surface or volume radiator as appropriate. If treated as a volume radiator, some geometrical transmission loss factors will need to be incorporated.

The calculation of the fluence and flux are straightforward when the thermal radiation devices are considered as an ensemble of point sources. The fluence F is simply

$$F = \sum_{i=1}^N S_i \frac{\cos \alpha_i}{4\pi r_i^2} \quad (47)$$

where S_i is the source strength of the i^{th} point source in calories

\vec{r}_i is the vector from the detector to the i^{th} point source

α_i is the angle between \vec{r}_i and the detector's normal, \vec{n} .

N is the total number of point sources in the ensemble.

If one device is represented by M point sources then

$$S_i = \frac{S_D}{M} \text{ where } S_D \text{ is the device's total output.}$$

Figure 31 shows the geometry used to calculate the radiative output from the k^{th} point source. The coordinate system chosen here requires the xy plane to be the ground, and the xz plane should contain the detector. Then,

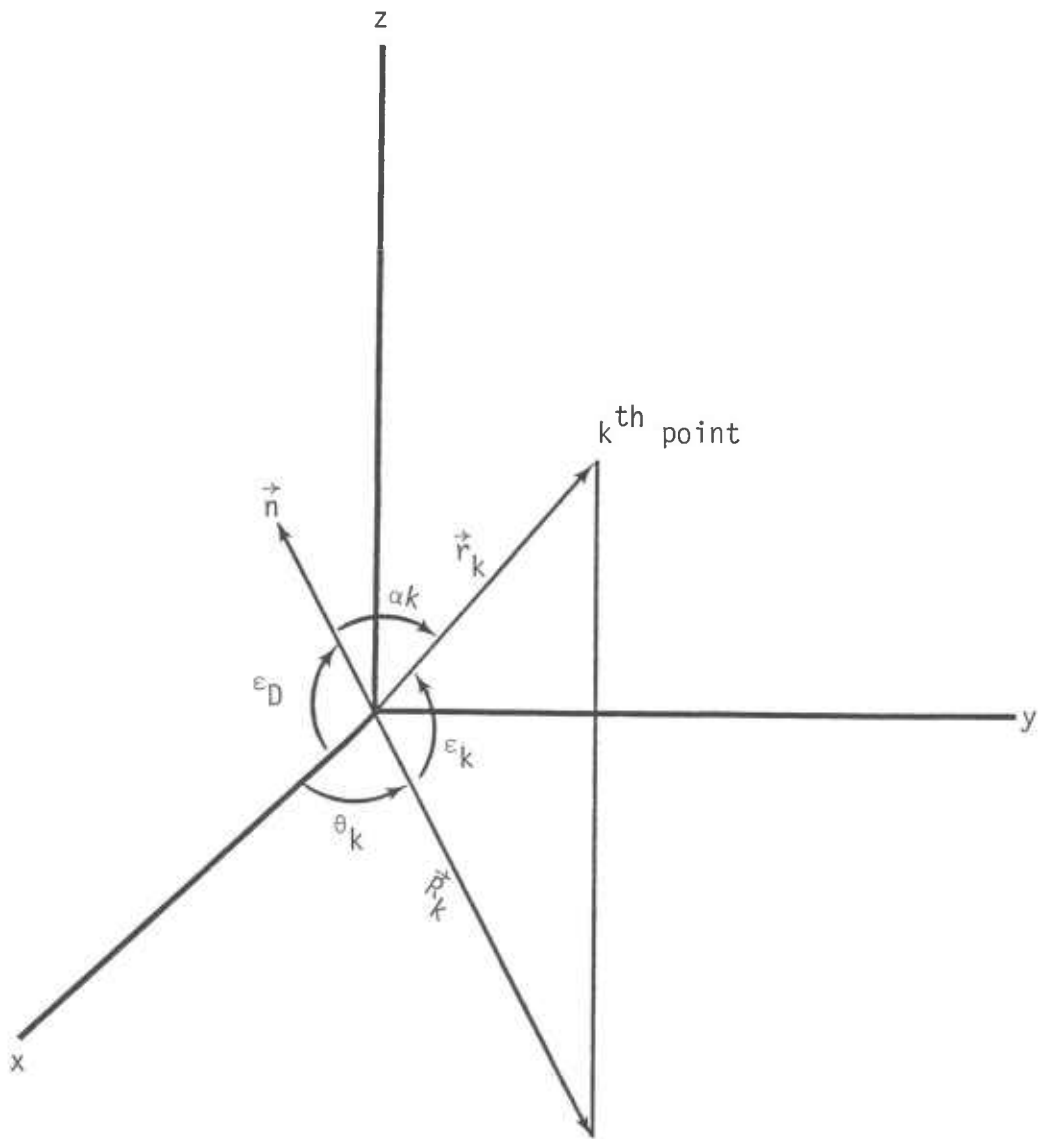


Figure 31. Geometry for computing contribution from k^{th} source.

$$\cos \alpha_k = \cos \varepsilon_D \cos \theta_k \cos \varepsilon_k + \sin \varepsilon_D \sin \varepsilon_k \quad (48)$$

or $\cos \alpha_k = \frac{1}{r_k} \left\{ R_k \cos \varepsilon_D \cos \theta_i + h_i \sin \varepsilon_D \right\} \quad (49)$

whence,

$$F = \sum_{i=1}^N \frac{1}{4\pi r_i^3} \left\{ R_i \cos \varepsilon_D \cos \theta_i + h_i \sin \varepsilon_D \right\} \quad (50)$$

The representation of a module as a set of point sources (more than one) is only necessary for detectors placed close to it, as illustrated in the following application of the module thermal predictor program to the configuration in Figure 32. The detector is oriented perpendicular to the ground (x-y plane); its normal along x. The centerline of the vertically-oriented module is at a distance R from the detector at an angle of 45° (in the x-y plane). The module center is placed at a height equal to one-half its length. The length of the chosen module is 6.7 m. Since its diameter is approximately 1.5 m, ranges closer than 1 m are not included. The module was represented as a set of N points equally spaced on its centerline. The results are shown in Figure 33 for four cases: N = 1, 3, 5 and 7. The results are insensitive to N for distance greater than a module length (6.7 m). For distances closer than this, representing the module as 1 point is unacceptable. A good rule of thumb for selection of the number of points seems to be to set N equal to an integer obtained by normalizing the length of the module by the range of interest and adding 1 to the truncated result.

$$\text{i.e., } N = \frac{L}{R} + 1 \quad (51)$$

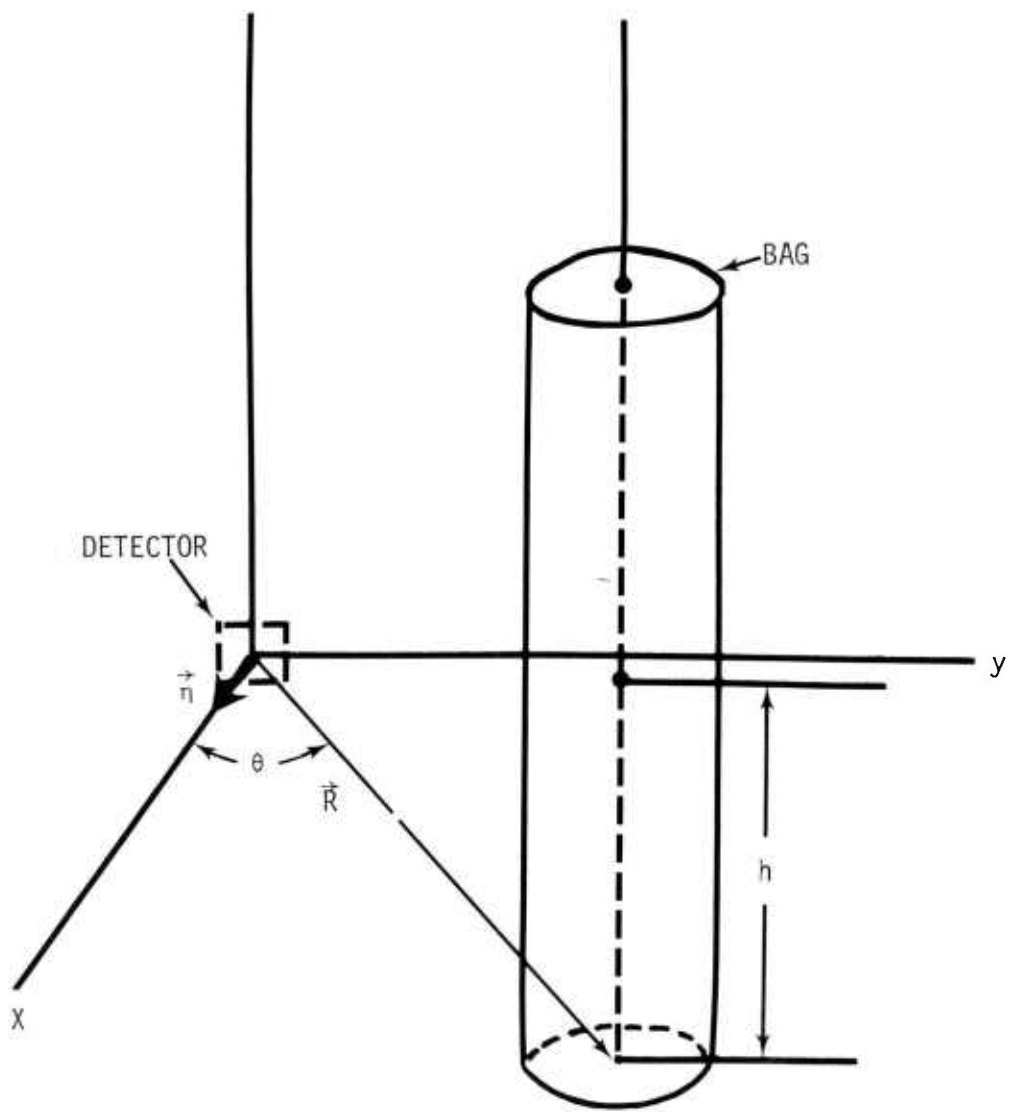


Figure 32. Orientation of detector and thermal simulator module.

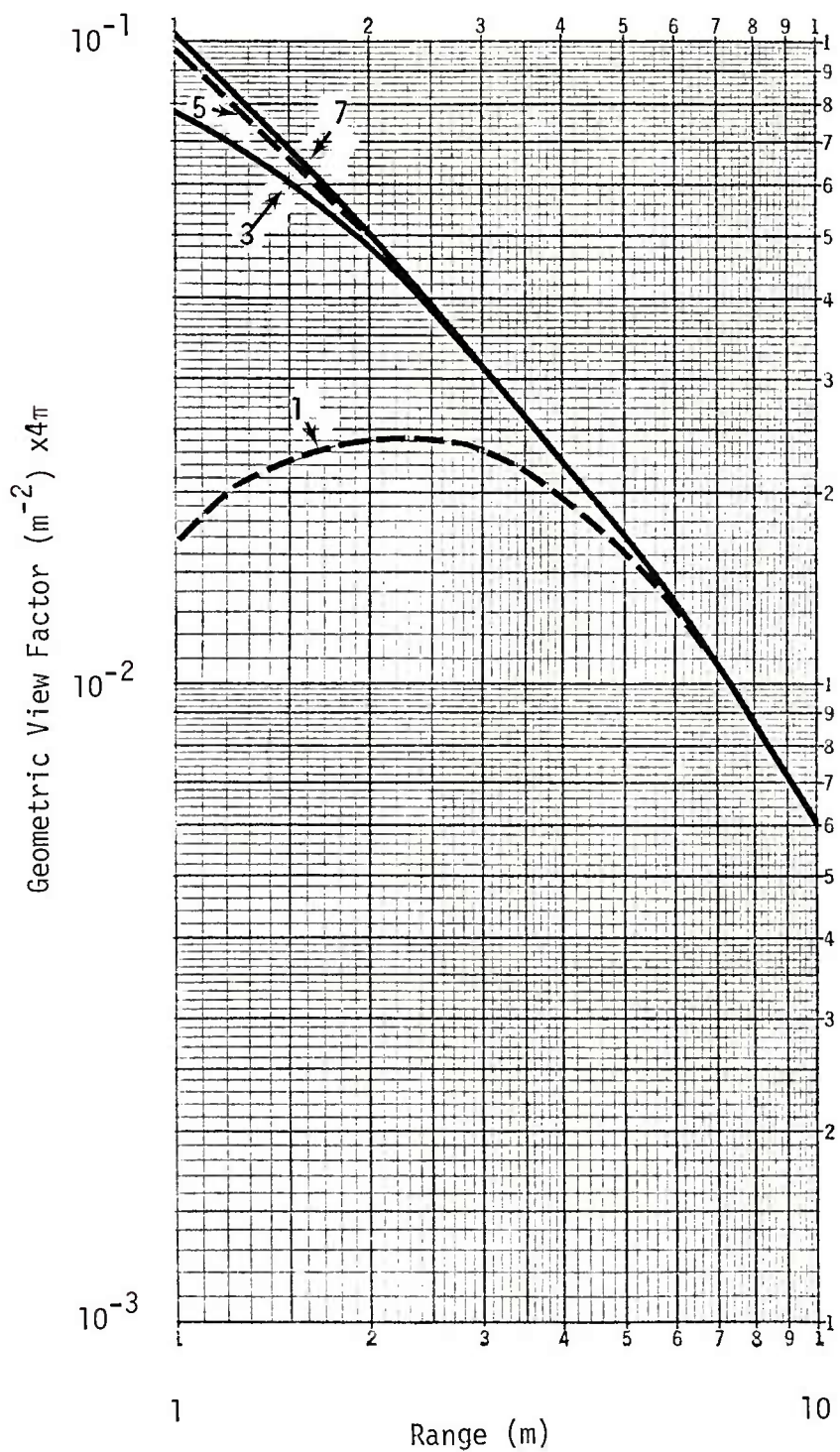


Figure 33. Variation of geometric view factor with number of source points for thermal simulator module.

Figure 34 presents an example of an ensemble of eight single thermal radiation simulator modules. For this ensemble the radiation can be computed by merely summing the contributions from each of the single modules. An example of such computations leads to Figure 35 which shows the effect on distance away from the ensemble. At 1 m the geometrical view factor* is 0.041 per square meter. The output of one module is 9×10^6 cal, whence the fluence would be 3.72×10^5 cal/m² or 37 cal/cm². The points shown in the plan view are each in the plane which is orthogonal to all the module centerlines and bisects each of them. Figures of this type should be generated for reference purposes once the thermal radiation simulator output is better characterized.

3.3 NEED FOR ADDITIONAL CHARACTERIZATION

The knowledge of the radiative output of the thermal radiation simulator needs to be improved. One aid in achieving this goal is to generate empirical data, such as shown in Figure 36, that are similar to the computational data shown in Figure 35. Figure 36 shows the approximate maximum view factor for the eight module array shown in Figure 34. For this case, iso-fluence contours are obtained by multiplying the view factors by 9×10^6 calories, yielding fluence in calories/m². The results of Figures 35 and 36 will be readily comparable when enough is understood about the physics to allow simplified models to be generated. When models are available, the fluence at various detectors and orientations can be reliably estimated. Data on the spectral characteristics of the TRS are also desirable so that spectral differences between nuclear environments and TRS devices can be taken into account. At this time reliable estimates of the spectral output of these devices are not available.

*Defined by setting the source terms of each module to unity in equation 47. This statement is applicable only for identical modules.

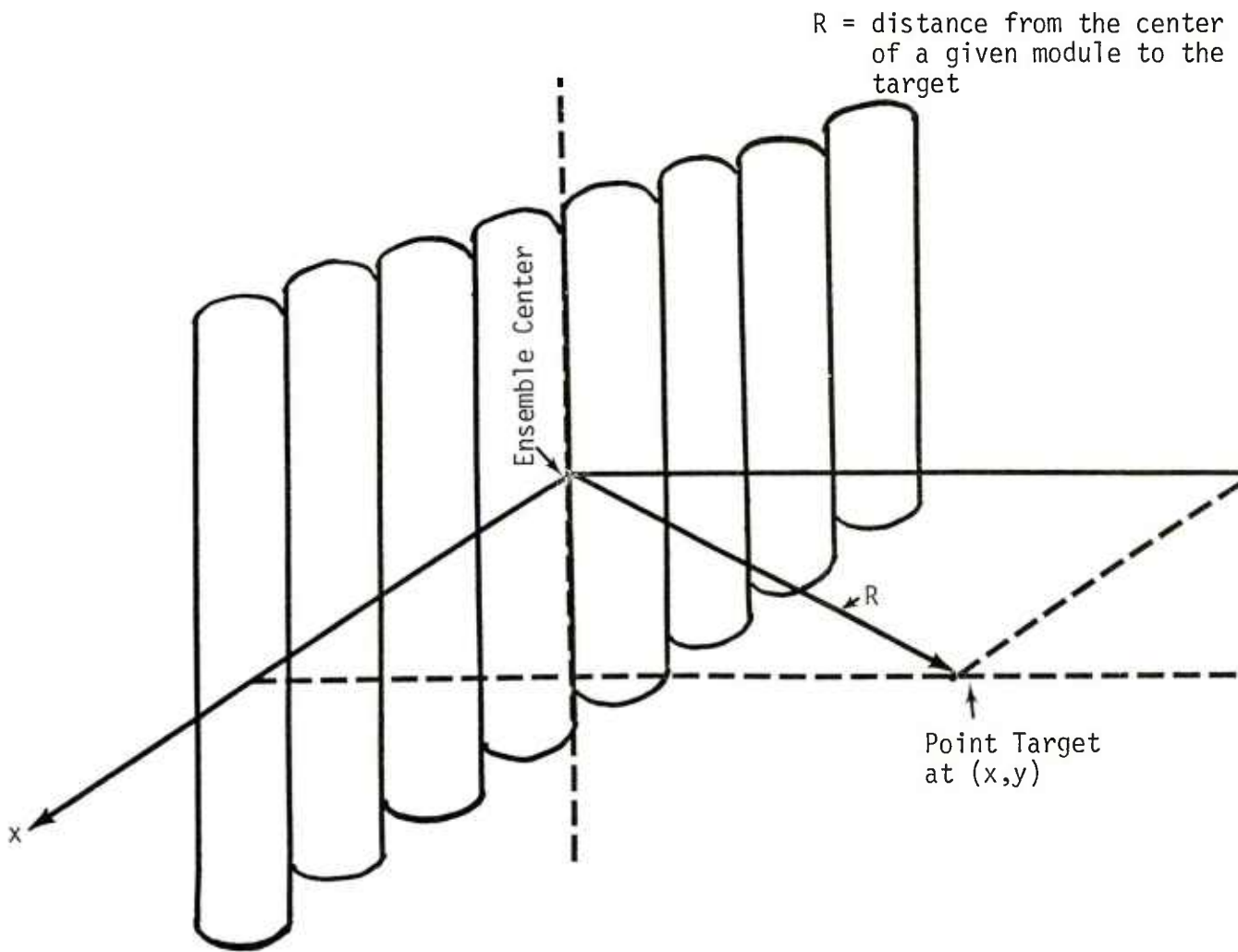


Figure 34. Ensemble of thermal radiation simulator modules.

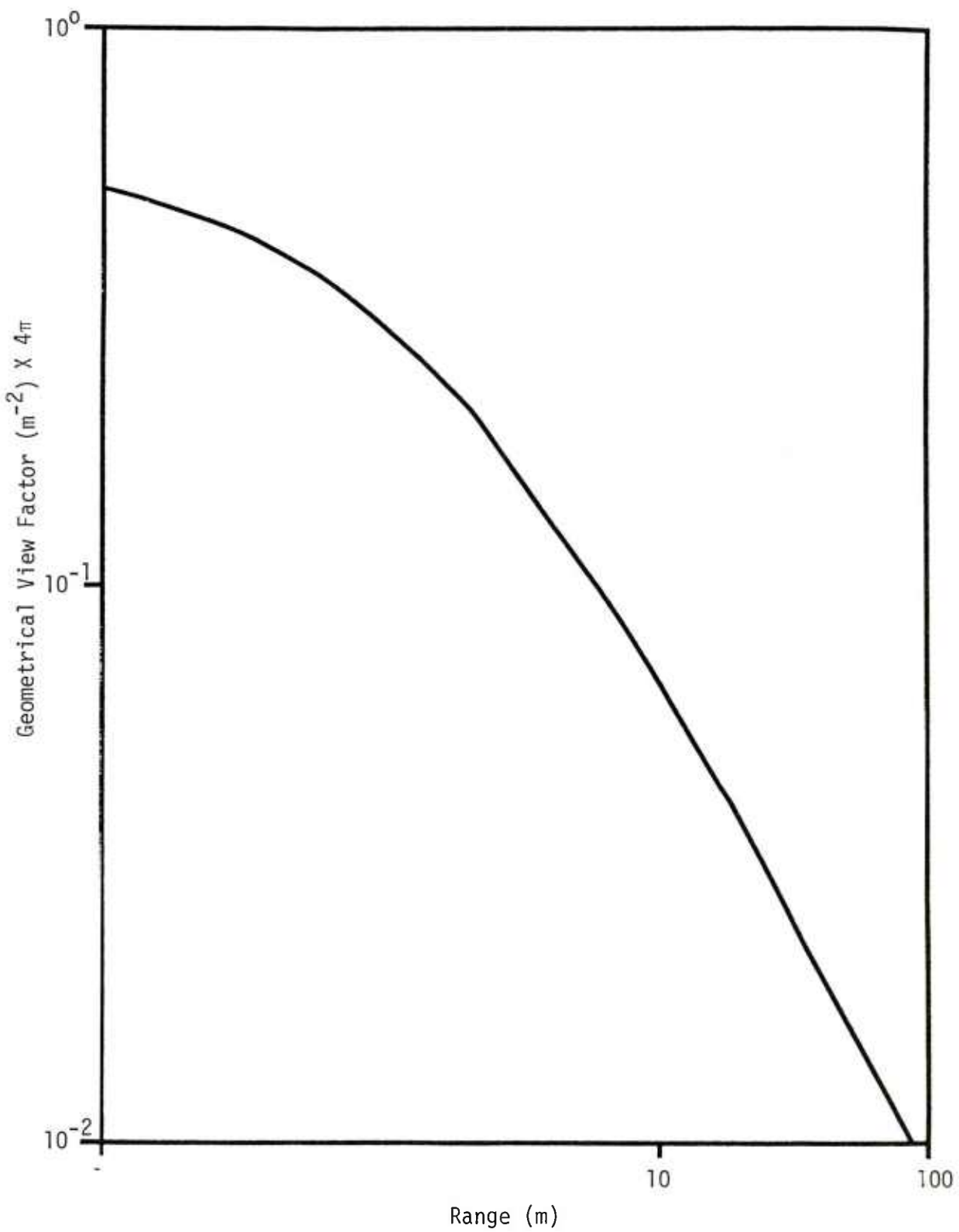


Figure 35. Effect of range on geometrical view factor.

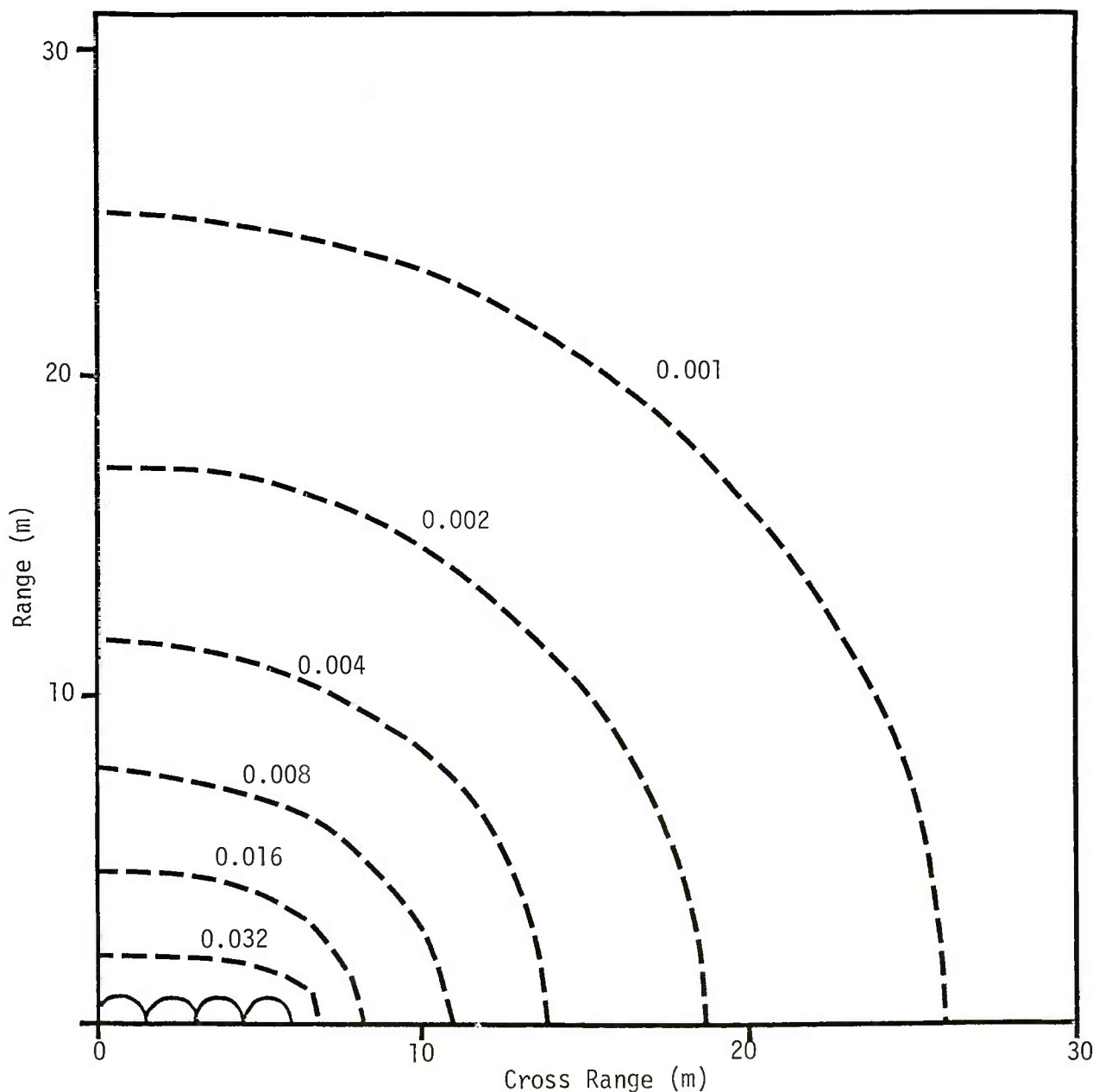


Figure 36. Contours of estimated maximum geometric view factors from an 8-module ensemble (normalized to output from one module).

SECTION 4

TRS PLACEMENT IN AN AIRBLAST ENVIRONMENT

The placement of the thermal simulation devices (TSD) is crucial to an adequate simulation of the thermal radiation environment. Ideally the easiest placement from the standpoint of producing the right distribution of radiation would be at the burst location. However, since the radiated power of a single TSD is much smaller than from a nuclear device, a large number of them are needed to obtain the appropriate levels. For example, assuming superposition, it would take about 39,000 modules, each radiating at 9×10^6 calories, to represent a 1 kiloton burst having a thermal efficiency of 35 percent. A typical module is a 6 meter high cylinder of 1.5 meters diameter. Therefore, if these modules were hexagonally packed they would fill a hemisphere approximately 60 meters in radius. If within each module 4 kilograms of aluminum were present, over 170 tons of aluminum powder would be consumed within this hemisphere. It is worthwhile noting that the radius of a one kiloton nuclear fireball (surface burst) is this size about 20 milliseconds after detonation.

Figure 37 presents the relative dimensions of the initial radius of a hemisphere of thermal radiation modules required to produce an equivalent fluence of thermal radiation from a 1 kiloton of the stated thermal efficiency (35 or 5 percent) with appropriate packing (hexagonal or square). No growth data are shown because they are not available.

Figure 37 also presents the time of arrival from Brode (see Section 2.3) and the fireball model for 1 kiloton free-field and 1 kiloton surface burst. It should be noted that the assumption of superposition is not believed to be valid in these circumstances. It is expected that the whole ensemble would be opaque at early times and consequently radiation will be issued over longer periods of time, probably of the order of ten seconds. This duration is much too long for simulating one kiloton. One can expect that pulse duration will scale as the cube root of the ensemble yield.

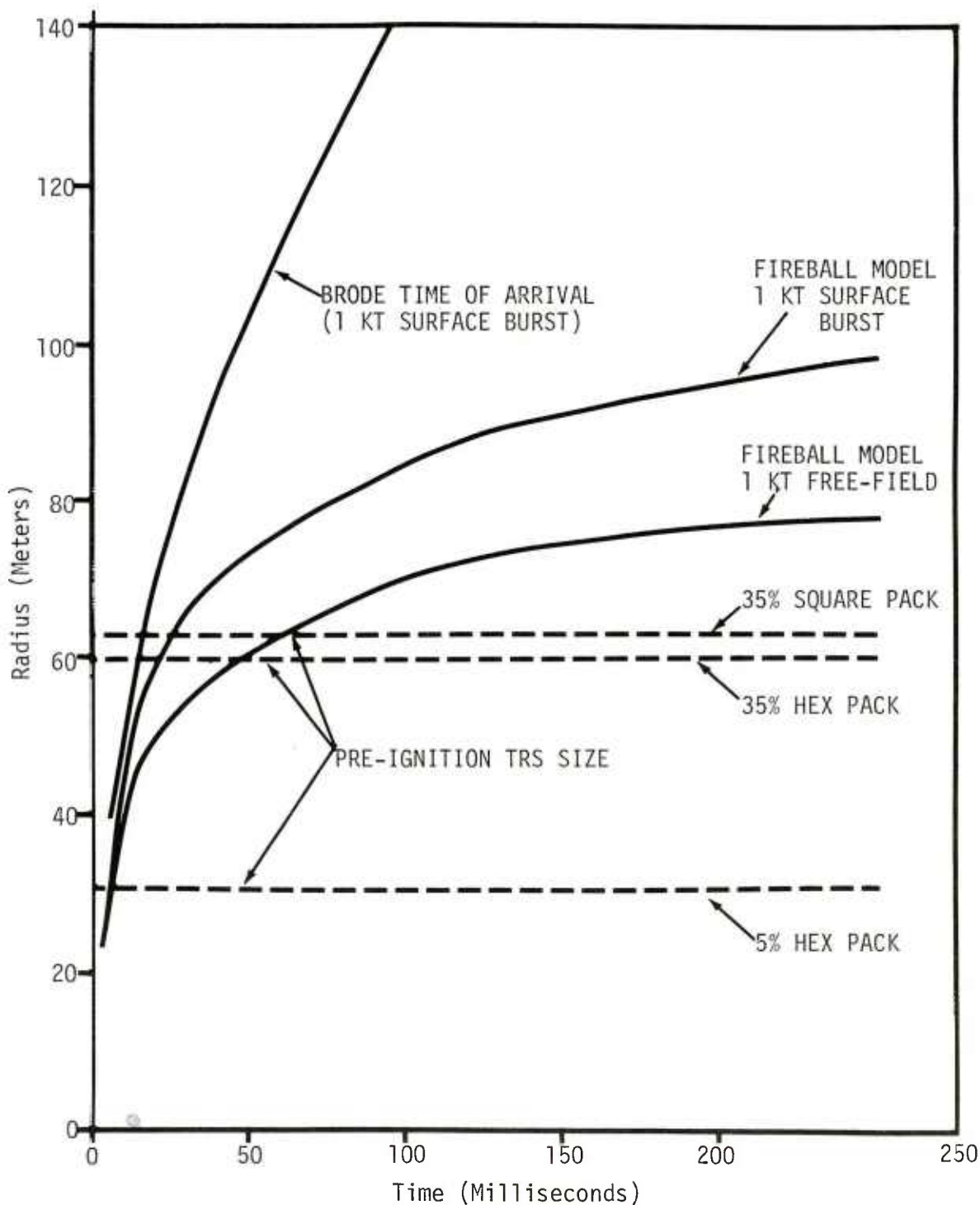


Figure 37. Fireball radius-time model for 1 KT surface burst (and 1 KT free-field).

The feasibility of utilizing such a large ensemble of thermal radiation simulators has not been investigated. Considerable work would need to be done to allow their use in such an arrangement. Another approach in deploying such devices is to substantially reduce their distance from the field point of interest. The thermal radiation can then be appropriately modeled at the field point of interest, although it will be too powerful for points closer to the device and too weak at distances farther away. Careful arrangement of an ensemble of TSDs can also be used to locally improve the thermal radiation environment simulation. Section 4.1 discusses how the required fluence or flux might be obtained with careful arrangement of these devices.

Additional effects associated with use of these devices close to targets must also be considered when arranging these devices to investigate synergistic blast and thermal loads. For example, care must be taken not to appreciably distort the blast wave flow field by the presence of the thermal simulation devices. This problem as well as techniques for its solution is discussed in Section 4.2.

Placement of these devices in a combined experiment also leads to consideration of the effects of one experiment on another. This is discussed in Section 4.3. Finally, additional work is recommended before fielding these devices on a HE test, and this is summarized in Section 4.4.

4.1 OBTAINING THE FLUENCE AND FLUX

An upper bound to radiative output from an ensemble of thermal radiation devices can be estimated by multiplying the output of one device by the number of devices. If each device is considered as a point source, the upper bound to the radiative output at some detector

can be estimated by placing each point source at a location that maximizes the geometric view factor, $\frac{\cos\alpha}{4\pi r^2}$, defined earlier in Section 3. Similarly the maximum possible distance an ensemble of devices can be placed to obtain some fluence can be estimated. For example, if the output of one device is 9×10^6 calories, a fluence of 10 cal/cm^2 is desired, the detector is oriented to obtain the maximum fluence (i.e., $\cos\alpha = 1$), and ten devices are to be used, then the range is simply

$$r = \left[\frac{10 \text{ devices} \times 9 \times 10^6 \text{ calories/device}}{(4\pi) \quad 10 \text{ cal/cm}^2} \right]^{\frac{1}{2}}$$

$$= 846 \text{ cm} = 8.5 \text{ meters}$$

Practically, the devices will not all be positioned at the same location, and therefore the view factor for some of the devices will be less than its maximum possible value. Hence, the ensemble will need to be placed closer to the point of interest and the estimated radius would be further refined by performing a set of calculations (Section 3) and interpolating on the range. One effect that could reduce the range further would be obscuration by other objects, including other devices.

Figure 38 is used to illustrate the computing of the total fluence at some object. Here the module height is taken to be 6 meters, and its diameter is 1.5 m. In this example, the experimental requirement is 1 cal/cm^2 normal to the object 3 m above the ground. Further it is desired to provide a window of width W through which the airblast can propagate relatively free of the effects of the TSD fireball. To simplify the problem somewhat, symmetry is employed about the plane containing the line of sight and normal to the ground. The range, R , and angles, θ and ϕ at which each ensemble of modules is placed can be varied as appropriate.

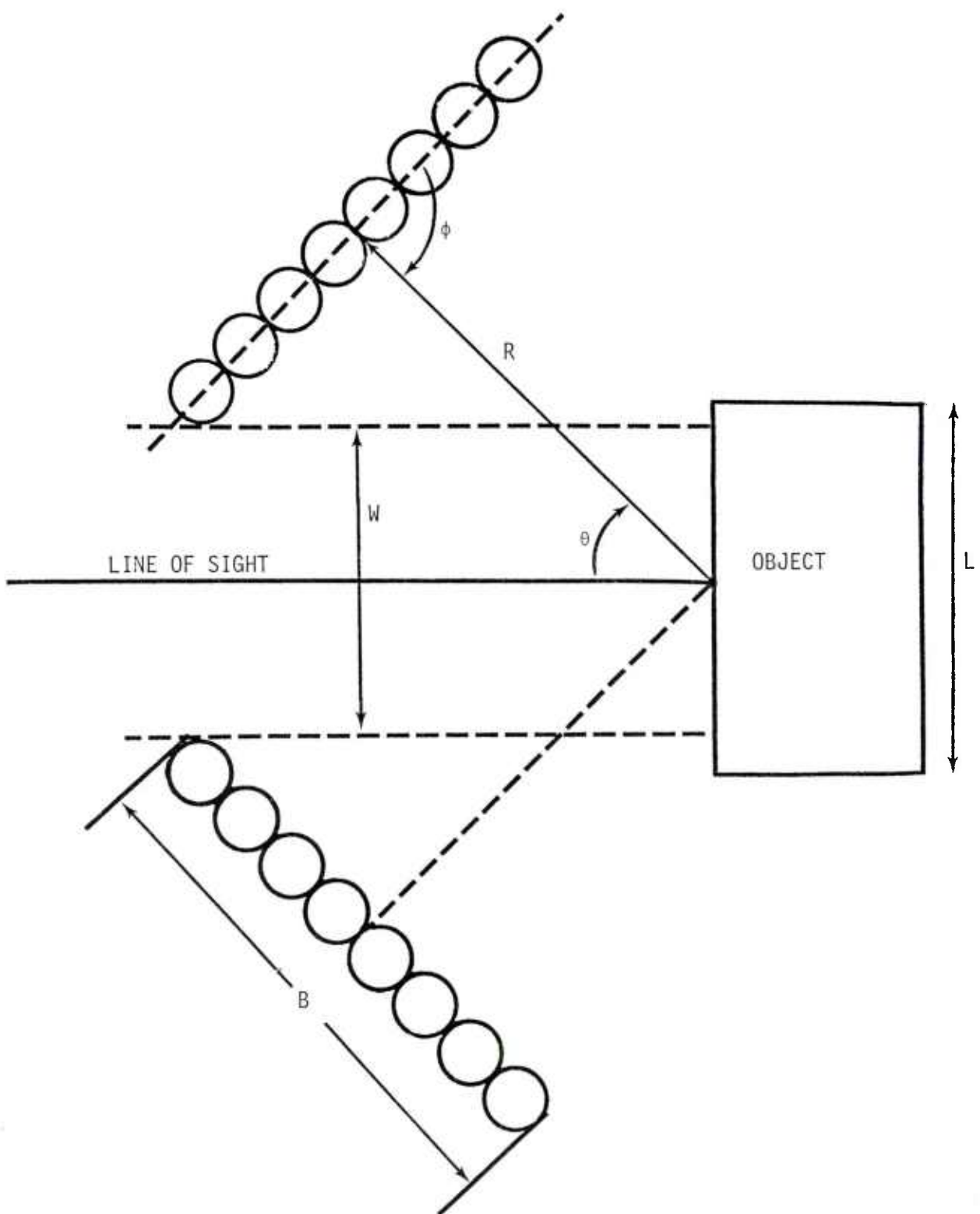


Figure 38. An example of module placement.

Estimating the distance the modules can be placed from the object

$$R \approx \left[\frac{16 \text{ devices} \times 9 \times 10^6 \text{ calories/device} \times \cos\theta}{(4\pi) \quad 1 \text{ cal/cm}^2} \right]^{\frac{1}{2}}$$

or $R \sim 34 \text{ meters } [\cos\theta]^{\frac{1}{2}}$

where the effect of different ϕ has initially been ignored. If the experimenter were to orient the ensemble such that ϕ was 90° (see Figure 36, which also showed the effect of various orientations on maximum possible fluence)* then

$$\frac{W}{2} = R \sin\theta - \frac{B}{2} \cos\theta$$

and therefore if θ were 45° R would be 24 meters and the window width would be 25.4 meters. If instead ϕ were set to θ then W would be increased to $2R \sin\phi$ or 34 meters for the same θ of 45° .

Estimating the output of those same two arrangements more accurately, the fluence is found to be 1.36 cal/cm^2 when the center of each ensemble is a range of 24 meters for $\phi = 90^\circ$, and 1.42 cal/cm^2 at the same range but for $\phi = \theta$. The comparison shows that the experimenter gains by using the latter arrangement in addition to providing the maximum window. The only loss will be the possible effect of transmission through adjacent module fireballs.

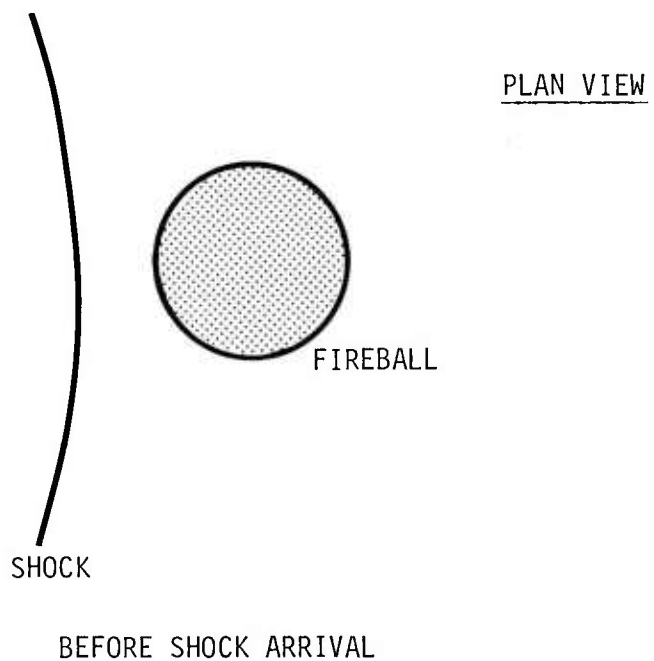
4.2 SHOCK INTERACTIONS WITH FIREBALL

It is desirable to avoid placing the thermal radiation simulators between the explosion source and the object being radiated. The result of firing the thermal radiation simulator module is to create a hot fireball of underdense gas that is eventually in pressure equilibrium with the atmosphere and is filled with the products of combustion (Al_2O_3 , ignitor residue, and small pieces of mylar). These latter constituents can be hot particulates. In Figure 39, the propagation of a shock wave through a fireball is shown qualitatively. Since the fireball is hot, the shock will propagate through it more quickly than through the surrounding atmosphere. It will also compress the hot fireball and move particulate matter within it closer together. This will tend to spread the shock out as shown in Figure 39, introducing two dimensional effects.*

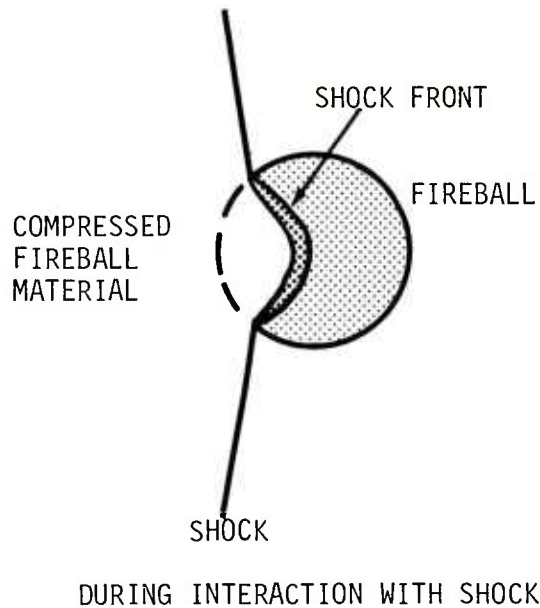
The passage of a planar shock through a hot region,** which is in pressure equilibrium with its surroundings before shock arrival, appears to have little effect at high overpressure on the transmitted pulse. This has been demonstrated using two calculations performed with the SAI one-dimensional version of the HULL code (References 17, 18). First, a reference calculation was performed at sea level atmospheric pressure, density, and internal energy. At an inlet boundary, a nuclear airblast waveform was used which corresponded to a 59.4 psi peak overpressure from a 1 kiloton surface burst. This airblast waveform was obtained using the AFWL LAMB code (described in references 19 and 20). A second calculation was then performed, but now the propagation path contained a hot region starting 20 m from the inlet boundary and lasting for 3 m as shown in Figure 40. Several observer locations were included in each calculation in order to allow for comparisons. A reflective boundary was placed at the end of the computational mesh so that signals

*Since the fireball is a finite cylinder, end effects will lead quickly to three-dimensional effects.

**without particulates



BEFORE SHOCK ARRIVAL



DURING INTERACTION WITH SHOCK

Figure 39. Airblast interaction with TRS device fireball.

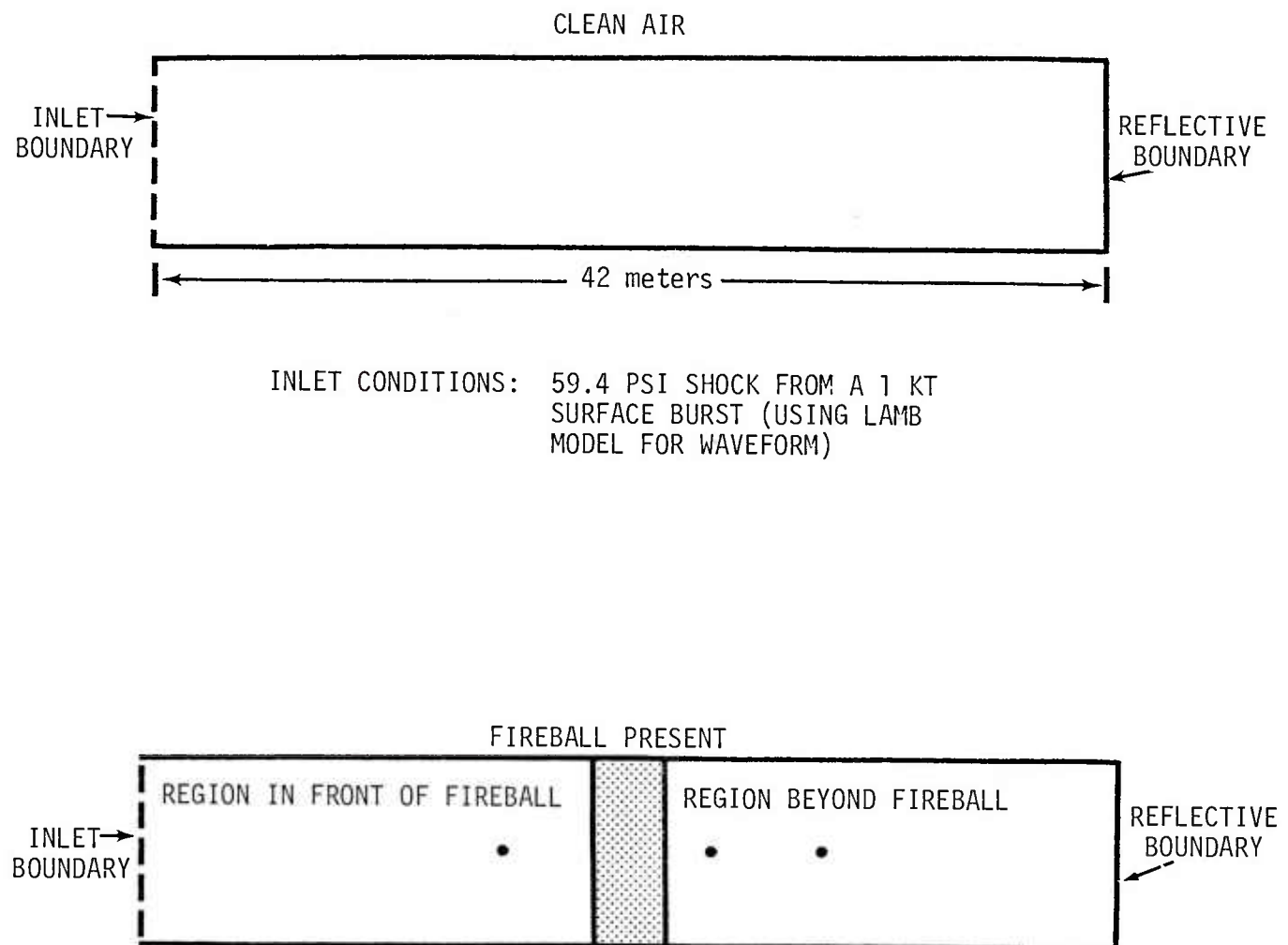


Figure 40. Idealization in one-dimension of shock propagating through fireball.

propagating back into the mesh would be obvious. The spatial ordinate is placed at the left hand side of the figure, 140 m from the 1 kiloton surface burst. The mesh is approximately 42 m long, therefore placing the right hand boundary 182 m from the burst. Both calculations were one-dimensional rectangular and therefore underpredict geometrical attenuation. However, our desire here is to assess the importance of the TRS fireball on airblast propagation. Initial conditions for each case are given in Table 6.

Table 6. Computational parameters.

<u>Calculations with Fireball Present</u>	<u>Clean Air Calculation</u>
$\rho = \rho_0, \epsilon = \epsilon_0, I = 1,100$	$\rho = \rho_0, \epsilon = \epsilon_0, I = 1,215$
$\rho = \rho_0 / 10, \epsilon = 10\epsilon_0, I = 101,115$	where $\epsilon_0 = 2.08 \times 10^9$ ergs/gm
$\rho = \rho_0, \epsilon = \epsilon_0, I = 116,215$	$\rho_0 = 1.225 \times 10^{-3}$ gm/cm ³
IMAX = 215	
DX = 20 cm	
$X_0 = 1.4 \times 10^4$ cm.	
OP = 59.4 psi	
W = 2 kilotons (i.e., 1 kiloton surface burst)	
T _{start} = 93.65 msec	

Figures 41 through 45 present comparisons of the two calculations for various observer locations. The observer locations are shown in Figure 40 at 5 m forward of the hot fireball and 2 m and 7 m beyond the hot region. Each calculation began 94 milliseconds after detonation of a 1 kiloton device, when the airblast arrives at a range of 140 meters. The wave propagates through the mesh in about 60 milliseconds. The reflected wave does not arrive at any observer stations shown in Figures 41 through 45.

When the shock passes through the hot region the density in the fireball is increased by a factor of about 15 to 20, and the hot compressed region travels in the direction of the incident shock wave. The presence of this fireball causes relatively small changes to the transmitted velocity and overpressure peaks. Specifically, a 7.7 percent reduction in the overpressure peak is seen 2 meters beyond the fireball as well as a 5 percent reduction in peak velocity. The comparison of velocities at this observer position is shown as Figure 41. Further downstream, 7 meters beyond the fireball, the peak overpressure is reduced by only 2 percent and the velocity by about one percent, with the differences diminishing more with increasing distance. The hot region thus causes the pulses to arrive sooner, together with a broadening of the pressure and velocity peaks especially for observers close to the fireball. The fireball also modifies the upstream results as shown in Figures 44 and 45, where it can be seen that overpressure drops more rapidly and velocity more slowly at late times with the fireball present. These calculations do not include the effect of any hot particulate matter. Since the ratio of total particle mass to fireball volume is approximately the same as the ambient air density, the effect may be important and may further reduce the strength of transmitted pressure pulse. In addition, the two-dimensional effects have not been estimated. A typical calculation that might be done to

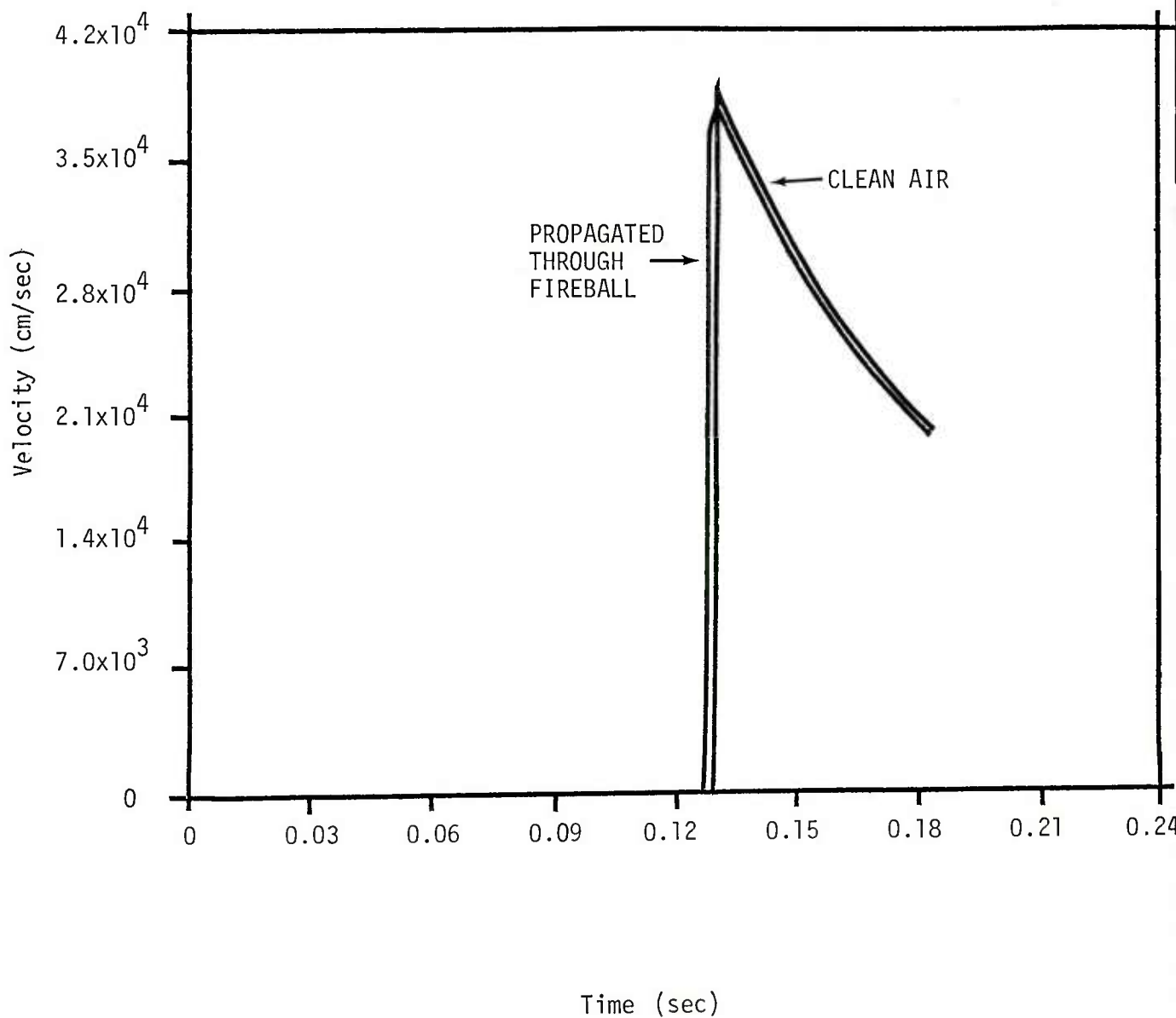


Figure 41. Comparison of velocity at observer approximately 2 meters beyond fireball.

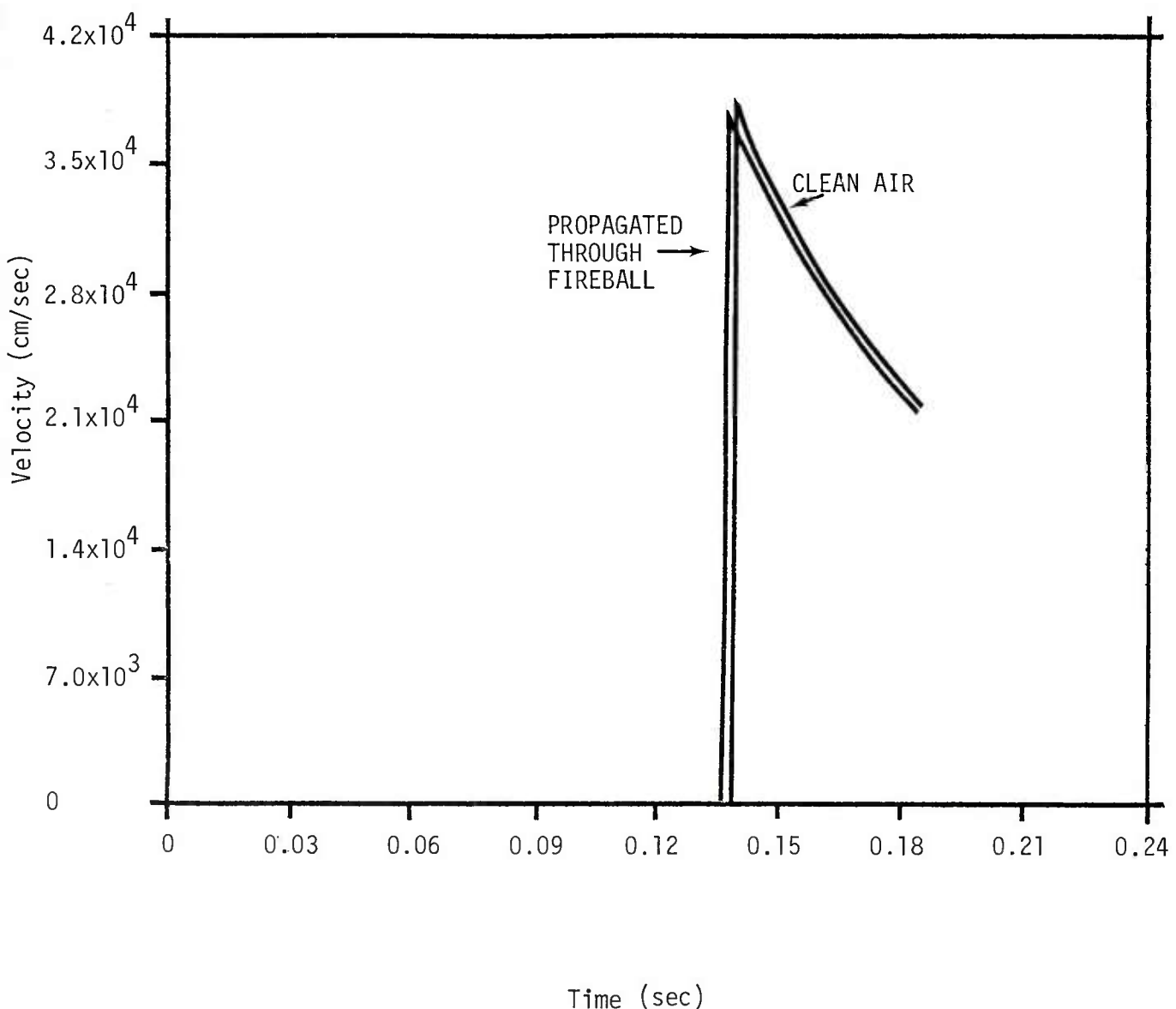


Figure 42. Comparison of velocity at observer approximately 7 meters beyond fireball.

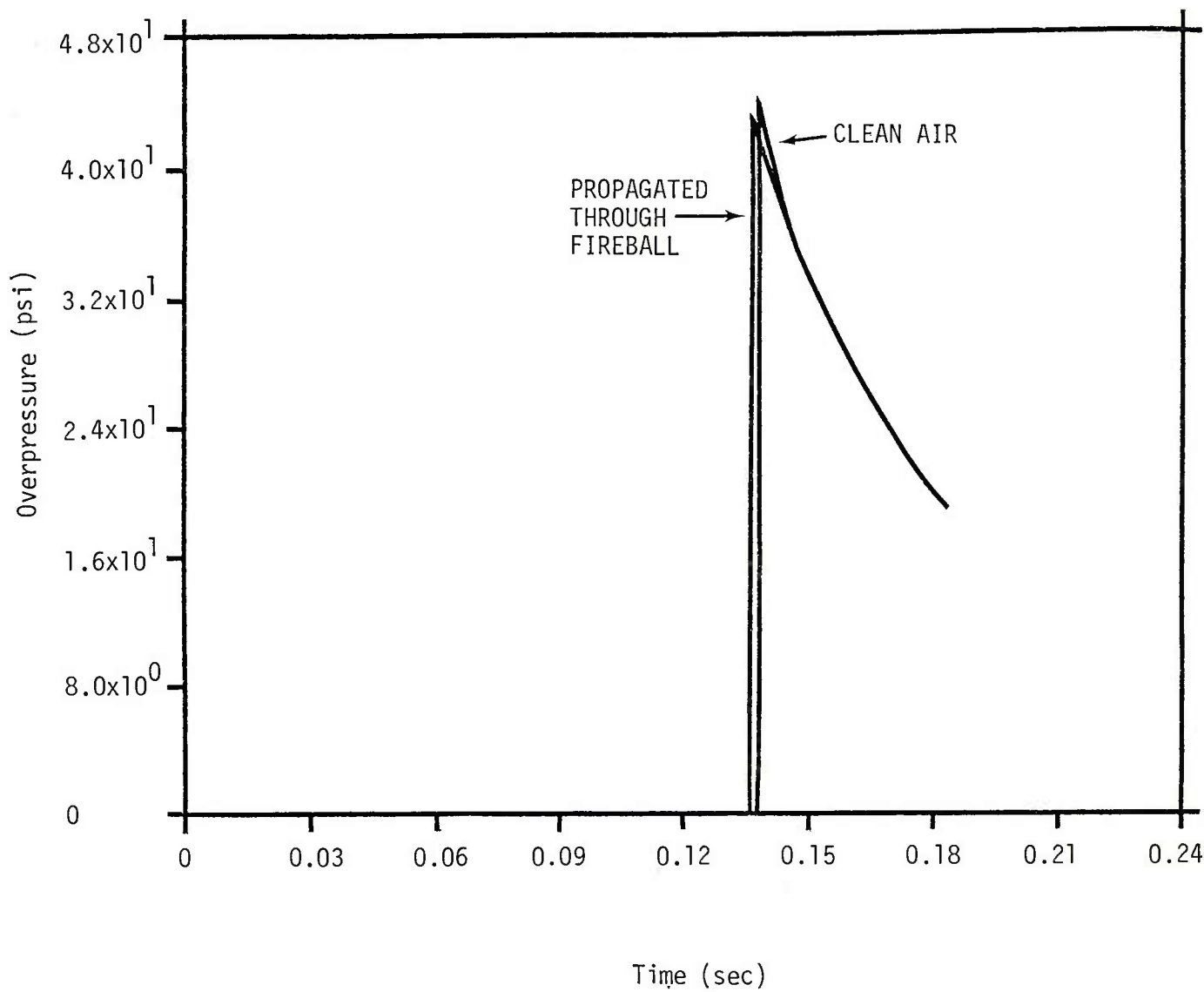


Figure 43. Comparison of overpressure at observer approximately 7 meters beyond fireball.

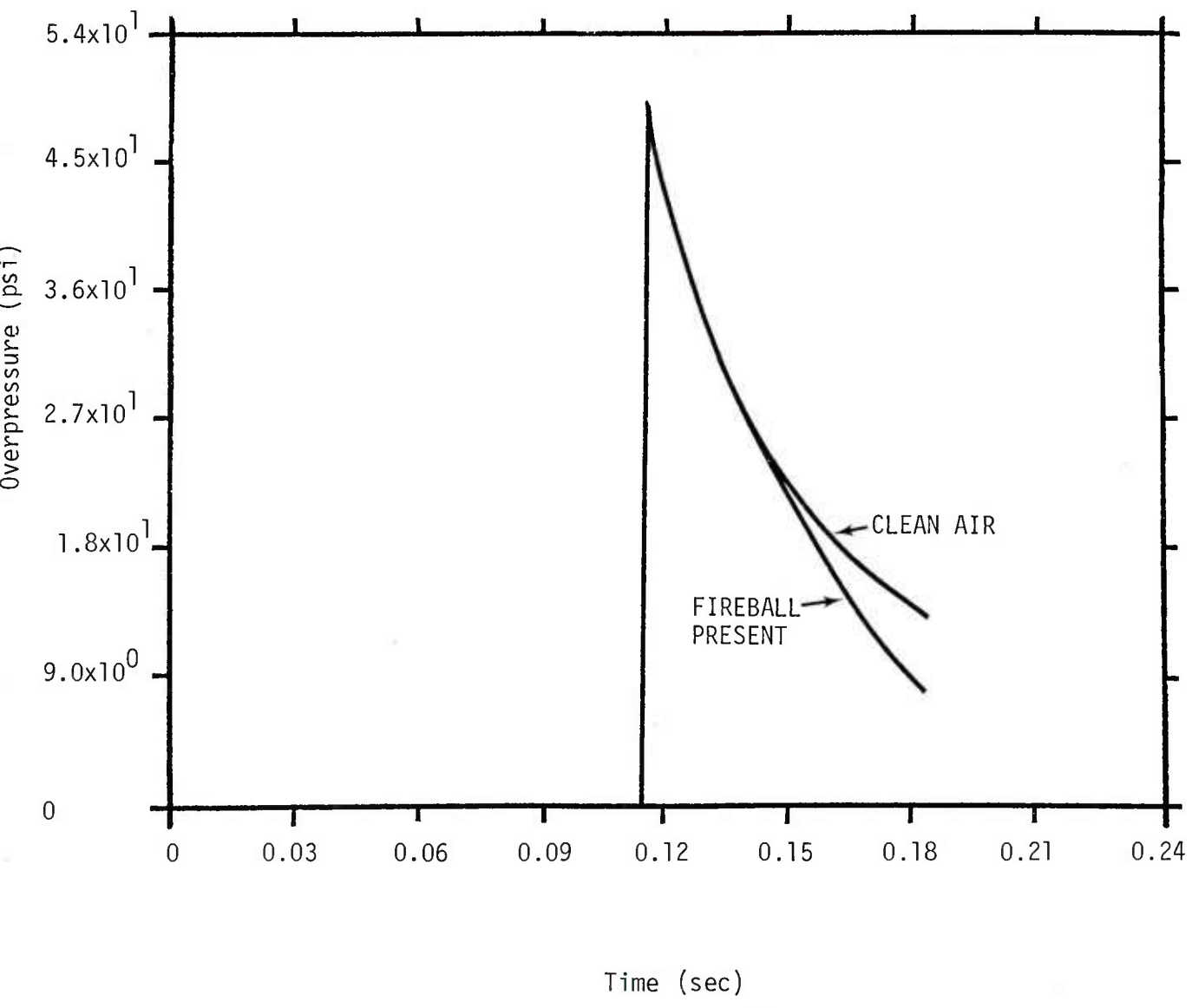


Figure 44. Comparison of overpressure at observer approximately 5 meters in front of fireball.

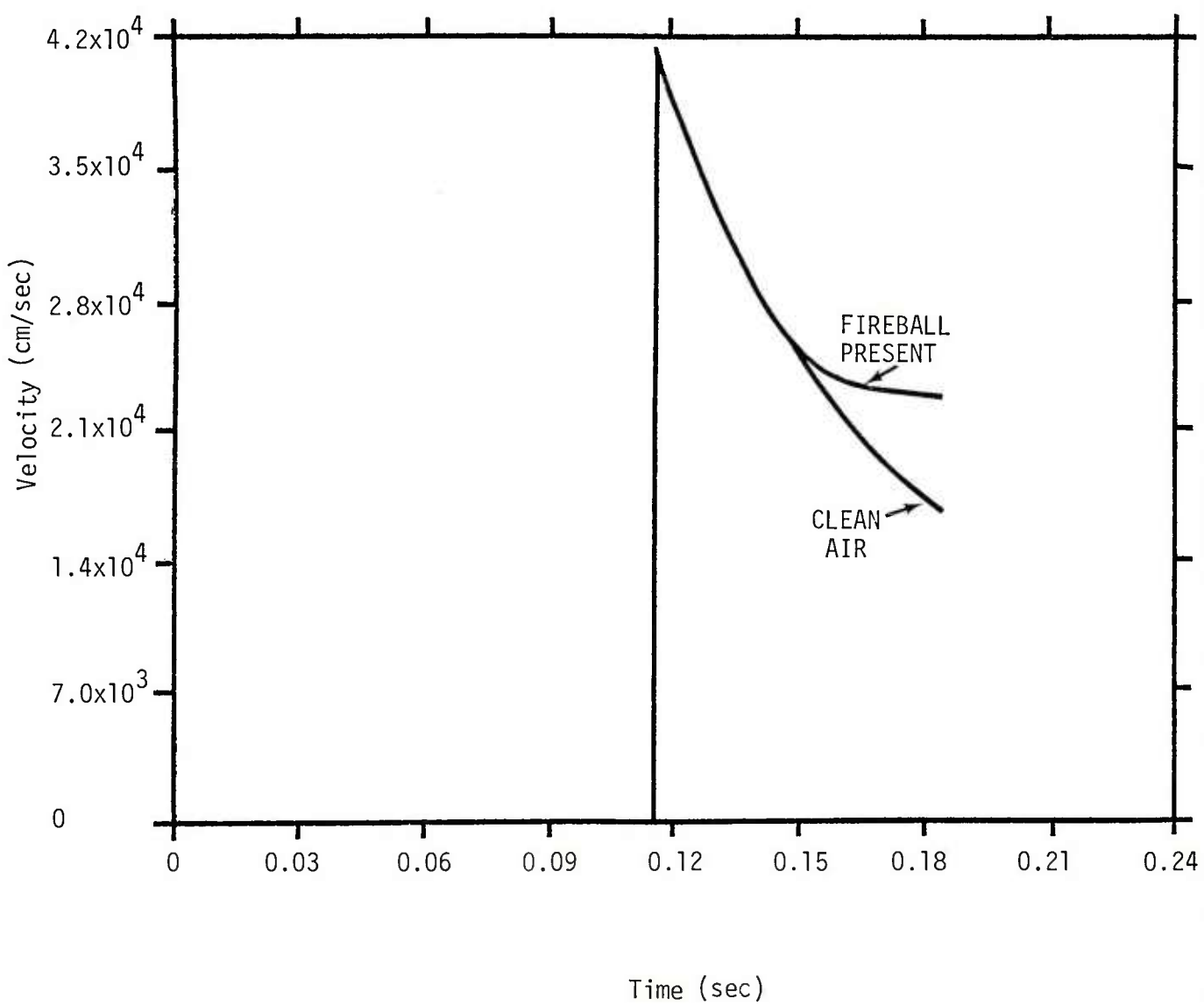


Figure 45. Comparison of velocity at observer approximately 5 meters in front of fireball.

estimate the importance of the two-dimensional effects is shown as Figure 46. An inlet boundary would again be used to introduce an airblast into hydrodynamic mesh, and a reflective boundary would be used to employ symmetry. Good transmissive boundaries would keep the costs down by not including more mesh than needed.

4.3 EFFECT OF OTHER EXPERIMENTS

When designing any program involving more than one experiment, the interaction of experiments must be considered. For example, as discussed previously, the presence of the thermal simulation devices may modify the airblast at the target of interest. Care must also be taken to recognize that the presence of an ensemble of TRS modules can also affect the airblast incident on ancillary experiments. The magnitude of these effects must be addressed quantitatively.

To illustrate these points, Figure 47 shows a possible arrangement of three experiments being performed on objects A, B, and C using a common source of airblast. The angular position of objects A and B are fixed by other constraints, and their ranges are set by required overpressure levels. C is assumed to be in the sector shown bounded by the radials to A and B. It would of course not be placed to close to either $\beta = 0^\circ$ or $\beta = \alpha$ so as to effect overpressures at A or B. The radiative environment added by the TRS ensembles associated with object C can be calculated at positions A and B as a function of angle β to determine the best location for C. Similarly the environments from A and B must be considered when designing experiment C. Shielding on the back side of the object may also be desirable in some cases.

In summary, the TRS modules on an HE event will involve the introduction of another variable on the fidelity of the simulation on each experiment.

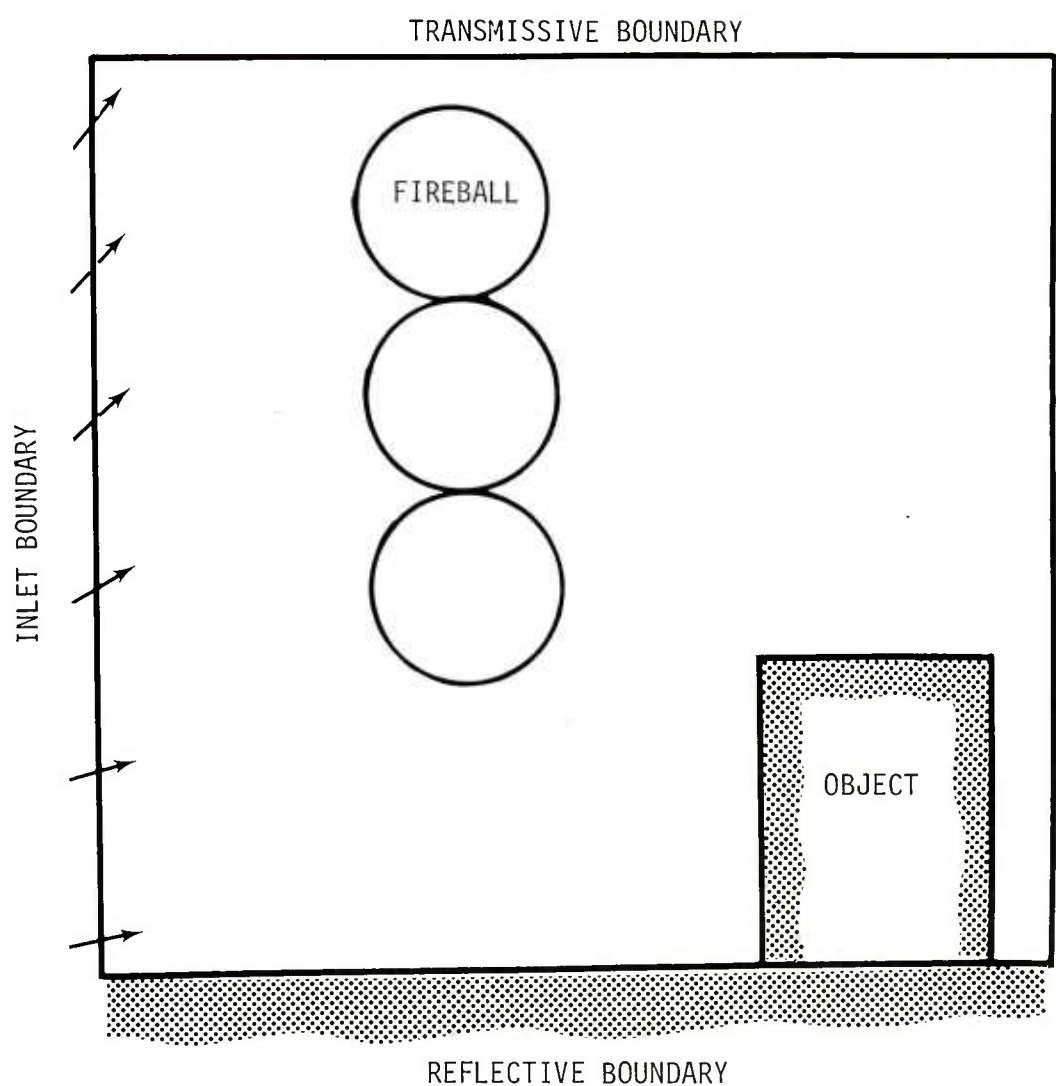


Figure 46. An example calculation.

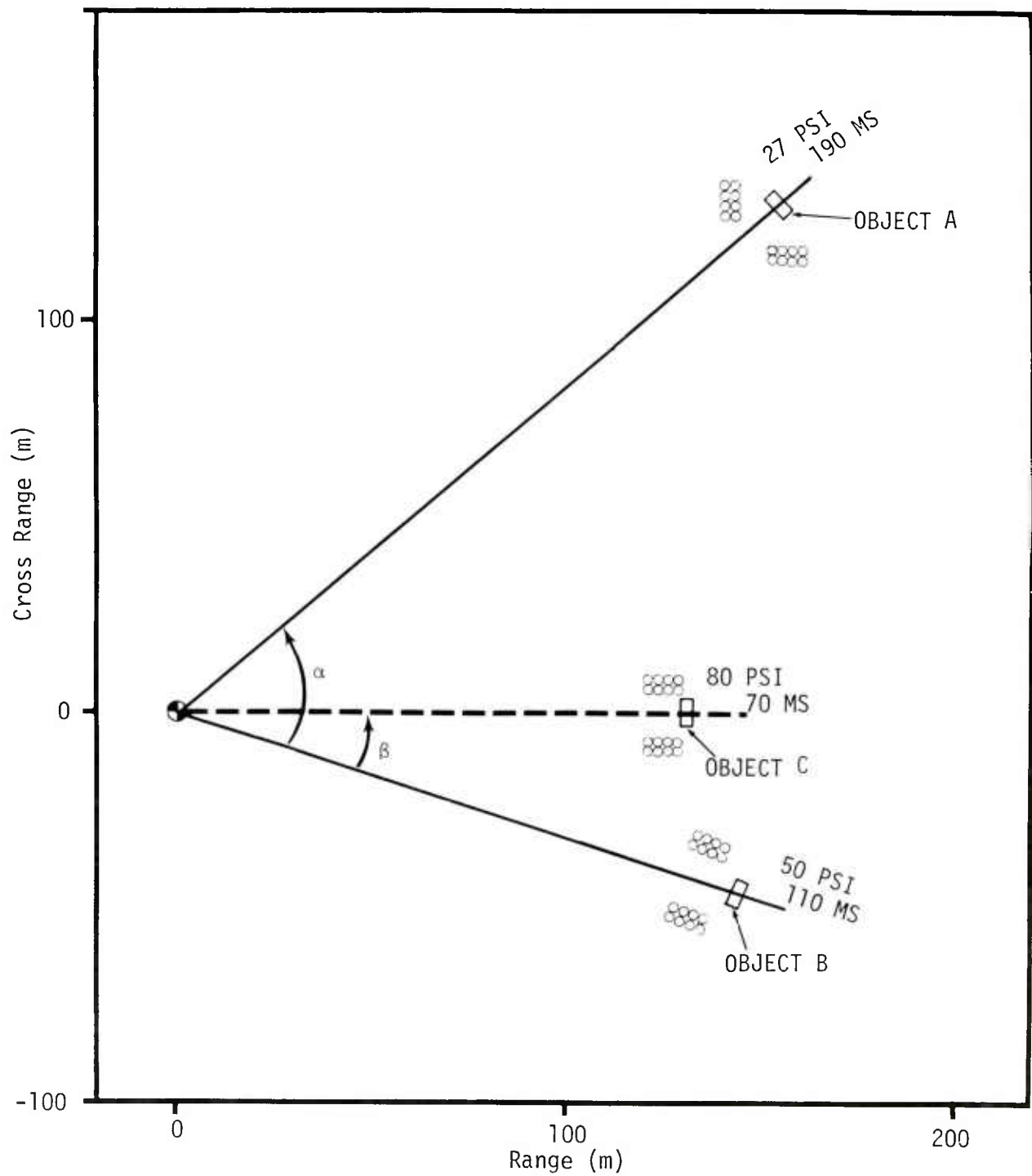


Figure 47. An example experimental layout.

4.4 NEED FOR ADDITIONAL WORK

An earlier section discussed the need for additional work to calibrate the radiative output of a thermal radiation simulator module. This section summarizes the need for additional work so that these modules can be used in an ensemble to simulate thermal radiation in airblast environments. In this summary, it is assumed that the experimenter will attempt to simulate the thermal radiation with a small ensemble of well placed modules rather than using a large hemisphere of modules near the HE airblast source. Furthermore, the discussion is restricted to ensembles of modules where each module is well characterized.

In Section 3, data were presented (Figure 30) that indicated that the peak power radiated was only a function of the number of modules in an ensemble (data limited to 12 modules). The presence of other modules does not seem to modify the pulse length and radiative waveform for conditions tested so far. Unfortunately these comparisons are not well documented. In addition better definition of the transmission losses through adjoining modules would be useful and would facilitate modeling of the thermal environment. This work needs to be done in order to determine fluence and flux, but also spectral content. Whether any module will preferentially absorb radiated energy from an adjoining module needs to be known.

The dynamic extent of the fireball must also be known. It is known that the burning of the aluminum powder in the oxygen environment leads rapidly to a fireball that does grow. Little quantitative data have been obtained. The effect of the presence of other modules on a fireball's growth also needs to be understood. It is possible that a module constrained by two adjacent modules might grow faster and maybe further in the direction where expansion is not confined. Figure 48 presents this idea pictorially showing a plane cutting the modules perpendicular to their cylindrical lines of symmetry.

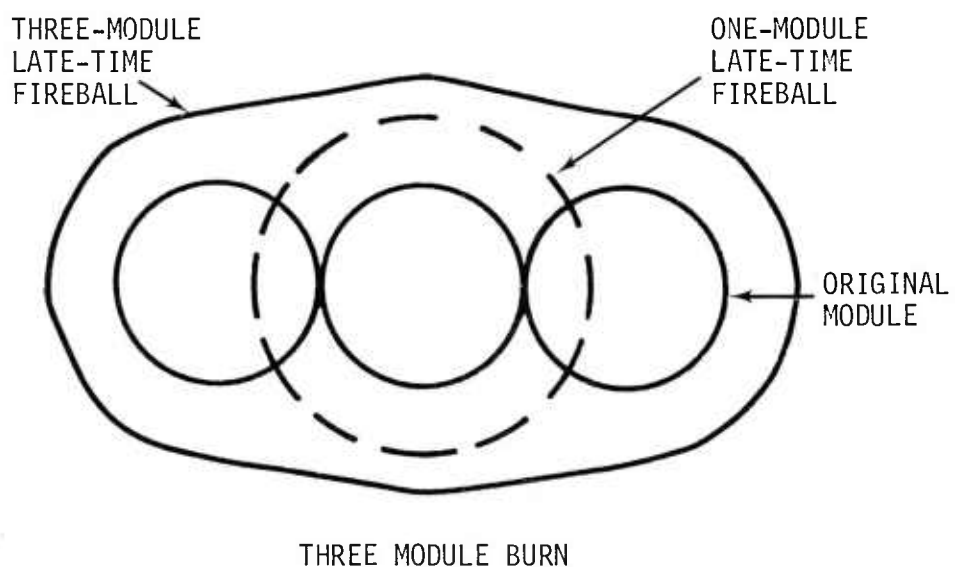
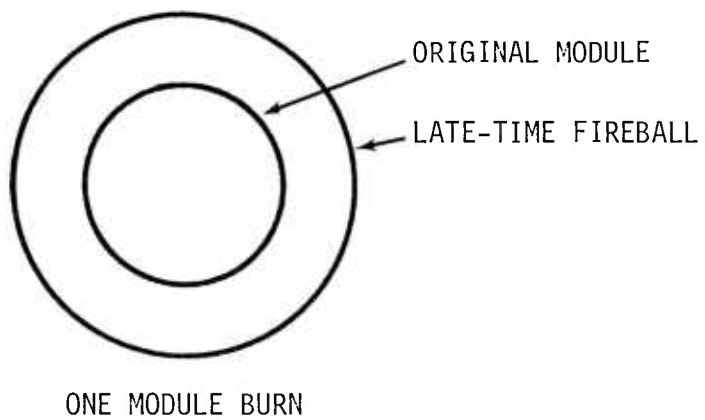


Figure 48. Possible effect of confinement on fireball growth.

Finally, more theoretical and experimental work are needed to better define the effect of the presence of the remaining TRS fireball on airblast propagation.

SECTION 5

CONCLUSIONS AND RECOMMENDATIONS

Although techniques are now available for rapidly burning aluminum in an oxygen environment in order to produce considerable radiant energy over large areas, additional data are needed to allow proper use of these techniques when simulating the thermal radiation environment of a nuclear device. Furthermore, at this time the nuclear environment is only partially simulated and questions remain about the degree of simulation fidelity.

The characterization of the radiative output of the SAI thermo-chemical thermal simulation device module is incomplete in a number of ways. Although some theoretical modeling has been done by SAI on pilot small scale systems (reference 21), more work needs to be done for recent large scale systems. Data that are essential to modeling radiative output of a TDS module include:

- 1) The fireball extent. After TSD module ignition, the TSD fireball begins to expand. Data on its size and shape from initiation to stabilization are needed in order to better characterize the TDS as a source of radiation. Some data exist but need to be analyzed and documented.
- 2) The spectrum of radiation. It is desirable to obtain spatial, temporal, and spectral data on specific intensity from the fireball. Some integrated data exist; however, they are insufficient for modeling the radiation on a target since they are not resolved in frequency and space.

Some recent experiments that have been performed have shown that placing one TDS module behind another can increase the radiation reaching a target. The increase is less than the factor of two obtained using superposition. The effect may be due to the fact that

the fireball nearest to target is partially transparent; however, estimates made in reference 21 imply that the expected fireball is much too opaque for this to occur. It is also possible that the adjacent module constrains the other fireball from radiating in its direction but beyond its position, leading ultimately to more radiation towards the target. This needs to be investigated further so that models can be either validated or improved sufficiently to characterize the use of such modules in an ensemble.

There exists no substantive data on the effect of the TRS devices on propagation of air blast, although very recent and preliminary air blast measurements on Misers Bluff seem to indicate that the air blast propagating through a TRS attenuates somewhat as the one-dimensional model indicates. We conclude that the one-dimensional effect needs to be further investigated to account for the influence of hot particles. The importance of two-dimensional effects also needs to be analyzed.

The prediction of the thermal radiation from nuclear bursts during an actual war requires consideration of surrounding conditions (such as clouds, haze, hills, etc.), as discussed in reference 2. Any description of the environment that is to be simulated is in itself non-trivial. Nevertheless if the thermal radiation environment from the fireball is known, these other effects can be estimated. Although thermal environments for detonations far above ground can be well characterized, the use of free-field thermal radiation descriptions for near-surface detonations may be incorrect both in flux level and spectral content. Radiation out to space can be much different from that reaching the ground for near detonations. This study has led to the development of a correlation between thermal efficiency and nearness of the device to the ground. Although this correlation may be fortuitous, it warrants considerable additional investigation.

Finally the following recommendations are offered based on efforts conducted under this contract. In the area of thermal radiation simulation, work should continue in order to develop a means to achieve repeatable light-flux variable-pulse-length thermal radiation waveforms over large areas. It is further recommended that the thermal radiation environment for these thermal waveforms be well characterized and modeled. In addition, scaling laws for radiative output, full requirements, and number and placement of modules should be determined for the simulators.

REFERENCES

1. Glasstone, S. and Dolan, P. J., "The Effects of Nuclear Weapons," United States DoD and DOE, 1977.
2. "Nuclear Weapons Blast Phenomena," Defense Nuclear Agency, 1973, report unpublished.
3. "Optical Interactions, The SPUTTER Program," RTD-TDR-63-3128, May 1964.
4. Chambers, B., et al., "Theoretical Calculations of Early Phenomenology--200 KT at 32 KM," report unpublished.
5. Whitaker, W.A. and Chambers, B., et.al., "Theoretical Calculations of Early Phenomenology--BLUEGILL." Report unpublished.
6. Whitaker, W.A. and Chambers, B., et.al., "Theoretical Calculations of Early Phenomenology--SLEIGHRISE." Report unpublished.
7. Sharp, A. L., "A Thermal Source Model from SPUTTER Calculations," Report No. AFWL-TR-72-49, March 1973.
8. Hoggins, Capt. J. T., and Sharp, A. L., "Spectral Characteristics of Thermal Radiation Predicted from SPUTTER Calculation," Report No. AFWL-TR-73-152, August 1973.
9. Chandrasekhar, S., An Introduction to the Study of Stellar Structure, Dover Publications, Inc., 1958.
10. Chandrasekhar, S., Radiative Transfer, Dover Publications, Inc., 1960.
11. Mansfield, J.E., et al., "HOB Effects on Dust Lofting Mechanisms," report unpublished.
12. Chambers, B., et.al., "Theoretical Air Blast Loading Estimates on the M-X Shelter, The Influence of Dust, and a Recommended Experimental Program," DNA 4610F, 30 June 1978.
13. Brode, H. L., "Height of Burst Effects at High Overpressures," RM-6301-DASA, July 1970.
14. Private communication, W. Dudziak; NTS data, report unpublished.

REFERENCES
(continued)

15. Dudziak, W. F., et. al., "Empirical SBM Data From Nuclear Detonation Photography," DNA 4132F, 30 September 1976.
16. Dishon, J., "The Thermal Radiation Simulator Development Program," presented to the DNA Nuclear Blast and Shock Simulation Symposium, 28-30 November 1978.
17. Fry, Capt. M.A., USAF, Durrett, Major R. E., USAF, et.al., "The HULL Hydrodynamics Computer Code," AFWL-TR-76-183, September 1976.
18. Clemens, R. and Matuska, D., "Air Force Weapons Laboratory Hydrodynamic Calculations in Two- and Three-Dimension," report unpublished.
19. Needham, C., Wittwer, L., et al., "Air Force Weapons Laboratory Low Altitude Multiburst (LAMB) Model," AFWL TN-75-2, report unpublished.
20. Miller, J.W., Chambers, B.S., et al., "Modeling of Multiple Burst Dust and Ice Environments," SAI-78-220-WA, 23 May 1977, to be published.
21. Cockayne, J.E., et al., "Analytical Study of Large Scale Optical Flash Sources," SAI-78-694-WA, 30 April 1978, to be published.

APPENDIX A

ESTIMATE OF THERMAL RADIATION FROM A 1 KILOTON NUCLEAR SURFACE BURST DETECTOR ELEVATION 0 DEGREES

This appendix contains plots for one elevation and consists of six sets of three figures. Each set corresponds to a particular range: 30.48, 60.96, 91.44, 152.4, 304.8, or 609.6 meters from ground zero. For each range fluence, flux, and average flux are presented as a function of time. Fluence is in units of cal-cm^{-2} , flux and average flux are in units of $\text{cal-cm}^{-2}\text{-sec}^{-1}$.

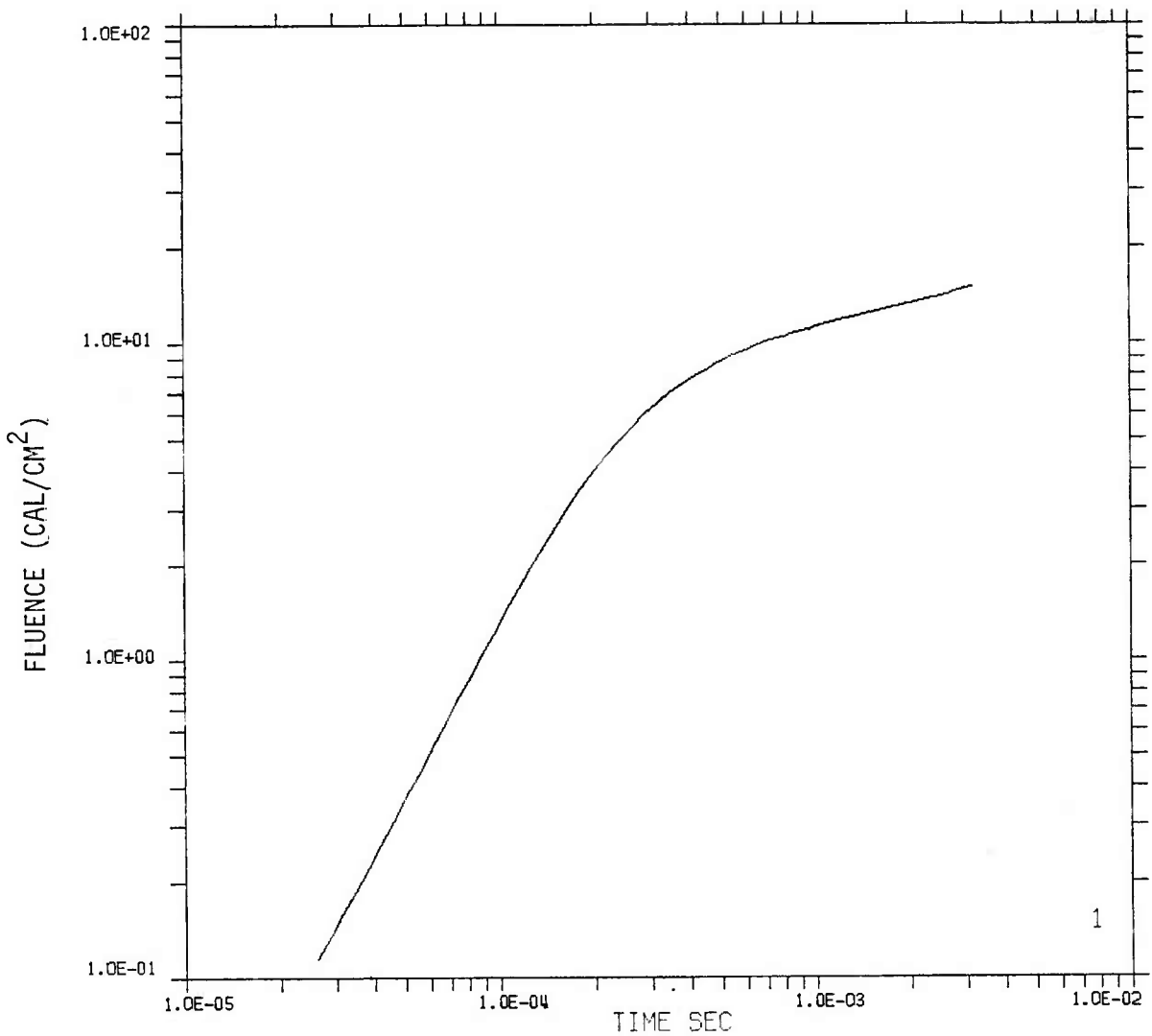


Figure 49. Fluence from 1 kt surface burst crossing detector with orientation 0 degrees at 30.48 meters ground range.

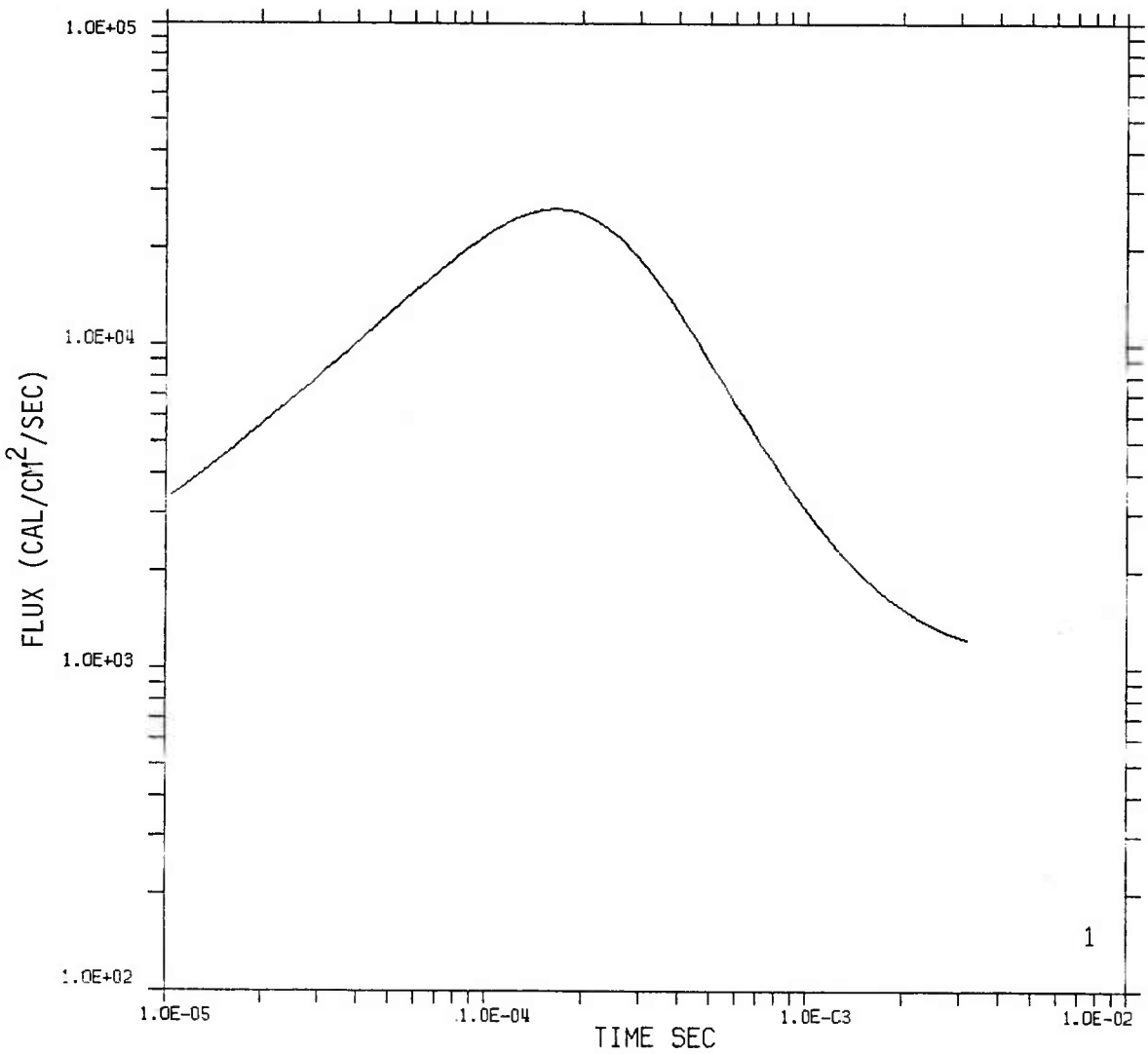


Figure 50. Flux from 1 kt surface burst crossing detector with orientation 0 degrees at 30.48 meters ground range.

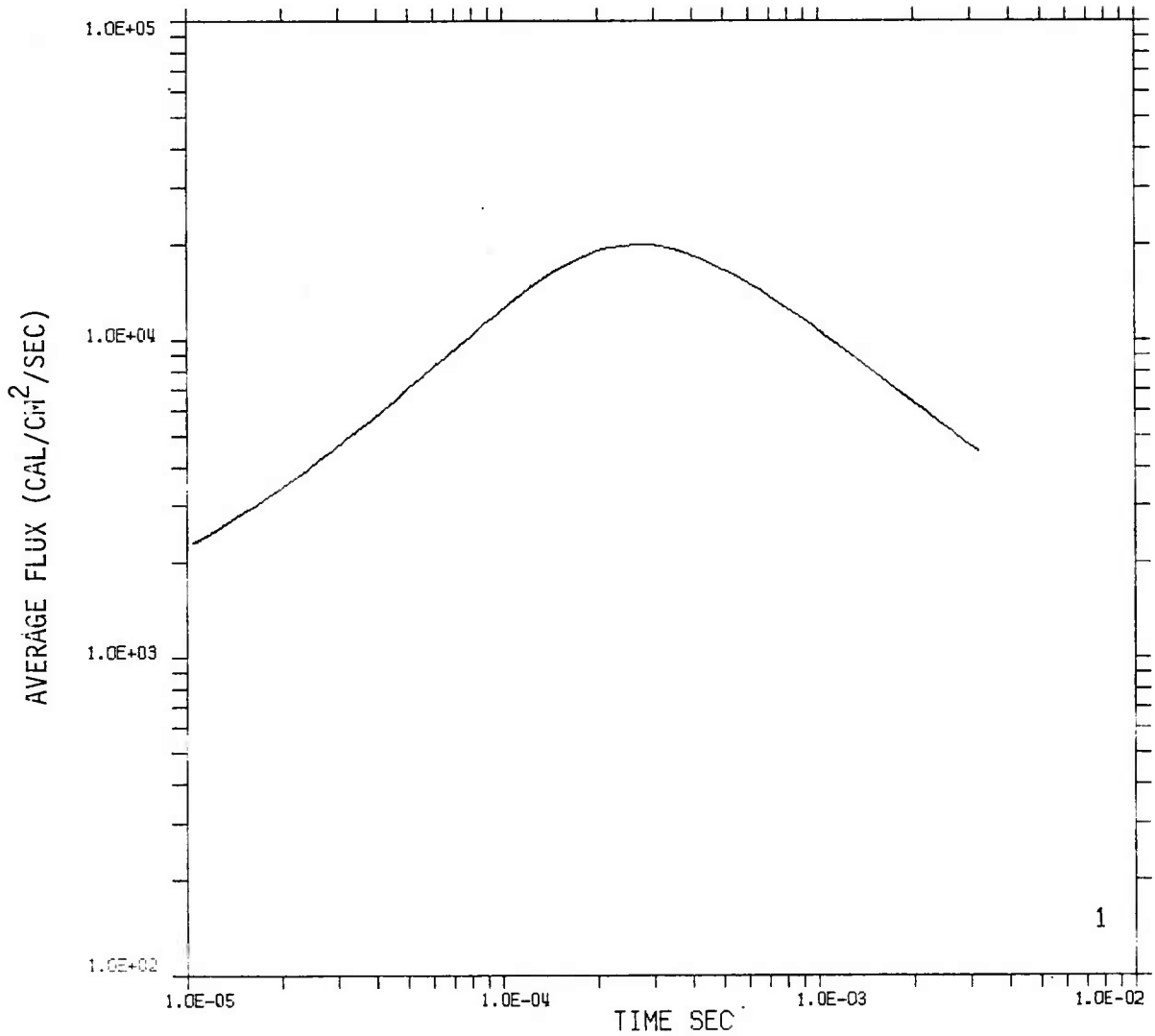


Figure 51. Average flux from 1 kt surface burst crossing detector with orientation 0 degrees at 30.48 meters ground range.

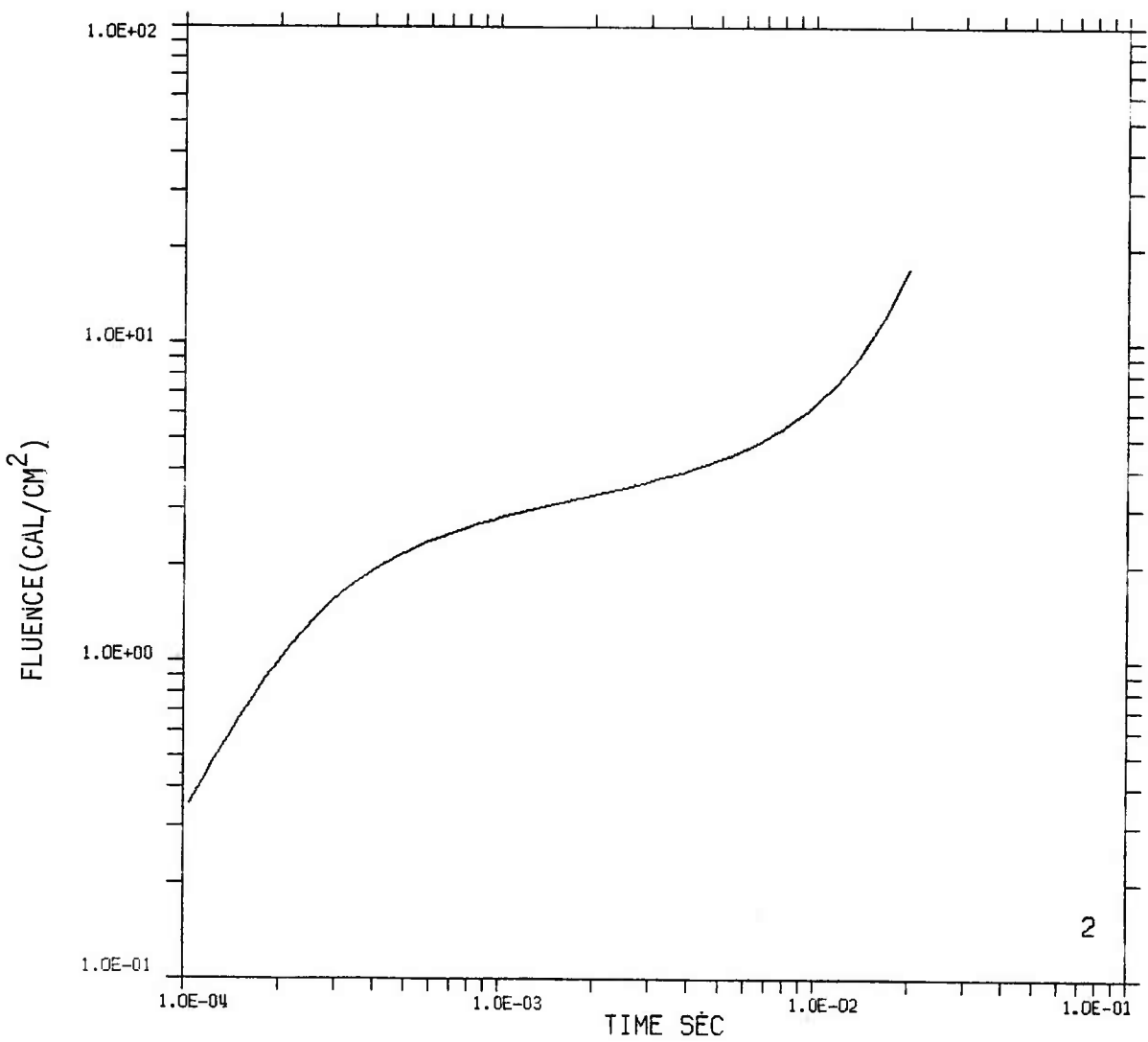


Figure 52. Fluence from 1 kt surface burst crossing detector with orientation 0 degrees at 60.96 meters ground range.

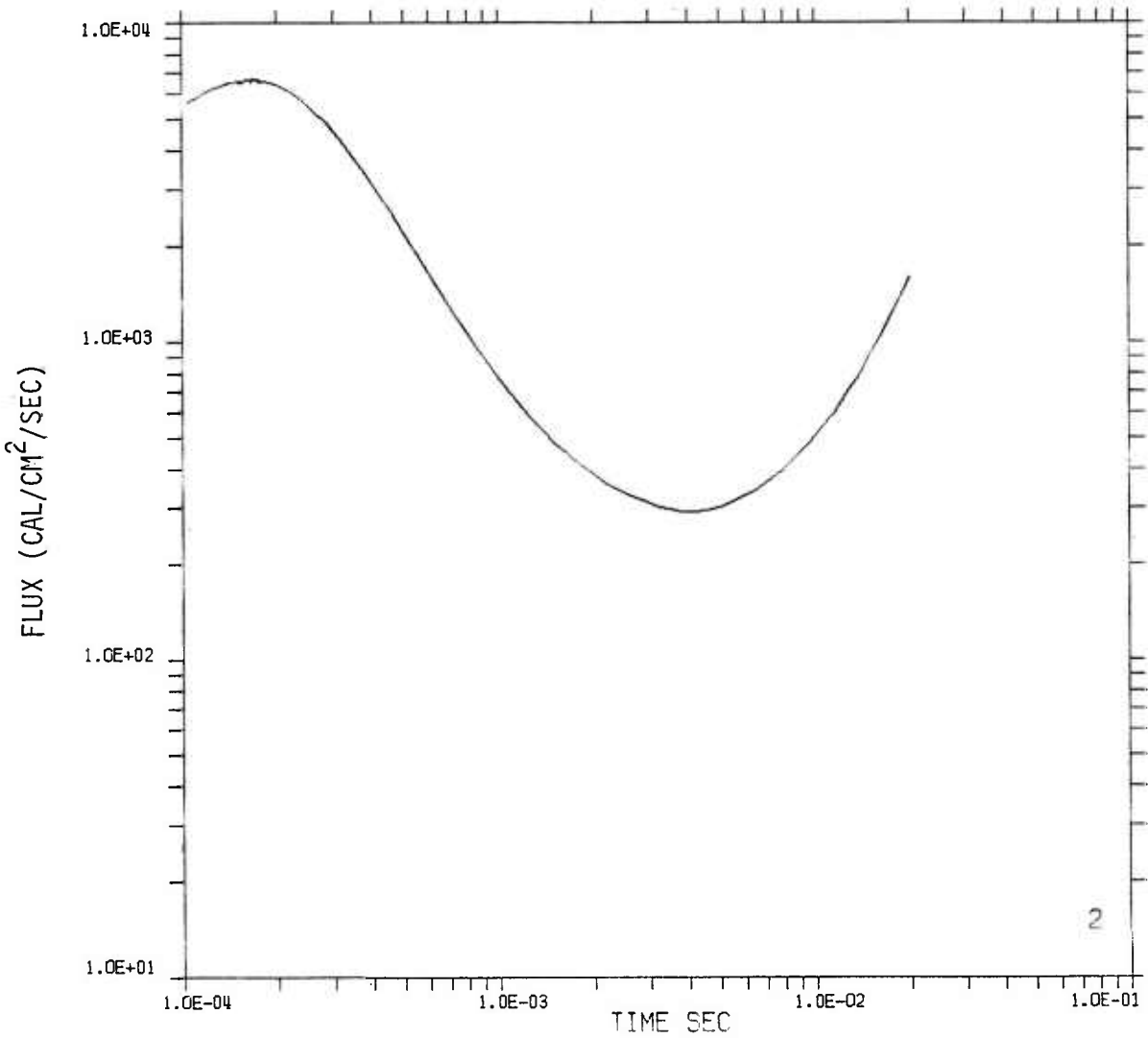


Figure 53. Flux from 1 kt surface burst crossing detector with orientation 0 degrees at 60.96 meters ground range.

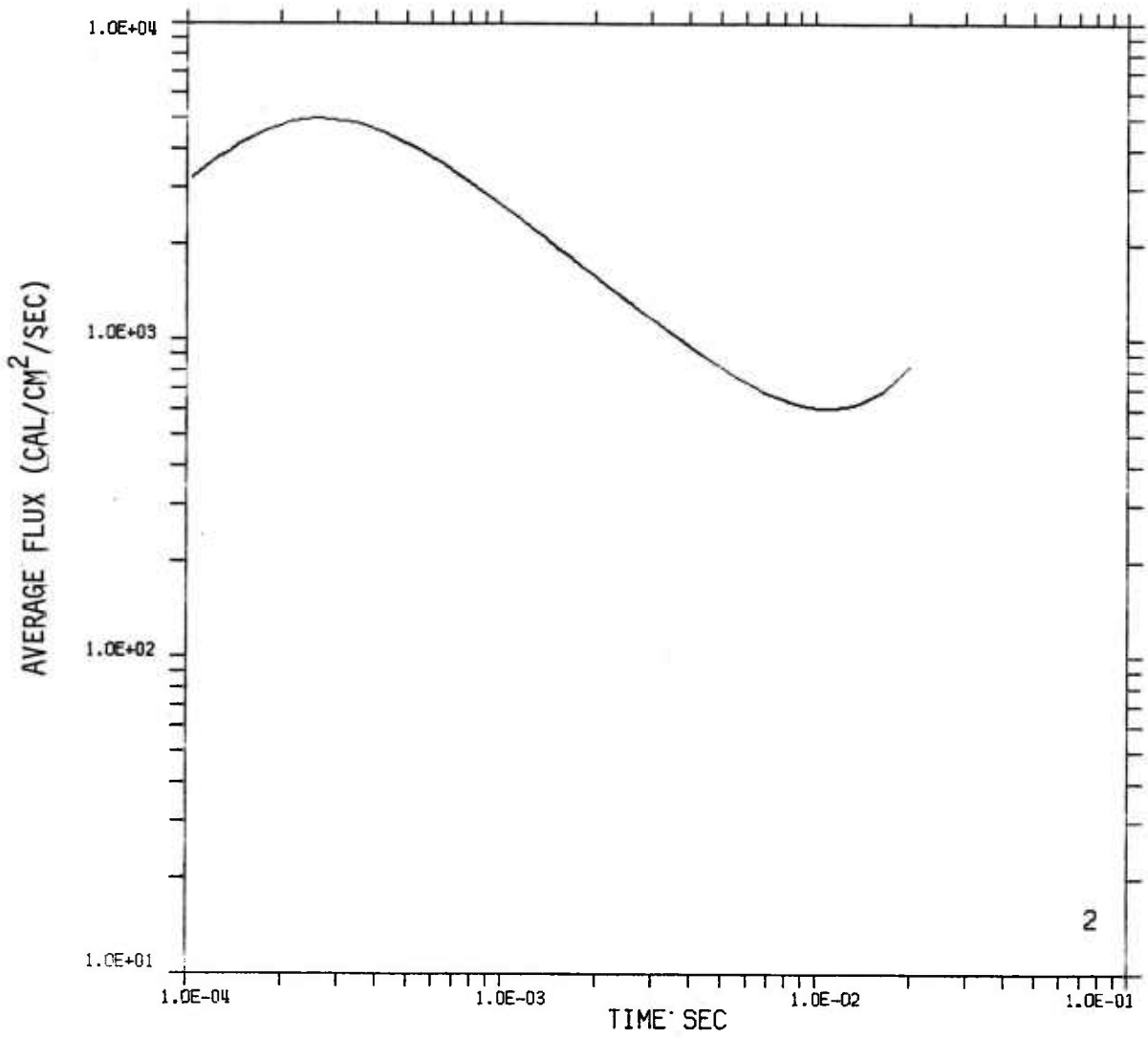


Figure 54. Average flux from 1 kt surface burst crossing detector with orientation 0 degrees at 60.96 meters ground range.

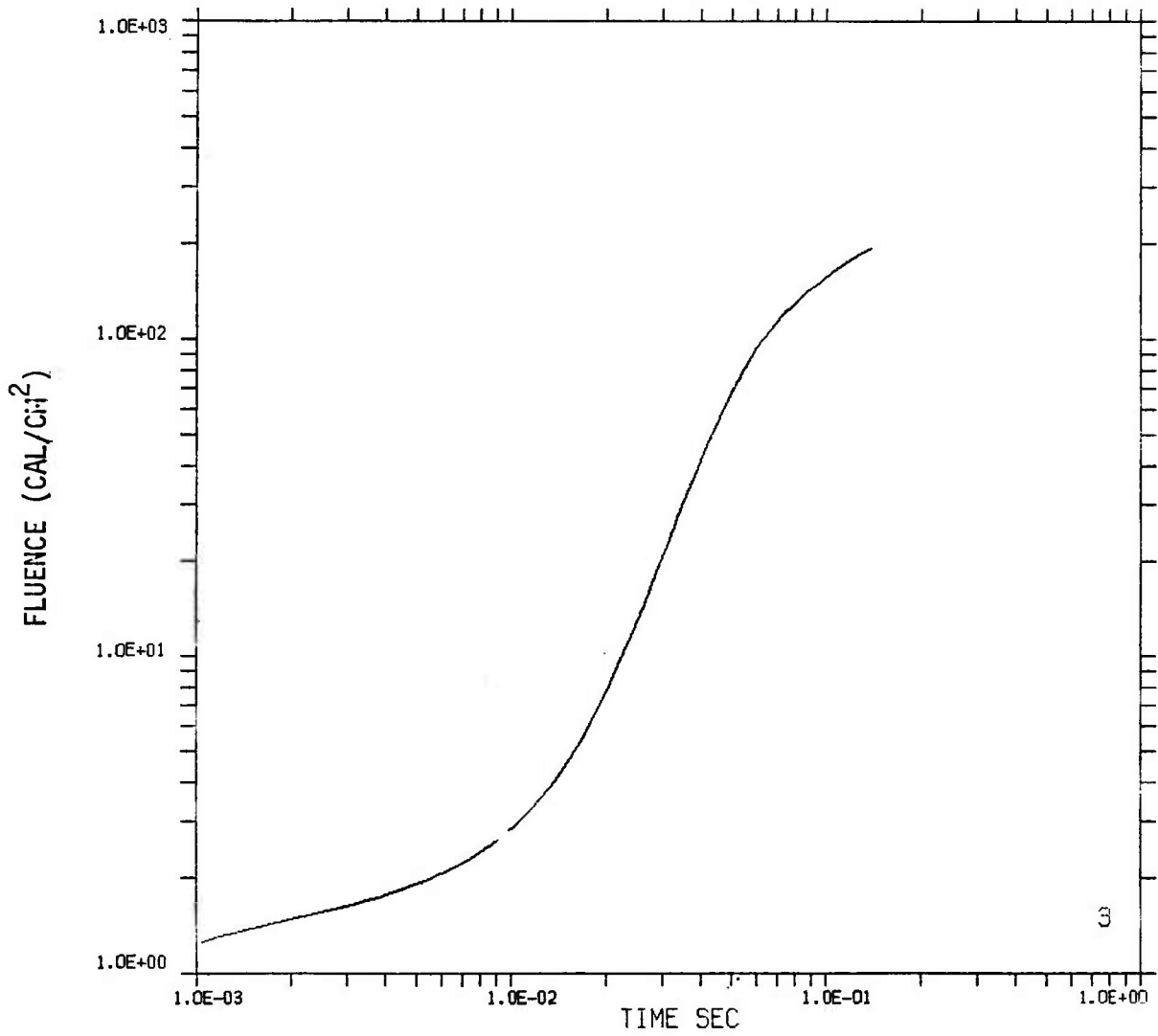


Figure 55. Fluence from 1 kt surface burst crossing detector with orientation 0 degrees at 91.44 meters ground range.

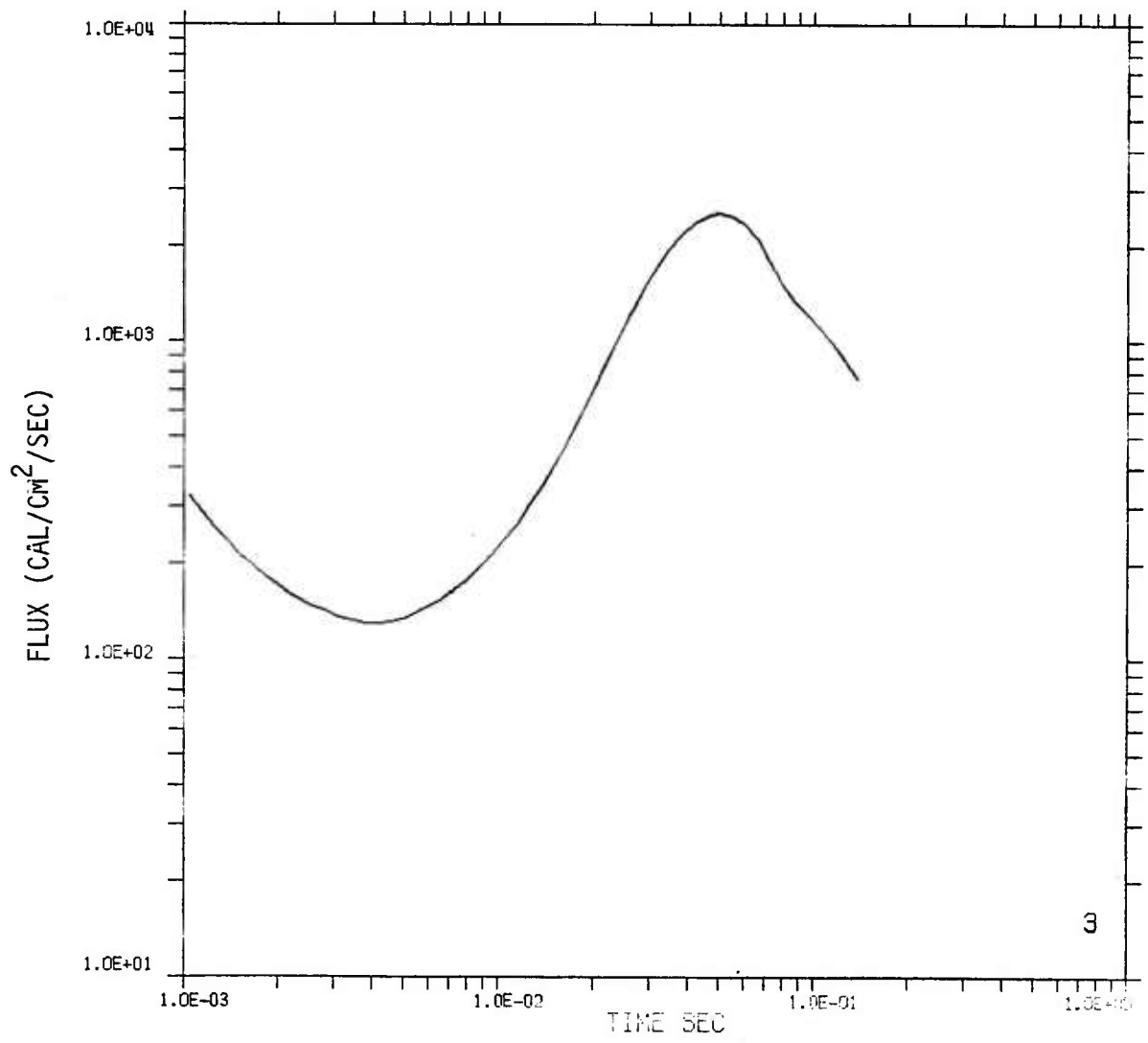


Figure 56. Flux from 1 kt surface burst crossing detector with orientation 0 degrees at 91.44 meters ground range.

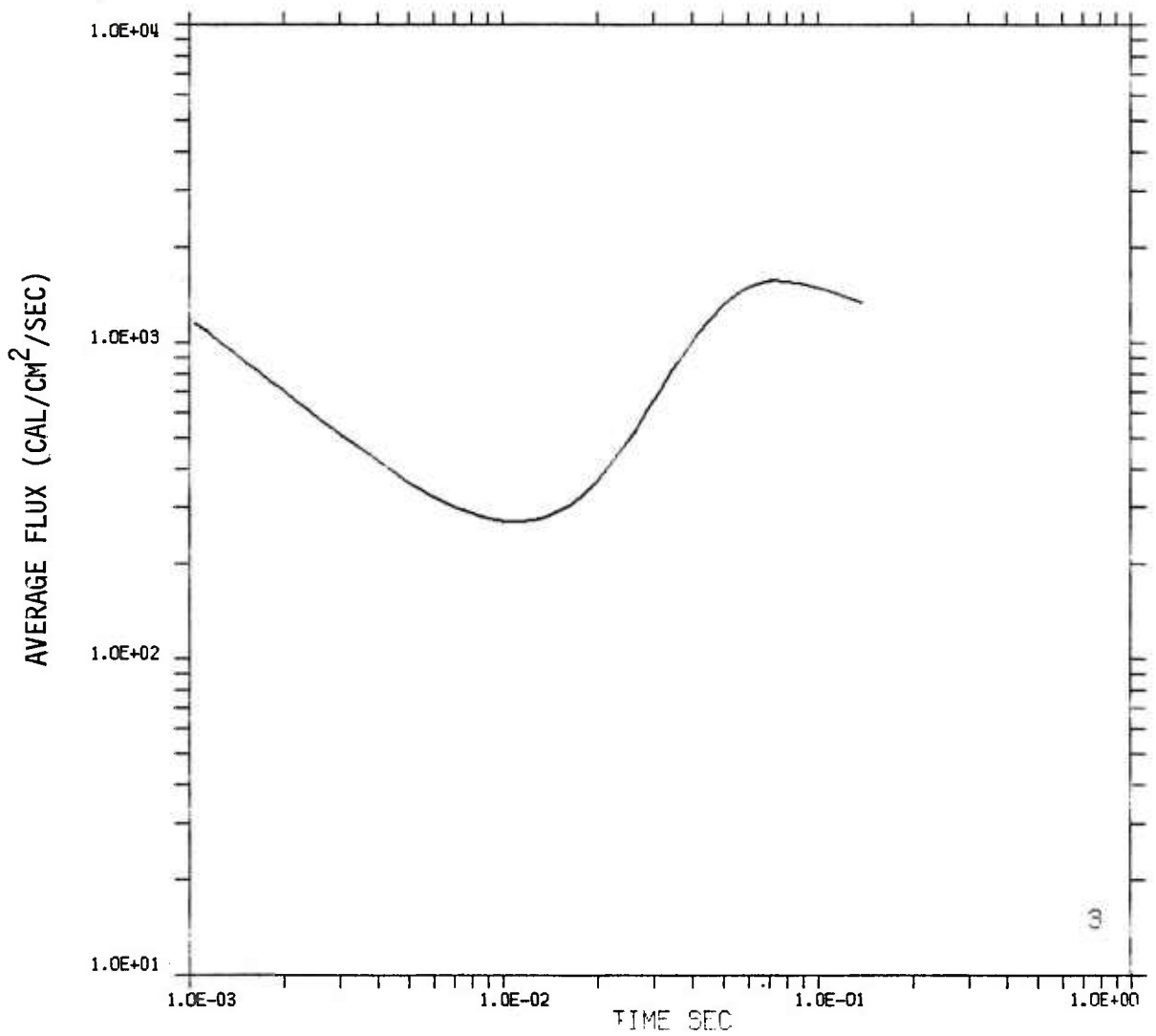


Figure 57. Average flux from 1 kt surface burst crossing detector with orientation 0 degrees at 91.44 meters ground range.

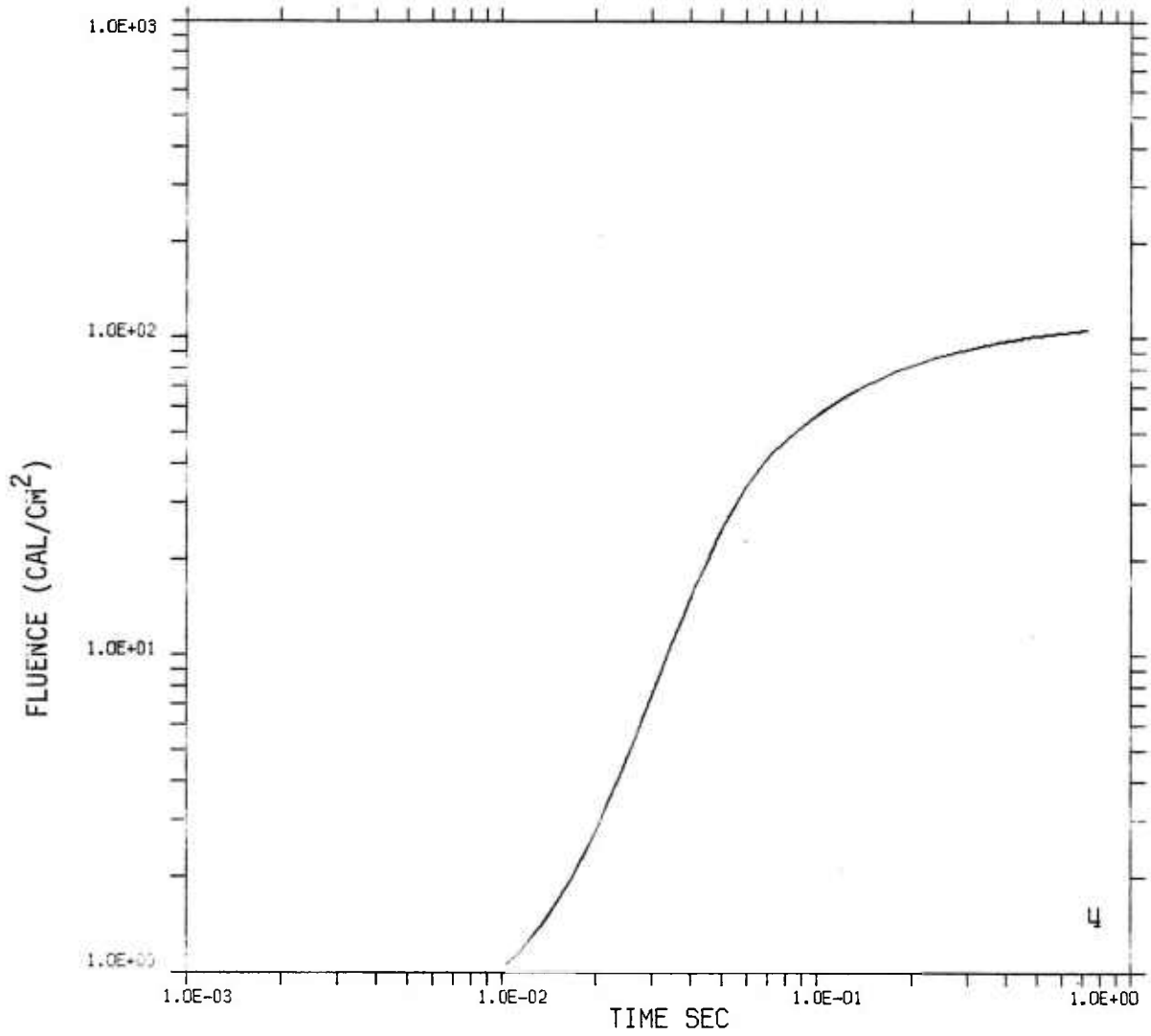


Figure 58. Fluence from 1 kt surface burst crossing detector with orientation 0 degrees at 152.4 meters ground range.

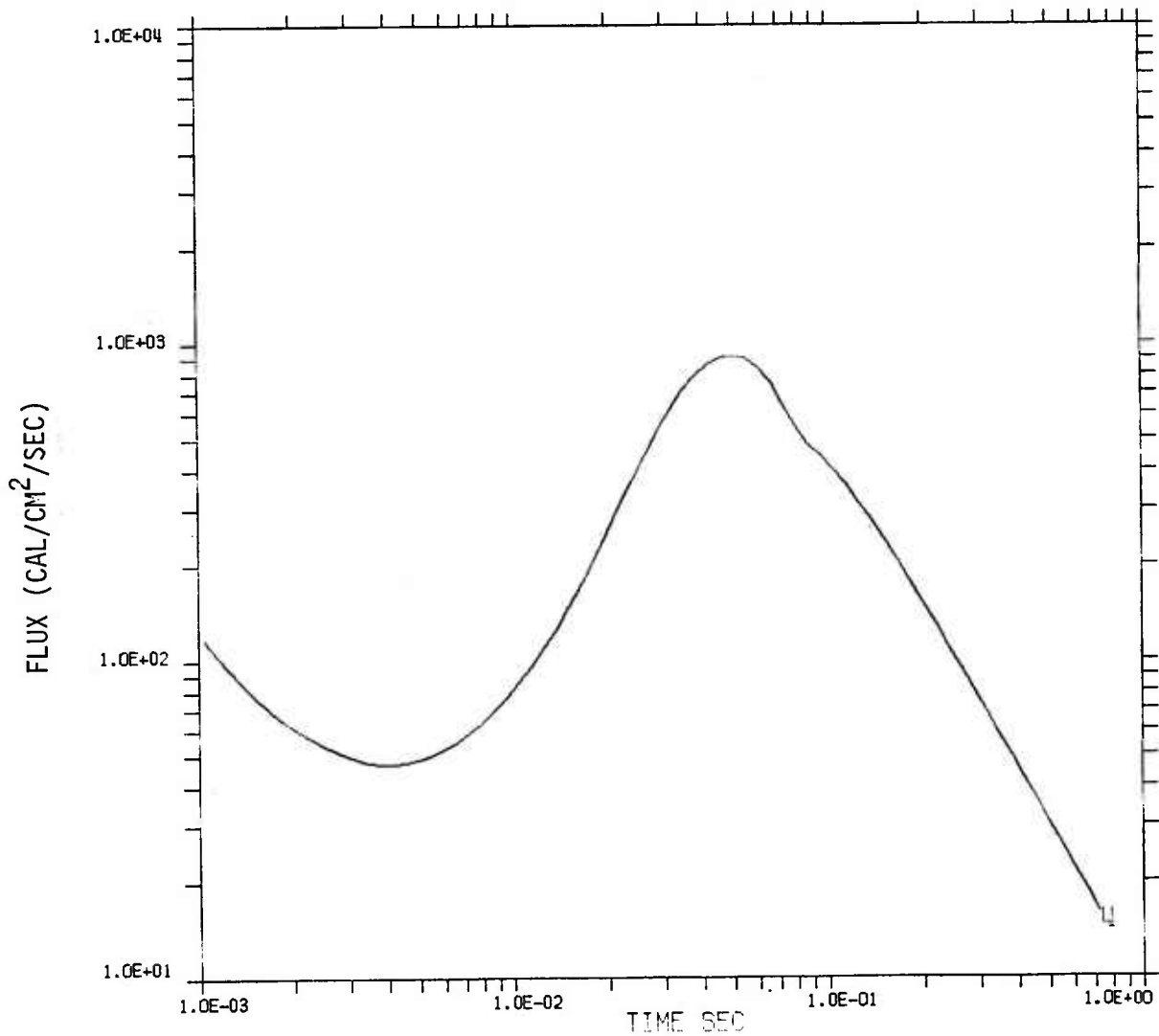


Figure 59. Flux from 1 kt surface burst crossing detector with orientation 0 degrees at 152.4 meters ground range.

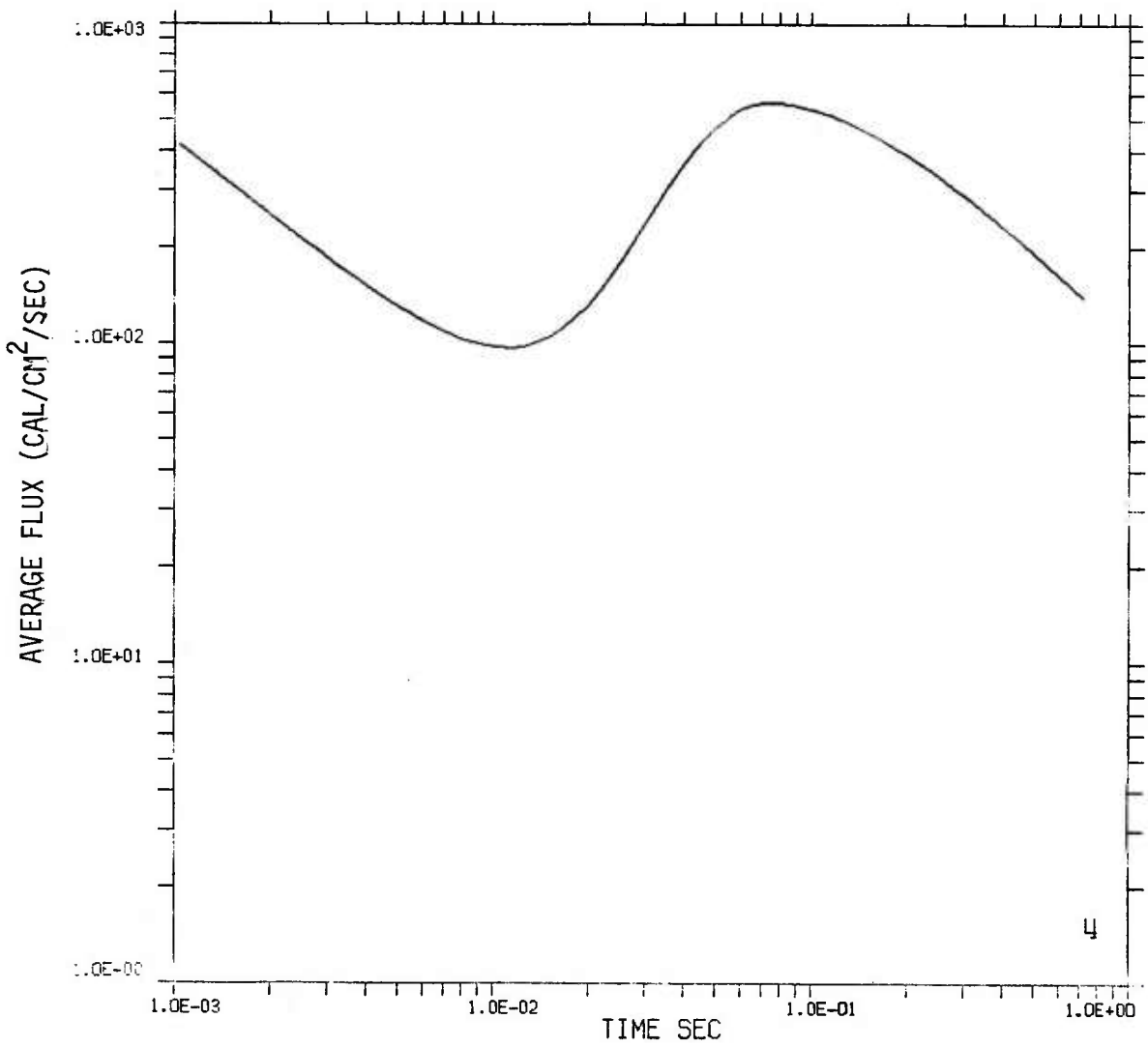


Figure 60. Average flux from 1 kt surface burst crossing detector with orientation 0 degrees at 152.4 meters ground range.

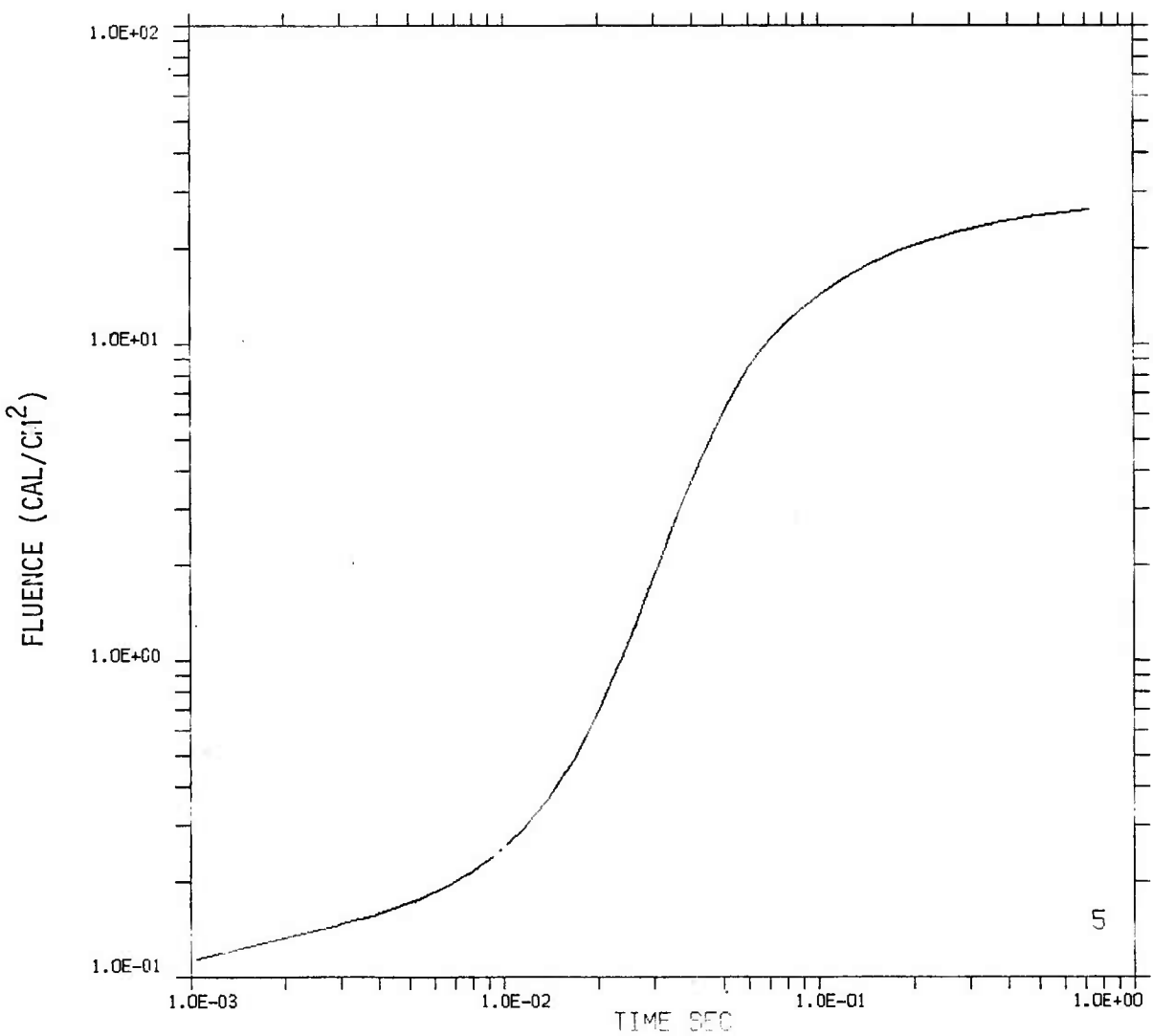


Figure 61. Fluence from 1 kt surface burst crossing detector with orientation 0 degrees at 304.8 meters ground range.

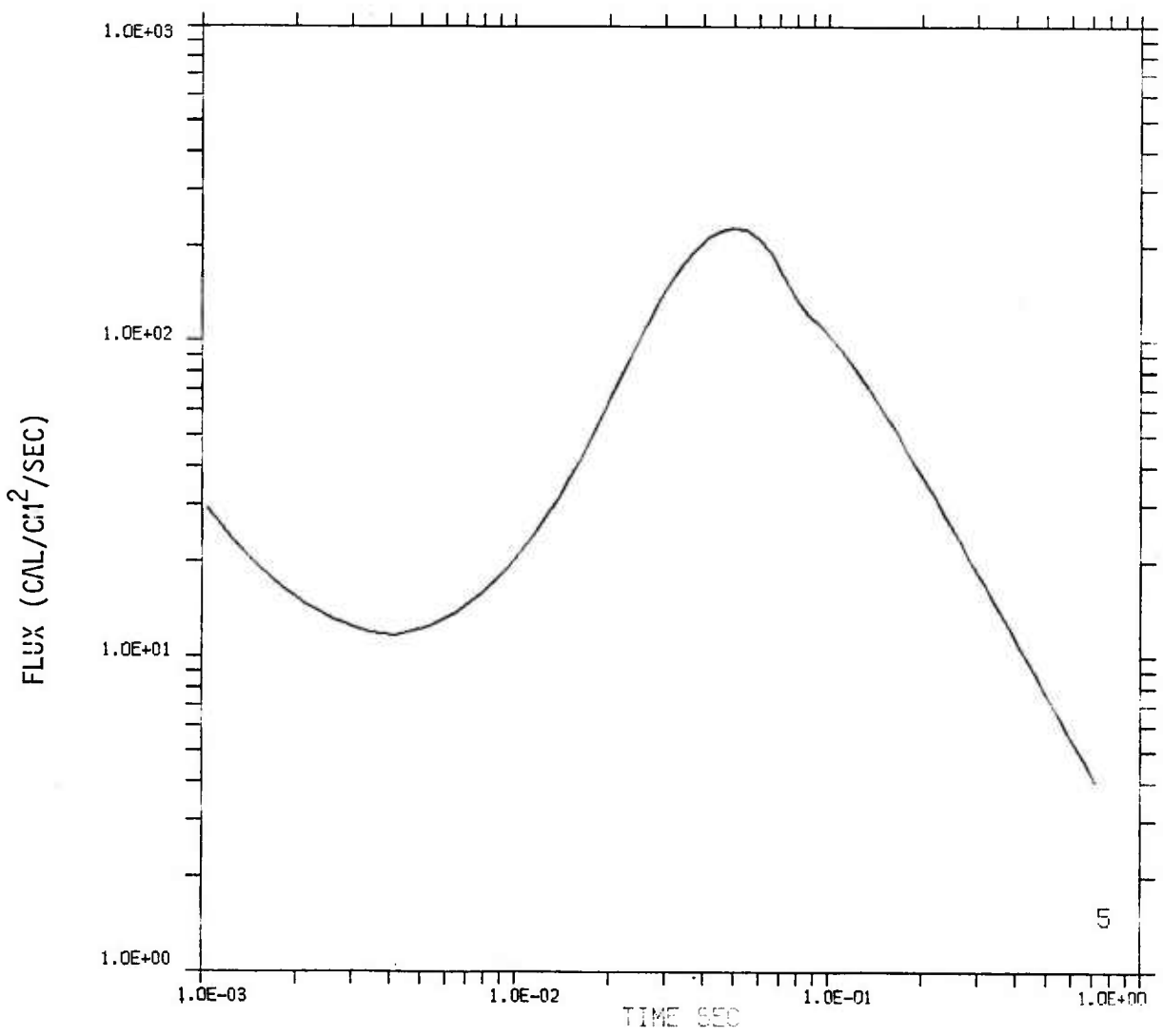


Figure 62. Flux from 1 kt surface burst crossing detector with orientation 0 degrees at 304.8 meters ground range.

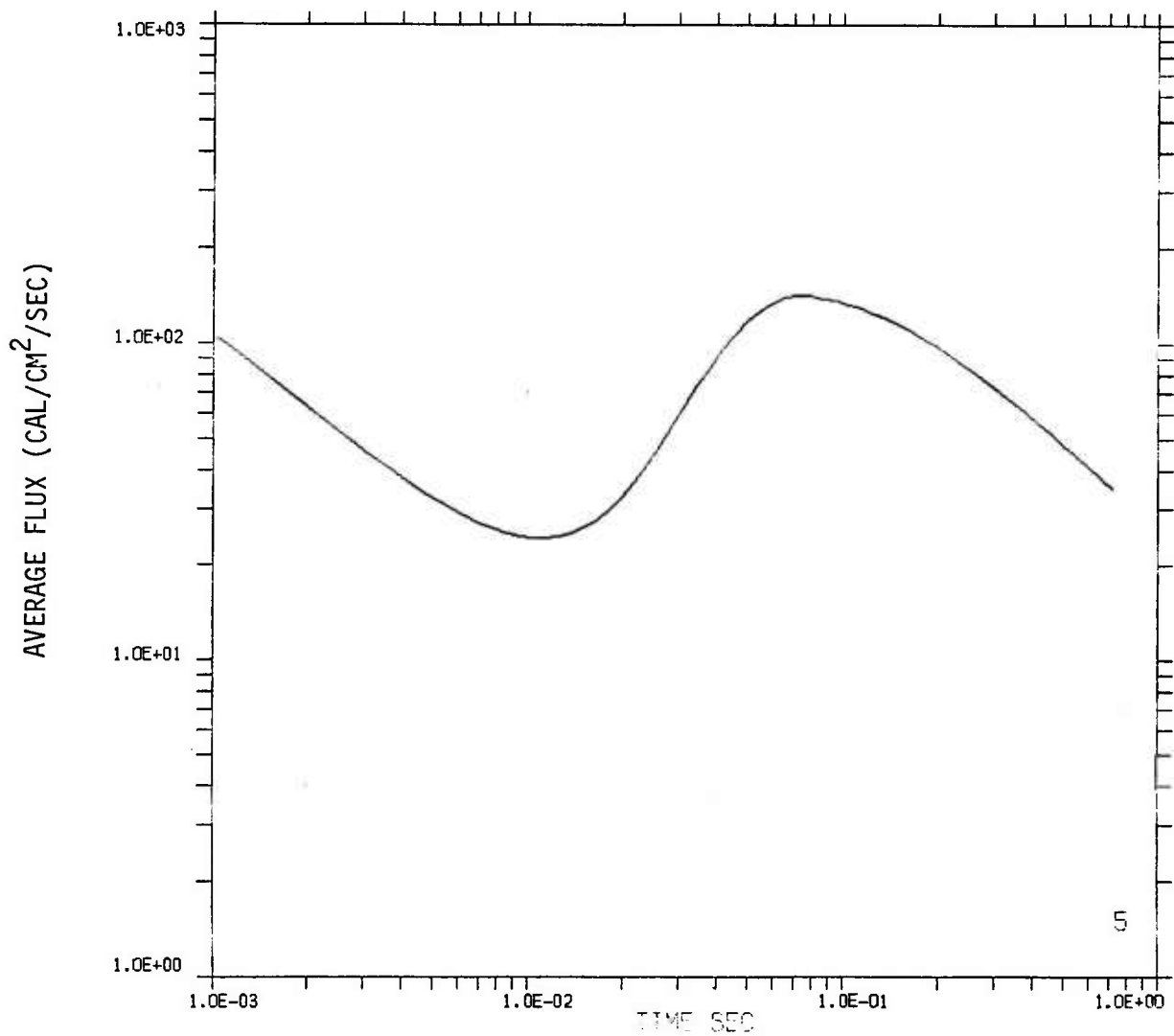


Figure 63. Average flux from 1 kt surface burst crossing detector with orientation 0 degrees at 304.8 meters ground range.

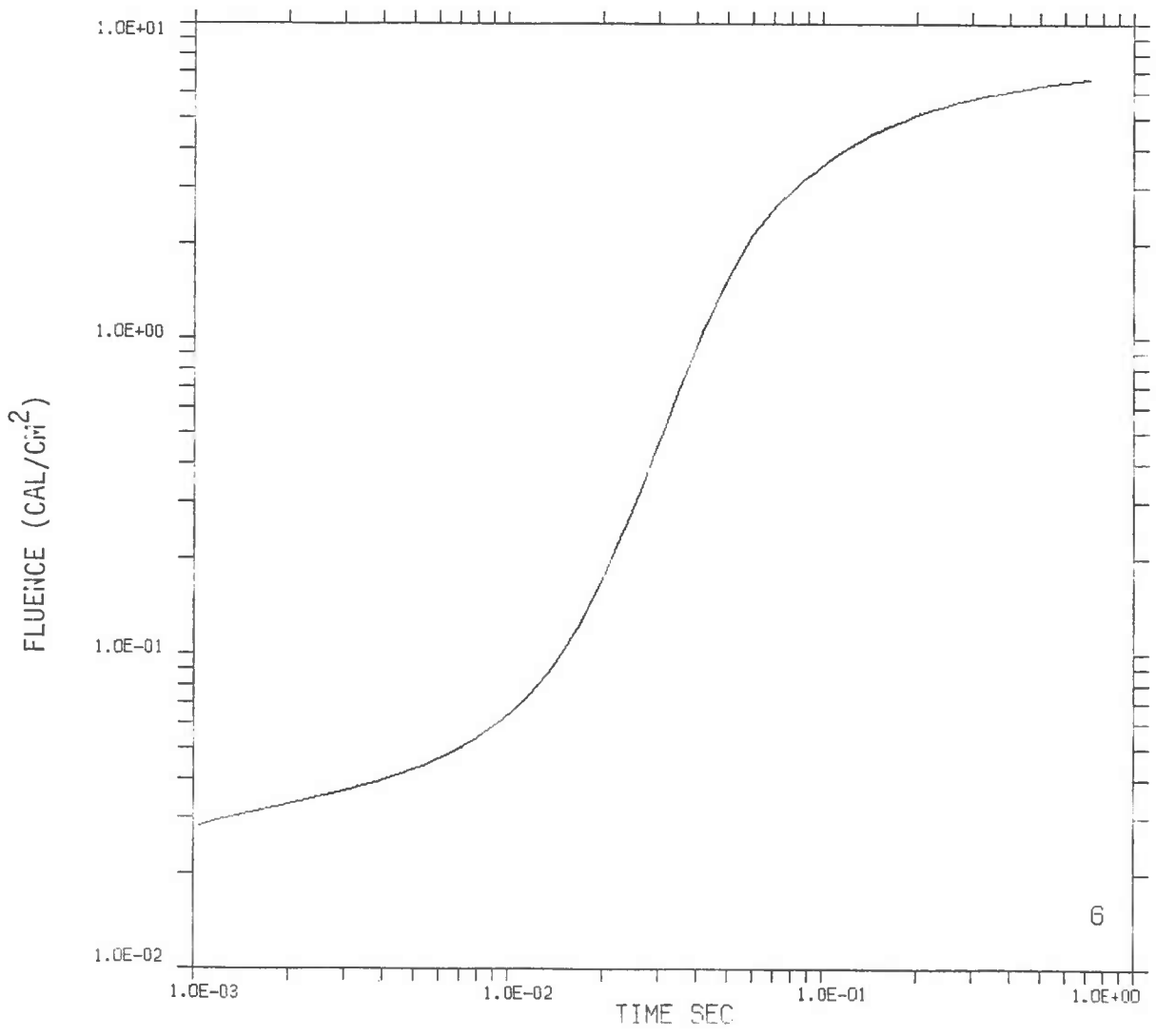


Figure 64. Fluence from 1 kt surface burst crossing detector with orientation 0 degrees at 609.6 meters ground range.

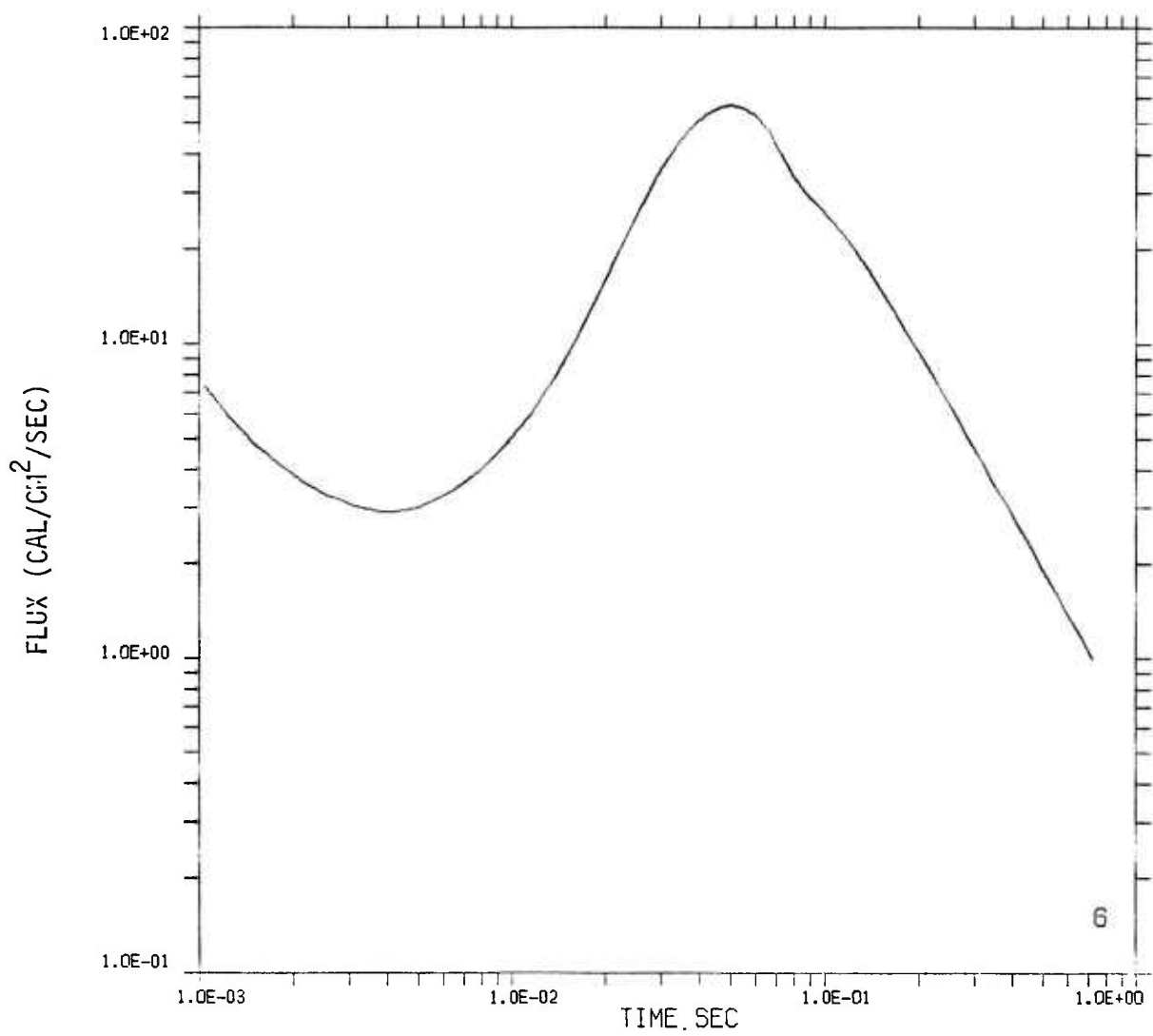


Figure 65. Flux from 1 kt surface burst crossing detector with orientation 0 degrees at 609.6 meters ground range.

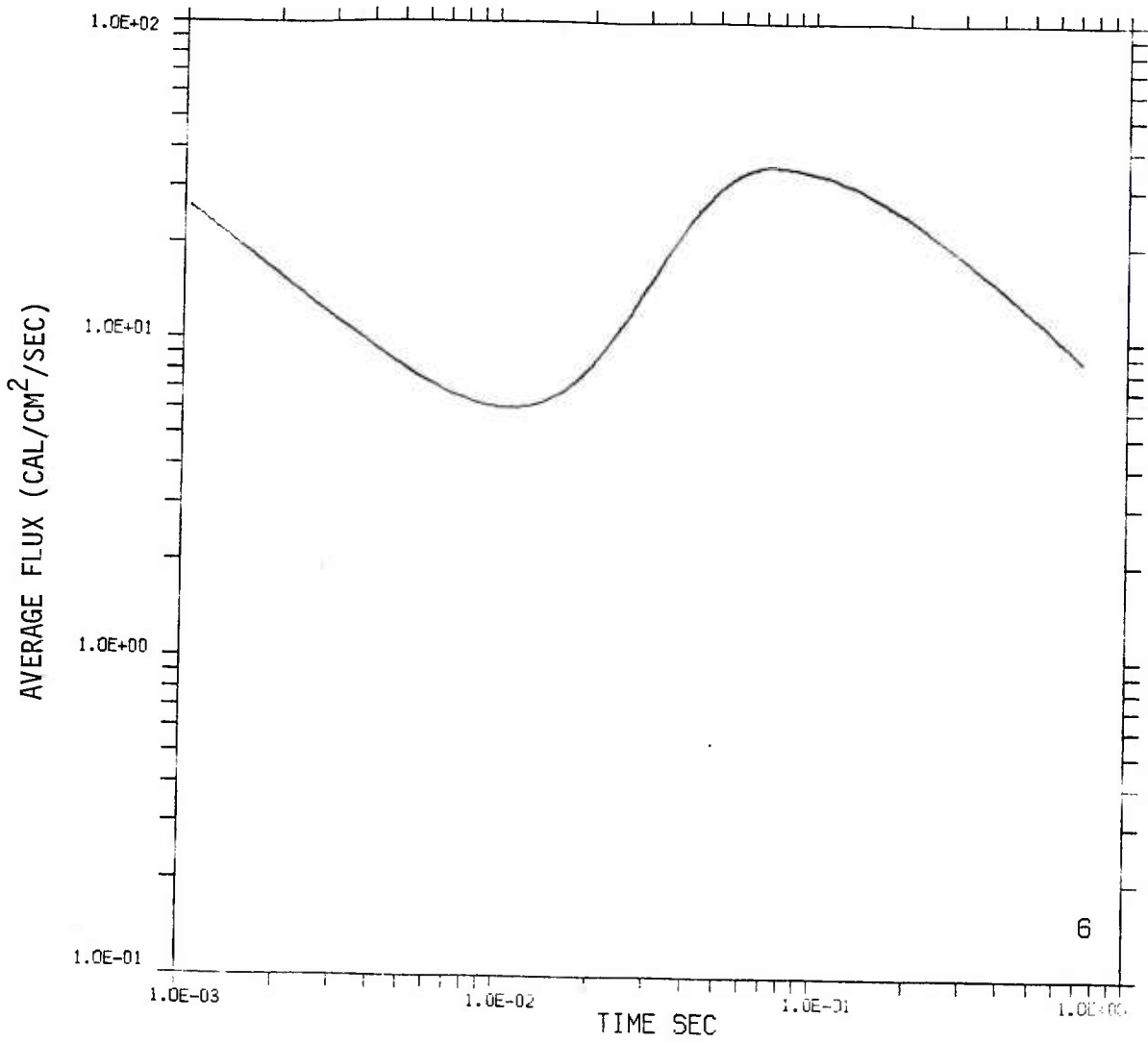


Figure 66. Average flux from 1 kt surface burst crossing detector with orientation 0 degrees at 609.6 meters ground range.

APPENDIX B

ESTIMATE OF THERMAL RADIATION FROM A 1 KILOTON NUCLEAR SURFACE BURST DETECTOR ELEVATION 30 DEGREES

This appendix contains plots for one elevation and consists of six sets of three figures. Each set corresponds to a particular range: 30.48, 60.96, 91.44, 152.4, 304.8, or 609.6 meters from ground zero. For each range fluence, flux, and average flux are presented as a function of time. Fluence is in units of cal-cm^{-2} , flux and average flux are in units of $\text{cal-cm}^{-2}\text{-sec}^{-1}$.

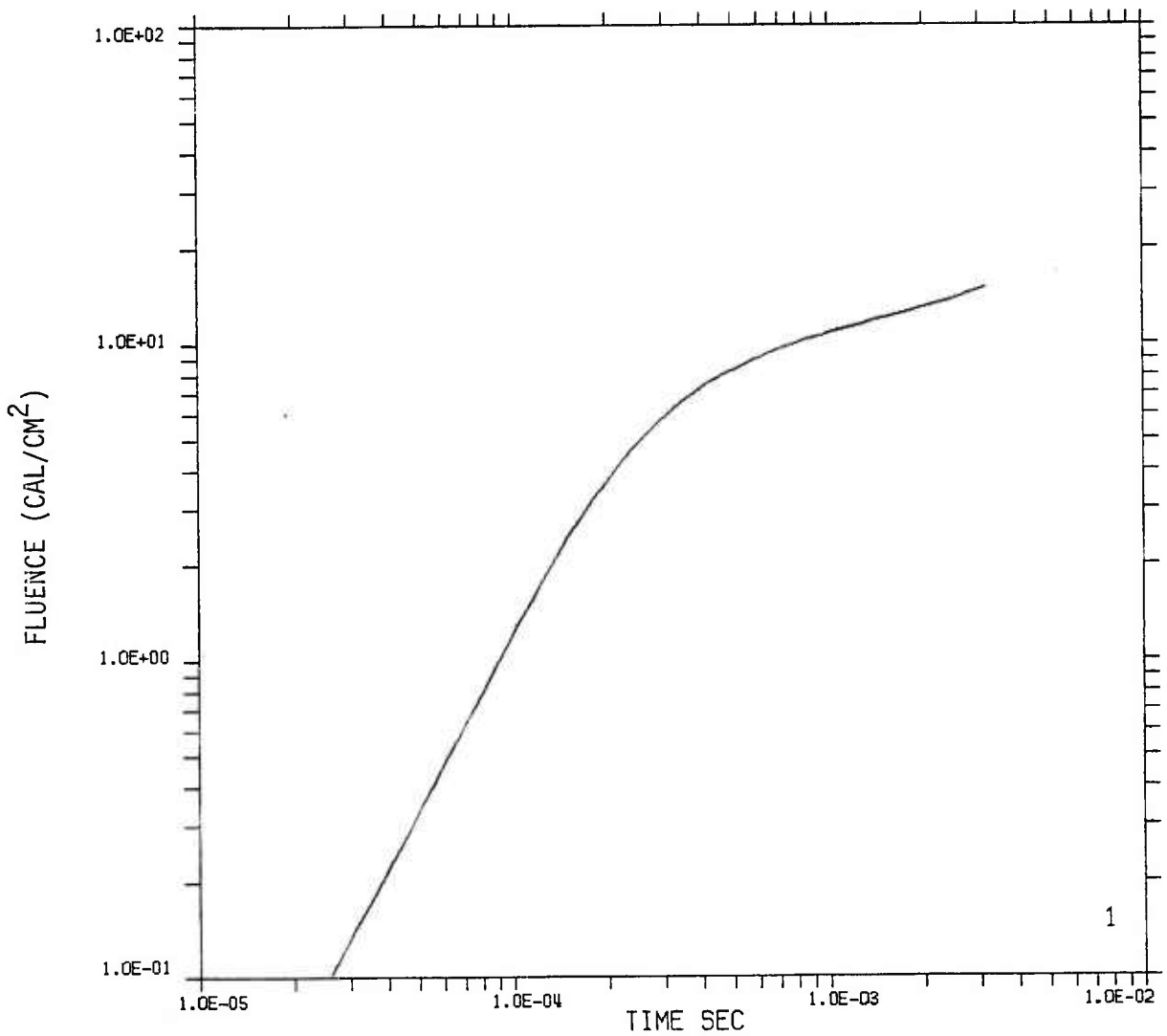


Figure 67. Fluence from 1 kt surface burst crossing detector with orientation 30 degrees at 30.48 meters ground range.

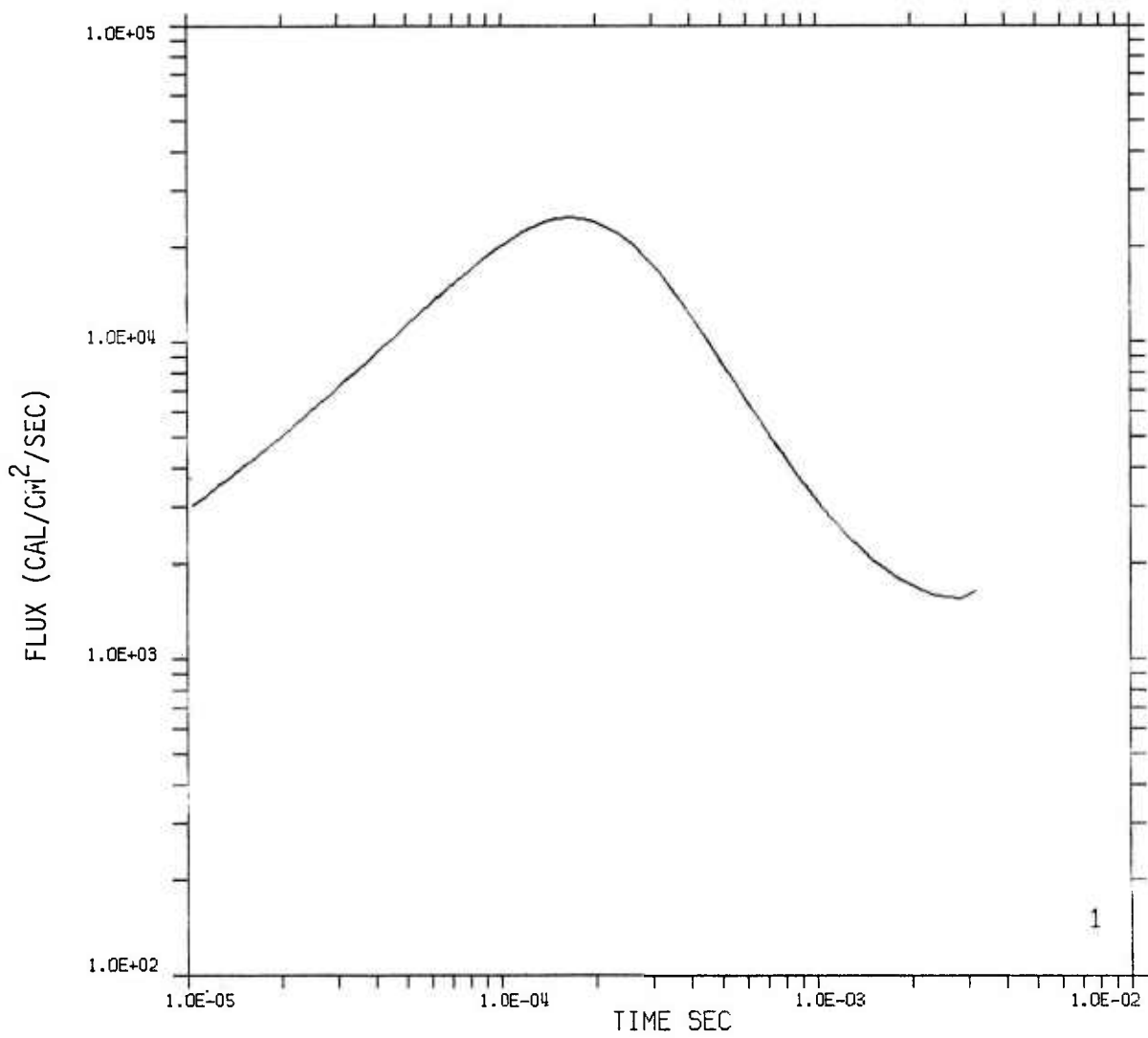


Figure 68. Flux from 1 kt surface burst crossing detector with orientation 30 degrees at 30.48 meters ground range.

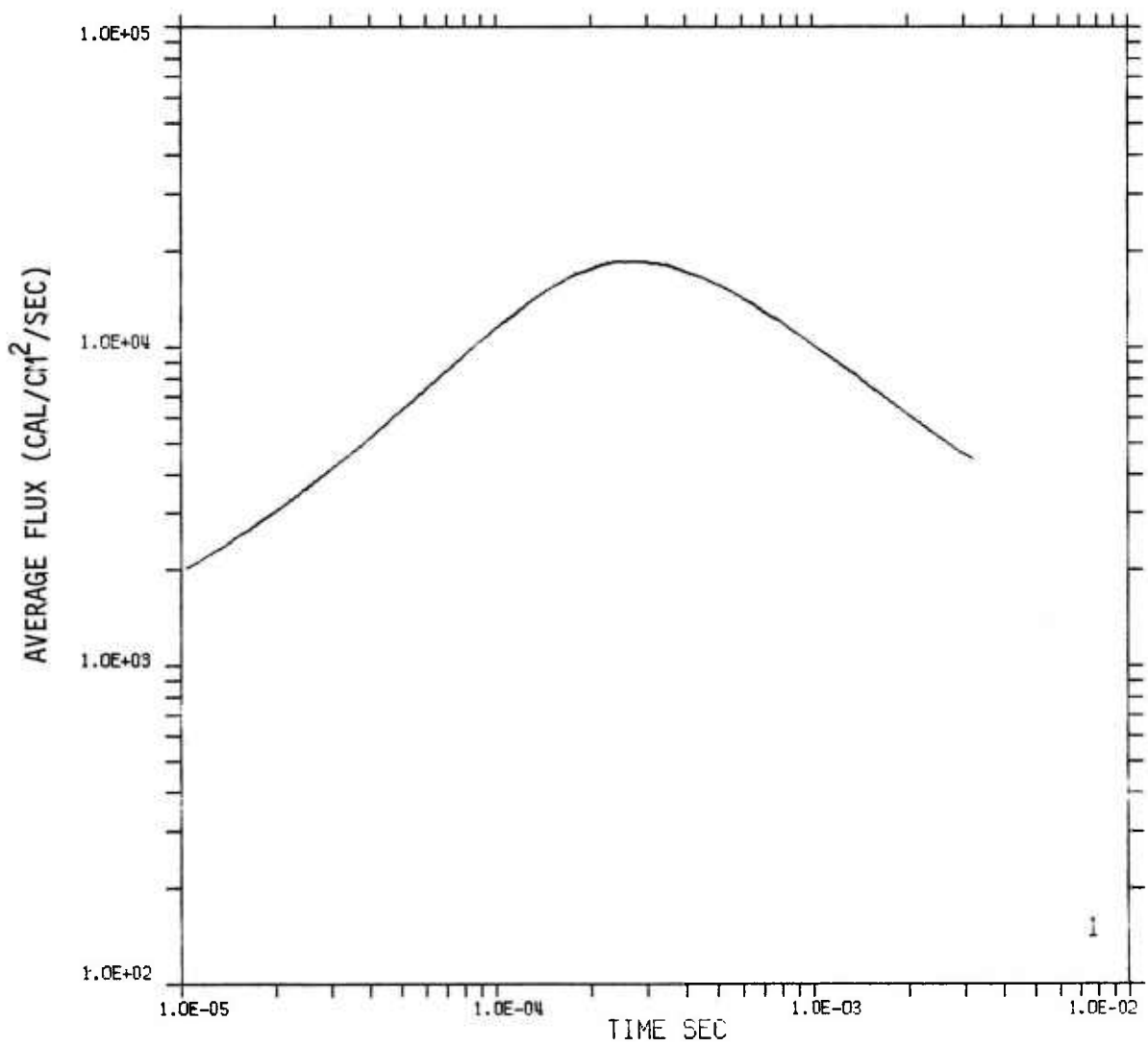


Figure 69. Average flux from 1 kt surface burst crossing detector with orientation 30 degrees at 30.48 meters ground range.

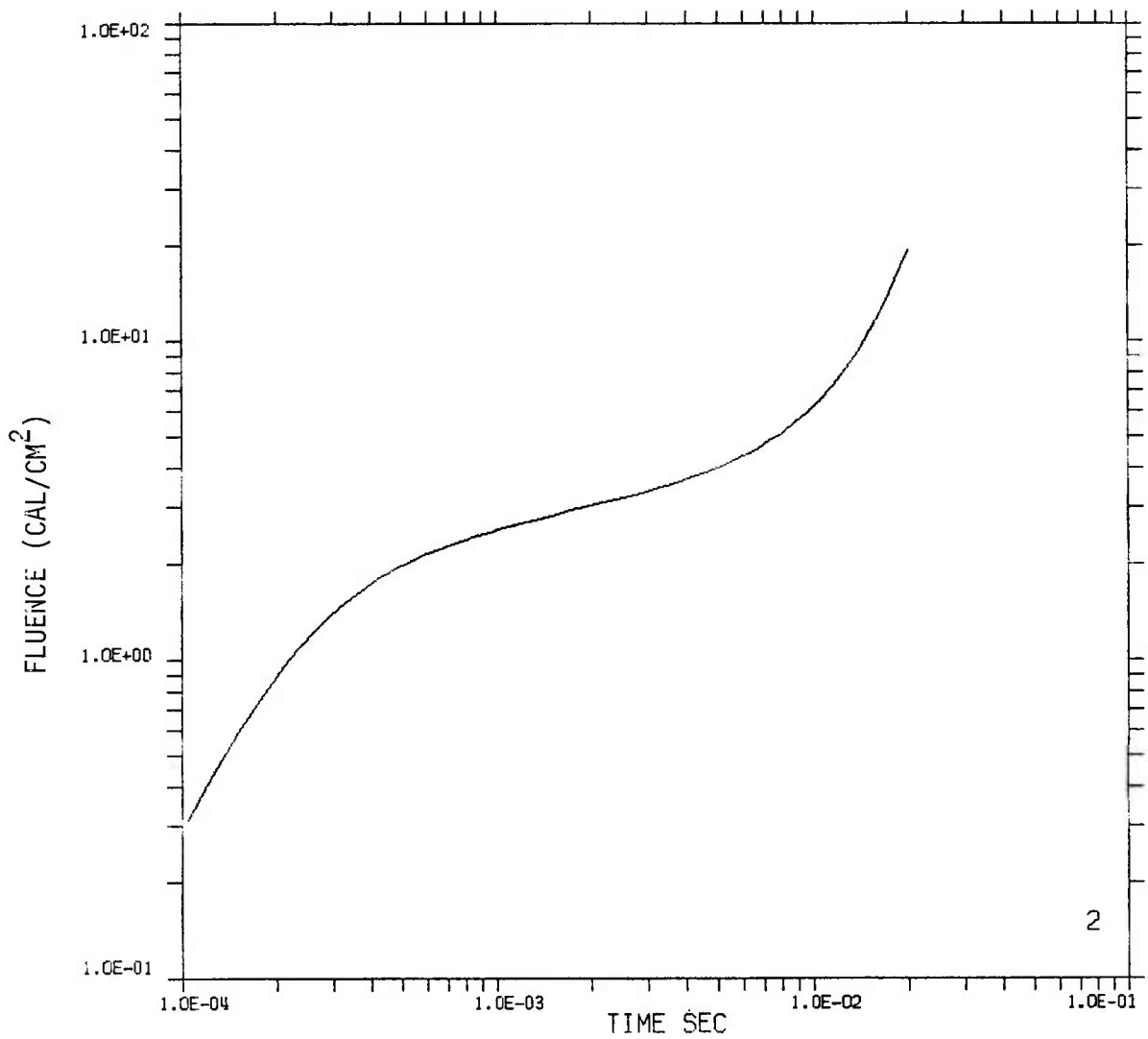


Figure 70. Fluence from 1 kt surface burst crossing detector with orientation 30 degrees at 60.96 meters ground range.

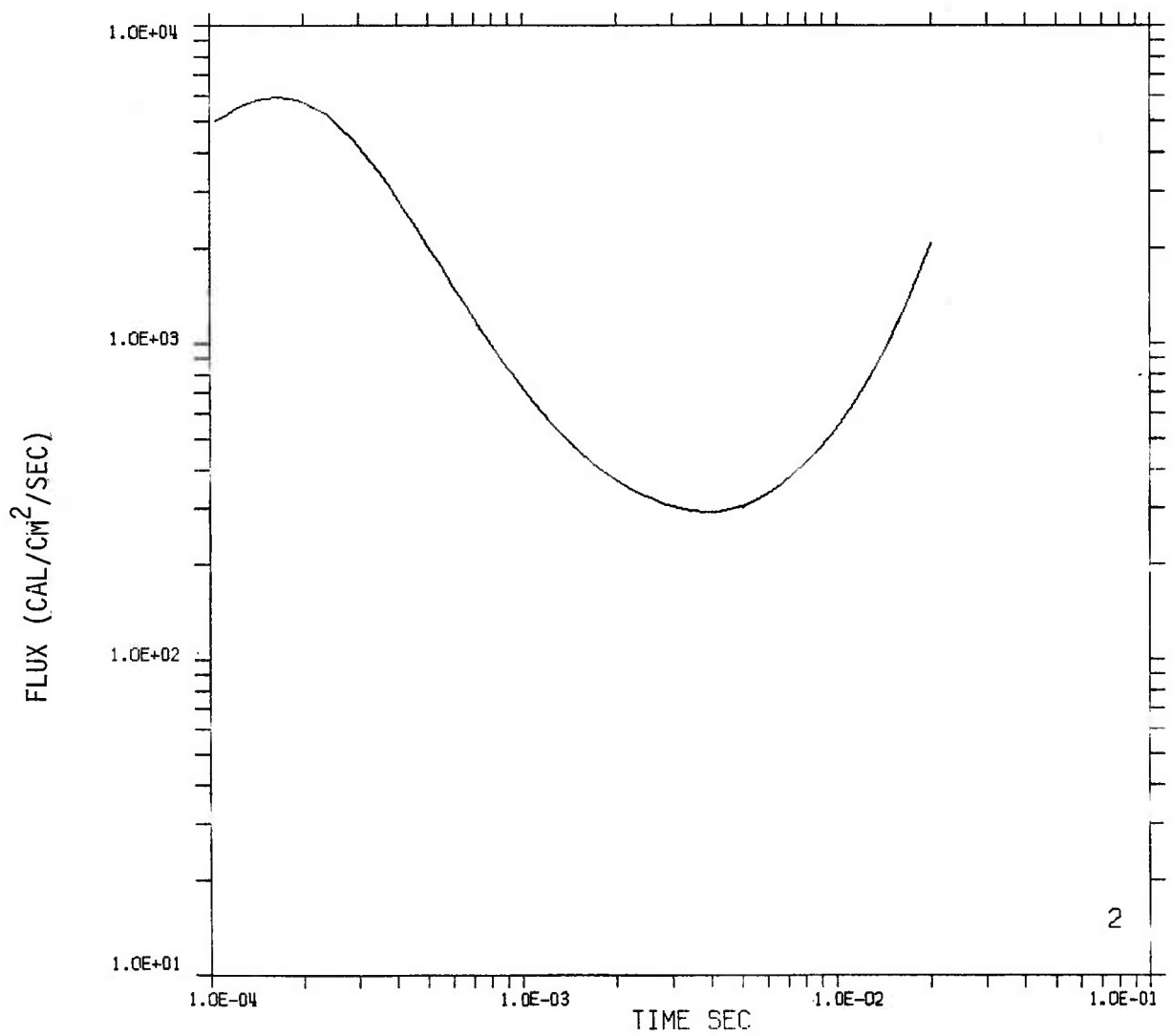


Figure 71. Flux from 1 kt surface burst crossing detector with orientation 30 degrees at 60.96 meters ground range.

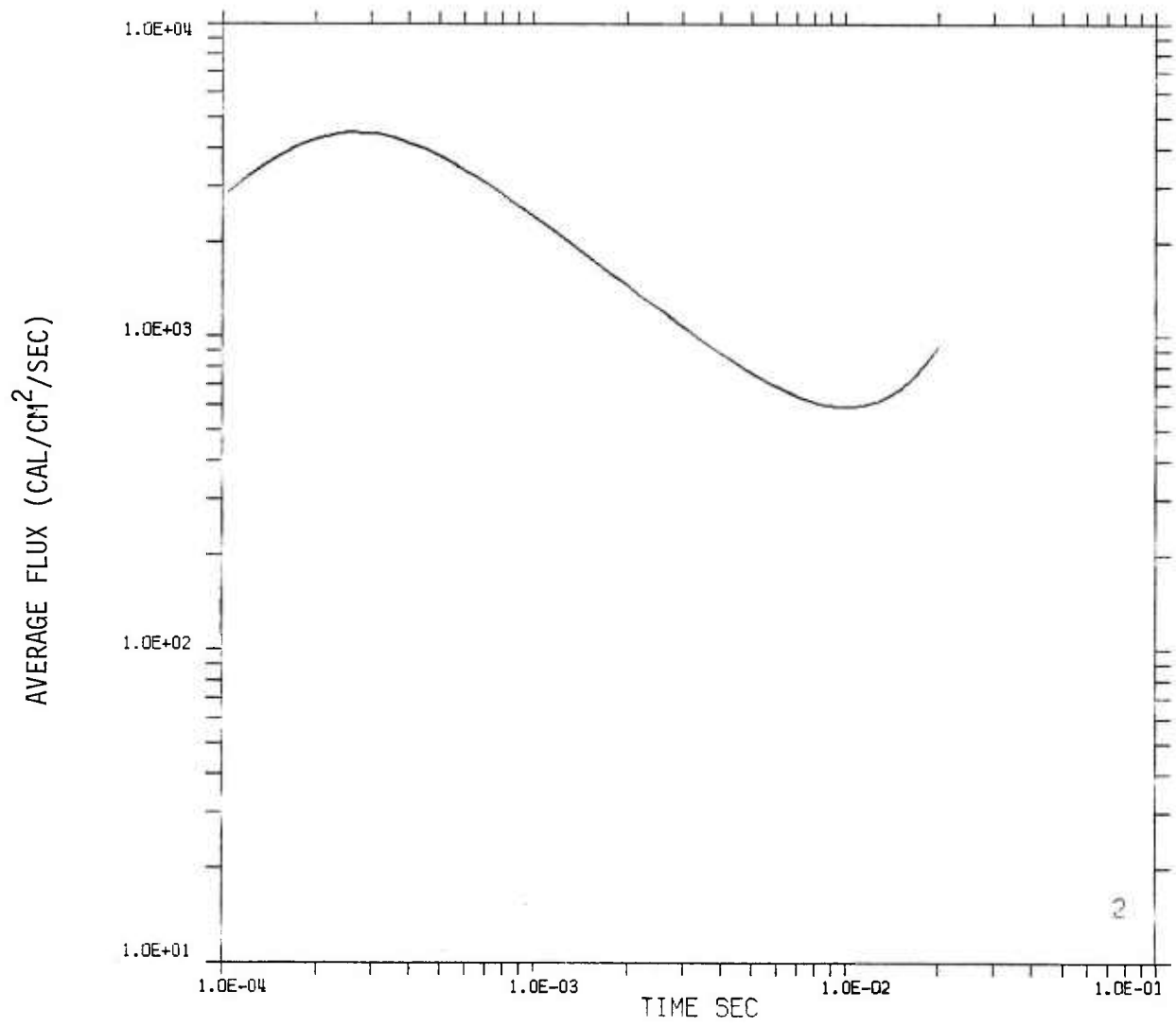


Figure 72. Average flux from 1 kt surface burst crossing detector with orientation 30 degrees at 60.96 meters ground range.

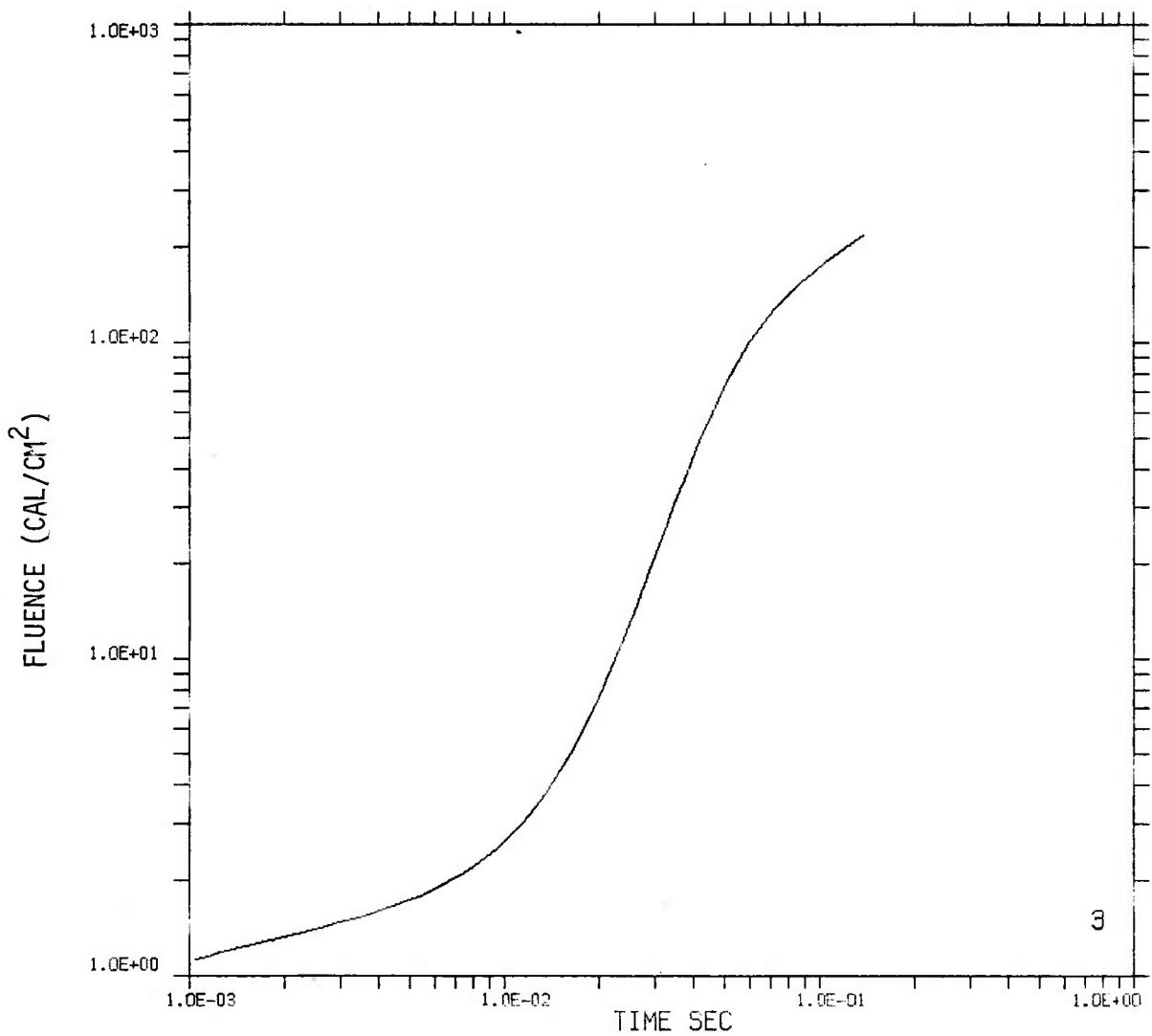


Figure 73. Fluence from 1 kt surface burst crossing detector with orientation 30 degrees at 91.44 meters ground range.

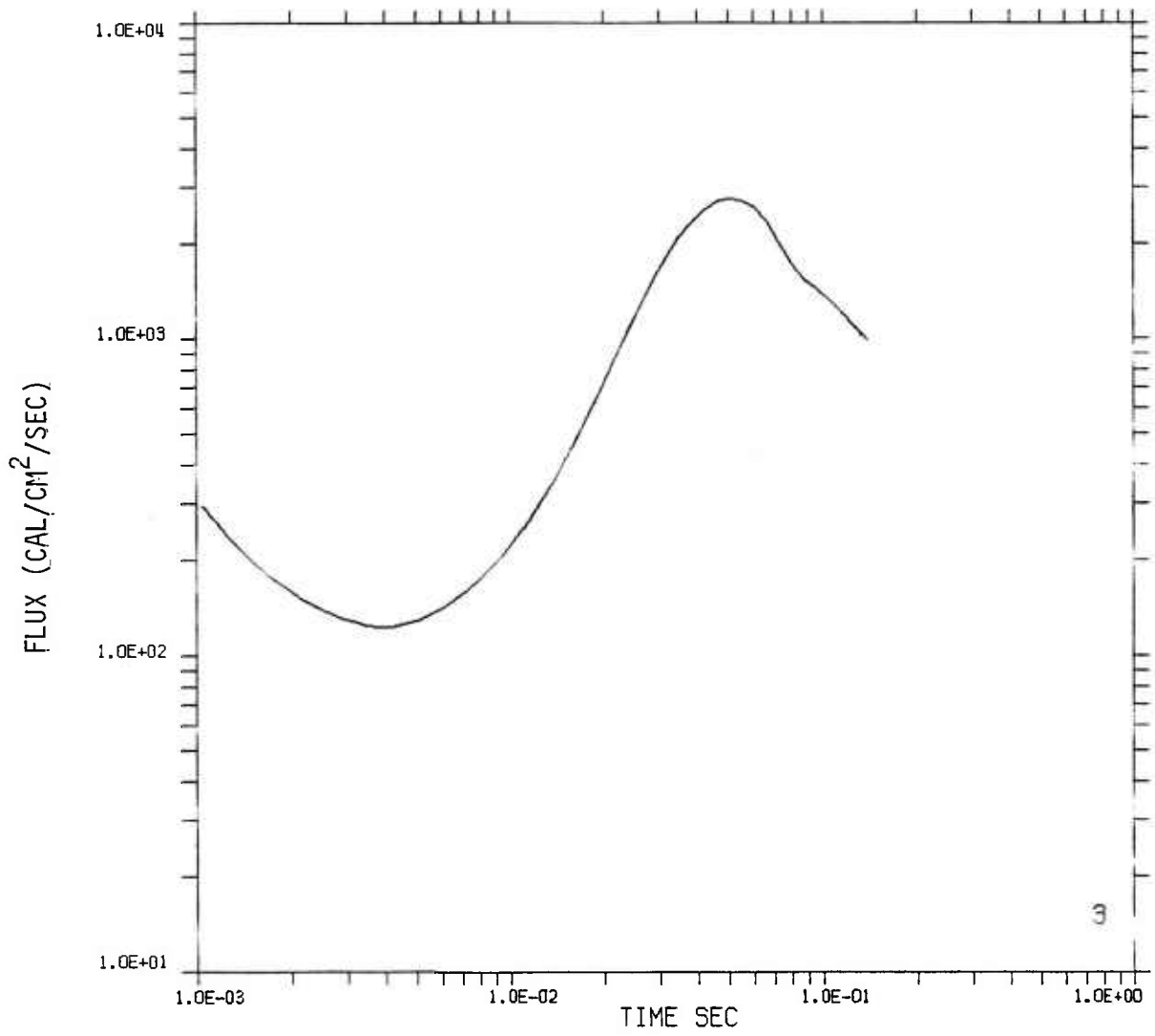


Figure 74. Flux from 1 kt surface burst crossing detector with orientation 30 degrees at 91.44 meters ground range.

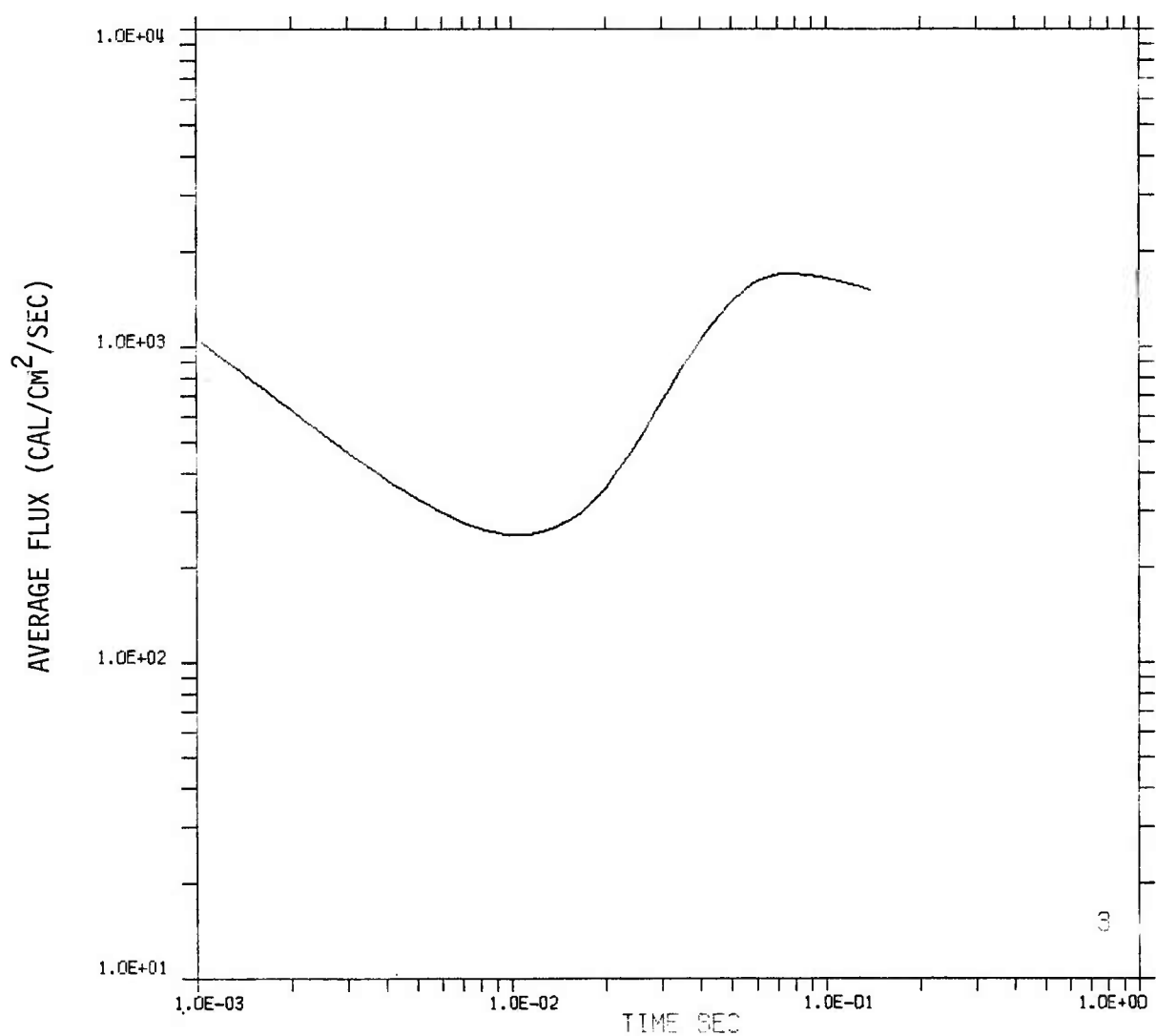


Figure 75. Average flux from 1 kt surface burst crossing detector with orientation 30 degrees at 91.44 meters ground range.

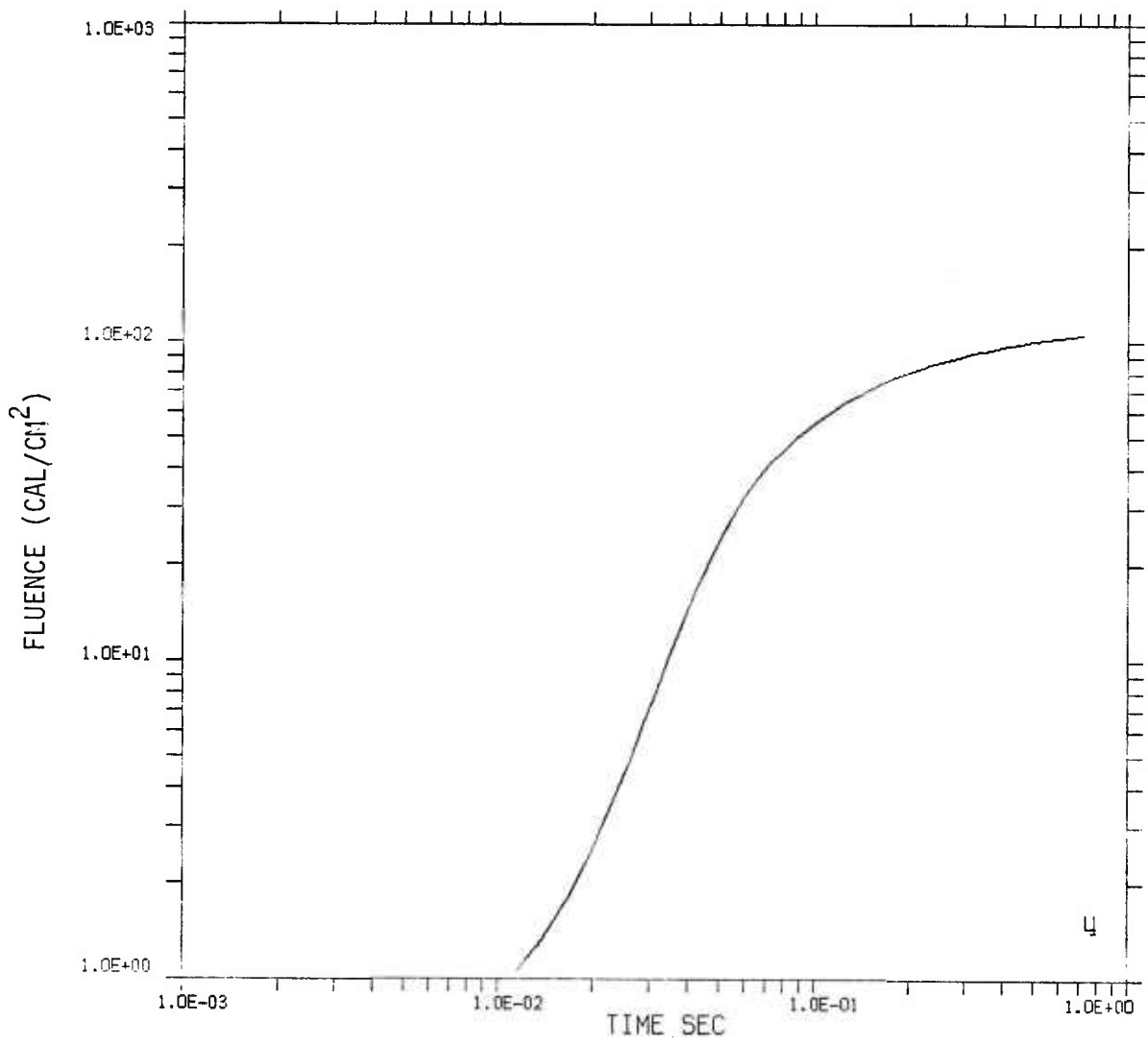


Figure 76. Fluence from 1 kt surface burst crossing detector with orientation 30 degrees at 152.4 meters ground range.

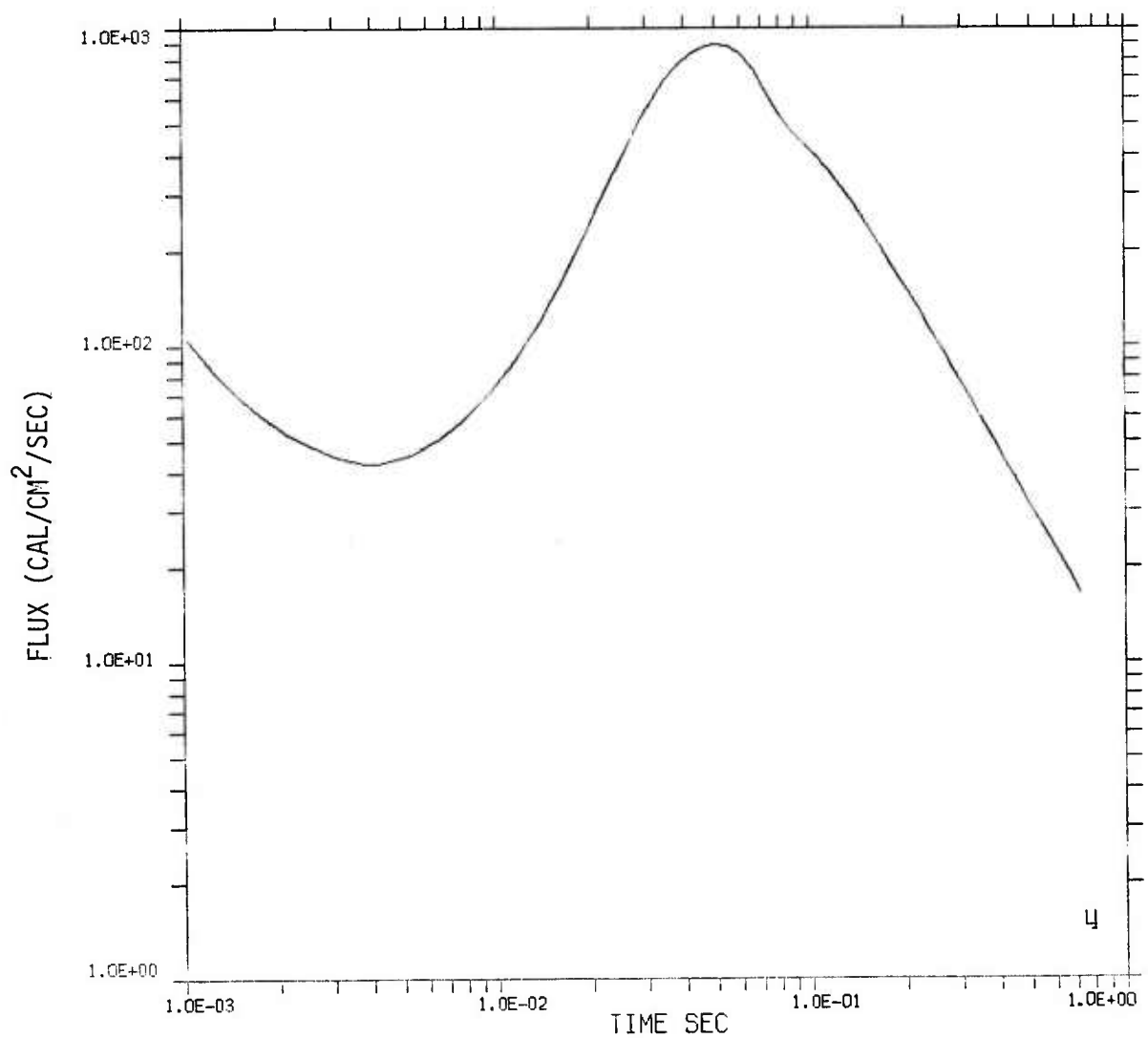


Figure 77. Flux from 1 kt surface burst crossing detector with orientation 30 degrees at 152.4 meters ground range.

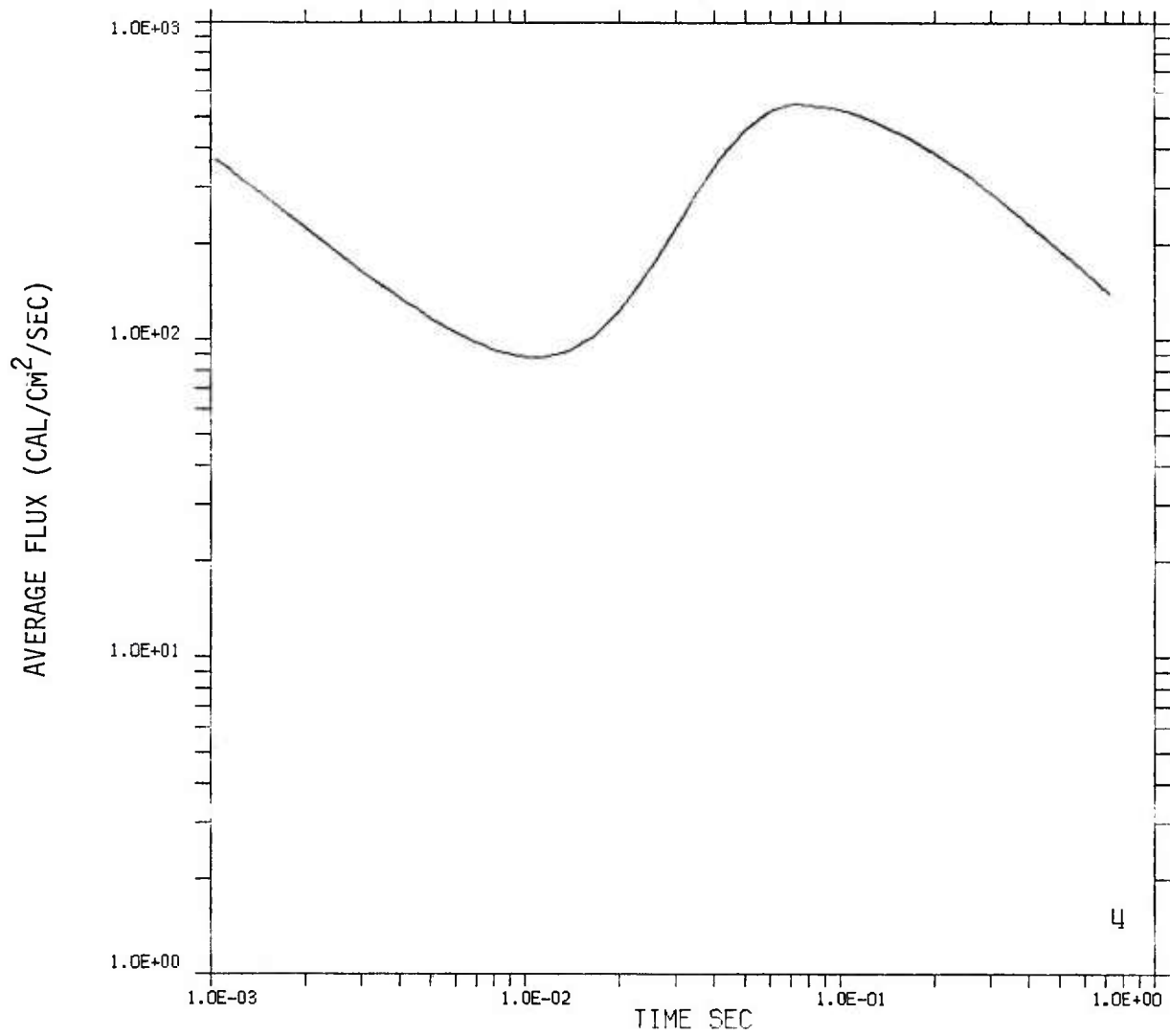


Figure 78. Average flux from 1 kt surface burst crossing detector with orientation 30 degrees at 152.4 meters ground range.

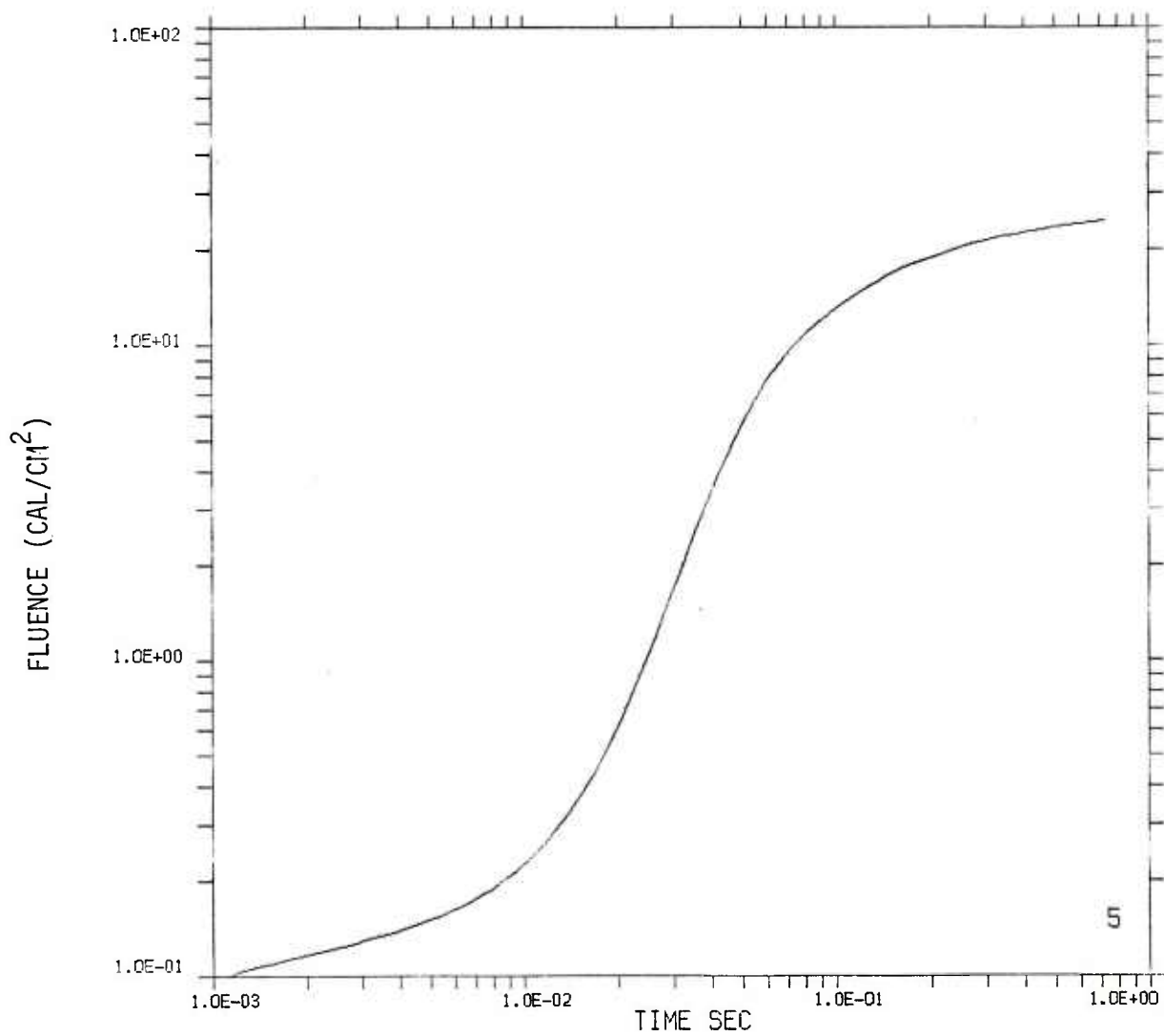


Figure 79. Fluence from 1 kt surface burst crossing detector with orientation 30 degrees at 304.8 meters ground range.

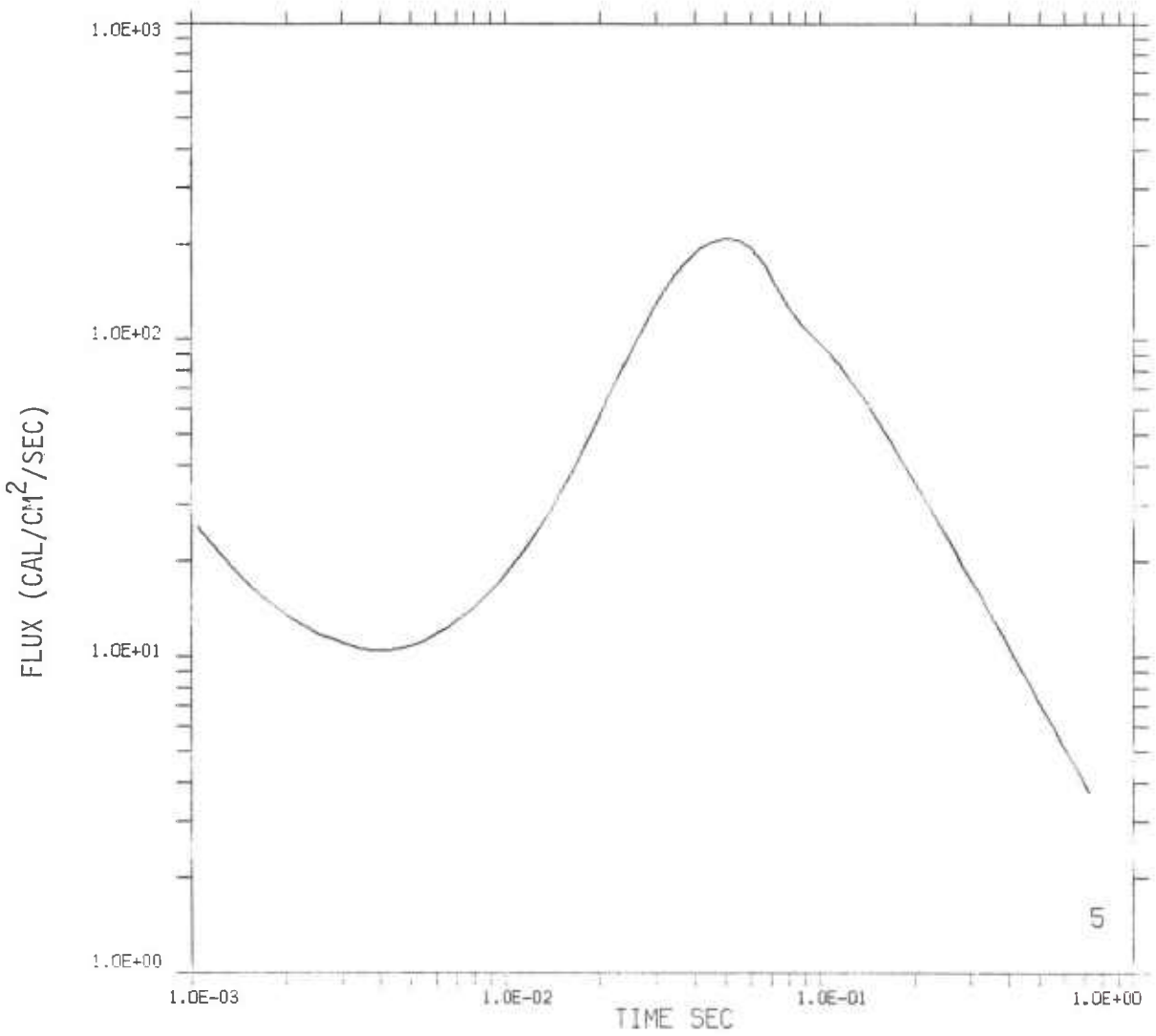


Figure 80. Flux from 1 kt surface burst crossing detector with orientation 30 degrees at 304.8 meters ground range.

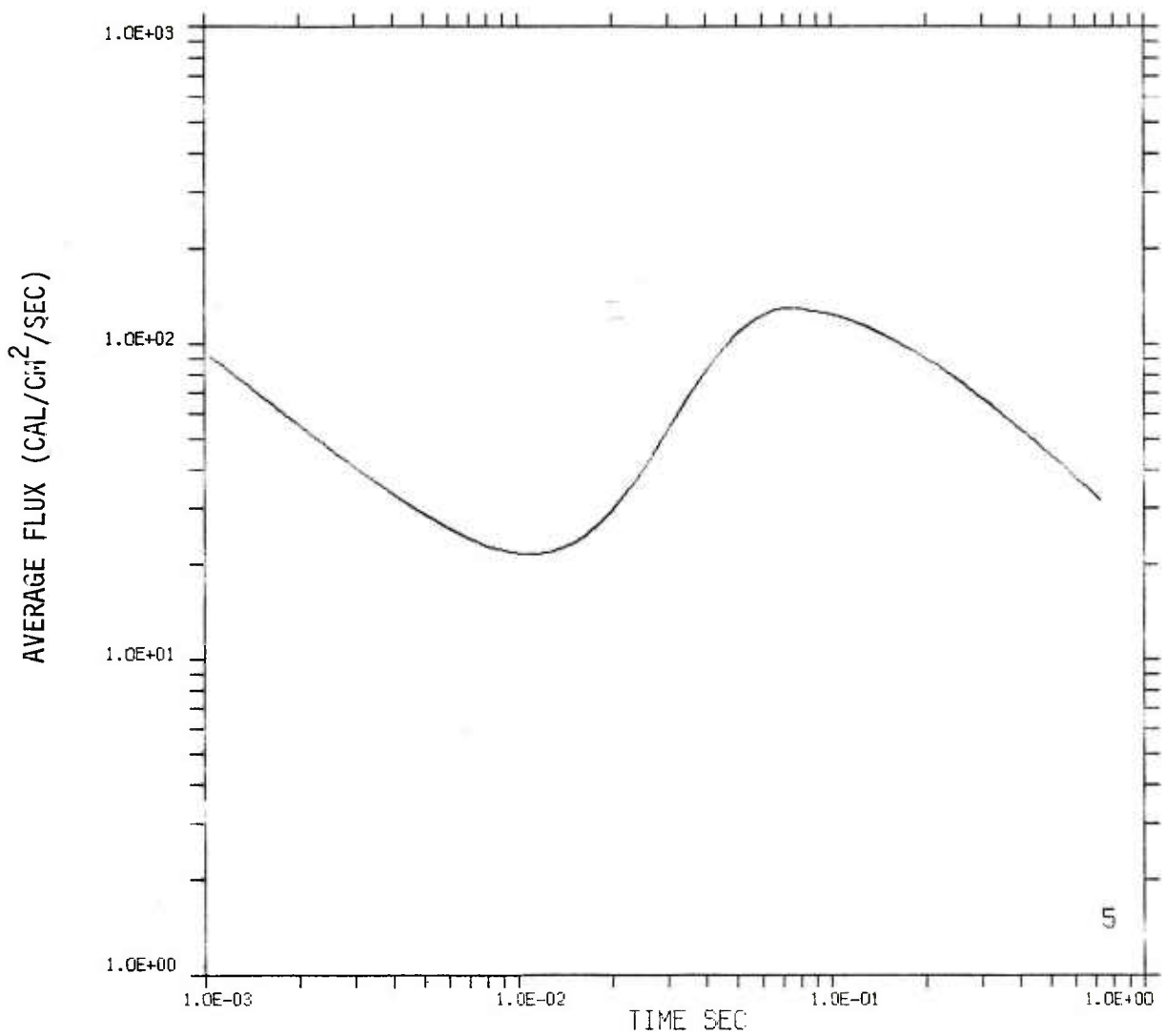


Figure 81. Average flux from 1 kt surface burst crossing detector with orientation 30 degrees at 304.8 meters ground range.

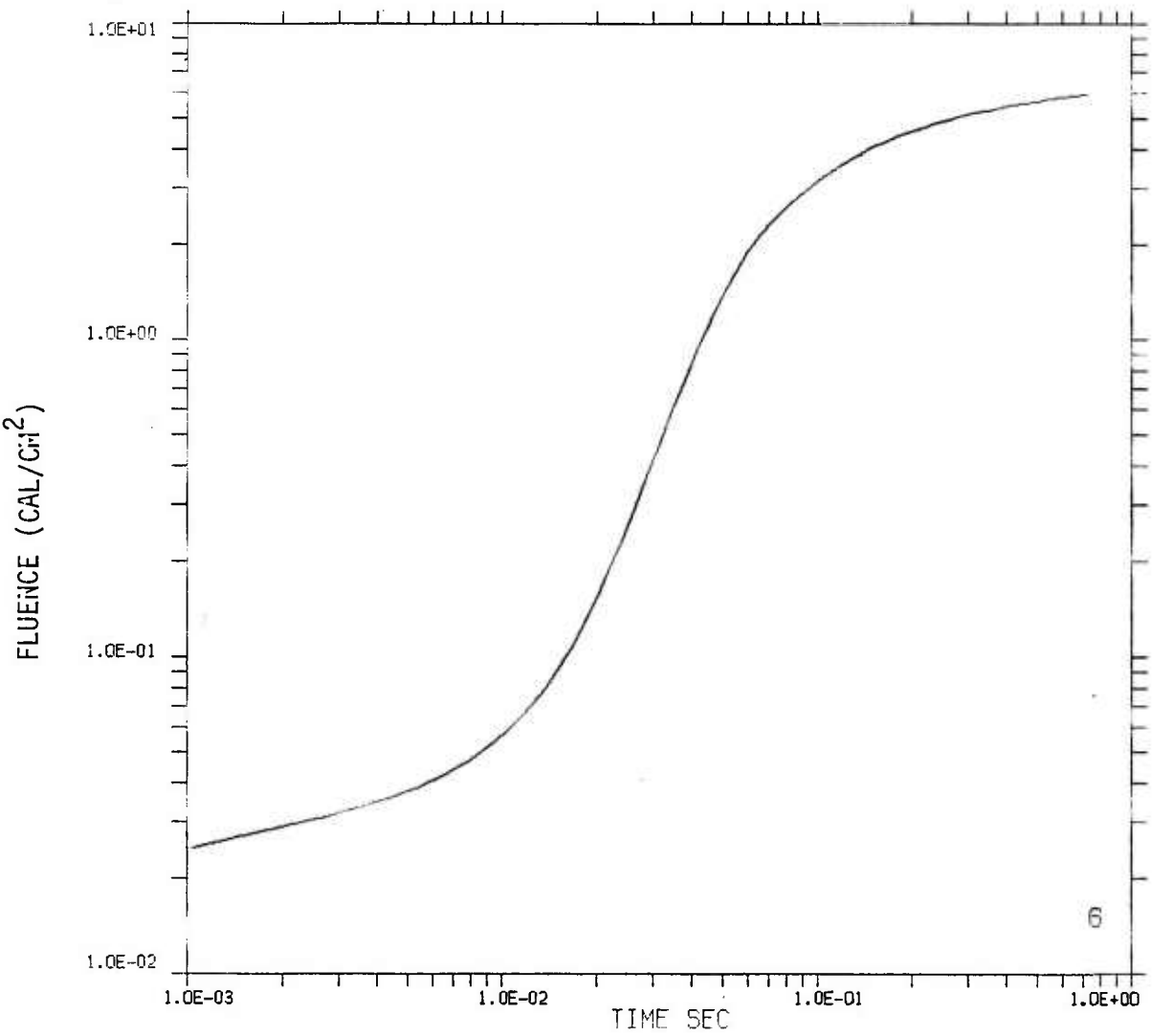


Figure 82. Fluence from 1 kt surface burst crossing detector with orientation 30 degrees at 609.6 meters ground range.

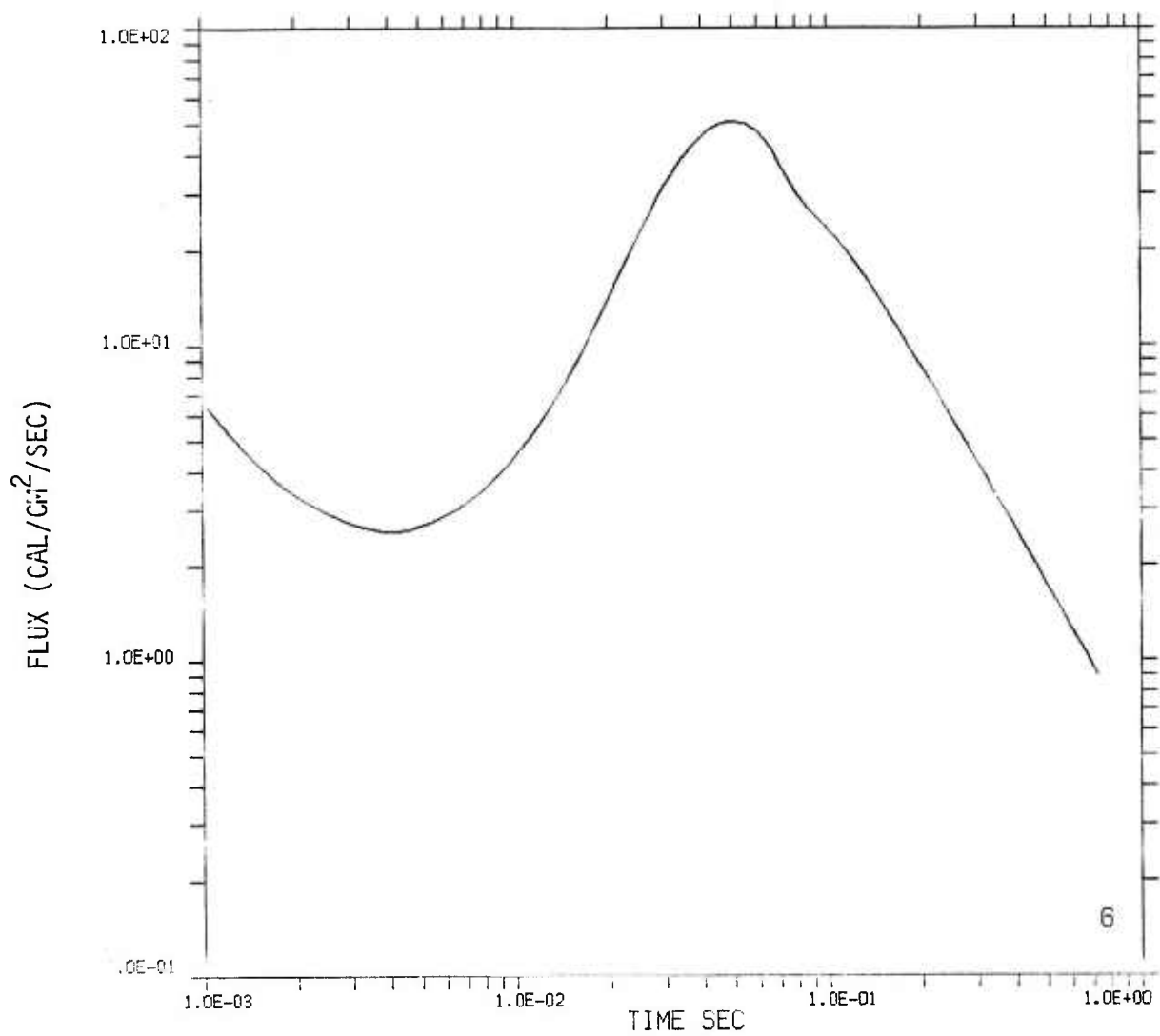


Figure 83. Flux from 1 kt surface burst crossing detector with orientation 30 degrees at 609.6 meters ground range.

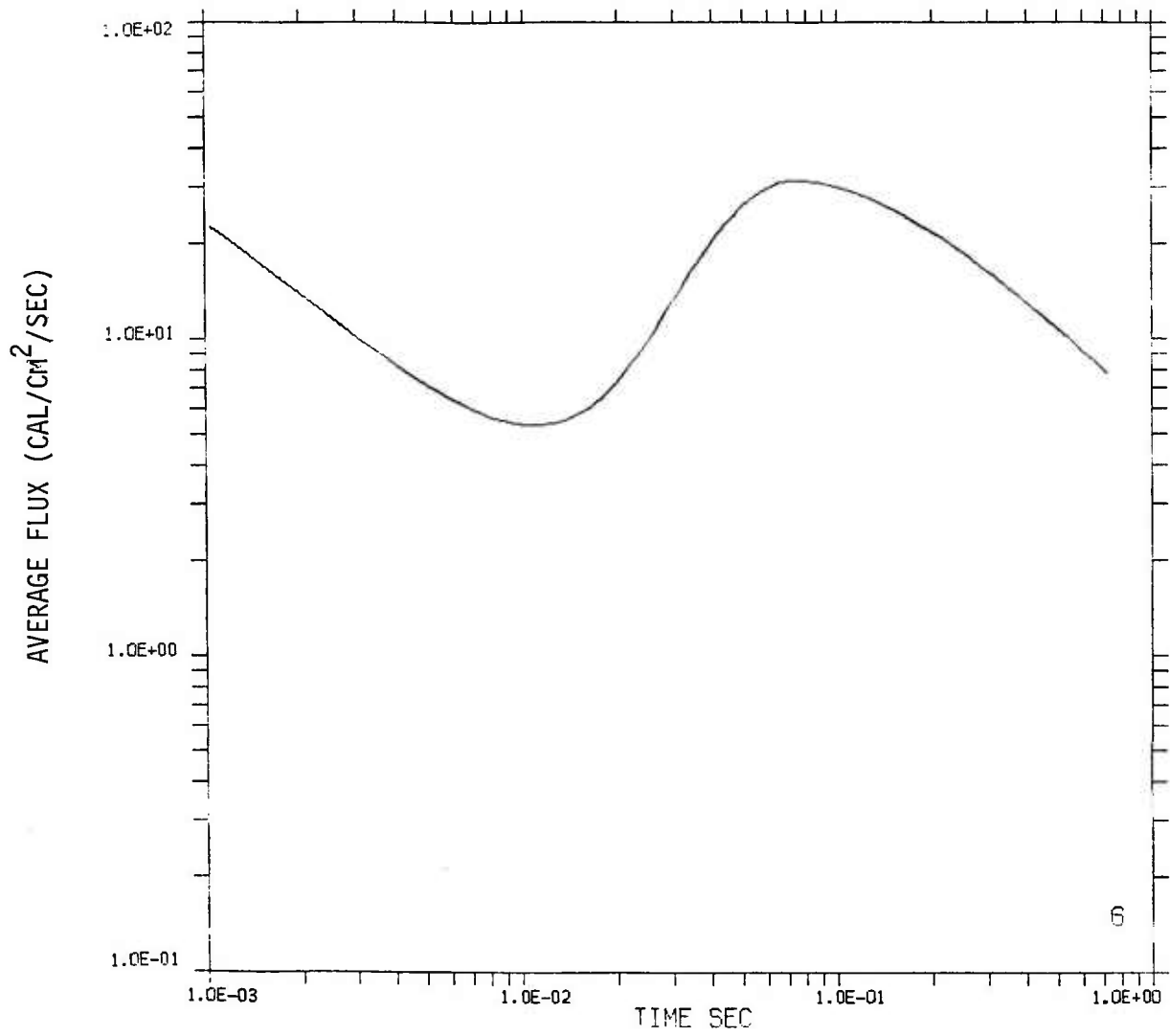


Figure 84. Average flux from 1 kt surface burst crossing detector with orientation 30 degrees at 609.6 meters ground range.

APPENDIX C

ESTIMATE OF THERMAL RADIATION FROM A 1 KILOTON NUCLEAR SURFACE BURST DETECTOR ELEVATION 60 DEGREES

This appendix contains plots for one elevation and consists of six sets of three figures. Each set corresponds to a particular range: 34.48, 60.96, 91.44, 152.4, 304.8, or 609.6 meters from ground zero. For each range fluence, flux, and average flux are presented as a function of time. Fluence is in units of cal-cm⁻², flux and average flux are in units of cal-cm⁻²-sec⁻¹.

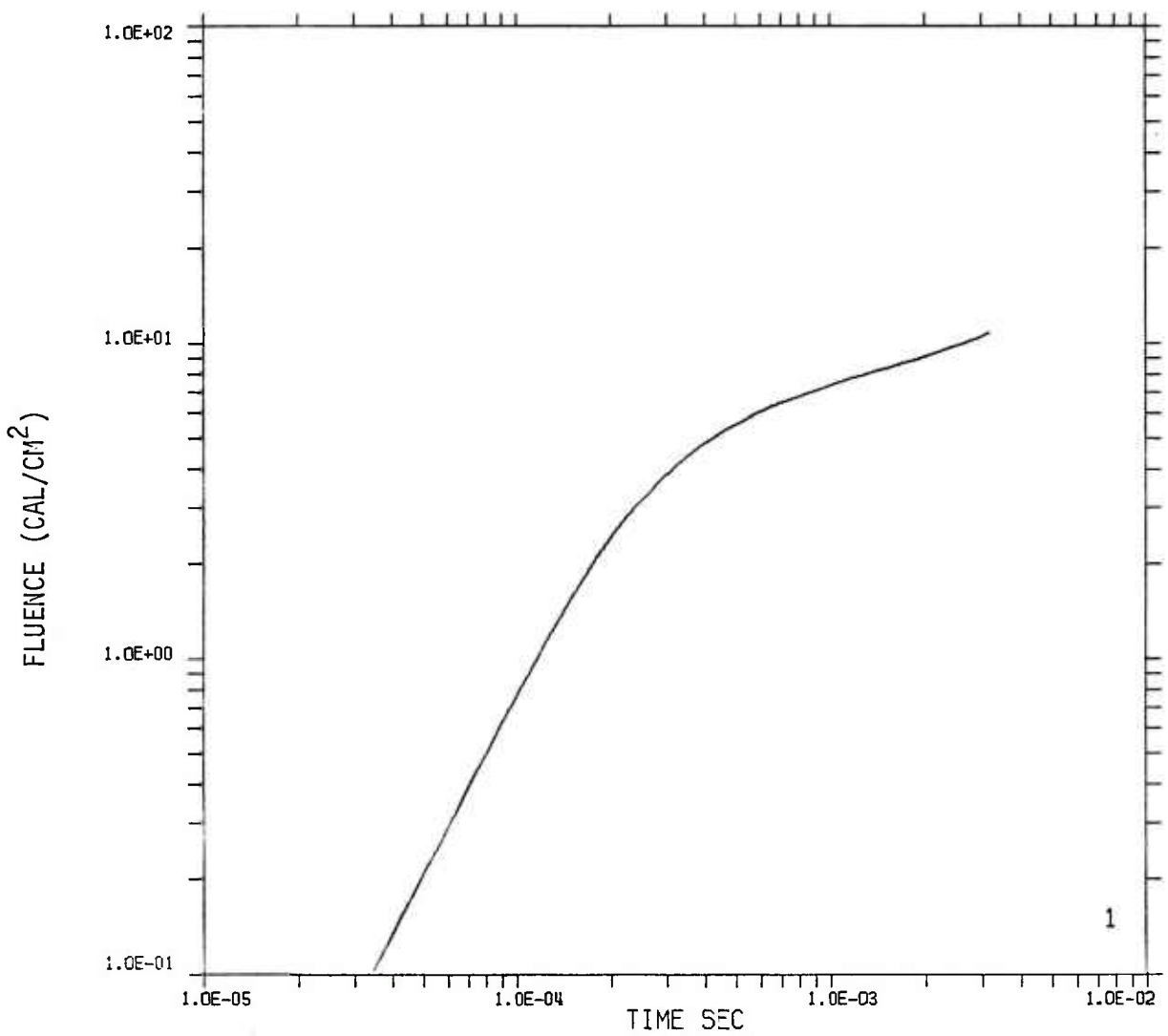


Figure 85. Fluence from 1 kt surface burst crossing detector with orientation 60 degrees at 30.48 meters ground range.

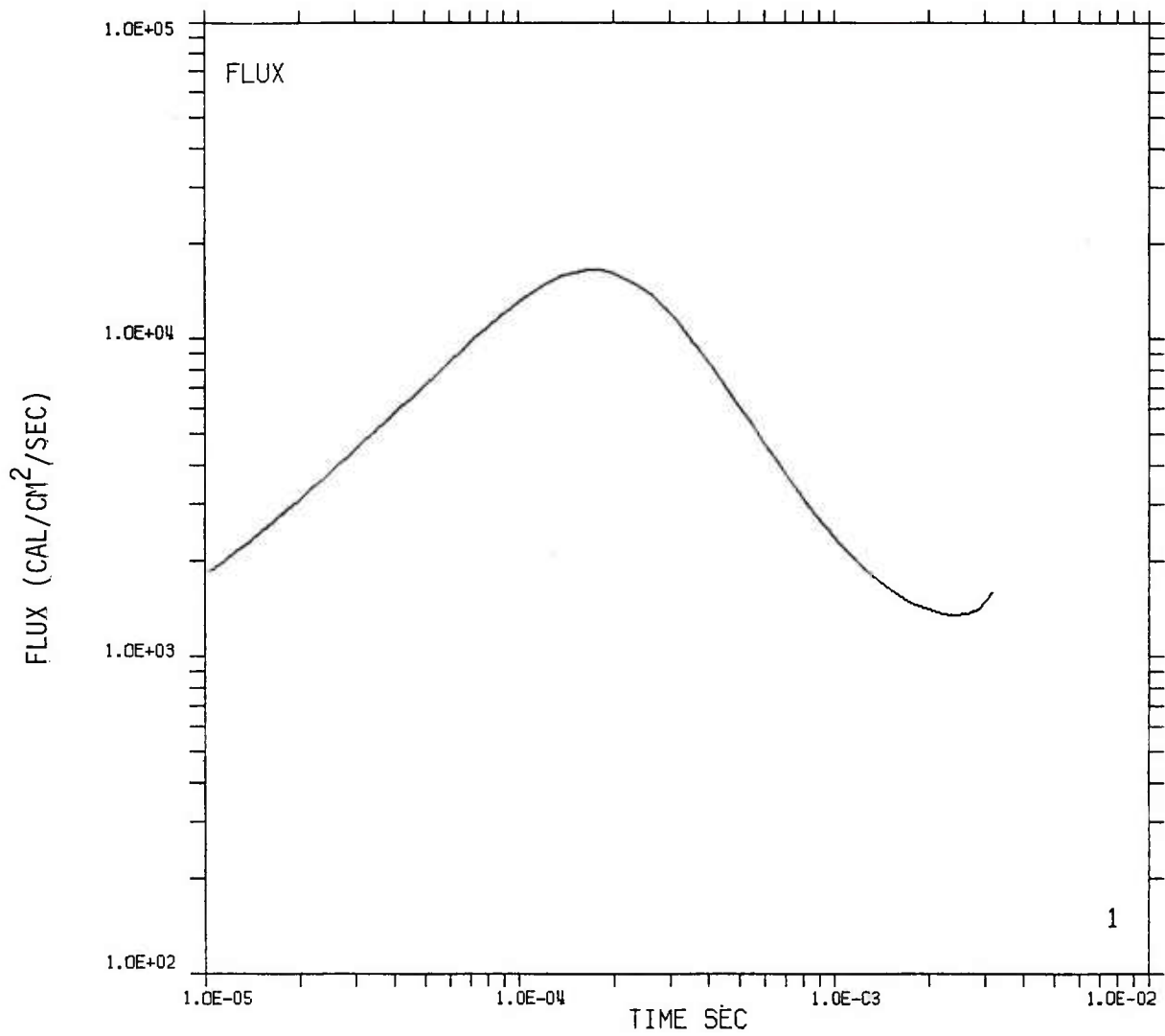


Figure 86. Flux from 1 kt surface burst crossing detector with orientation 60 degrees at 30.48 meters ground range.

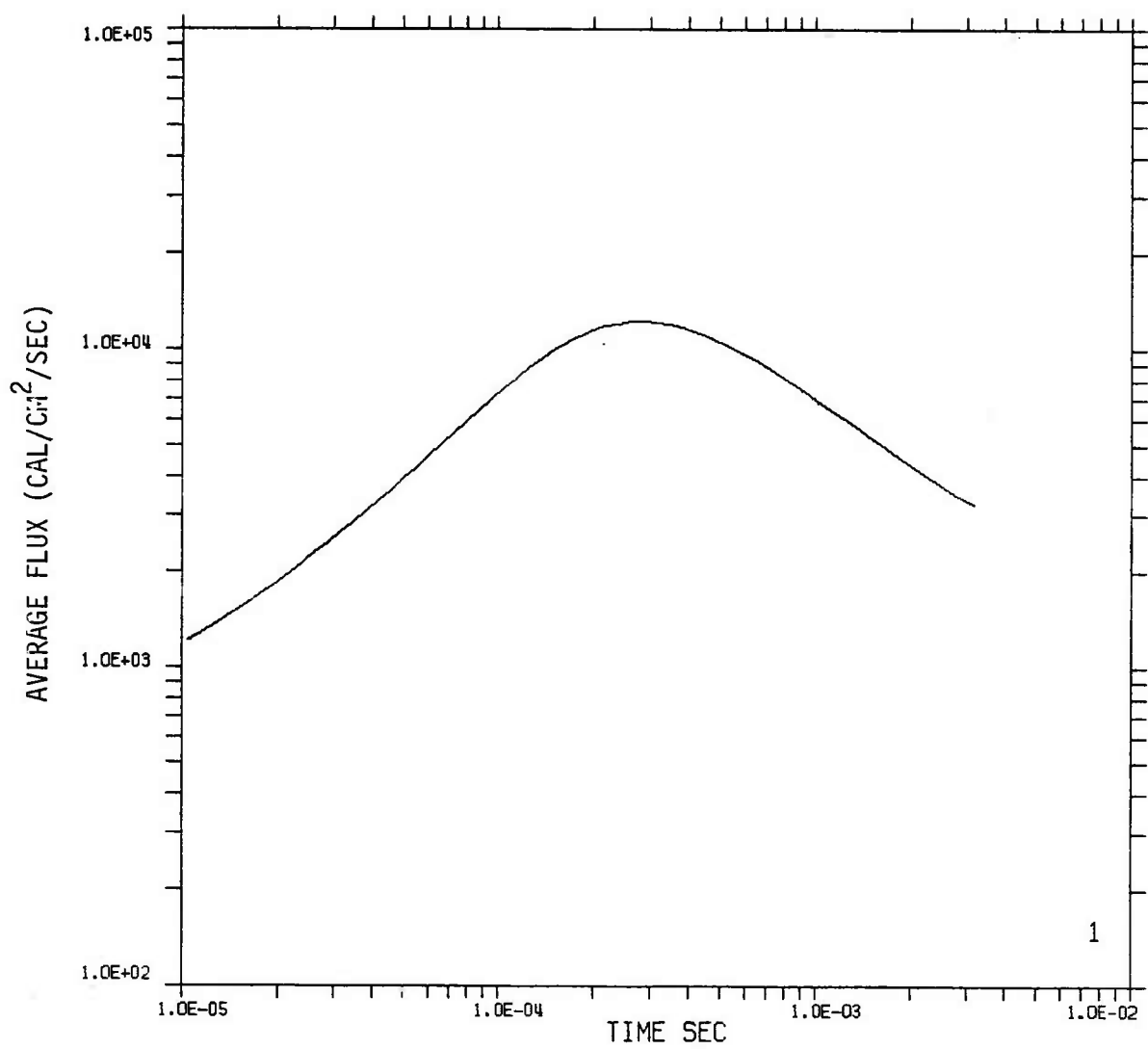


Figure 87. Average flux from 1 kt surface burst crossing detector with orientation 60 degrees at 30.48 meters ground range.

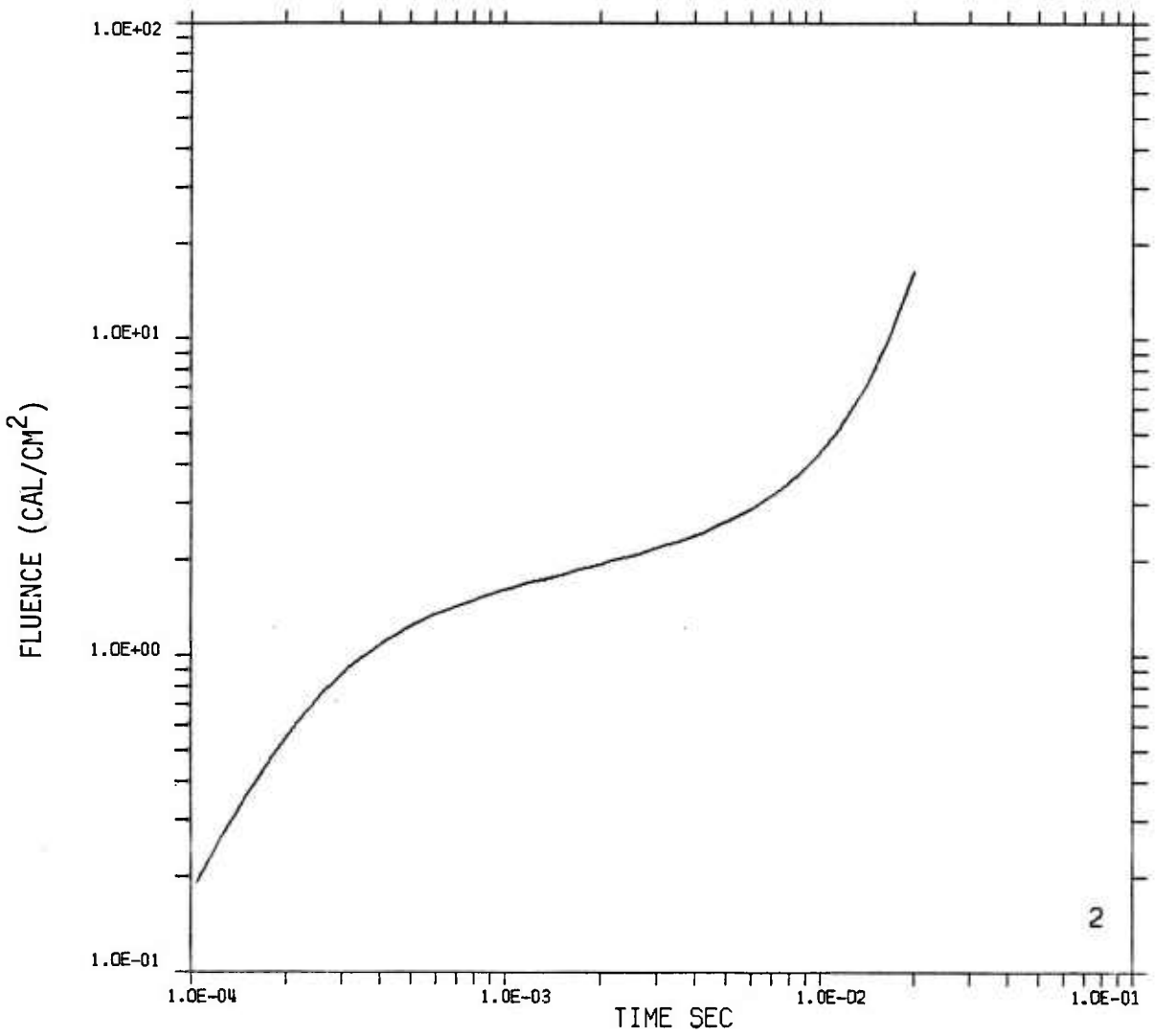


Figure 88. Fluence from 1 kt surface burst crossing detector with orientation 60 degrees at 60.96 meters ground range.

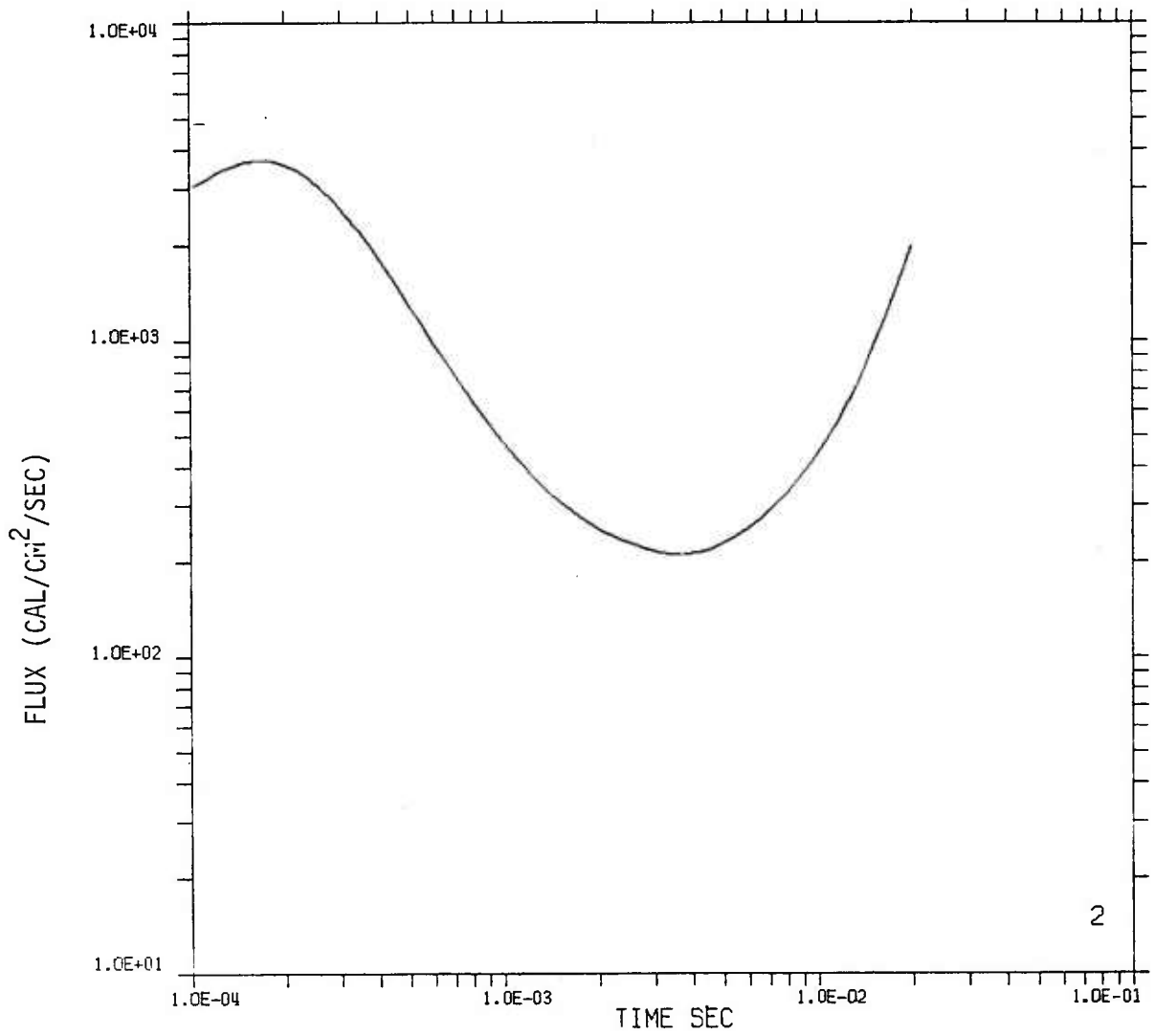


Figure 89. Flux from 1 kt surface burst crossing detector with orientation 60 degrees at 60.96 meters ground range.

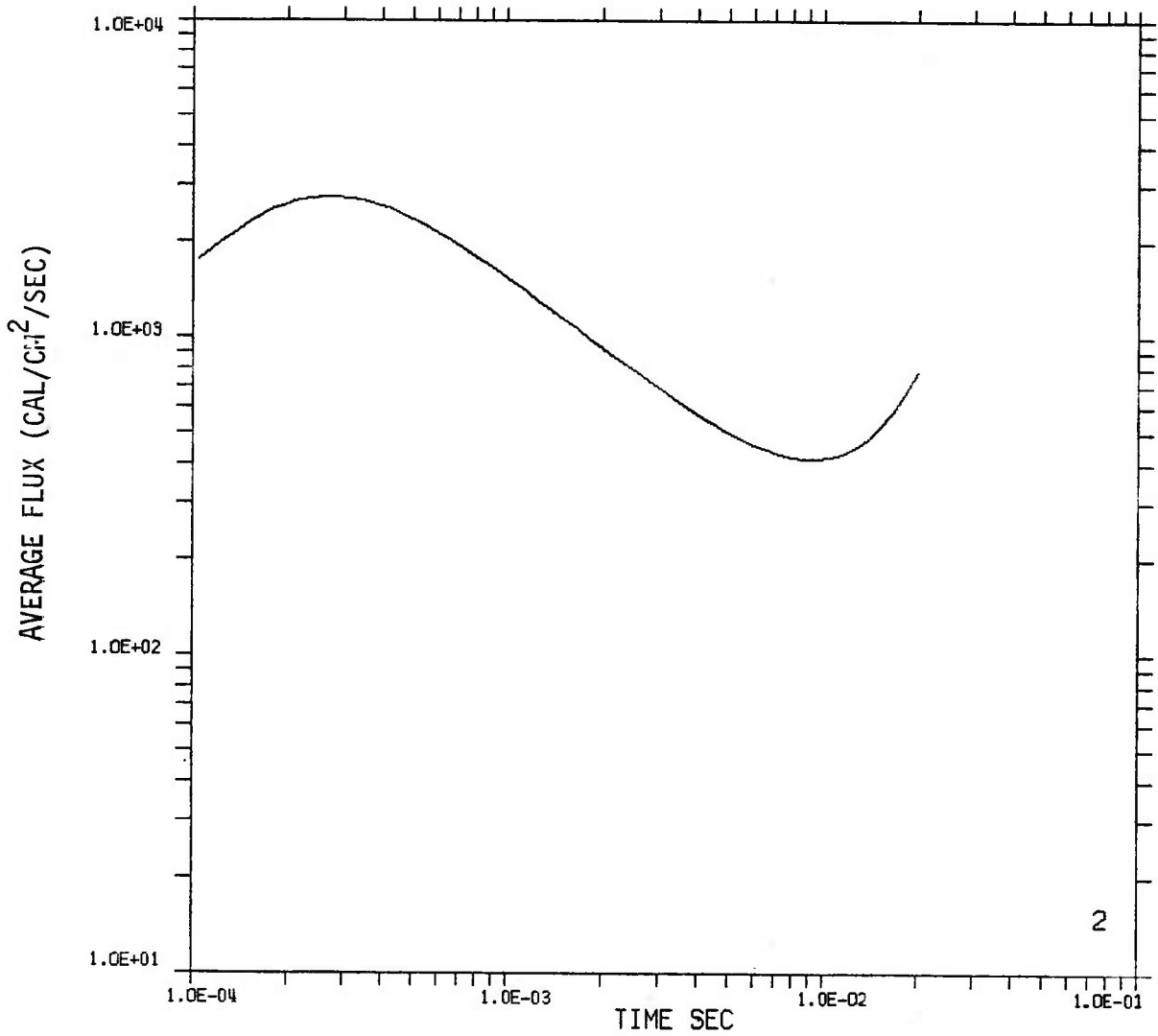


Figure 90. Average flux from 1 kt surface burst crossing detector with orientation 60 degrees at 60.96 meters ground range.

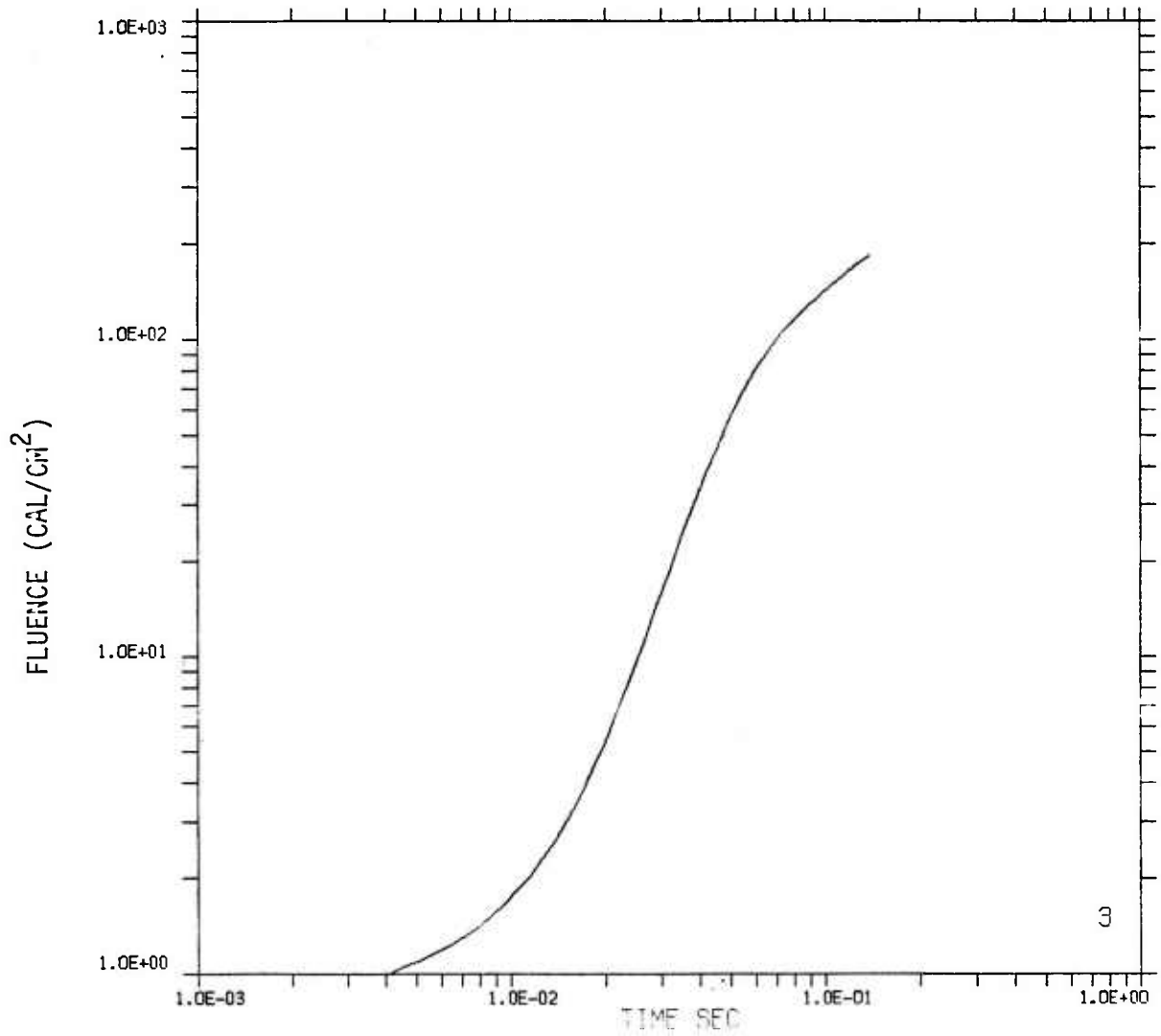


Figure 91. Fluence from 1 kt surface burst crossing detector with orientation 60 degrees at 91.44 meters ground range.

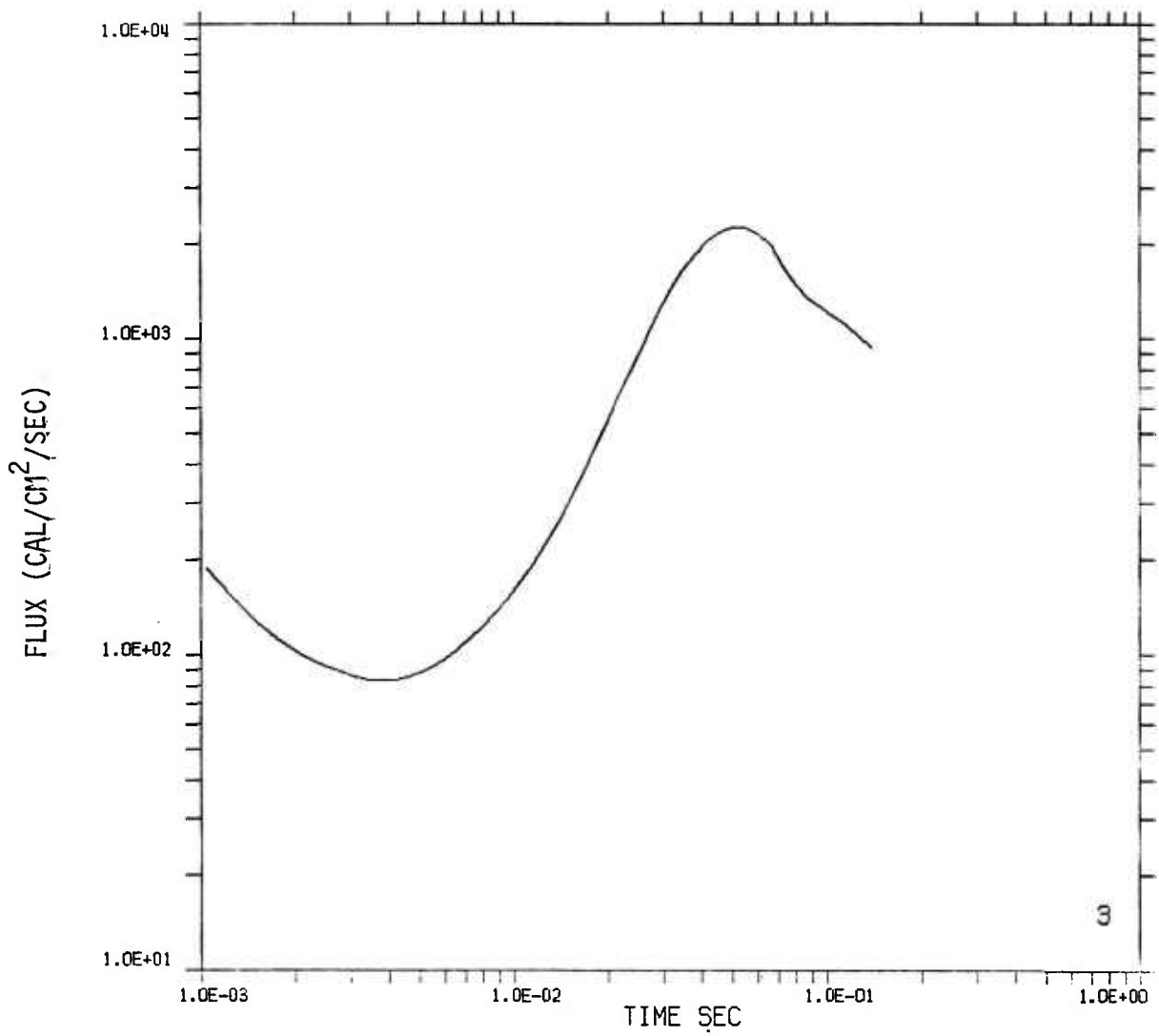


Figure 92. Flux from 1 kt surface burst crossing detector with orientation 60 degrees at 91.44 meters ground range.

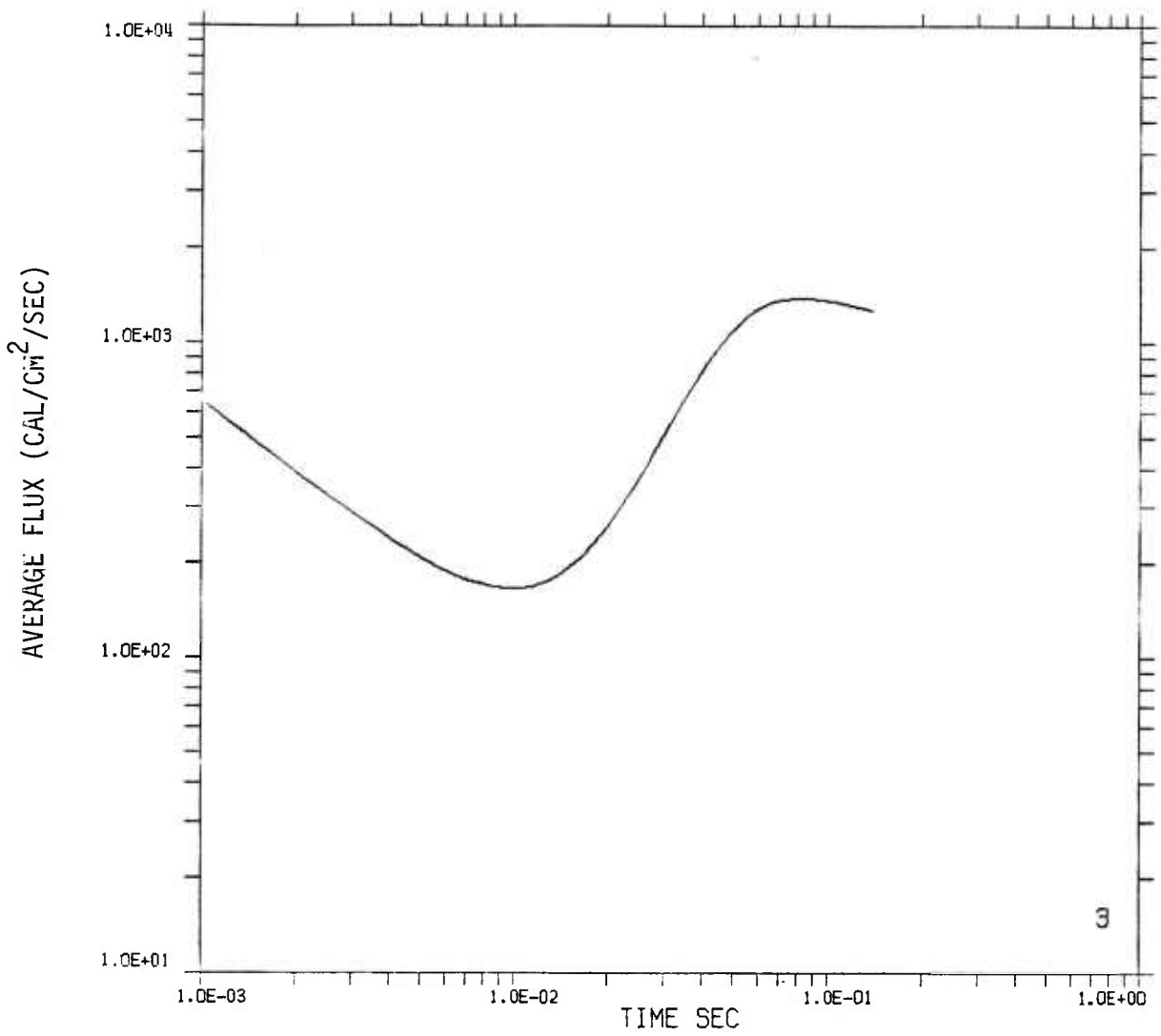


Figure 93. Average flux from 1 kt surface burst crossing detector with orientation 60 degrees at 91.44 meters ground range.

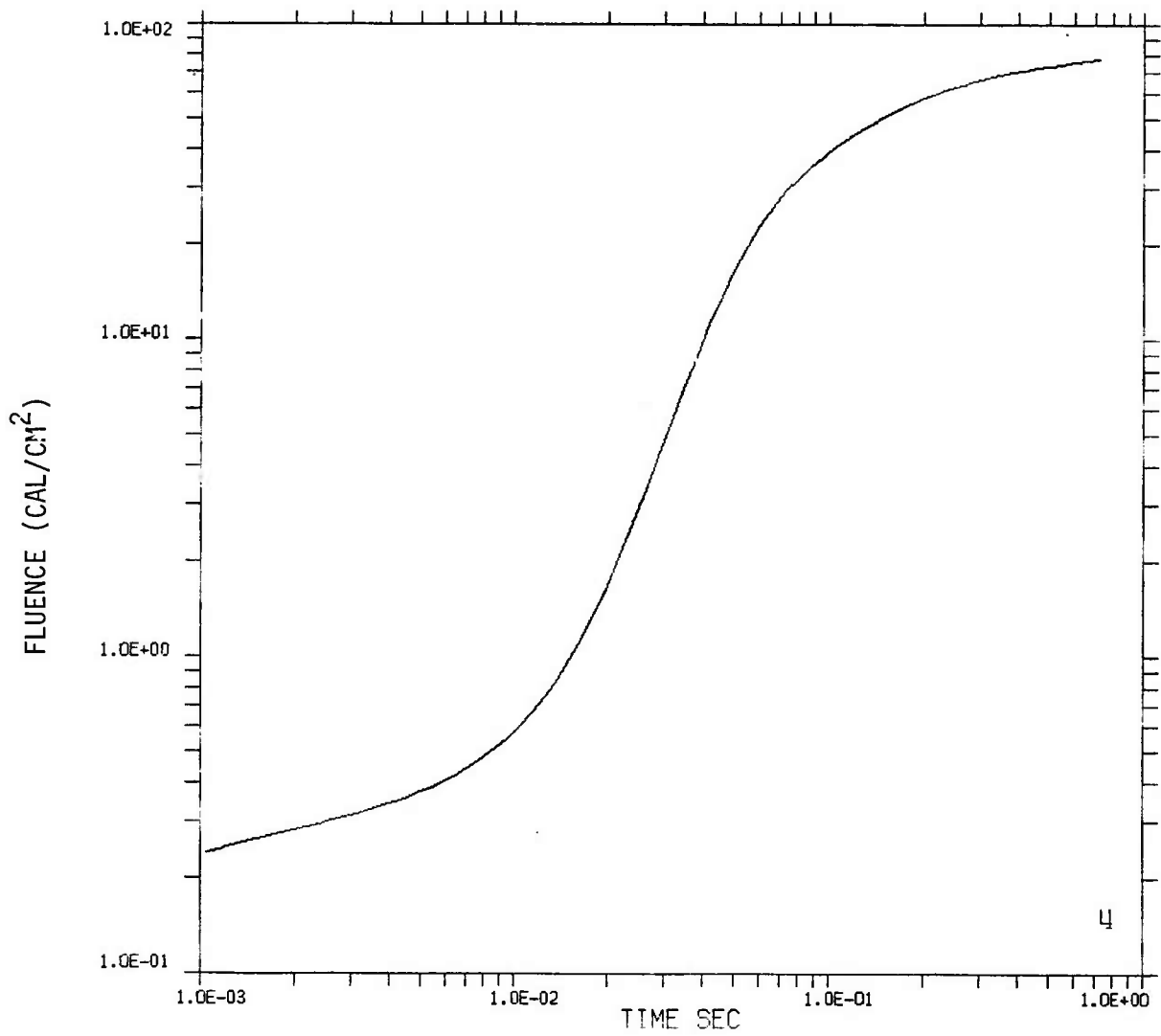


Figure 94. Fluence from 1 kt surface burst crossing detector with orientation 60 degrees at 152.4 meters ground range.

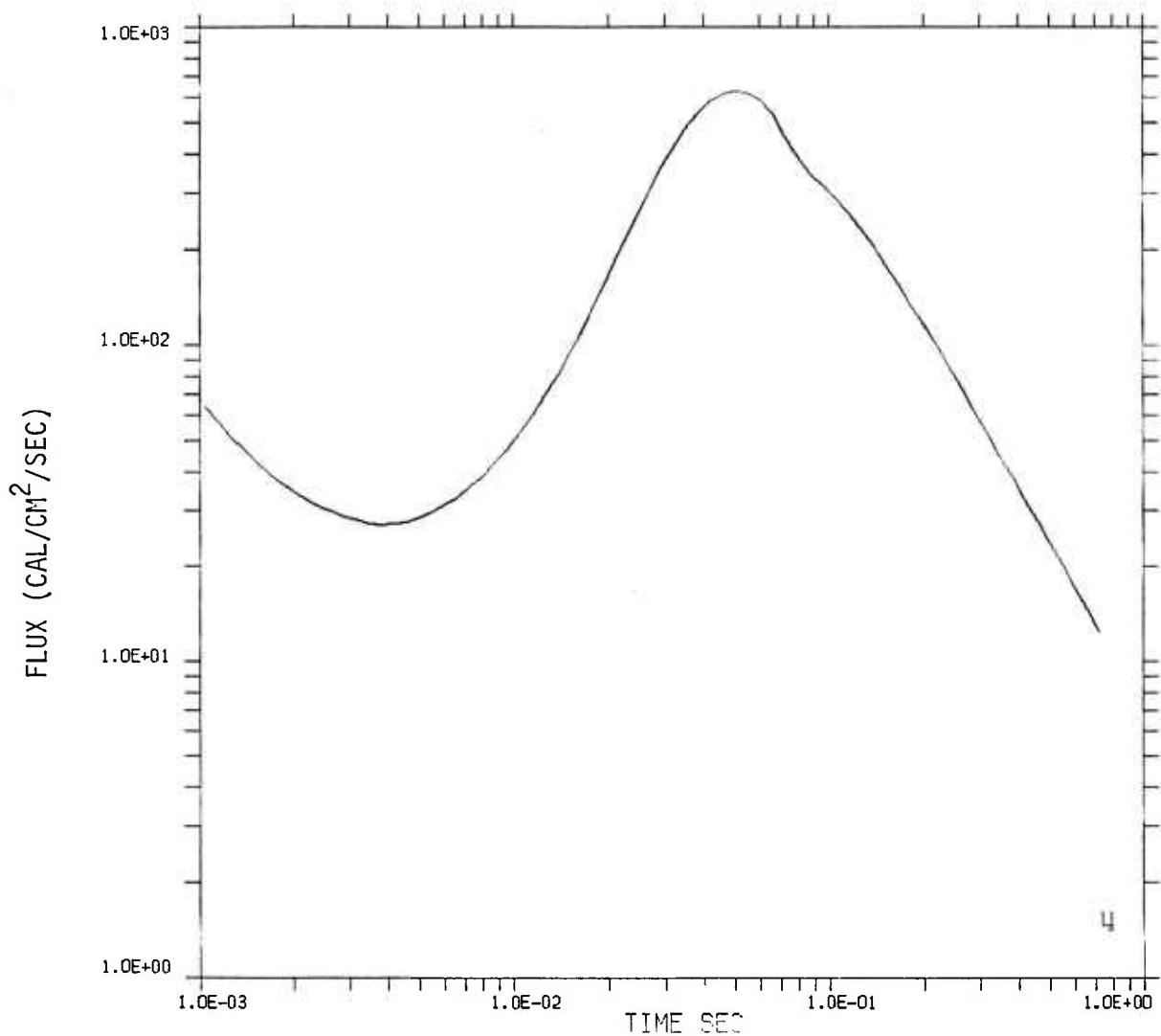


Figure 95. Flux from 1 kt surface burst crossing detector with orientation 60 degrees at 152.4 meters ground range.

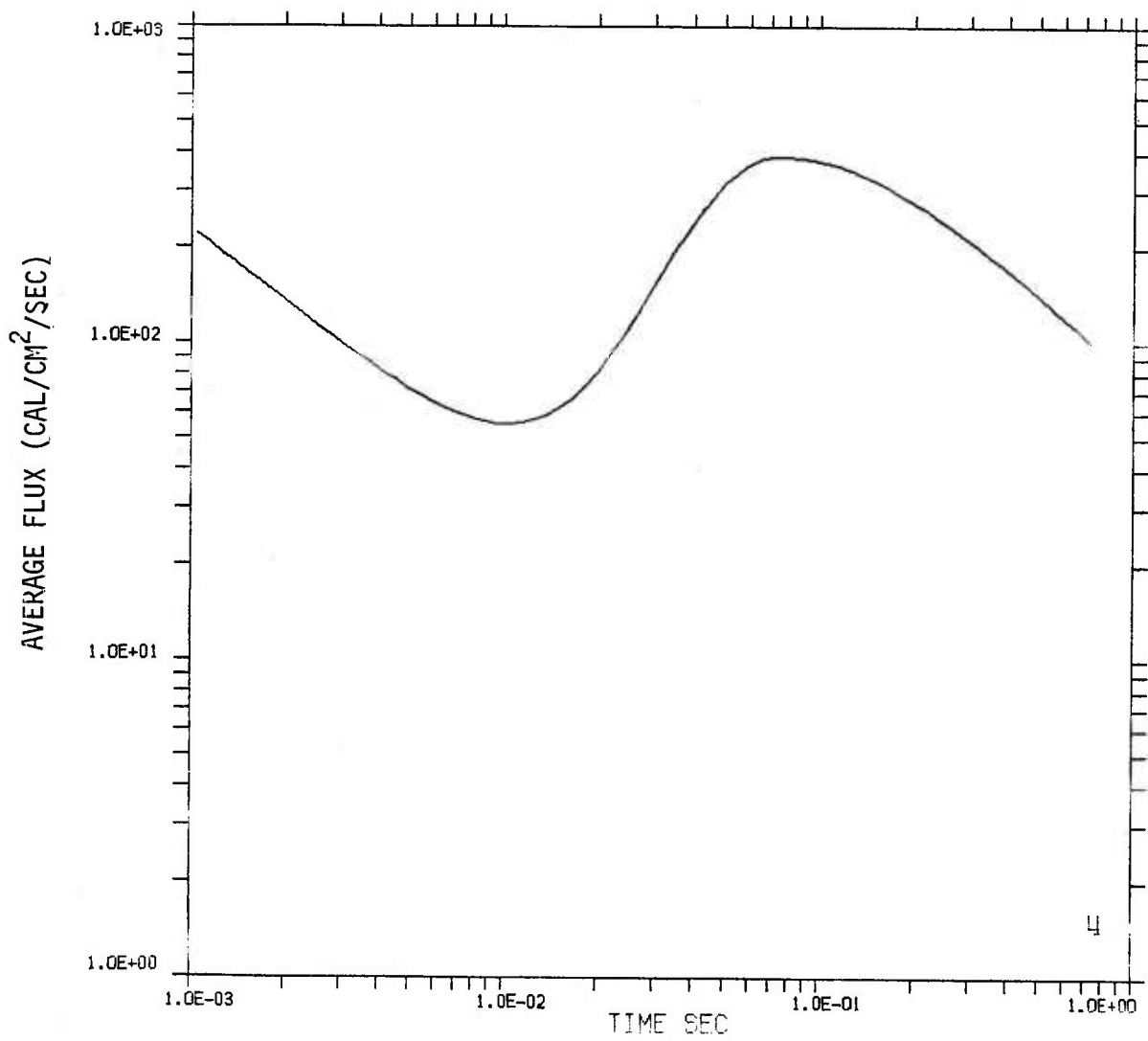


Figure 96. Average flux from 1 kt surface burst crossing detector with orientation 60 degrees at 152.4 meters ground range.

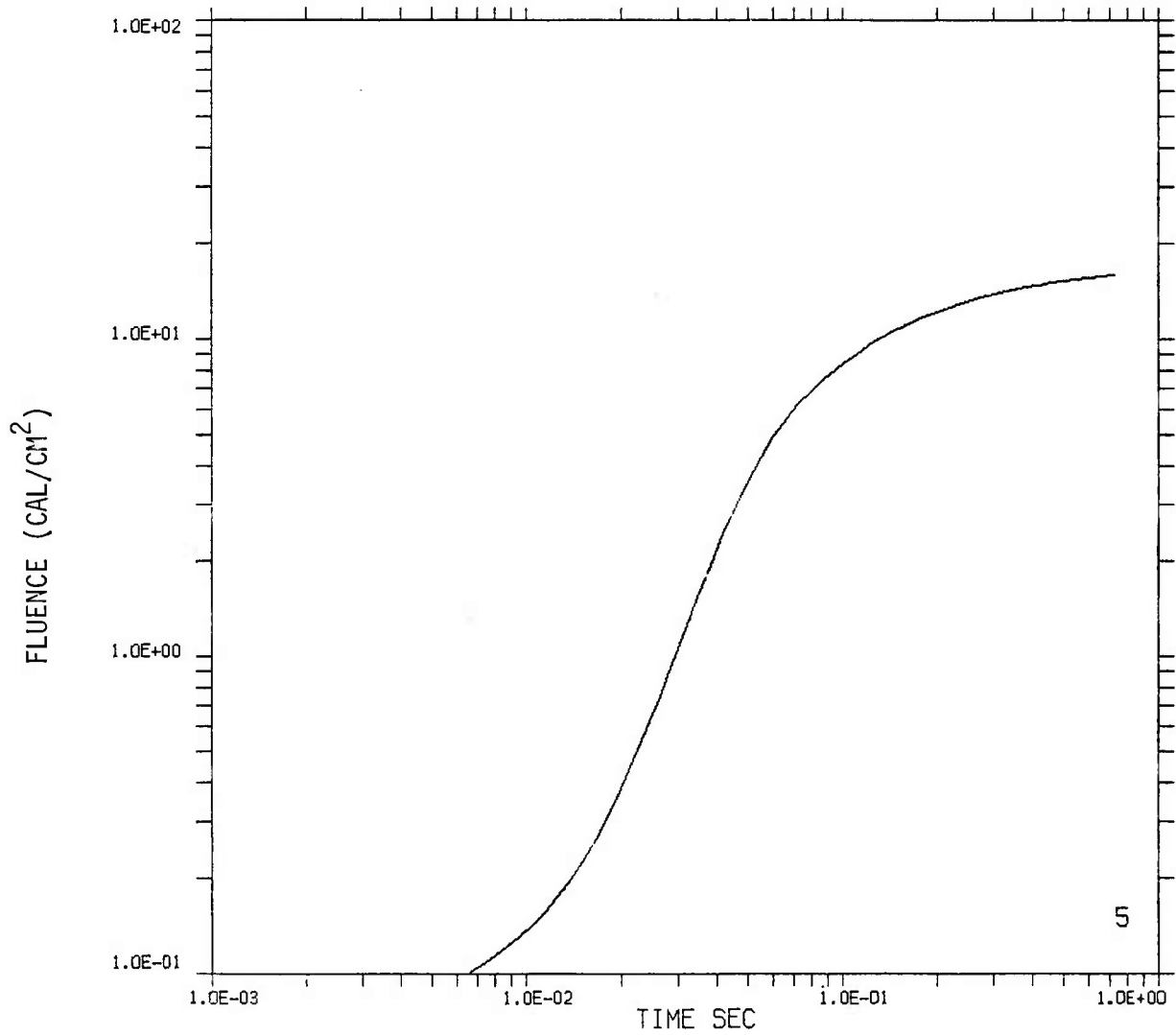


Figure 97. Fluence from 1 kt surface burst crossing detector with orientation 60 degrees at 304.8 meters ground range.

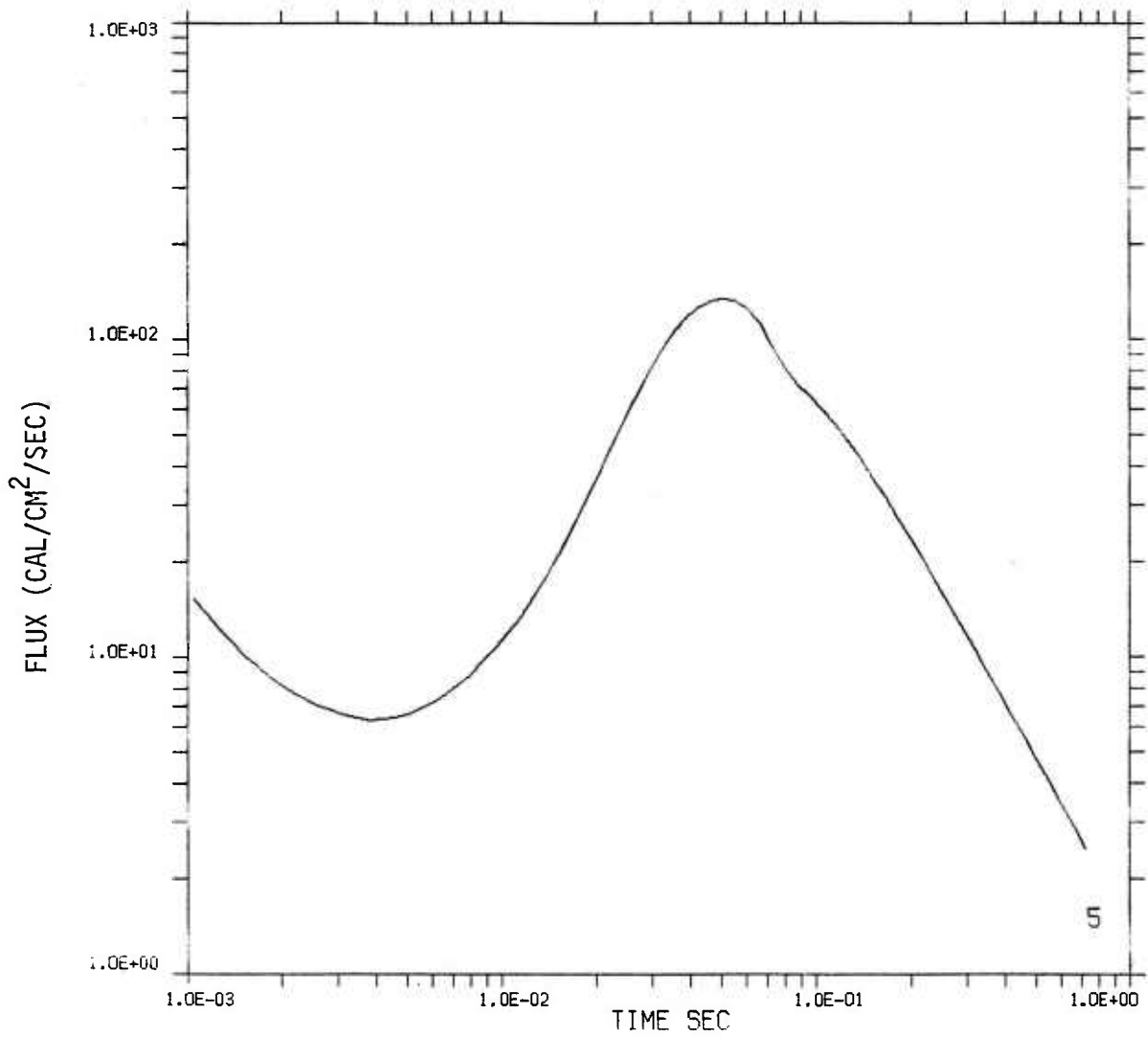


Figure 98. Flux from 1 kt surface burst crossing detector with orientation 60 degrees at 304.8 meters ground range.

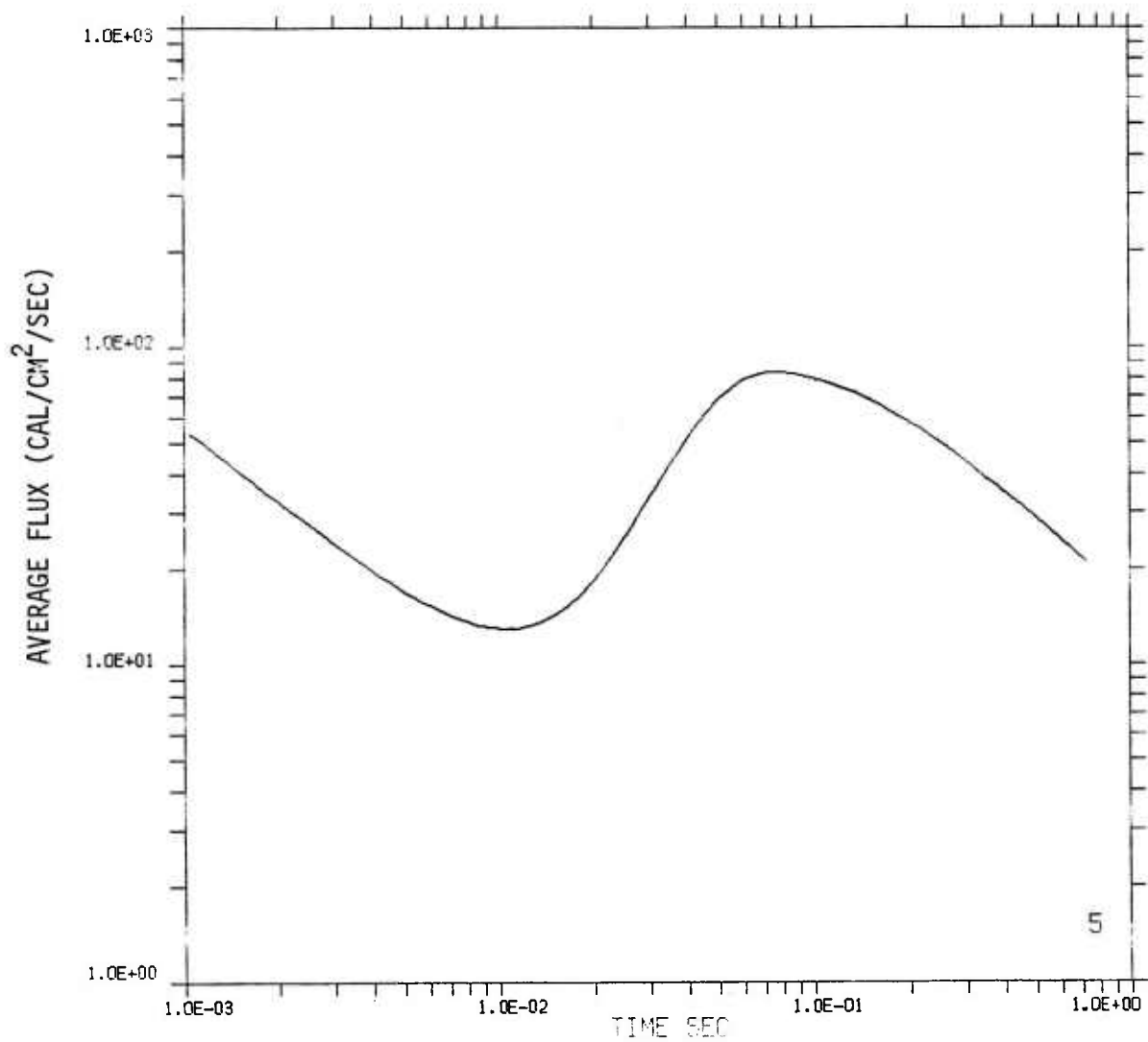


Figure 99. Average flux from 1 kt surface burst crossing detector with orientation 60 degrees at 304.8 meters ground range.

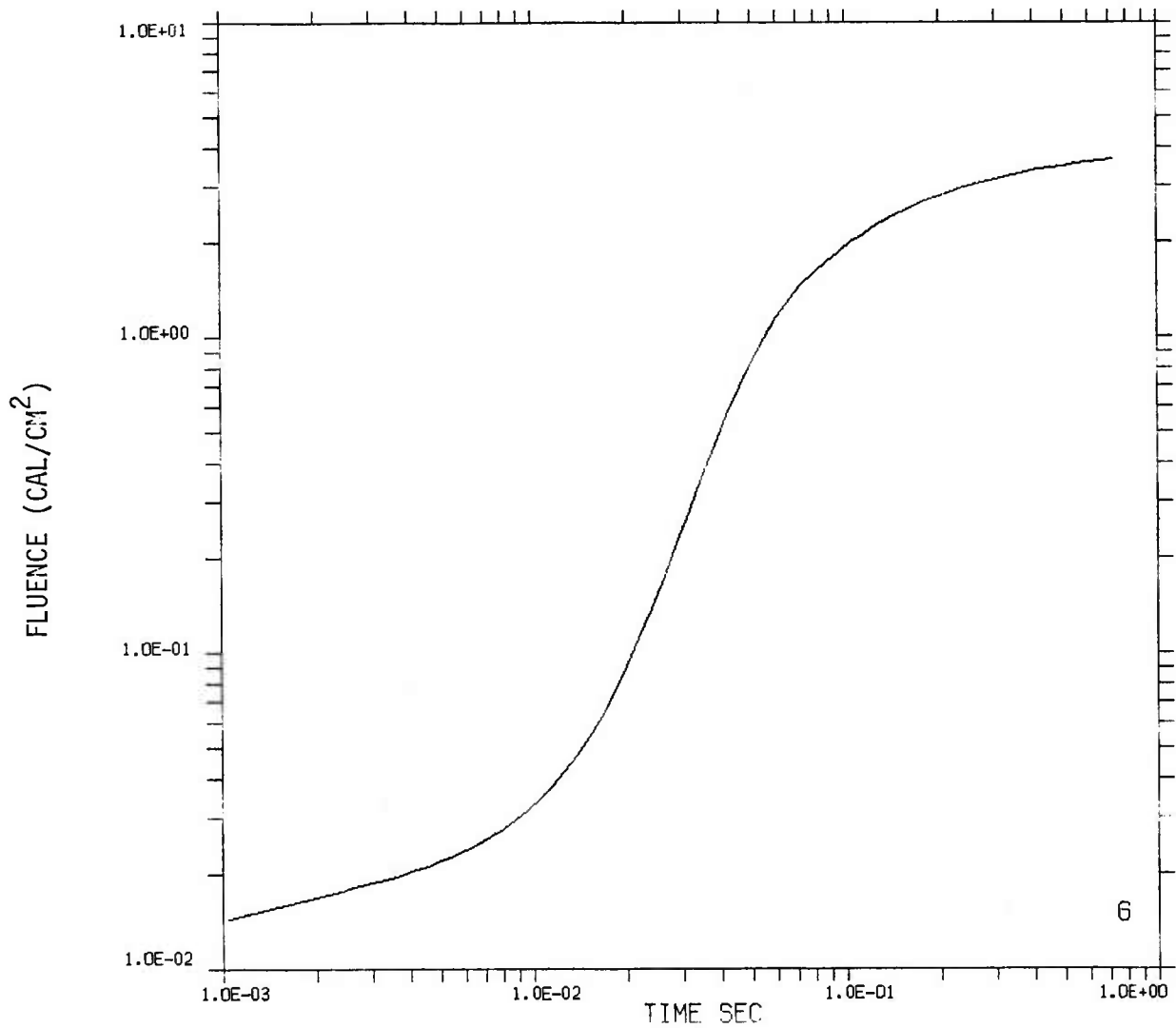


Figure 100. Fluence from 1 kt surface burst crossing detector with orientation 60 degrees at 609.6 meters ground range.

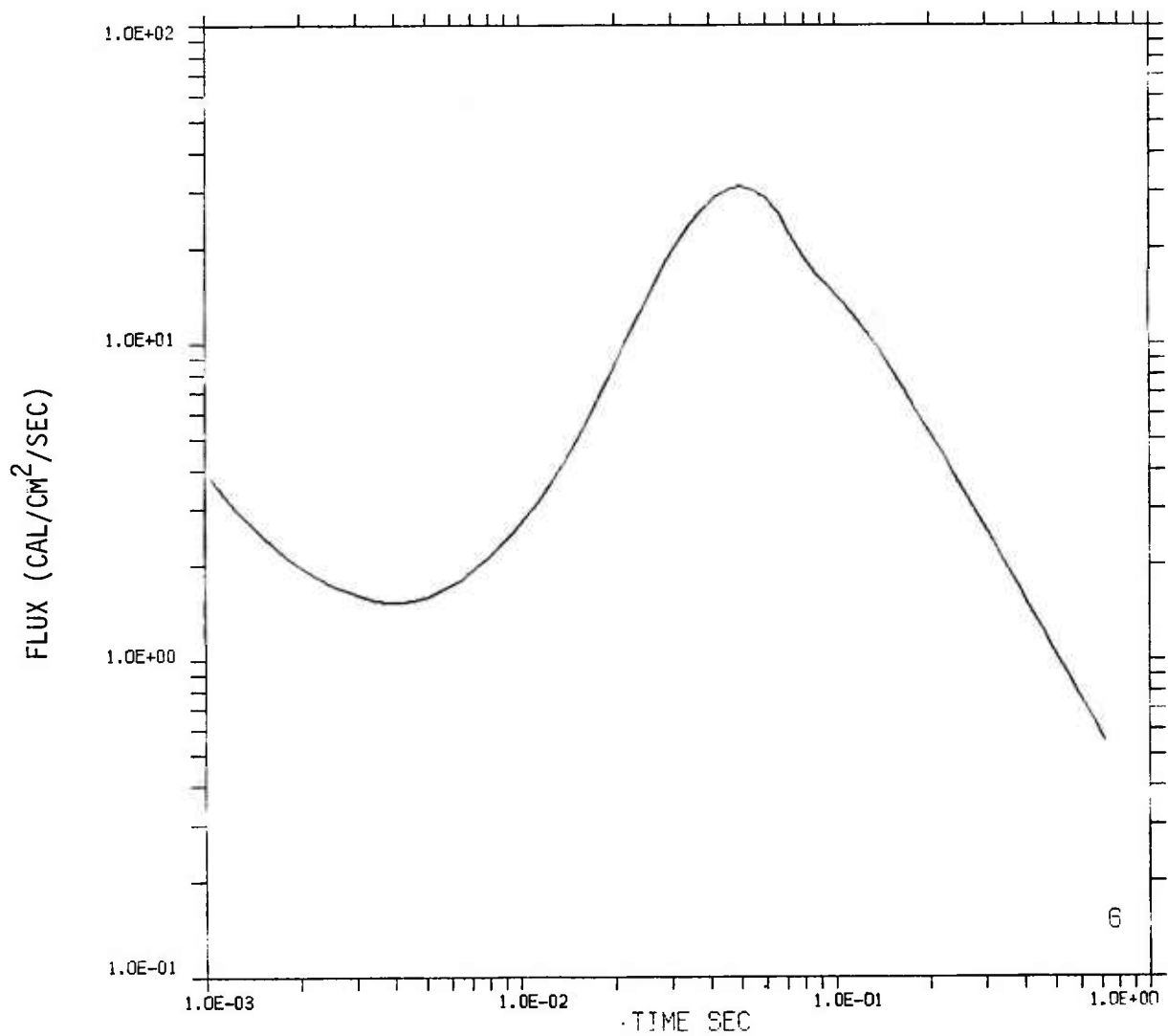


Figure 101. Flux from 1 kt surface burst crossing detector with orientation 60 degrees at 609.6 meters ground range.

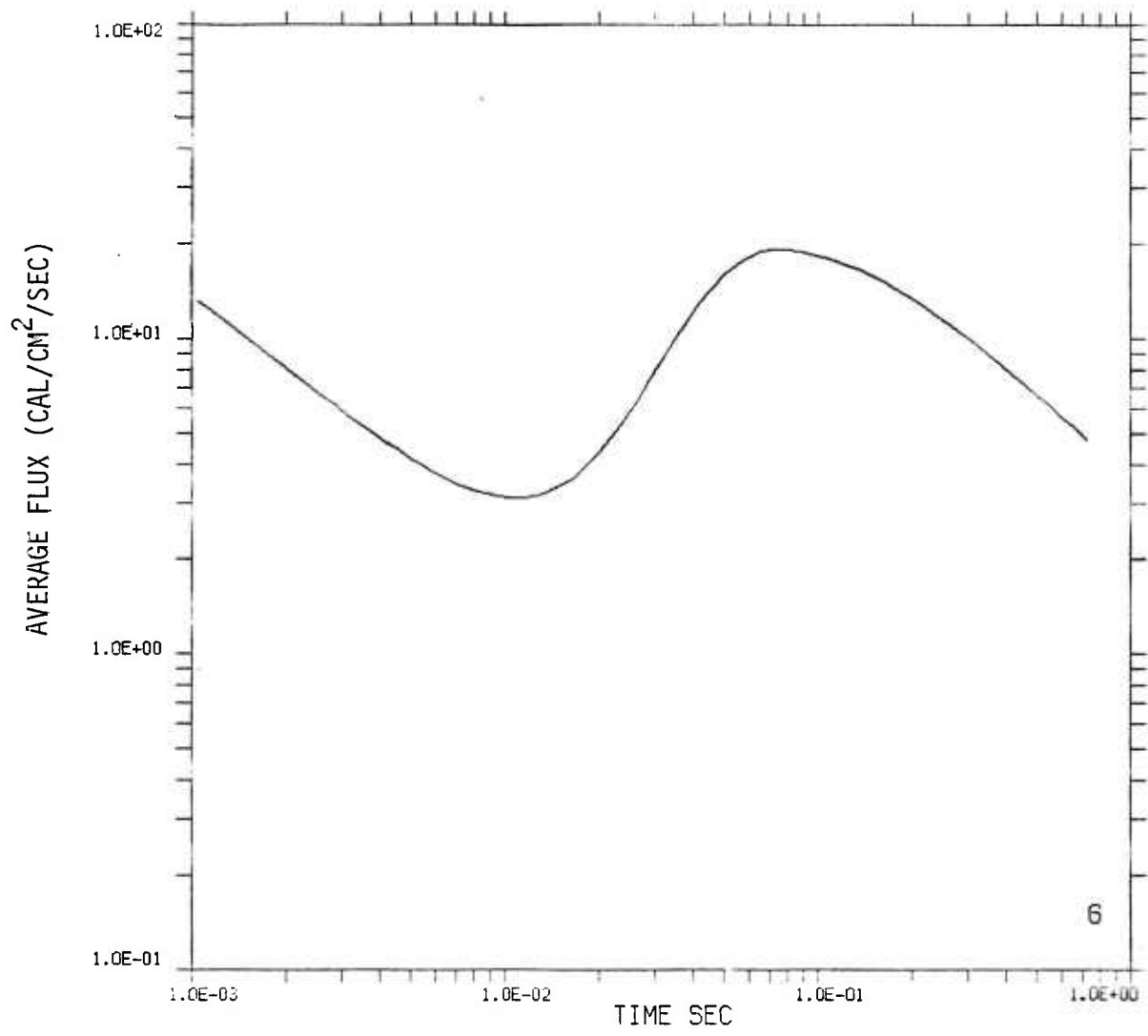


Figure 102. Average flux from 1 kt surface burst crossing detector with orientation 60 degrees at 609.6 meters ground range.

APPENDIX D

ESTIMATE OF THERMAL RADIATION FROM A 1 KILOTON NUCLEAR SURFACE BURST DETECTOR ELEVATION 90 DEGREES

This appendix contains plots for one elevation and consists of six sets of three figures. Each set corresponds to a particular range: 30.48, 60.96, 91.44, 152.4, 304.8, or 609.6 meters from ground zero. For each range fluence, flux, and average flux are presented as a function of time. Fluence is in units of cal-cm⁻², flux and average flux are in units of cal-cm⁻²-sec⁻¹.

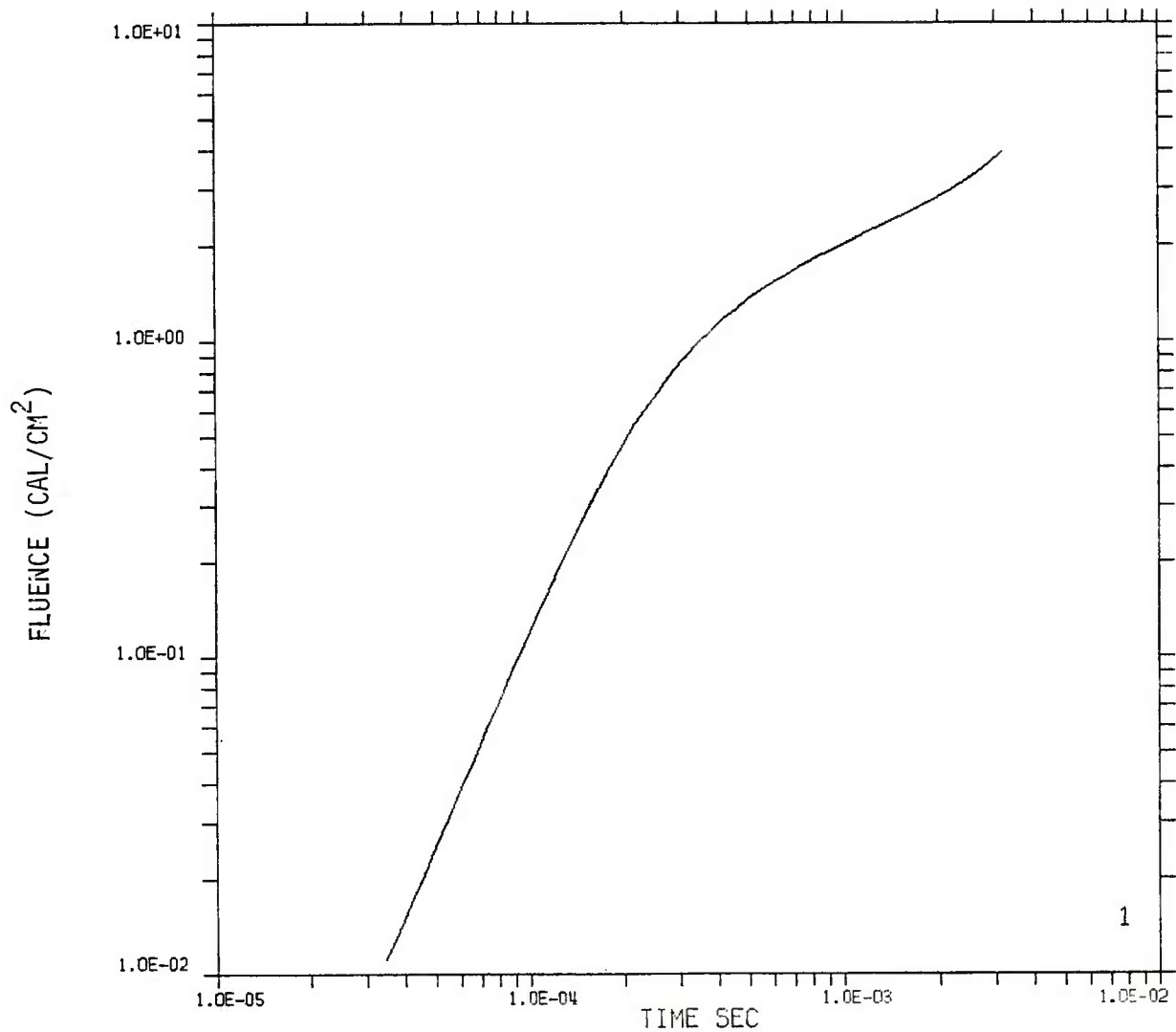


Figure 103. Fluence from 1 kt surface burst crossing detector with elevation 90 degrees at 30.48 meters ground range.

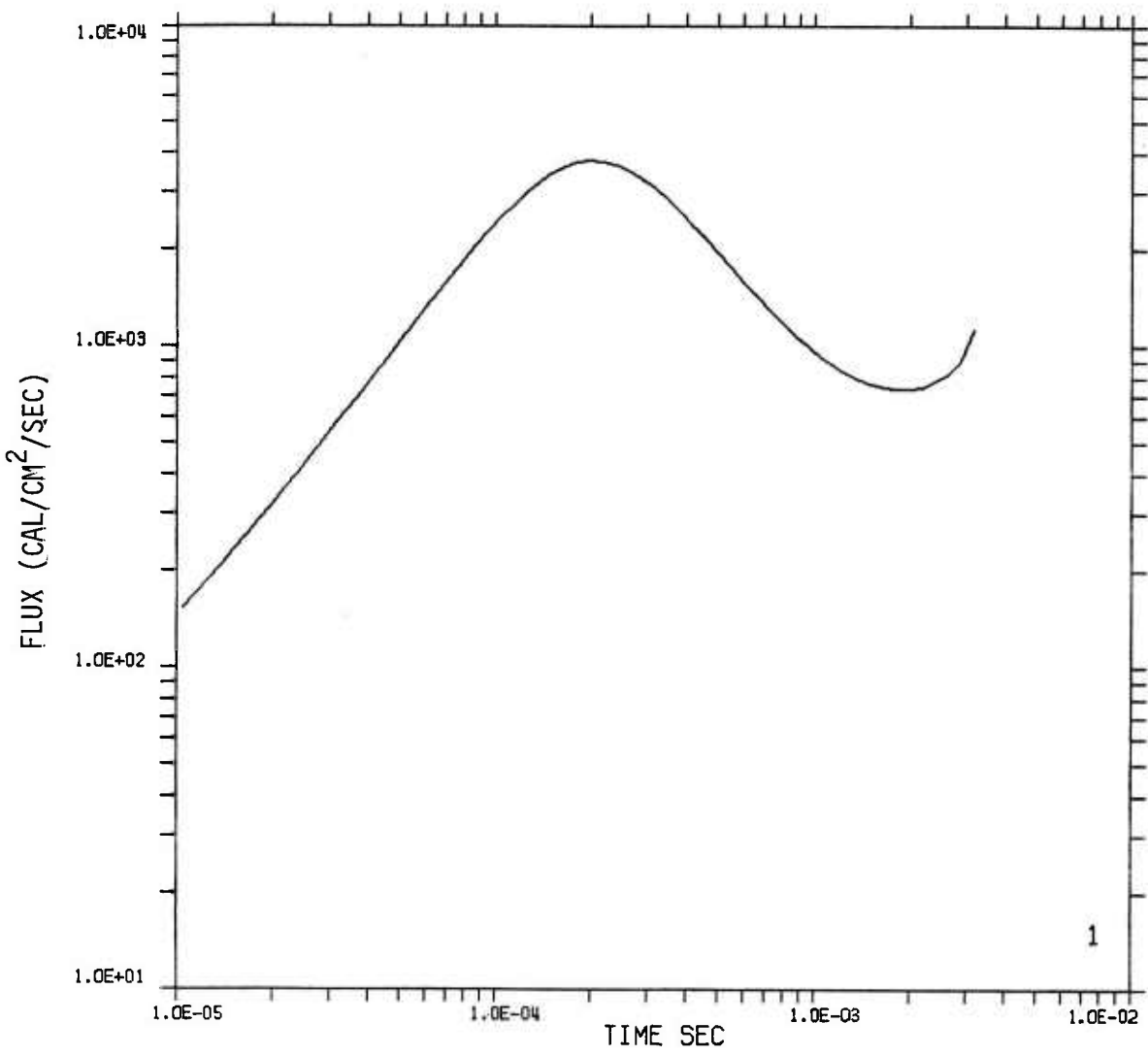


Figure 104. Flux from 1 kt surface burst crossing detector with orientation 90 degrees at 30.48 meters ground range.

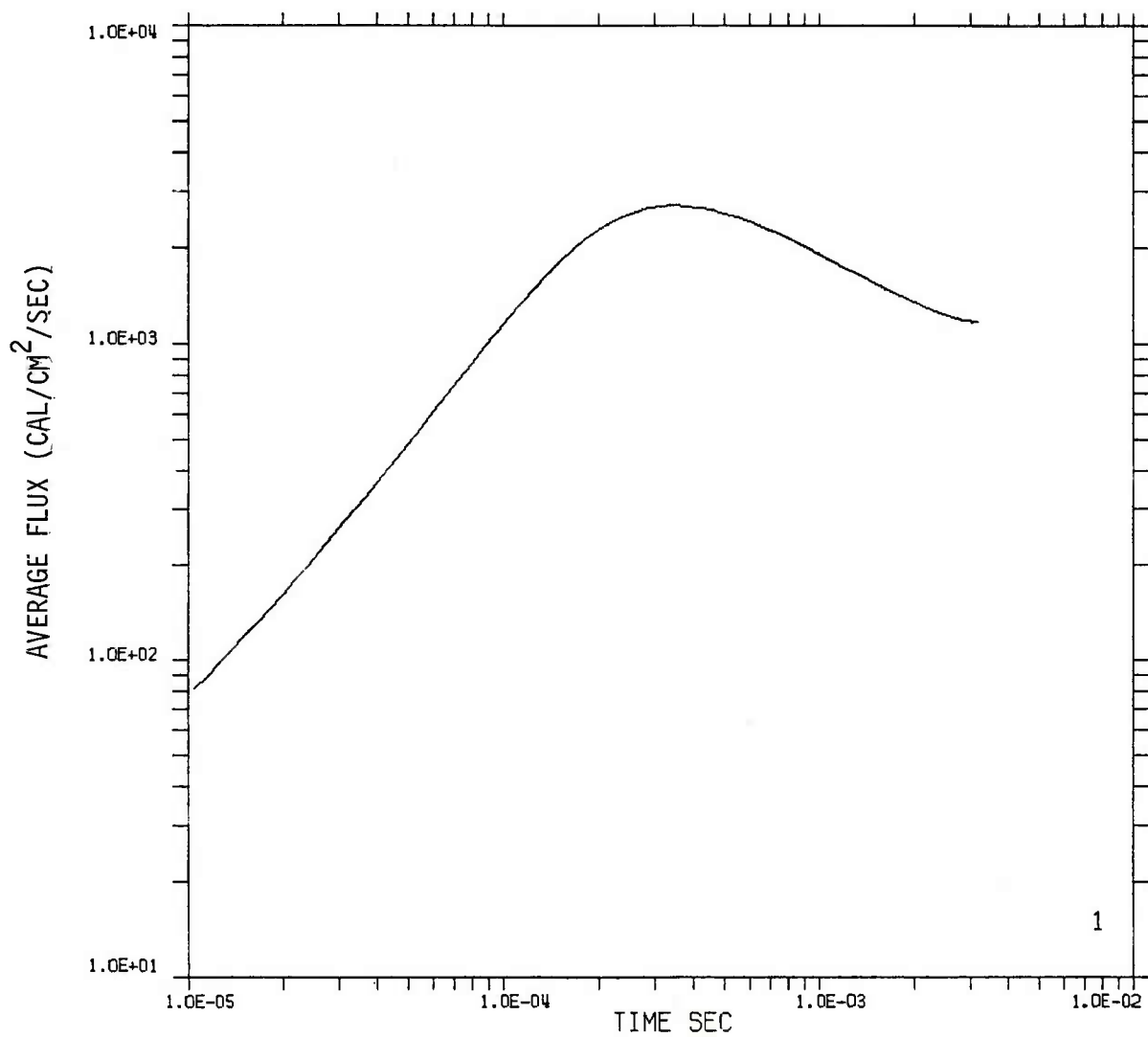


Figure 105. Average flux from 1 kt surface burst crossing detector with orientation 90 degrees at 30.48 meters ground range.

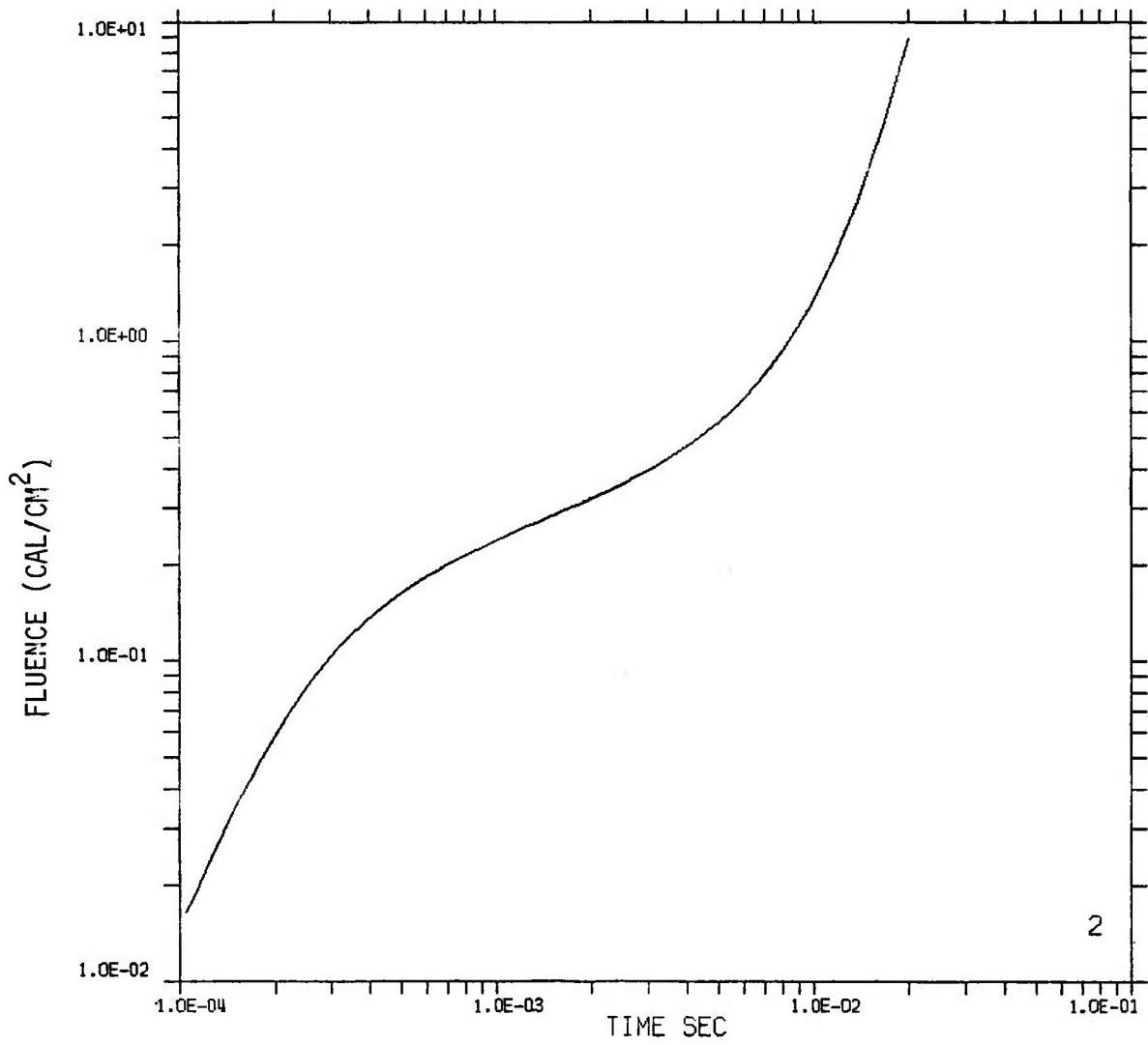


Figure 106. Fluence from 1 kt surface burst crossing detector with orientation 90 degrees at 60.96 meters ground range.

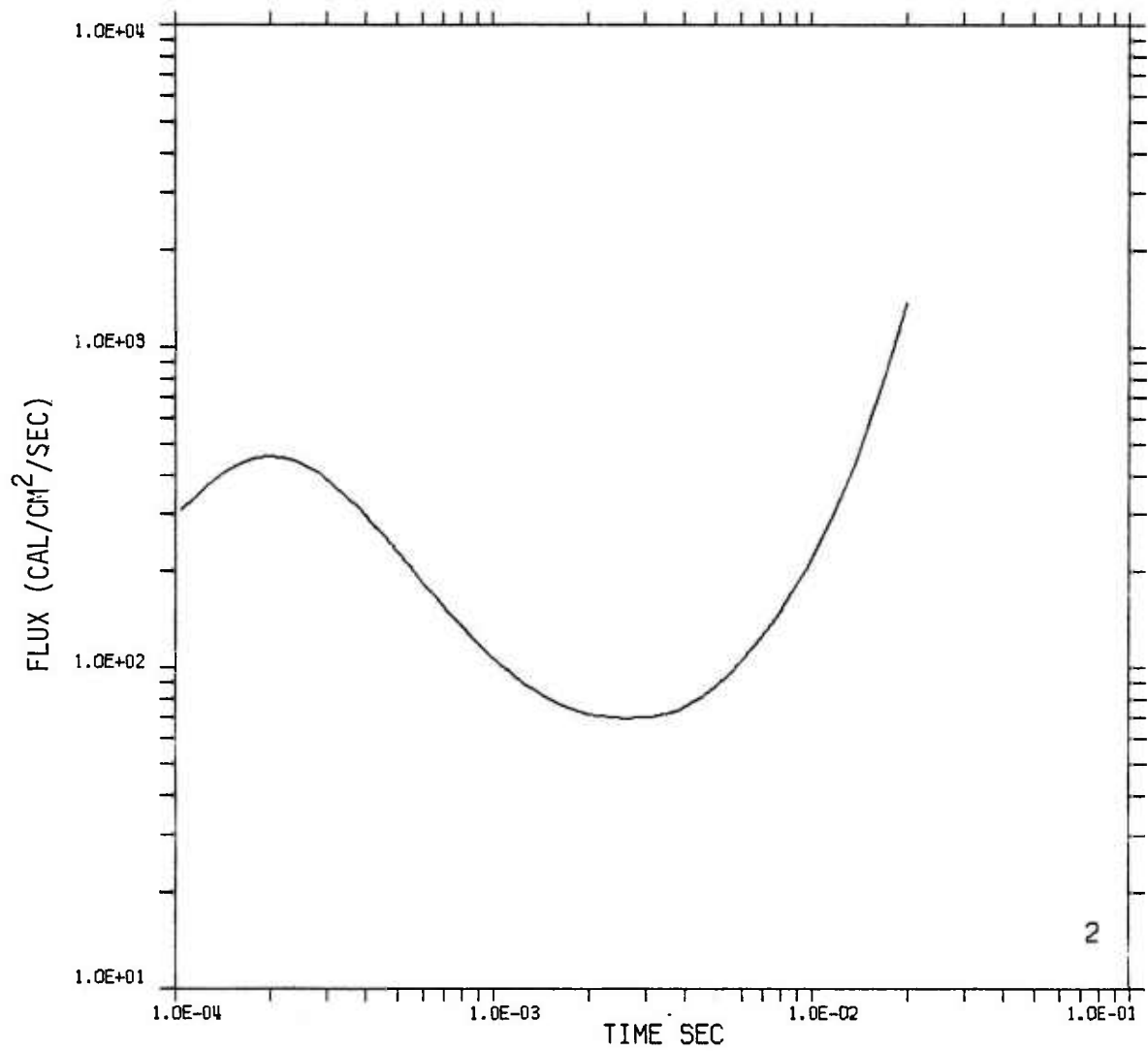


Figure 107. Flux from 1 kt surface burst crossing detector with orientation 90 degrees at 60.96 meters ground range.

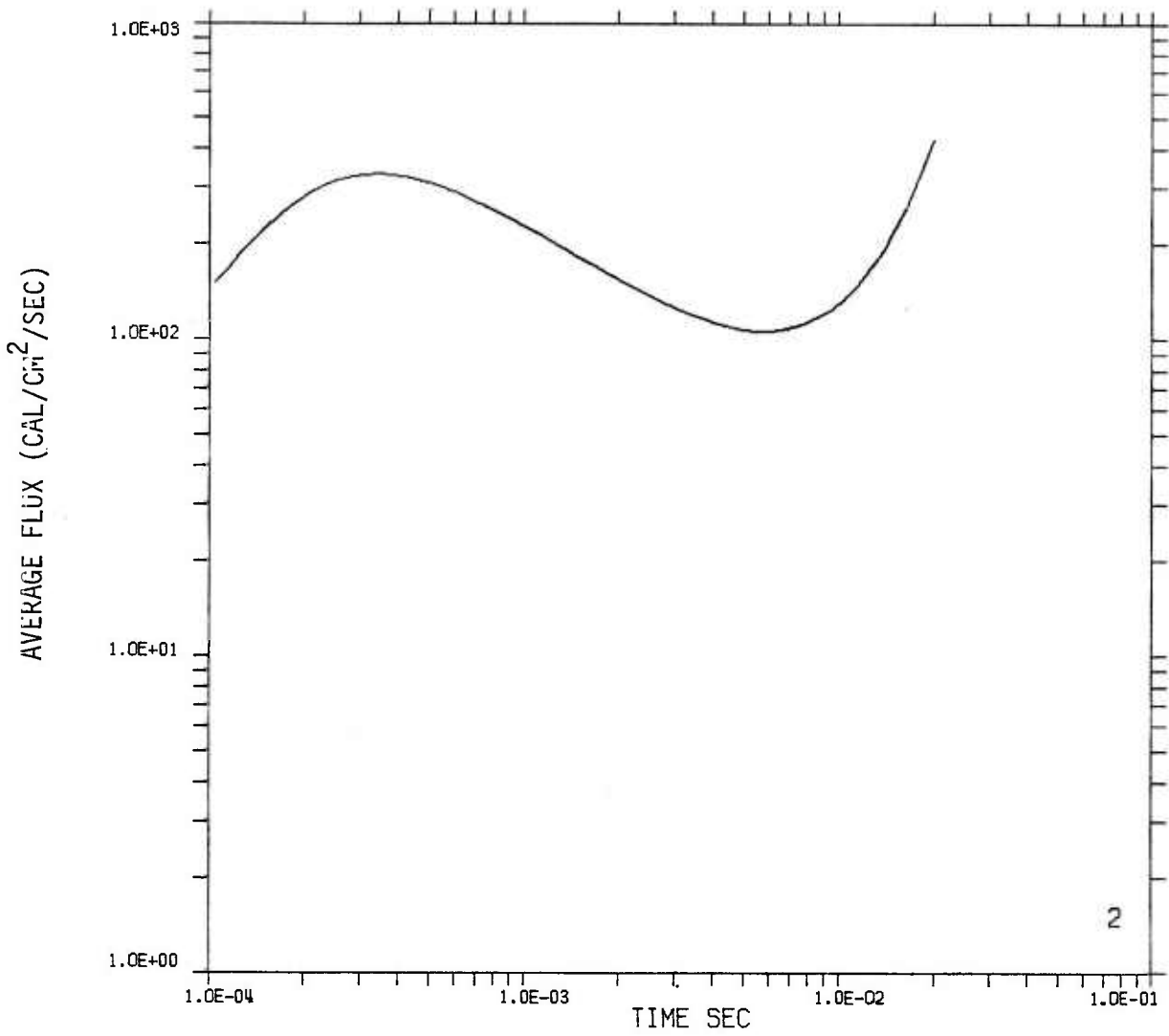


Figure 108. Average flux from 1 kt surface burst crossing detector with orientation 90 degrees at 60.96 meters ground range.

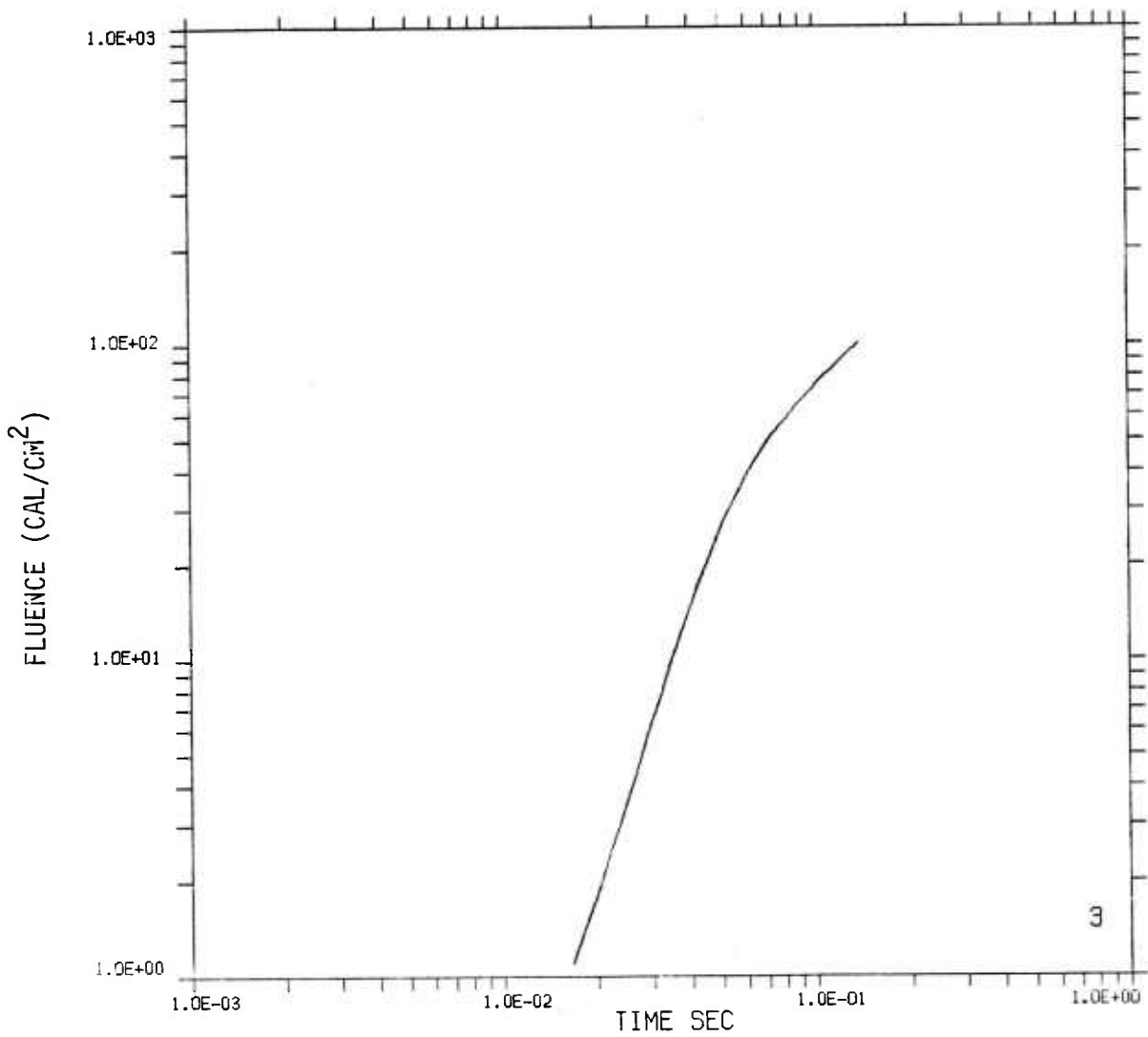


Figure 109. Fluence from 1 kt surface burst crossing detector with orientation 90 degrees at 91.44 meters ground range.

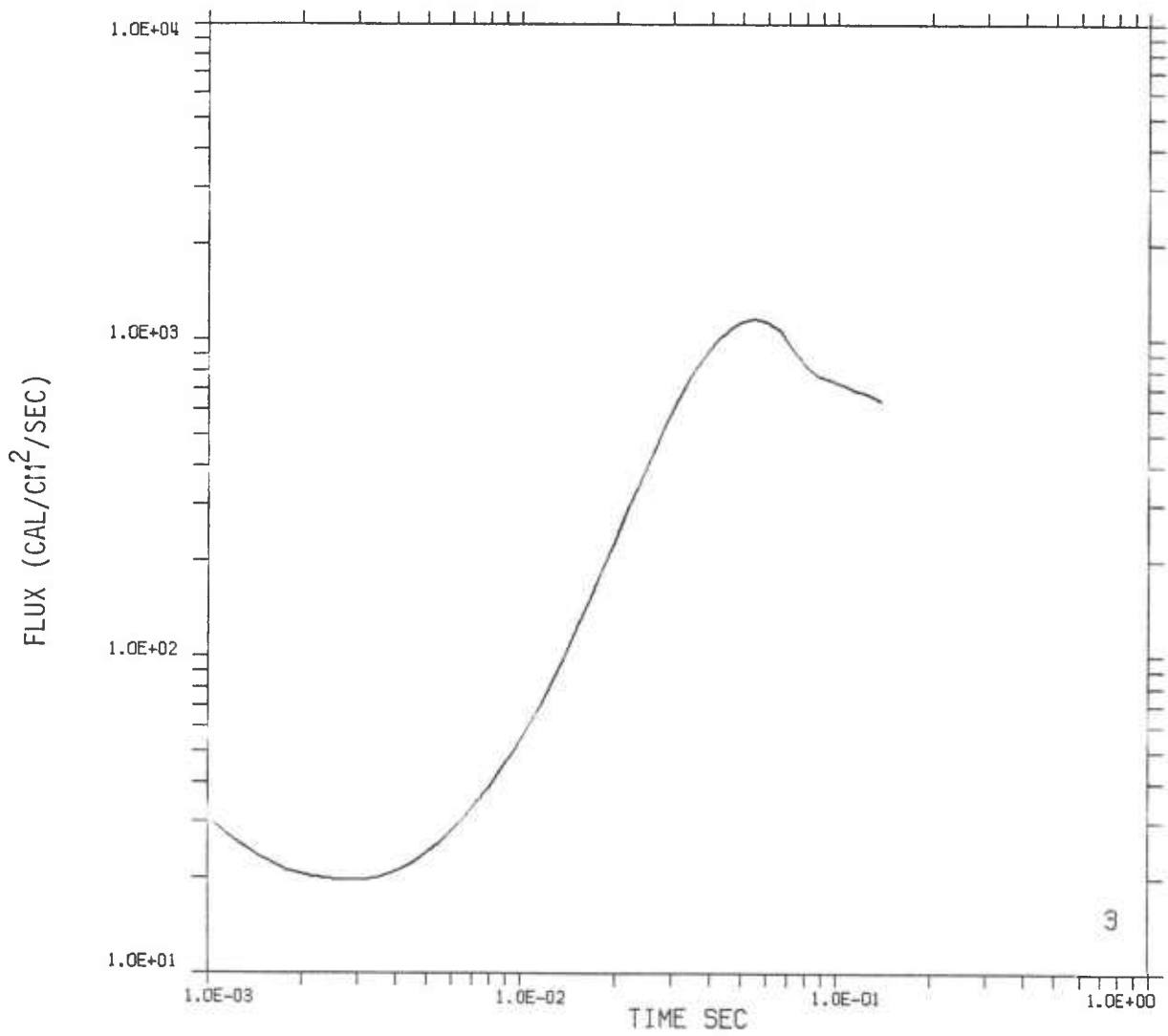


Figure 110. Flux from 1 kt surface burst crossing detector with orientation 90 degrees at 91.44 meters ground range.

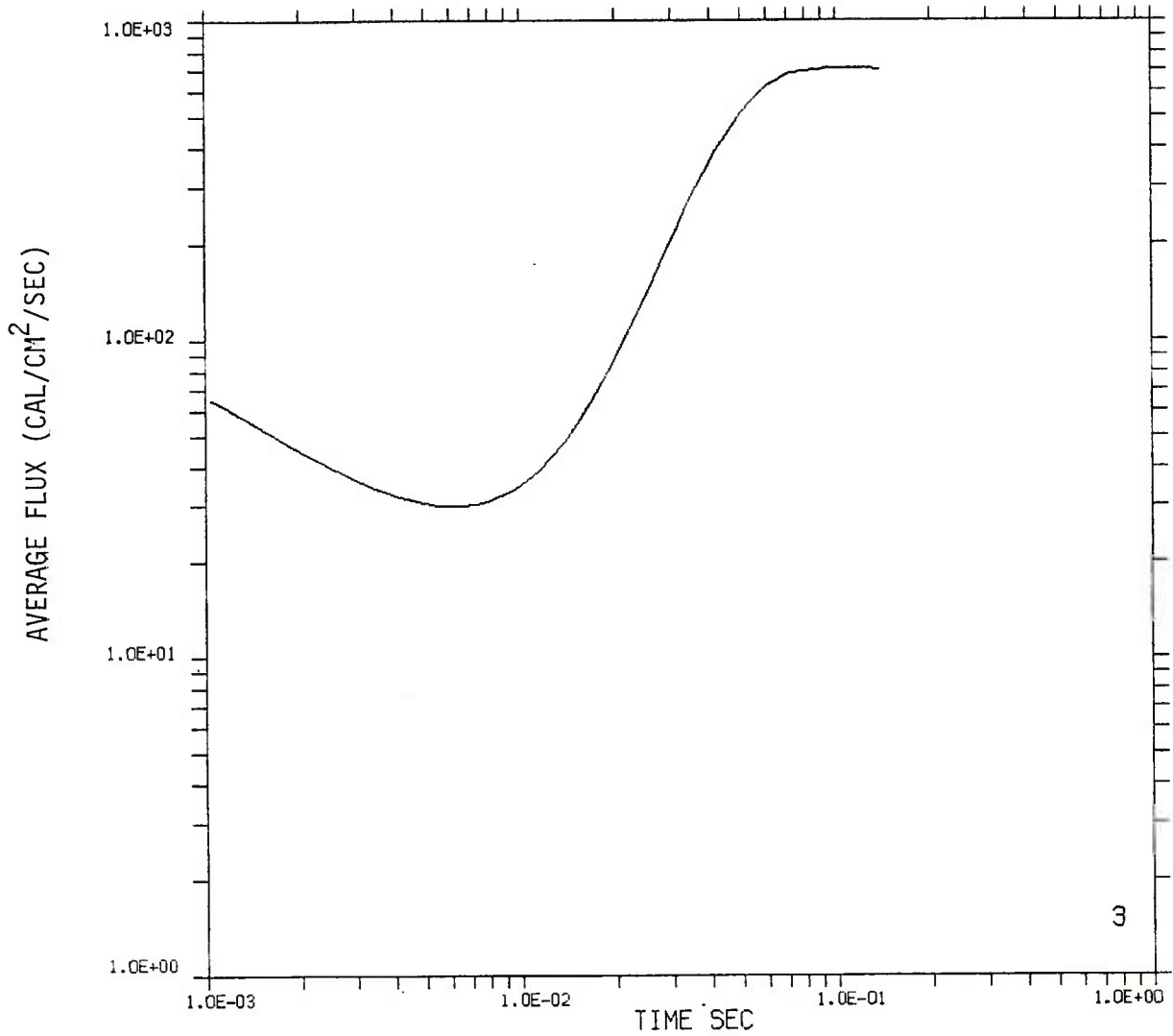


Figure 111. Average flux from 1 kt surface burst crossing detector with orientation 90 degrees at 91.44 meters ground range.

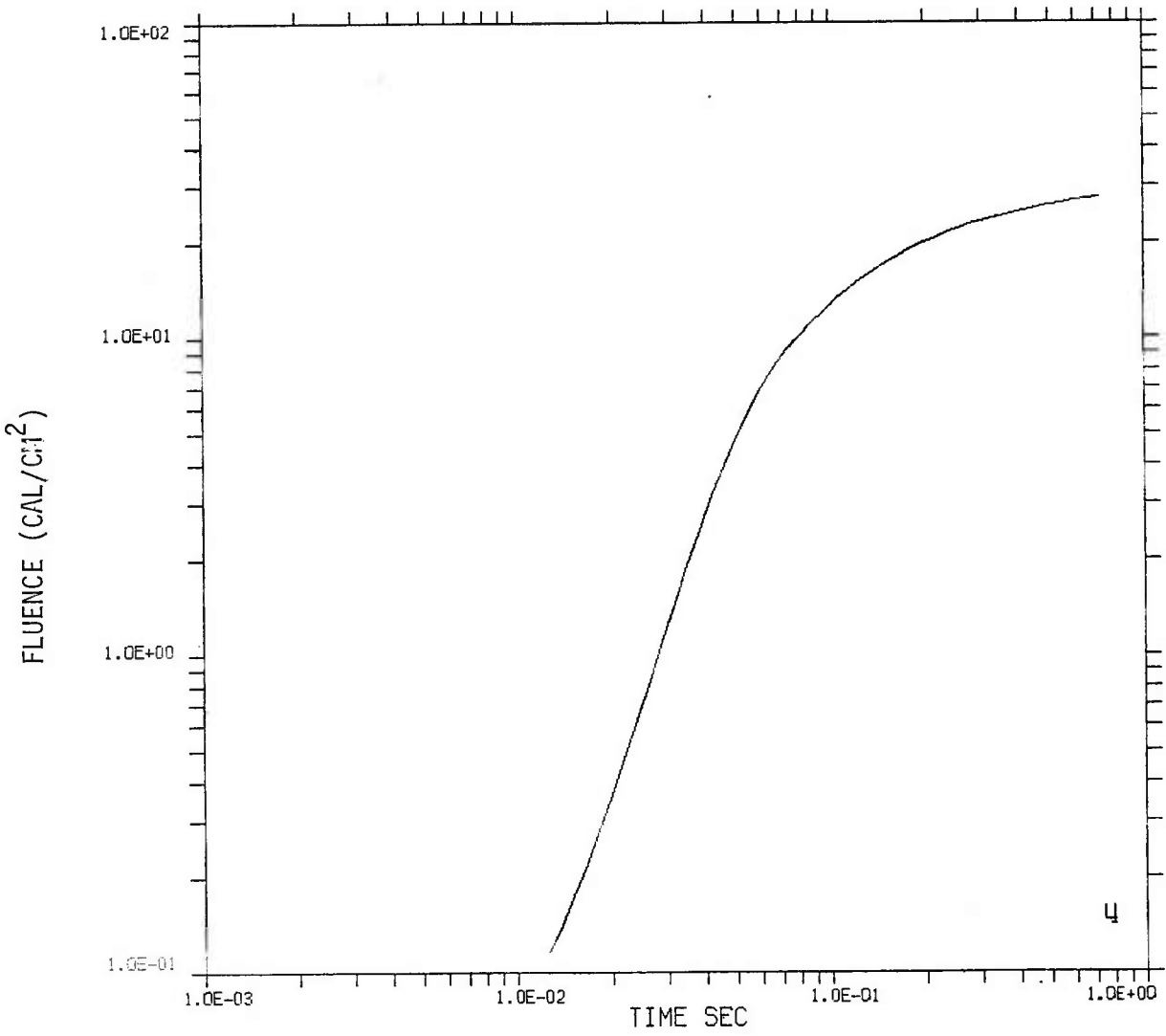


Figure 112. Fluence from 1 kt surface burst crossing detector with orientation 90 degrees at 152.4 meters ground range.

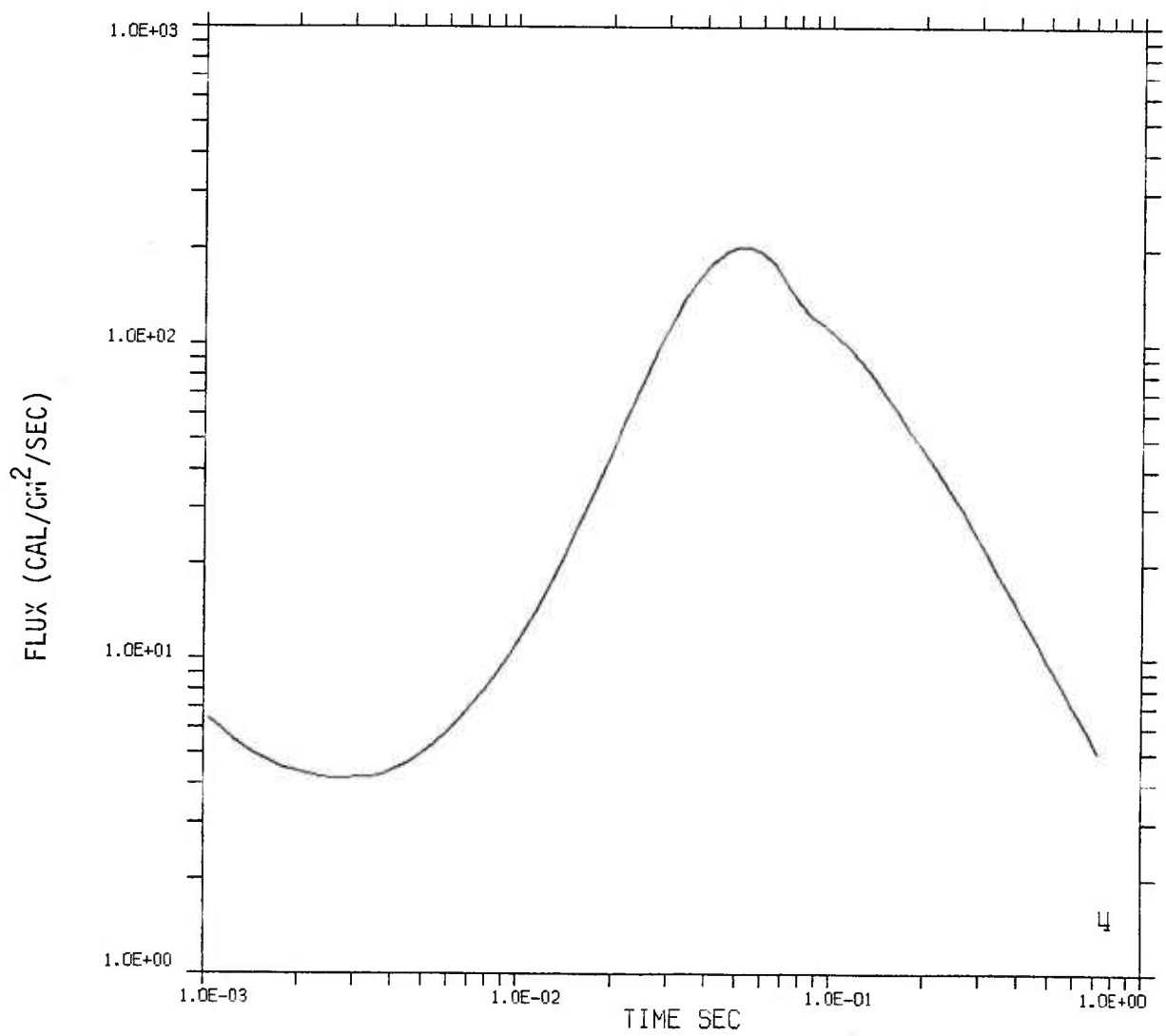


Figure 113. Flux from 1 kt surface burst crossing detector with orientation 90 degrees at 152.4 meters ground range.

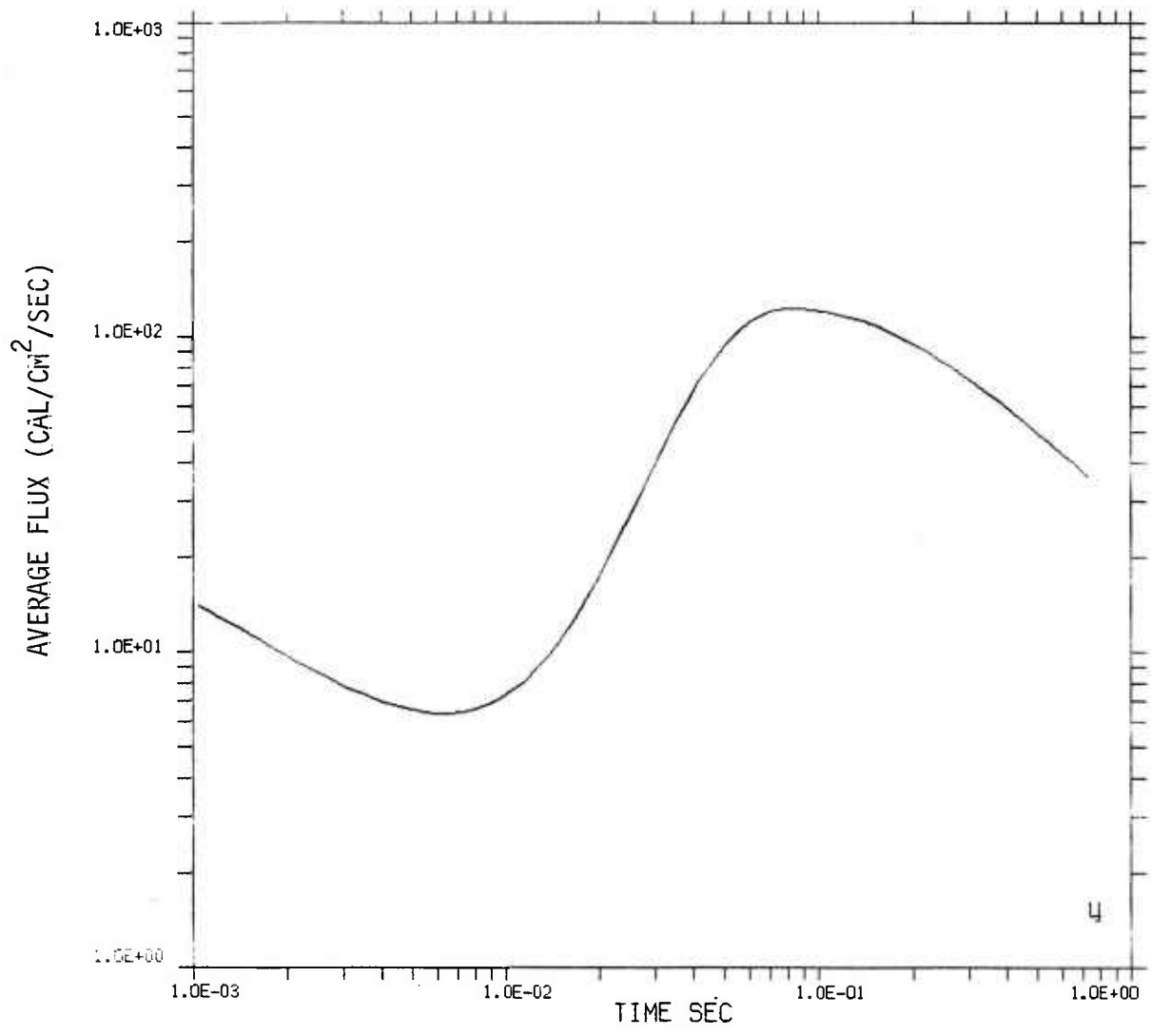


Figure 114. Average flux from 1 kt surface burst crossing detector with orientation 90 degrees at 152.4 meters ground range.

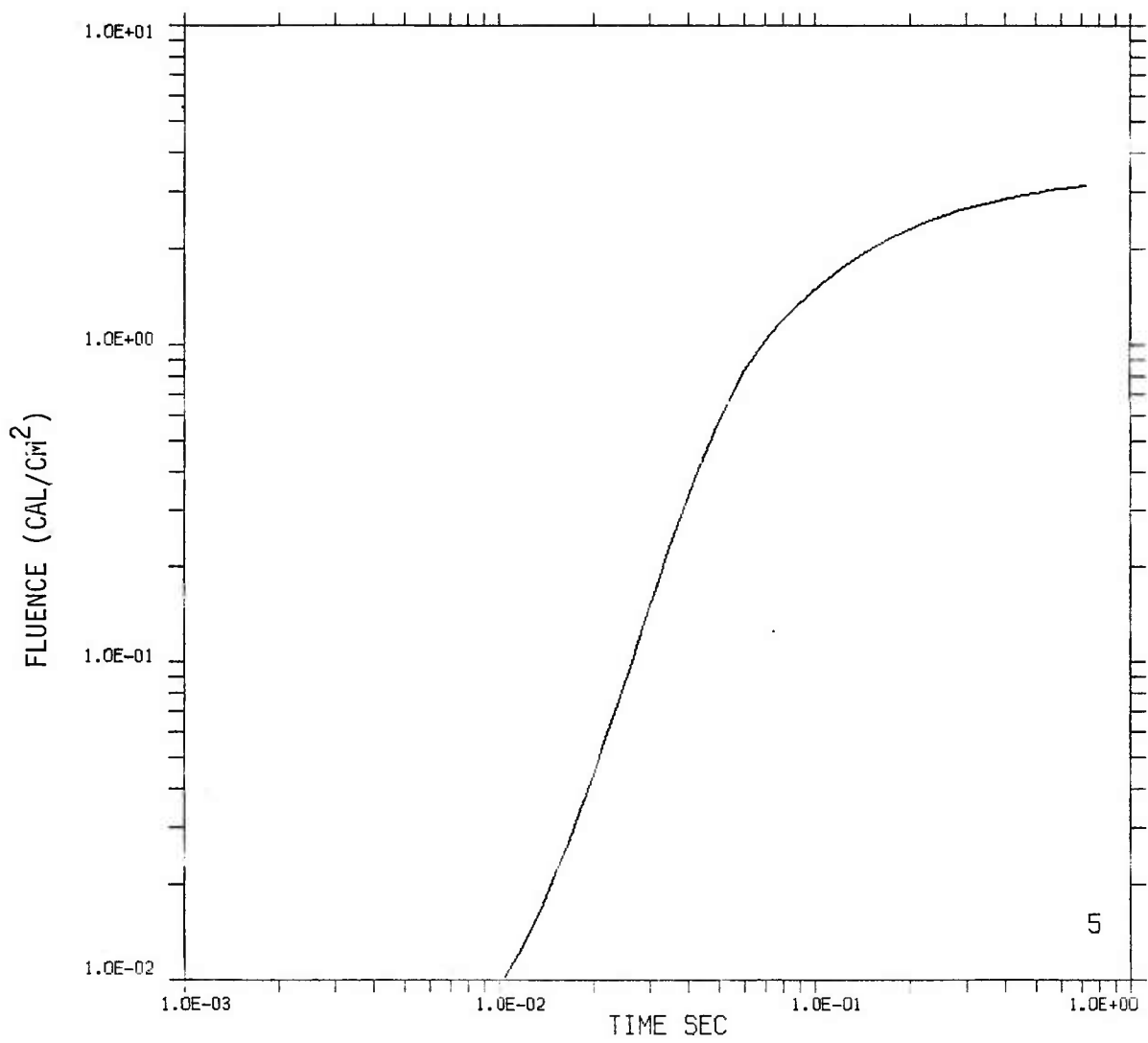


Figure 115. Fluence from 1 kt surface burst crossing detector with orientation 90 degrees at 304.8 meters ground range.

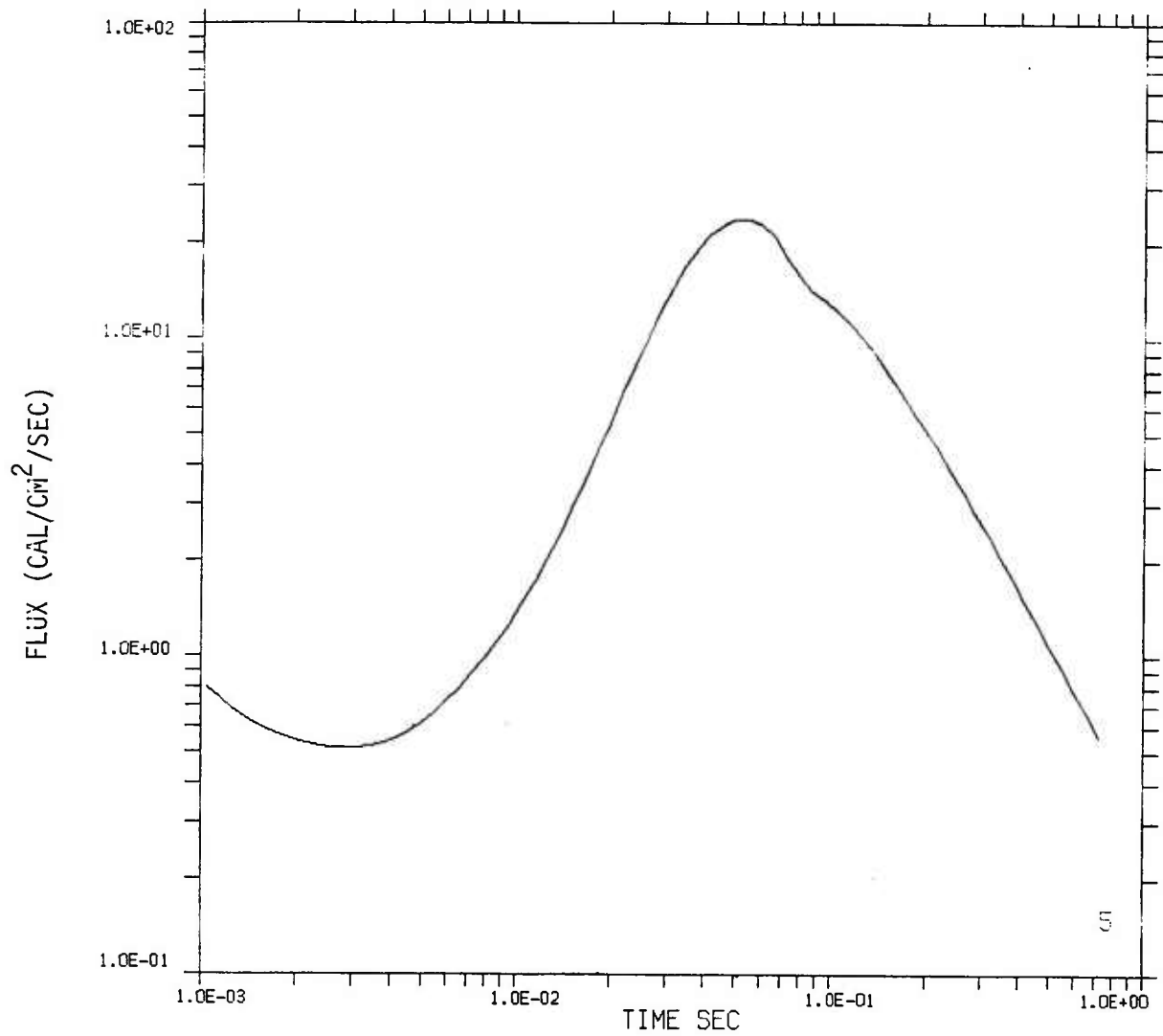


Figure 116. Flux from 1 kt surface burst crossing detector with orientation 90 degrees at 304.8 meters ground range.

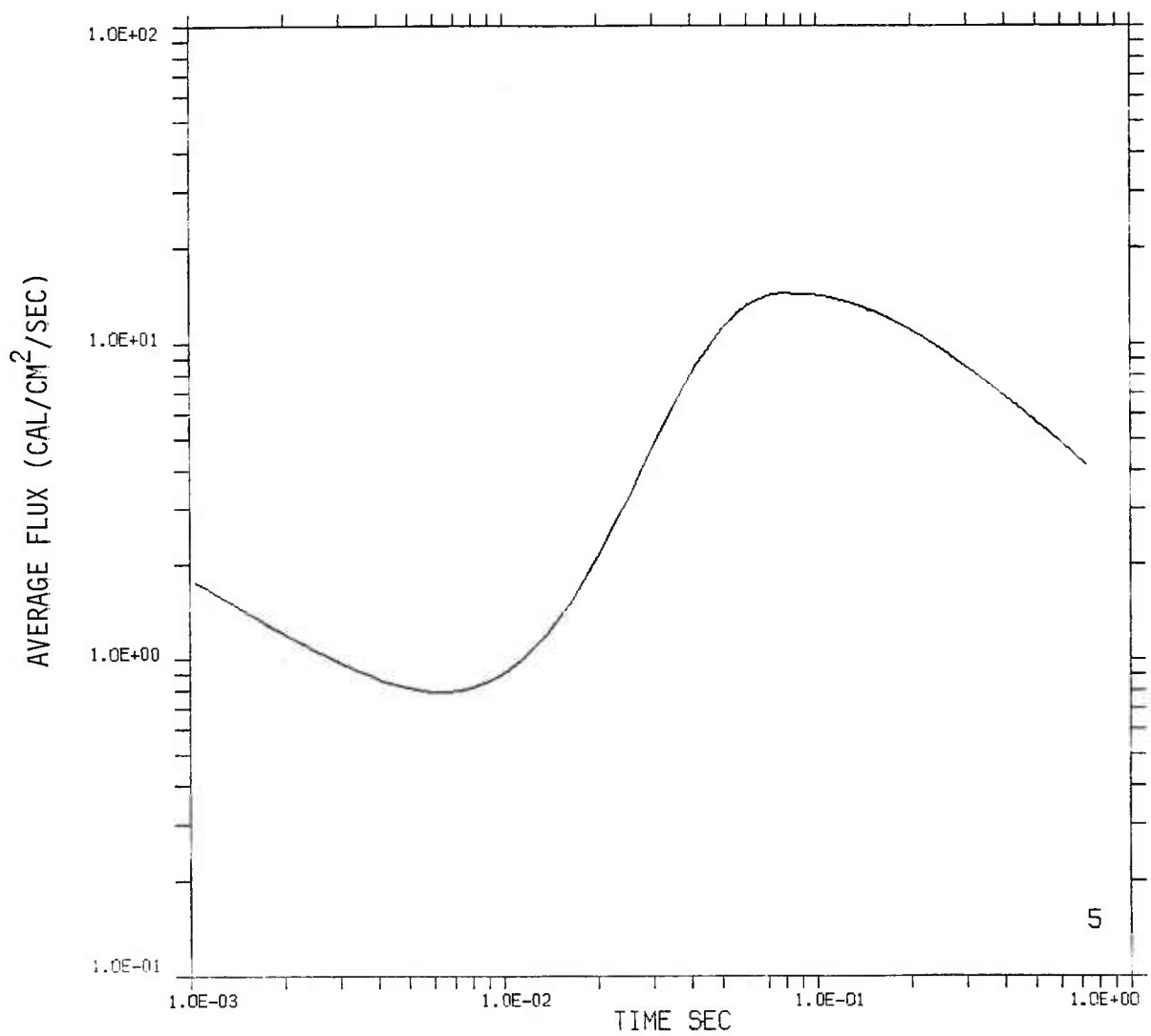


Figure 117. Average flux from 1 kt surface burst crossing detector with orientation 90 degrees at 304.8 meters ground range.

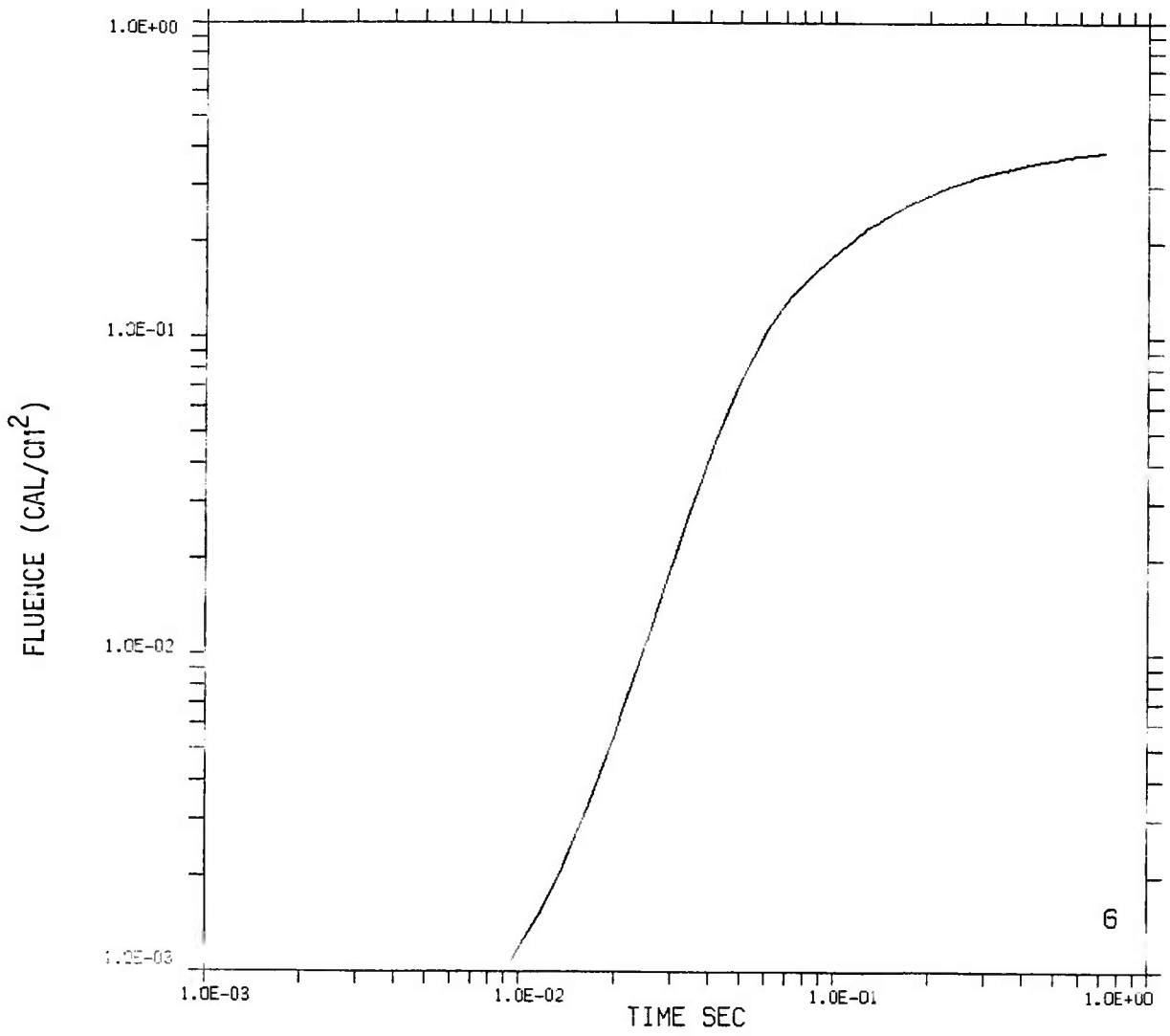


Figure 118. Fluence from 1 kt surface burst crossing detector with orientation 90 degrees at 609.6 meters ground range.

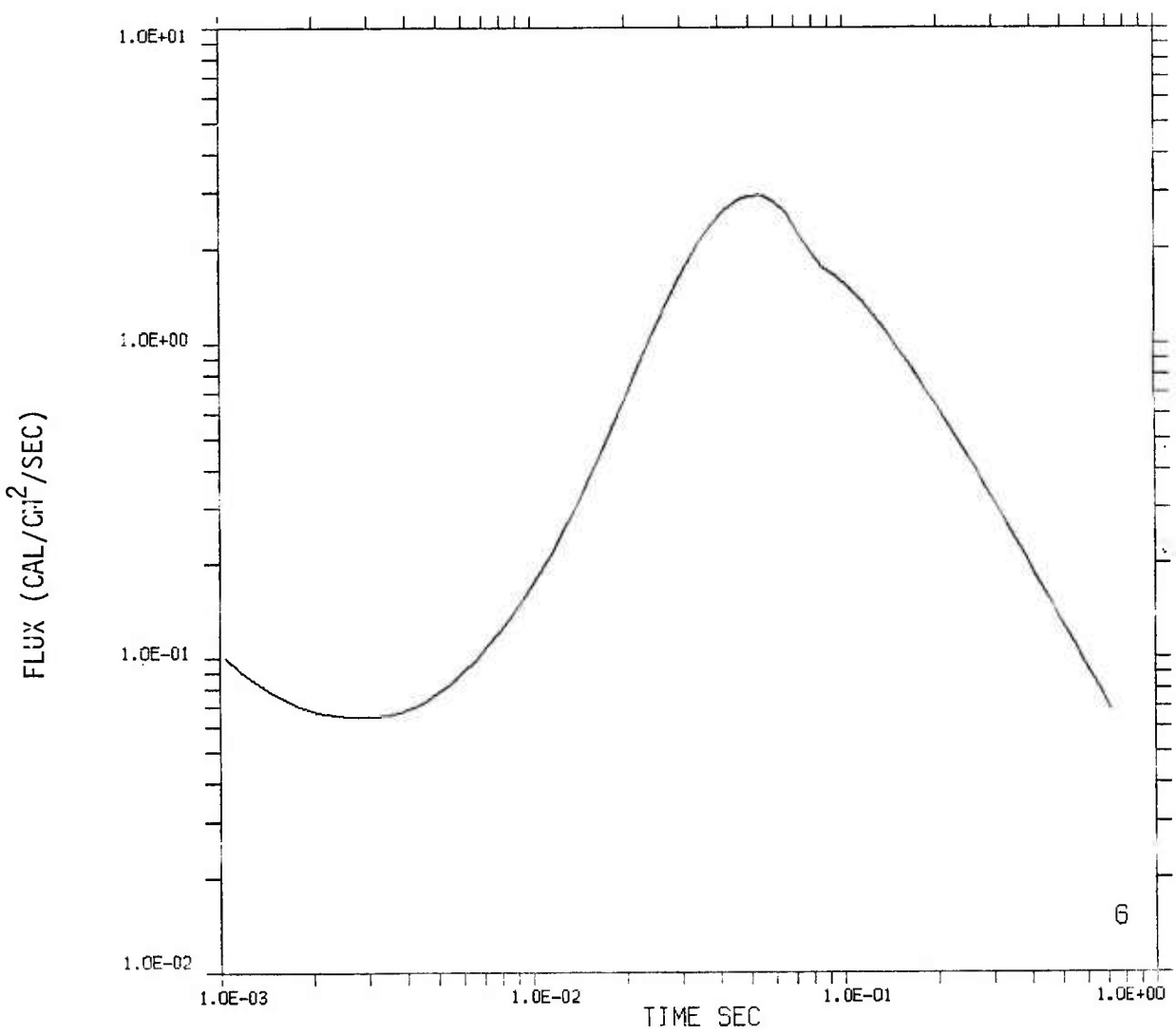


Figure 119. Flux from 1 kt surface burst crossing detector with orientation 90 degrees at 609.6 meters ground range.

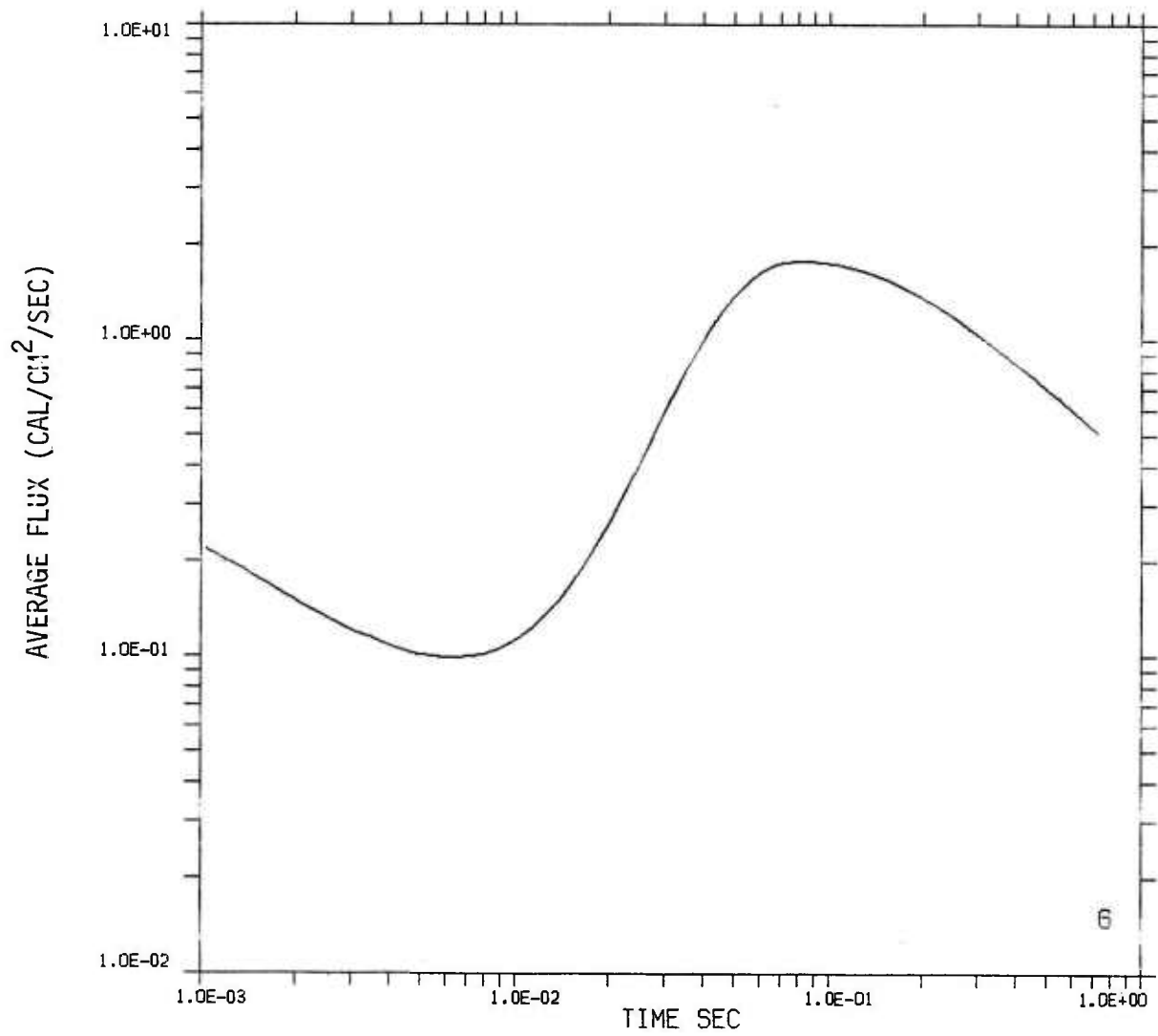


Figure 120. Average flux from 1 kt surface burst crossing detector with orientation 90 degrees at 609.6 meters ground range.

DISTRIBUTION LIST

DEPARTMENT OF DEFENSE

Assistant Secretary of Defense
Comm, Cmd, Cont & Intell
ATTN: Principal DASD (C3I) H. Van Trees

Assistant to the Secretary of Defense
Atomic Energy
ATTN: Executive Assistant

Defense Advanced Rsch Proj Agency
ATTN: PMO
ATTN: TIO
ATTN: DIR (Strat Tech Off)
ATTN: NMRO
ATTN: NMRO, G. Bulin
ATTN: H. Winsor

Defense Communications Agency
ATTN: Code 670, R. Lipp
ATTN: Code 510

Defense Electronic Supply Center
ATTN: DEFC-ESA

Defense Intelligence Agency
ATTN: RDS-3A
ATTN: DB-4C2
ATTN: DB-4C

Defense Nuclear Agency
ATTN: STSP
ATTN: SPAS
ATTN: RAAE, H. Fitz, Jr
ATTN: NATA
ATTN: STRA
ATTN: SPSS
ATTN: STNA
ATTN: NATD
2 cy ATTN: SPTD
4 cy ATTN: TITL
4 cy ATTN: RAAE, W. McKechnie

Defense Technical Information Center
12 cy ATTN: DD

Department of Defense Explo Safety Board
ATTN: Chairman

Field Command
Defense Nuclear Agency
ATTN: FCTMD
ATTN: FCPR
ATTN: FCTMOT
ATTN: FCTMD, W. Summa
ATTN: FCTMOF
ATTN: FCPR, J. Hill
ATTN: FCTMEI
ATTN: FCT

Field Command
Defense Nuclear Agency
ATTN: FCPRL

DEPARTMENT OF DEFENSE (Continued)

Field Command Test Directorate
Test Construction Division
Defense Nuclear Agency
ATTN: FCTC

Interservice Nuclear Weapons School
ATTN: TTV

Joint Chiefs of Staff
ATTN: SAGA
ATTN: J-5 Nuclear Division
ATTN: J-5 Force Planning & Pro Div

Undersecretary of Def for Rsch & Engrg
ATTN: Strategic & Space Sys (OS)
ATTN: Engineering Tech, J. Persh

DEPARTMENT OF THE ARMY

Atmospheric Sciences Laboratory
U.S. Army Electronics R&D Command
ATTN: DELAS-EO

BMD Advanced Technology Center
Department of the Army
ATTN: ATC-T, M. Capps
ATTN: ICRDABH-X
ATTN: ATC-O, F. Hoke
ATTN: ATC-R, F. King

BMD Program Office
Department of the Army
ATTN: DACS-BMT
ATTN: DACS-BMZ

BMD Systems Command
Department of the Army
ATTN: BMDSC, E. Williams
ATTN: BMDSC-HW
ATTN: BMDSC-H, N. Hurst
ATTN: BMDSC-NW
ATTN: BMDSC-HLA, R. Webb

Chief of Engineers
Department of the Army
ATTN: DAEN-MCE-D

Construction Engineering Rsch Lab
Department of the Army
ATTN: CERL-SOI-L

Deputy Chief of Staff for Rsch Dev & Acq
Department of the Army
ATTN: DAMA-CSM-N

Electronics Tech & Devices Lab
U.S. Army Electronics R&D Command
ATTN: DRSEL
ATTN: DELET-ER
ATTN: WPNS Effects Section

DEPARTMENT OF THE ARMY (Continued)

Harry Diamond Laboratories
Department of the Army

ATTN: DELHD-I-TL
ATTN: DELHD-N-P, L. Belliveau
ATTN: DELHD-N-P, F. Wimenitz
ATTN: DELHD-N-P
ATTN: DELHD-N-TS
ATTN: DELHD-N-P, J. Meszaros

U.S. Army Armament Material Readiness Command
ATTN: MA Library

U.S. Army Armament Rsch & Dev Command
ATTN: DRDAR-LCW

U.S. Army Ballistic Research Labs
ATTN: DRDAR-BLT, J. Keefer
ATTN: DRDAR-BLT, N. Schuman
ATTN: DRDAR-BLT, W. Taylor
ATTN: DRDAR-TSB-S

U.S. Army Cold Region Res Engr Lab
ATTN: Technical Director

U.S. Army Comm-Elec Engrg Instal Agency
ATTN: Tech Library

U.S. Army Missile R&D Command
ATTN: DRDMI-TKP

U.S. Army Mobility Equip R&D Cmd
ATTN: DRDME-WC

U.S. Army Nuclear & Chemical Agency
ATTN: Library
ATTN: Library for ATCA-NAW
ATTN: Library for MONA-SAL
ATTN: MONA-WE

U.S. Army Tank Automotive R&D Command
ATTN: DRDTA-UL

U.S. Army TRADOC Systems Analysis Activity
ATTN: ATAA-TDC, R. Benson

U.S. Army Training & Doctrine Cmd
ATTN: ATCD-T
ATTN: ATORI-OP

White Sands Missile Range
Department of the Army
ATTN: STEWS-FE-R
ATTN: Library

U.S. Army Communications Command
ATTN: Technical Reference Division
ATTN: CC-OPS-WR, R. Nelson
ATTN: CC-OPS-PD

U.S. Army Communications R&D Command
ATTN: DRDCO-COM RM, L. Dorkin

U.S. Army Edgewood Arsenal
ATTN: SMUEA-TS-TM, R. Navin

U.S. Army Engineer Center
ATTN: DT-LRC

DEPARTMENT OF THE ARMY (Continued)

U.S. Army Engineer Div Huntsville
ATTN: HNDED-SR

U.S. Army Engineer Div Ohio River
ATTN: ORDAS-L

U.S. Army Engineer School
ATTN: ATZA-DTE-ADM

U.S. Army Engr Waterways Exper Station
ATTN: WESSS, J. Ballard
ATTN: WESSE, L. Ingram
ATTN: Library
ATTN: WEssa, W. Flathau

U.S. Army Foreign Science & Tech Ctr
ATTN: DRXST-SD

U.S. Army Materiel Dev & Readiness Cmd
ATTN: DRXAM-TL
ATTN: DRCDE-D

U.S. Army Missile Command
ATTN: DRSMI-MSM, D. Loney
ATTN: Library

DEPARTMENT OF THE NAVY

David Taylor Naval Ship R&D Ctr
ATTN: Code L42-3

Naval Air Systems Command
ATTN: AIR-360G JP-2, J. Schultz

Naval Coastal Systems Laboratory
ATTN: D. Sheppard

Naval Construction Battalion Center
ATTN: Code L51, S. Takahashi
ATTN: Code L08A
ATTN: Code L51, R. Odello

Naval Electronic Systems Command
ATTN: PME 117-21

Naval Electronics Systems Command
ATTN: Commander

Naval Facilities Engineering Command
ATTN: Code O4B

Naval Material Command
ATTN: MAT 08T-22

Naval Research Laboratory
ATTN: Code 5584, E. Friebelie
ATTN: Code 7780
ATTN: Code 4709, W. Ali
ATTN: Code 7550, J. Davis
ATTN: Code 5584, G. Sigel
ATTN: Code 6770
ATTN: Code 8404, H. Pusey
ATTN: Code 2627

Naval Surface Weapons Center
ATTN: Code E21
ATTN: Code X211

DEPARTMENT OF THE NAVY (Continued)

Naval Surface Weapons Center
ATTN: W. Wishard
ATTN: Tech Library & Info Services Branch

Naval Weapons Center
ATTN: Code 233
ATTN: Code 3263, J. Bowen
ATTN: Code 266, C. Austin

Naval Weapons Evaluation Facility
ATTN: Code 10
ATTN: R. Hughes

Office of Naval Research
ATTN: Code 474, N. Perrone
ATTN: Code 715

Office of the Chief of Naval Operations
ATTN: OP 654E14
ATTN: OP 654C3, R. Piacesi

Strategic Systems Project Office
Department of the Navy
ATTN: NSP-43

DEPARTMENT OF THE AIR FORCE

Aeronautical Systems Division
Air Force Systems Command
ATTN: ASD/ENFTV
ATTN: ASD/YH-YEF, Capt Guice

Air Force Armament Laboratory
ATTN: DLYV, J. Collins

Air Force Institute of Technology
ATTN: Library

Air Force Systems Command
ATTN: Technical Library

Air Force Weapons Laboratory
Air Force Systems Command
ATTN: DYV
ATTN: NTE, M. Plamondon
ATTN: NTED, R. Matalucci
ATTN: NTES-G
ATTN: NTES-C, R. Henny
ATTN: SUL
ATTN: DEX

Assistant Chief of Staff
Intelligence
Department of the Air Force
ATTN: INT
ATTN: IN

Ballistic Missile Office
Air Force Systems Command
ATTN: MNNH

Deputy Chief of Staff
Research, Development, & Acq
Department of the Air Force
ATTN: AFRD

Foreign Technology Division
Air Force Systems Command
ATTN: NIIS Library
ATTN: SDBF, S. Spring

DEPARTMENT OF THE AIR FORCE (Continued)

Headquarters Space Division
Air Force Systems Command
ATTN: RST
ATTN: RSS

Headquarters Space Division
Air Force Systems Command
ATTN: SZJ, L. Doan

Strategic Air Command
Department of the Air Force
ATTN: XPQM
ATTN: NRI-STINFO Library

DEPARTMENT OF ENERGY

Department of Energy
Nevada Operations Office
ATTN: Mail & Records for Tech Lib

DEPARTMENT OF ENERGY CONTRACTORS

Brookhaven National Laboratory
ATTN: P. Levy

Lawrence Livermore National Laboratory
ATTN: Tech Information Dept

Los Alamos National Scientific Laboratory
ATTN: M. Pongratz
ATTN: Librarian
ATTN: MS 670, J. Hopkins

Oak Ridge National Laboratory
ATTN: Central Research Library
ATTN: Civ Def Res Proj, Kearny

Sandia National Laboratories
ATTN: Library & Security Class Div

Sandia National Laboratories
ATTN: L. Vortman
ATTN: 3I4I
ATTN: L. Anderson

OTHER GOVERNMENT

Central Intelligence Agency
ATTN: OSWR/NED

Department of Commerce
National Bureau of Standards
ATTN: R. Levine

Federal Emergency Management Agency
ATTN: Asst Dir for Rsch, J. Buchanon
ATTN: Hazard Eval & Vul Red Div

DEPARTMENT OF DEFENSE CONTRACTORS

Aerospace Corp
ATTN: L. Selzer
ATTN: Technical Information Services

Applied Theory, Inc
2 cy ATTN: J. Trulio

Artec Associates, Inc
ATTN: D. Baum

DEPARTMENT OF DEFENSE CONTRACTORS (Continued)

AVCO Research & Systems Group

ATTN: W. Reinecke
ATTN: A. Pallone
ATTN: Library A830

BDM Corp

ATTN: Corporate Library

Boeing Co

ATTN: Aerospace Library
ATTN: M/S 85/20, E. York
ATTN: R. Holmes

Boeing Co

ATTN: M/S 42/37, K. Friddell

Charles Stark Draper Lab, Inc

ATTN: Tech Library

University of Denver

Colorado Seminary

Denver Research Institute

ATTN: Sec Officer for J. Wisotski

Effects Technology, Inc

ATTN: R. Wengler

EG&G Washington Analytical Svcs Center, Inc

ATTN: Library

EG&G, Inc

ATTN: P. Zavaharo

Electromechanical Sys of New Mexico, Inc

ATTN: R. Shunk

Eric H. Wang

Civil Engineering Rsch Fac

University of New Mexico

ATTN: E. Wang
ATTN: D. Calhoun
ATTN: Technical Library
ATTN: G. Lane

Gard, Inc

ATTN: G. Neidhardt

General Electric Company—TEMPO

ATTN: W. Chan
ATTN: DASIAC
ATTN: J. Shoutens

Geocenters, Inc

ATTN: E. Marram

H-Tech Labs, Inc

ATTN: B. Hartenbaum

IIT Research Institute

ATTN: A. Longinow
ATTN: Documents Library

Information Science, Inc

ATTN: W. Dudziak

Kaman AviDyne

ATTN: N. Hobbs
ATTN: Library

DEPARTMENT OF DEFENSE CONTRACTORS (Continued)

Kaman Sciences Corp

ATTN: D. Sachs
ATTN: Library

Karagozian and Case

ATTN: J. Karagozian

Lockheed Missiles & Space Co, Inc

ATTN: TIC-Library

Los Alamos Technical Associates, Inc

ATTN: P. Hughes
ATTN: J. Kimmerly

Lovelace Biomedical Envir Rsch Inst, Inc

ATTN: Technical Library

Lulejian & Associates, Inc

ATTN: R. Daniels

Management Science Associates

ATTN: K. Kaplan

Merritt CASES, Inc

ATTN: Library

Mission Research Corp

ATTN: Tech Library

Mission Research Corp-San Diego

ATTN: V. Van Lint

Nathan M. Newmark Consul Eng Svcs

ATTN: W. Hall

National Academy of Sciences

National Materials Advisory Board

ATTN: D. Groves

Nichols Research Corp, Inc

ATTN: N. Byrn

Pacific-Sierra Research Corp

ATTN: H. Brode

Pacifica Technology

ATTN: Tech Library

Physics Applications, Inc

ATTN: F. Ford

Physics International Co

ATTN: J. Shea

ATTN: F. Sauer

R & D Associates

ATTN: A. Kuhl

ATTN: J. Carpenter

ATTN: F. Field

ATTN: P. Rausch

ATTN: R. Port

ATTN: Technical Information Center

R & D Associates

ATTN: B. Yoon

Rockwell International Corp

ATTN: Library

DEPARTMENT OF DEFENSE CONTRACTORS(Continued)

Science Applications, Inc
ATTN: D. Hove
ATTN: Tech Library

Science Applications, Inc
ATTN: J. McRary
ATTN: W. Mendes

Science Applications, Inc
ATTN: R. Miller
ATTN: Tech Library
ATTN: J. Dishon

Science Applications, Inc
ATTN: W. Chadsey
ATTN: W. Layson
ATTN: M. Knasel
ATTN: J. Cockayne
ATTN: G. Binninger
ATTN: R. Sievers
ATTN: W. Moechner
3 cy ATTN: B. Chambers III

Science Applications, Inc
ATTN: K. Sites

Southwest Research Institute
ATTN: W. Baker

SRI International
ATTN: D. McDaniels
ATTN: D. Keough
ATTN: A. Burns
ATTN: G. Abrahamson

DEPARTMENT OF DEFENSE CONTRACTORS (Continued)

Systems, Science & Software, Inc
ATTN: Library
ATTN: R. Duff

TeleDyne Brown Engineering
ATTN: Technical Library
ATTN: J. Ravenscraft

Tetra Tech, Inc
ATTN: Library

TRW Defense & Space Sys Group
ATTN: Technical Information Ctr
ATTN: N. Lipner
ATTN: J. Tambe
ATTN: B. Sussholtz
ATTN: R. Eastman

TRW Defense & Space Sys Group
ATTN: G. Hulcher
ATTN: P. Dai

FOREIGN GOVERNMENTS

Admiralty Surface Weapons Establishment
Ministry of Defense
ATTN: W. Delany

Atomic Weapons Research Establishment
2 cy ATTN: D. Samuels

British Defense Staff
British Embassy
ATTN: ACOW